

Amyloid Fibril Formation of the Parathyroid Hormone

Kumulative Dissertation

zur Erlangung des
Doktorgrades der Naturwissenschaften (Dr. rer. nat.)

der
Naturwissenschaftlichen Fakultät I
Biowissenschaften
der Martin-Luther-Universität
Halle-Wittenberg

vorgelegt von
Bruno Voigt

Gutachter:

- (1) Prof. Dr. Mike Schutkowski (Martin-Luther-Universität Halle-Wittenberg, Institut für Biochemie und Biotechnologie)
- (2) Prof. Dr. Jochen Balbach (Martin-Luther-Universität Halle-Wittenberg, Institut für Physik)
- (3) Jun.-Prof. Dr. Wolfgang Hoyer (Heinrich-Heine-Universität Düsseldorf, Institut für physikalische Biologie)

eingereicht am: 22.11.2023

verteidigt am: 27.05.2024

*The difficult is what takes a little time; the
impossible is what takes a little longer.*

Fridtjof Nansen

*I believe it is in our nature to explore, to
reach out into the unknown. The only true
failure would be not to explore at all.*

Ernest Shackleton

Table of Contents

Table of Contents	IV
List of Abbreviations.....	VI
List of Figures and Tables	X
1 Introduction.....	1
1.1 Amyloid Fibrils – Disease and Function.....	1
1.1.1 Introduction to Amyloid Fibrils.....	1
1.1.2 Functional Amyloids	4
1.1.3 Structural Differences between Pathogenic and Functional Amyloids.....	6
1.2 The Mechanism of Amyloid Formation	9
1.2.1 Macroscopic Fibrillation as Network of Microscopic Processes	9
1.2.2 The Role of Oligomers in Amyloid Growth.....	16
1.2.3 Kinetic Descriptions of Nucleated Polymerization and Nucleated Conformational Conversion.....	17
1.2.4 The Critical Concentration of Amyloid Formation.....	22
1.3 The Parathyroid Hormone.....	24
1.4 Scientific Questions	27
2 Publications and Results.....	29
2.1 Paper I: B. Voigt <i>et al.</i> (2023), A Competition of Secondary and Primary Nucleation Controls Amyloid Fibril Formation of the Parathyroid Hormone	30
2.2 Paper II: B. Voigt <i>et al.</i> (2023), The Prenucleation Equilibrium of the Parathyroid Hormone Determines the Critical Aggregation Concentration and Amyloid Fibril Nucleation	44
2.3 Paper III: L.M. Lauth <i>et al.</i> (2022), Heparin promotes rapid fibrillation of the basic parathyroid hormone at physiological pH.....	58
2.4 Additional Results Extending the Findings of Papers I-III.....	72
2.4.1 General Remarks	72
2.4.2 Effects of Denaturing and α -Helix Inducing Agents on the Structure of Free PTH ₈₄	73

2.4.3	Fibril Elongation of PTH ₈₄	75
2.4.4	Structural Aspects of PTH ₈₄ Fibrils.....	80
2.4.5	PTH ₈₄ Concentration Dependent Structure and Oligomerization at Acidic pH and the Influence of Heparin on Fibril Morphology	83
3	Comprehensive Discussion.....	89
3.1	The Mechanism of Amyloid Fibril Formation by PTH ₈₄ at Neutral pH	89
3.2	PTH ₈₄ Fibril Formation at Physiological-Like Conditions and Considerations on PTH ₈₄ as a Functional Amyloid.....	97
3.3	The Morphology and Molecular Structure of PTH ₈₄ Fibrils.....	100
3.4	Consequences of the Results on the Interpretation of Other Experiments	103
4	Summary	104
5	Zusammenfassung.....	106
6	References.....	108
	Appendix.....	XIII
A.1	Supporting Information for Paper I.....	XIII
A.2	Supporting Information for Paper II.....	XIX
A.3	Supporting Information for Paper III.....	XXXI
A.4	Supporting Information for Chapter 2.4	XXXVI
	List of Publications.....	XLIX
	Other Contributions	LII
	Acknowledgments.....	LIV
	Curriculum Vitae.....	LVII
	Statutory Declaration (Eidesstattliche Erklärung).....	LIX

List of Abbreviations

2D	two-dimensional
°C	degree Celsius
Å	Ångström (1 Å = 0.1 nm)
AA, AL, ATTR	amyloidosis derived from serum amyloid A, antibody light chain or transthyretin, respectively
A β , A β ₃₉ , A β ₄₀ , A β ₄₂	Amyloid β (Alzheimer peptide) comprising residues 1-39, 1-40 or 1-42, respectively
AC-PKA	adenylyl cyclase - protein kinase A
ANF	atrial natriuretic factor
β 2m	β 2 microglobulin
c_0	initial monomer concentration (in μ M)
c_{crit}	critical concentration (in μ M)
c_{eq}	concentration of soluble peptide in equilibrium with fibrils (in μ M)
CaSR	calcium sensitive receptor
CD	circular dichroism
cdc19	pyruvate kinase (<i>S. cerevisiae</i>)
cryoEM	cryogenic electron microscopy
CsgA, CsgB	curli specific genes A and B, encoding major and minor curli protein
CSP	chemical shift perturbation (CSP equals $\Delta\delta$)
d	diameter
δ	chemical shift
DewA	dew A
DOI	digital object identifier
EAS	easy wettable
ER	endoplasmic reticulum
F_{320} , F_{350}	fluorescence intensity at the indicated emission wavelength
FapC	fimbriae amyloid-like protein C
<i>Fib</i>	fibril
FGF23, FGFR1	fibroblast growth factor 23, FGF23 receptor
FUS	fused in sarcoma
γ	scaling factor
ΔG^0 , ΔG_{el}^0	difference of the Gibbs free energy in the absence of denaturants for protein folding or fibril elongation, respectively
GAG	glycosaminoglycan
GPCR	G protein coupled receptor
H	height
h	hour
HET-s	Heterokaryon incompatibility protein s
hIAPP	human islet amyloid polypeptide
HMW	high molecular weight
HSQC	heteronuclear single quantum coherence
IDP	intrinsically disordered protein/peptide
K	equilibrium constant

K_E, K_M	equilibrium constant at half maximal speed of elongation and secondary nucleation, respectively
$\kappa, \bar{\kappa}$	sum of secondary processes (NP and NCC, respectively)
k_+	rate constant of elongation
k_-	rate constant of fragmentation
k_2	rate constant of secondary nucleation from bulk solution (NP)
k_{conv}	rate constant of oligomer conversion (NCC)
k_d	rate constant of oligomer dissociation
k_n	rate constant of primary nucleation from bulk solution (NP)
k_{off}	rate constant
$k_{\text{oligo},1}, k_{\text{oligo},2}$	rate constant of oligomer formation in solution or assisted by a fibril surface, respectively (NCC)
$\lambda, \bar{\lambda}$	sum of primary processes (NP and NCC, respectively)
$\lambda_{\text{exc}}, \lambda_{\text{min}}$	excitation wavelength, wavelength at minimal signal
L	fibril length
LARKS	low-complexity aromatic-rich kinked segments
m	cooperativity factor, mass
m	meter
M	molar, 1 M = 1 mol l ⁻¹
$M_0, M(t)$	(initial) fibril mass concentration (referring to monomer equivalents, given in μM)
$dM/dt _0$	initial gradient of fibril mass increase
M_w	molecular mass
MBP	major basic protein
Mon	monomer
Mot3	modifier of transcription 3
n	refractive index, amount of substance
N, N_A	particle number, Avogadro constant
N_{aa}	chain length, number of amino acids
$N_{\text{mon}}, N_{\text{fib}}, N_{\text{m/f}}$	number of monomers, fibrils and monomers per fibril, respectively
n_2	reaction order of secondary nucleation from bulk solution (NP)
n_c	reaction order of primary nucleation from bulk solution (NP)
n_{conv}	reaction order of oligomer conversion (NCC)
n_{elon}	reaction order of elongation
$n_{\text{oligo},1}, n_{\text{oligo},2}$	reaction order of oligomer formation in solution or assisted by a fibril surface, respectively (NCC)
NCC	nucleated conformational conversion
NMR, ssNMR	(solid state) nuclear magnetic resonance
NP	nucleated polymerization
NWD2	NACHT and WD repeat domain-containing protein 2
$O(t)$	concentration of oligomers
OPG	osteoprotegerin
Orb2	oo18 RNA binding gene encoded protein 2
pdb	protein data base
$P_0, P(t)$	(initial) fibril number concentration (in μM)

List of Abbreviations

PHD	peptide hormone derived
pI	isoelectric point
PI3-SH3	Src-homology 3 domain of phosphatidylinositol-3-kinase
PLC-PKC	phospholipase C - protein kinase C
Pmel17	premelanosome protein 17
PSM α 3	phenol-soluble modulins α 3
PTH ₈₄	mature parathyroid hormone with 84 amino acids
PTH1R, PTH2R	PTH receptor 1 and 2, respectively
r	radius
r_0	initial gradient of ThT fluorescence increase
R	gas constant
ρ	density
$r_{H,app}$	apparent (ensemble) hydrodynamic radius
RANK, RANKL	receptor activator of nuclear factor κ B (ligand)
RNA, mRNA	(messenger) ribonucleic acid
s	second
Sup35	suppressor 35
Swi1p	switching deficient 1
t	time
T	temperature
$t_{1/2}$	half-time of fibril formation
TFE	2,2,2-Trifluoroethanol
Θ_{MRW}	mean residue ellipticity
TGN	trans Golgi network
TEM, nsTEM	(negative staining) transmission electron microscopy
ThT	Thioflavin T
Ure2p	urease encoding gene protein 2
V	volume
VDR	vitamin D receptor
Whi3	whiskey 3

Amino acids are referred to by their respective full name or one-letter abbreviation.

List of Figures and Tables

Figures

Figure 1.1	Schematic and exemplary structures of amyloid fibrils.	p. 3
Figure 1.2	Concept of the storage of peptide hormones as functional amyloid fibrils.	p. 5
Figure 1.3	Comparison of reported fibril core structures of functional and pathological amyloids.	p. 7
Figure 1.4	Schematic overall kinetic profile of amyloid self-assembly.	p. 9
Figure 1.5	Individual microscopic processes involved in amyloid fibril formation.	p. 12
Figure 1.6	Possible cases of concentration dependences of fibril formation.	p. 13
Figure 1.7	Principles of seeded fibril growth.	p. 15
Figure 1.8	Simplified schematic Gibbs free energy landscapes for three scenarios of oligomer formation.	p. 17
Figure 1.9	Simplified nucleation schemes according to the models of nucleated polymerization and nucleated conformational conversion.	p. 19
Figure 1.10	Influence of variations of the two parameters $\bar{\lambda}$ and $\bar{\kappa}$ of Equation 1.14 on the appearance of the fits.	p. 21
Figure 1.11	Concept of the critical concentration.	p. 22
Figure 1.12	PTH ₈₄ biosynthesis and action.	p. 25
Figure 2.1	Summary of the investigation of the mechanism of PTH ₈₄ fibril formation as described in the papers and resulting open questions.	p. 73
Figure 2.2	CD spectra monitoring the effect of urea and TFE on PTH ₈₄ secondary structural ensemble at 50 μ M (regime II) and 500 μ M (regime IV).	p. 74
Figure 2.3	Effects of urea on elongation and c_{crit} of PTH ₈₄ .	p. 76
Figure 2.4	Increase of fibril mass $M(t)$ during seeded fibril growth and effects of fibril elongation at low concentrations.	p. 77
Figure 2.5	Increase of fibril mass $M(t)$ during seeded fibril growth.	p. 79
Figure 2.6	Fibril growth below the critical concentration.	p. 80
Figure 2.7	Prediction and preliminary PTH ₈₄ structure determination by cryoEM.	p. 82
Figure 2.8	Analysis of the concentration dependence of PTH ₈₄ at pH 5.5.	p. 84
Figure 2.9	Electron micrographs acquired for PTH ₈₄ samples after fibril formation at pH 5.5 in the presence of heparin at a magnification of 3000 x, 12000 x and 20000 x.	p. 86
Figure 3.1	Details of individual processes and their interactions.	p. 90
Figure 3.2	Representation of the analogy between the thermodynamic equilibrium in the presence of fibrils and the prenucleation equilibrium at regime II ($c_0 < c_{\text{crit}}$).	p. 92
Figure 3.3	Representation of seeded fibril growth at concentrations below c_{crit} .	p. 94
Figure 3.4	Summary of the presented findings concerning the molecular mechanism of PTH ₈₄ fibril formation.	p. 96

Figure 3.5	Models of PTH ₈₄ fibril formation at physiological-like conditions.	p. 98
Figure 3.6	Structural models of PTH ₈₄ fibrils.	p. 100
Figure 3.7	Sequence determinants for curvilinear fibrils found in PTH ₈₄ .	p. 101
Figure 3.8	Model of the influence of conditions and control mechanisms on PTH ₈₄ fibril morphology.	p. 102
Figure A.1	CD monitored analysis of urea mediated PTH ₈₄ unfolding at peptide concentrations of 50 μ M (regime II) and 500 μ M (regime IV).	p. XXXVI
Figure A.2	Effects of urea on seeded fibril growth of PTH ₈₄ .	p. XXXVII
Figure A.3	Increase of fibril mass $M(t)$ during seeded fibril growth and effects of fibril elongation at low concentrations.	p. XXXIX
Figure A.4	Estimation of the average length and height of fibril seeds.	p. XL
Figure A.5	Monitoring of seeded fibril growth for cryoEM fibril preparation.	p. XLIII
Figure A.6	Examples of cryoEM images from the first PTH ₈₄ fibril sample.	p. XLIV
Figure A.7	TEM monitored screening of potential PTH ₈₄ fibril preparation protocols for the structural analysis by cryoEM.	p. XLV
Figure A.8	Structural analysis of PTH ₈₄ fibrils.	p. XLVI

Figures presented in Papers I-III are referred to in this thesis as “Paper *number* - Figure *number*” in contrast to figures and tables being part of this work which are referred to as mentioned above.

Tables

Table 2.1	Summary of the PTH ₈₄ concentration regimes identified in Paper II.	p. 72
Table 3.1	Indications of functional amyloids and experimental evidence for PTH ₈₄ .	p. 99
Table A.1	Results of the analysis of the soluble fraction in dependence on the urea concentration.	p. XXXVIII
Table A.2	Determination of the soluble fraction after seeded fibril growth in the presence and absence of ThT.	p. XLIII

1 Introduction

1.1 Amyloid Fibrils – Disease and Function

1.1.1 Introduction to Amyloid Fibrils

The roots of amyloid research date back to 1906 when the German psychiatrist Alois Alzheimer was the first to describe a “peculiar” disease with starch-like plaques deposited in the brain of a patient diagnosed with dementia.¹ The exploration of the structure of such protein deposits and similar sources of aggregated protein was initiated 1934 by Astbury working on X-ray diffraction of denatured protein and fibres.^{2,3} In the year 1968, Eanes and Glenner were the first to show the characteristic X-ray diffraction pattern of amyloid fibrils with two main reflexes (Figure 1.1A).⁴ In the meantime, the invention and development of the electron microscope⁵ allowed the exploration of amyloids in human tissue, as first reported in 1959 for fibrils extracted from liver.⁶ Kidd and Terry independently demonstrated in 1963 that paired helical filaments, or neurofibrillary tangles, accumulated in affected brains of Alzheimer patients.^{7,8} Research on amyloid formation and structure exponentially increased after the amyloid hypothesis for Alzheimer’s disease was postulated in 1991. Here, the deposition of amyloid fibrils of the Alzheimer peptide A β in the extracellular space of the brain was postulated to be causative for the disease.^{9,10} A β comprises 39 to 43 residues due to proteolytic cleavage of the trans-membrane amyloid precursor protein APP.¹¹ Chain lengths of 40 and 42 are the most abundant forms, termed A β ₄₀ and A β ₄₂, respectively.¹² Later, experimental evidence suggested stable early-stage oligomeric states of A β to actually be the cytotoxic species rather than the mature fibrils.¹³

The first atomic resolution structures of amyloid fibrils calculated by the use of NMR spectroscopy were presented in 2016.^{14,15} The development of cryogenic electron microscopy (cryoEM) classifies a milestone in amyloid research enabling a high-throughput method to determine the three-dimensional structure of amyloid fibril core segments, with the first example published in 2017 with 3.4-3.5 Å resolution.¹⁶

In fact, the term “amyloid”, and the corresponding disease termed amyloidosis, is not restricted to Alzheimer’s disease or neurological disorders in general. Amyloid diseases are classified as deposits restricted to local sites or affecting more than one organ, i.e. systemic.¹⁷ Furthermore, hereditary diseases, associated to a genetic component, are distinguished from sporadic forms. Other amyloid diseases affecting the central nervous system are Parkinson’s disease associated with fibrils of α -synuclein,¹⁸ different tauopathies originating from the protein tau¹⁹ or amyotrophic lateral sclerosis associated with fibrils of the RNA binding protein FUS (fused in sarcoma).^{20,21} Among the most common forms of systemic amyloidosis are those derived from fibrils of serum amyloid A (AA),²²⁻²⁴ antibody light

chains (AL)²⁵ or transthyretin (ATTR).²⁶ Amyloid deposition can also be related to medical treatments like long-term dialysis (β 2-microglobulin)²⁷ or to the injection of insulin for diabetes patients which is restricted to the injection site.²⁸ Amyloidosis can also be derived from peptide hormones (PHD) and are locally deposited in the respective endocrine tissue.²⁹ Examples for PHD amyloidosis are deposited fibrils composed of calcitonin,³⁰ human islet amyloid polypeptide (hIAPP),³¹ atrial natriuretic factor (ANF)³² and prolactin.³³

All amyloid fibrils share common characteristic structural features. Fibrils are protein assemblies, containing usually hundreds to thousands of individual chains, ordered in one dimension and in a repetitive fashion with the so-called cross- β motif as the repeating substructure (Figure 1.1A).^{6,34,35} The motif consists of stacked β -strands oriented perpendicular to the fibril axis. In fibrillar assembly, β -sheets, which are an important element of secondary structure for proteins, represent a quaternary organization here. Typically, two β -sheets are stacked and stabilized by side-chain interactions. The interdigitation of (hydrophobic) side chains, referred to as a steric zipper, leads to a tight, dry (water excluded) interface mediating a high thermodynamic stability (Figure 1.1B).³⁶ In fibrils assembled from small peptides, the β -sheets can be organized in parallel or antiparallel manner, but are commonly found “in register”. This refers to the type of stacking of the individual strands. For parallel sheets, the strands are positioned directly above each other, whereas a strand in antiparallel sheets is oriented directly above the strand two rows next to it (see also Figure 1.1A).³⁷ In addition to steric zippers, an alternative, less stable form of fibril organization has been reported involving low-complexity domains.³⁸ Such domains can weakly assemble as kinked β -sheets stabilized by aromatic side chains, therefore termed low-complexity aromatic-rich kinked segments (LARKS, Figure 1.1C).

However, amyloid fibrils assembled from full length proteins or peptides display a much greater structural variability and complexity than fibrils of short oligopeptides (Figure 1.1D). The conformation of β -sheets consisting of L-amino acids, inducing a torsion by steric hindrance of side chains, transfers the chirality across length scales leading to a characteristic macromolecular helical twist of the fibrils.³⁹ The analysis of X-ray diffraction data of amyloid filaments shows two characteristic distances present in the fibril core, i.e. \approx 4.7 nm and 8-12 nm representing the interstrand (hydrogen bonded β -strands) and intersheet distances (spacing of distinct β -sheets), respectively (Figure 1.1A).^{2,4,40}

Amyloid fibrils of e.g. A β ₄₀ appear as long, straight, rigid filaments. In contrast, globular oligomers as well as curvilinear fibrils are found to be morphologically distinct, persistent, metastable intermediates during fibril growth, e.g. in early stages of A β fibrillogenesis (Figure 1.1E).⁴¹ Thus, curvilinear fibrils are also referred to as protofibrils assembling towards mature, straight fibrils. Investigations of lysozyme fibril formation showed that the exact pathway is determined by protein concentration (dependent on the salt concentration).⁴²⁻⁴⁴ Curvilinear fibrils were found to rapidly assemble *via* oligomer fusion,⁴²

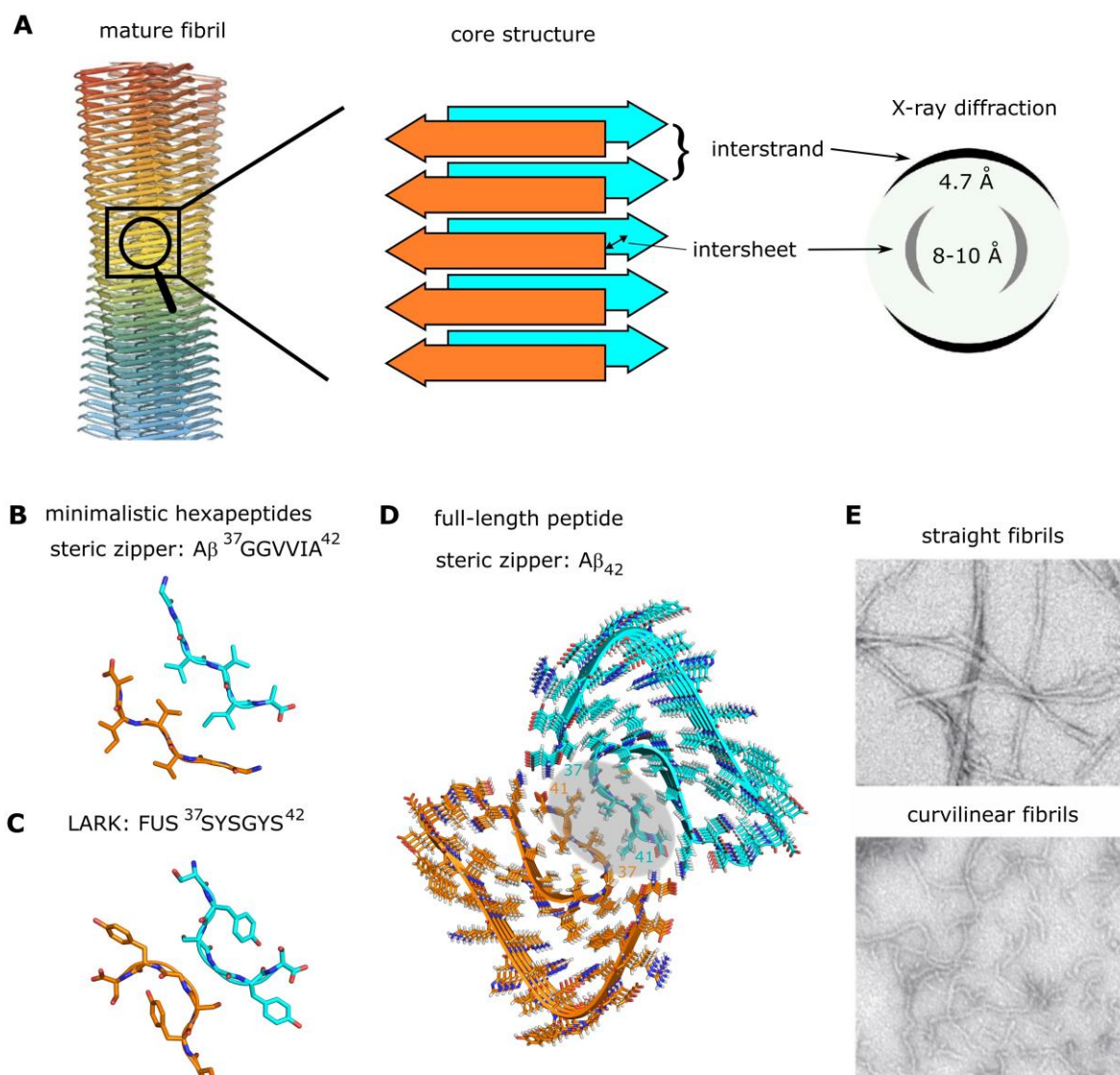


Figure 1.1: Schematic and exemplary structures of amyloid fibrils. **A** – CryoEM structure of a mature fibril (left), the core structure consists of stacked β -sheets (middle) with defined interstrand and intersheet distances of typically ≈ 4.7 Å and 8-10 Å, respectively, as indicated by distinct reflections of the X-ray diffraction pattern (right). **B** – Minimalistic hexapeptides typically show defined packing states with interdigitated side chains (steric zippers) as in the case of A β ^{37GGVVIA}⁴² (pdb: 2ONV⁴⁵, X-ray diffraction of crystalline fibers). **C** – Additionally, kinky segments (LARKS), often observed for functional fibrils, e.g. for FUS^{37SYSGYS}⁴² (pdb: 6BWZ,³⁸ X-ray diffraction of crystalline fibers) are much less stable. **D** – Fibrils assembled from full-length peptides often show a higher degree of complexity, as in the case of A β ₄₂ (pdb: 5OQV⁴⁶, cryoEM). **E** – Mostly, straight fibrils are observed (upper panel), whereas curvilinear fibrils (lower panel) are less frequently found. Fibril core structures are viewed down the fibril axis. Each individual peptide unit is colored separately (same color is used for the two copies), nitrogens are colored in dark blue, hydrogens in red. In panel D, six copies of the stacked β -strands are displayed. The fibril shown in panel A was taken from ref.⁴⁶, the schematic X-ray diffraction pattern from ref.⁴⁷ and the electron micrographs in panel E from ref.⁴⁸.

thus, such fibrils grow above a certain critical oligomer concentration and are finally replaced by straight fibrils.⁴³ Below the critical oligomer concentration, the absence of globular oligomers directly allows nucleation and growth of straight fibrils. Similar observations were reported for a dimeric A β ₄₀ that was designed as a single expressed construct where the two A β ₄₀ peptides are linked by a (G₄S)₄ sequence.⁴⁹

1.1.2 Functional Amyloids

This intensive research with focus on disease and therapy might be the origin of the strong connection of amyloid fibrils with protein misfolding and pathology. However, amyloids can also represent phase separated functional states and are widespread in bacteria.⁵⁰ Extracellular amyloid formation has been demonstrated for 10-50 % of bacterial species from different habitats.⁵¹ Additionally, functional fibril formation is important in other realms of life, e.g. for yeast, fungi, amphibians and mammals.⁵⁰ The inherent ability of amyloids to self-replicate even for minimal chain lengths gave rise to the hypothesis that amyloids were the first (bio-)molecules able to catalyze chemical reactions, transmit information and evolve, even before RNA, and might therefore be the “origin of life”.⁵²⁻⁵⁴ The specific fields of action of functional amyloids can be summarized in five categories.⁵⁰ This classification involves (1) storage of proteins, (2) structure, (3) information, (4) loss of function and (5) gain of function. Note that specific amyloids can be assigned to more than one of the described groups.

A well-recognized function of non-pathogenic amyloids is the storage of proteins (category 1). A variety of peptide hormones, demonstrated for hormones from the pituitary glands, is stored in the fibrillar form before its release into the blood stream (Figure 1.2A).⁵⁵ Amyloids are also present in the mammal immune system. Eosinophils, a type of white blood cells, contain the major basic protein (MBP) destabilizing the membranes both of the intruder and the host in its toxic monomeric form, therefore it is stored in an inert manner as amyloid.⁵⁶ Additionally, it has been demonstrated that inclusion bodies of heterologous expressed proteins in *E. coli* contain amyloid structures.⁵⁷ Examples for amyloids involved in functional structure formation (category 2) are amyloids of Pmel17 in mammals templating tyrosine oxidation during melanogenesis.⁵⁸ In *E. coli* and *Pseudomonas*, amyloids of CsgA (curli protein) and FapC, respectively, are components of the extracellular matrix forming biofilms.⁵⁹⁻⁶¹ The hydrophobins DewA or EAS play a role in aerial hyphae formation as well as in surface attachment of filamentous fungi.⁶²⁻⁶⁴ An interesting function of amyloids is the protection of oocytes from fish, silk moth or of mammalian sperms.⁶⁵⁻⁶⁷ Amyloids associated to information (category 3) can be excessively found in yeast, e.g. *S. cerevisiae*. Prion proteins bearing a polyQ sequence, for which the amyloid form displays the inactive state, are involved in translational termination (sup35),⁶⁸ chromatin remodeling (Swi1p)⁶⁹ or transcriptional regulation (Ure2p, Mot3).^{70,71} Intriguingly, amyloids can be involved in long term memory as demonstrated for *S. cerevisiae* (mnemons, e.g. Whi3, fibrillating as consequence of pheromone exposure promoting cell cycle entry)⁷² and *Drosophila melanogaster* (translational repressor function of Orb2 turned into activator upon fibril formation).^{73,74} In addition to the examples mentioned for category 3, the pyruvate kinase Cdc19 in *S. cerevisiae* can be stored in stress granules to suppress its enzymatic function.⁷⁵ The release of the active monomeric protein after stress ensures a cell cycle restart preventing the cell from stress-induced degradation. Category 5 represents amyloid systems in which the fibril state or fibrillar oligomers represent an active form, i.e. a gain of function

mechanism. The HET-s prion of *Podospora anserine* acts in the recognition of heterokaryon incompatibility (cell fusion of different strains) and leads to limited cell death by membrane penetration.^{76,77} In the same fungi species, amyloid oligomers of e.g. NWD2 play a role in signal transduction connected to cell fate pathways ensuring the defense of the host.⁷⁸

In endocrine cells, peptide hormones can be stored at high concentrations in secretory granules which are enclosed by a membrane (Figure 1.2A).⁷⁹ The concentration of peptides in these granules can reach a very high level.⁸⁰ This mechanism allows the cells to release peptides faster and in a higher amount upon an external signal compared to *de novo* synthesis. Moreover, peptides are stored in the amyloid state providing the densest packing as well as stability.^{55,81} This has implications on hormone sorting in the Golgi apparatus as well as on granule formation. One possibility of peptide hormone fibril formation control is a high local concentration enabling primary nucleation.^{50,80} The pH decrease from pH 7.4 in the endoplasmic reticulum (ER) towards pH 5.5 in the granules can also be a control mechanism.^{55,82} Initiation of fibril formation by helper molecules, such as glycosaminoglycans (GAG), e.g. heparin, represents a third mechanism of control (Figure 1.2B).^{55,83-86} As a response to signaling, peptide hormone amyloids are released into the blood stream where they disassemble into functional monomers. The dilution effect could be a simple control mechanism for dissociation.^{55,87} For example, β -endorphin requires protonation of a core glutamine residue to initiate fibril formation.⁸⁸ The deprotonation upon pH increase in the case of release triggers dissociation of β -endorphin fibrils.

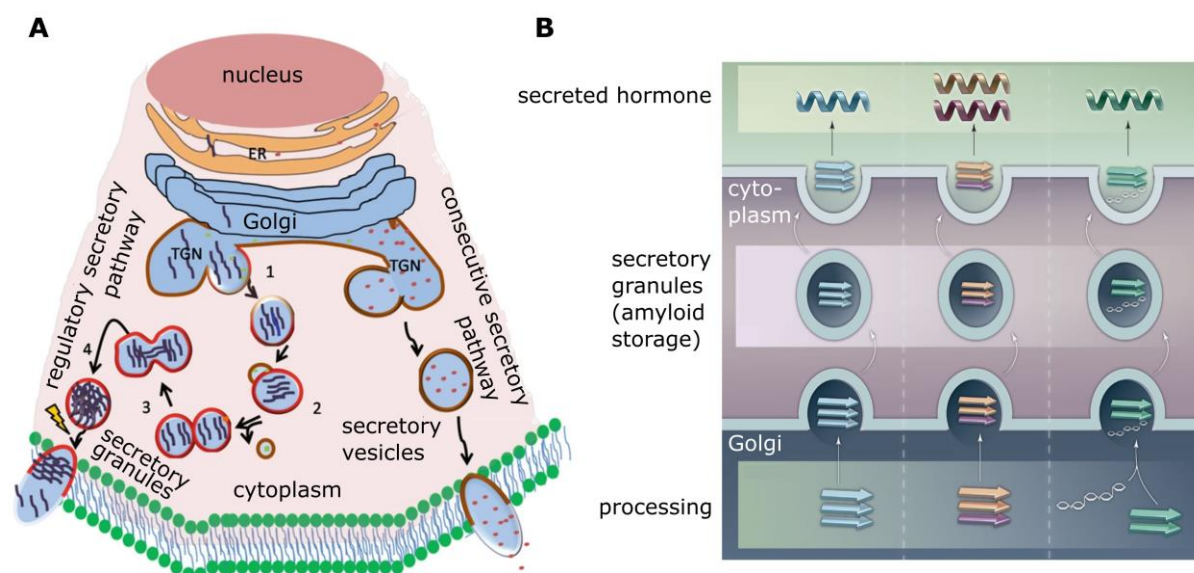


Figure 1.2: Concept of the storage of peptide hormones as functional amyloid fibrils. **A** – Scheme of the biosynthesis and processing of peptide hormones and their subsequent storage as fibrils in secretory granules upon their release (left) or their subsequent release *via* the consecutive secretory pathway (right). **B** – Functional fibril formation of peptide hormones can form spontaneously (left), assisted by coassembly with other peptides (middle) or with GAGs (right). The scheme in A is adapted from ref.⁹¹, the scheme in B from ref.⁹².

Additionally, chaperones could possibly be involved in disassembly of fibrils.^{89,90} Such tight control mechanisms ensure correct timing and localization of functional amyloids as well as monomer release.⁵⁰ Misregulation bears potential toxicity, e.g. fibril formation at the wrong site. Fibrillation in the ER instead of granules for vasopressin, which induces reabsorption of water in the kidney and an increased arterial blood pressure, leads to ER stress and finally to cell death.⁹³

As already pointed out, control as well as speed of fibril formation are key features of functional amyloids. For hormones, prohormone cleavage by prohormone convertases is in most cases essential to initiate fibril formation, e.g. in the case of Pmel17.⁹⁴ The modulation of rates or even the fibrillation level by “gatekeeper” residues, e.g. asparagine, glycine, lysine, arginine and proline flanking fibril core sequences, is an intriguing control example as demonstrated for CsgA.⁹⁵ In addition, CsgB mediates CsgA nucleation. Such control mechanisms are proposed to be the reason why functional amyloids are not toxic towards their host organism.⁹⁶ Indeed, the carbohydrate-free M α subunit of Pmel17 fibrillates within seconds,⁵⁸ Orb2 within minutes⁹⁷ and FapC as well as CsgA within a few hours.⁹⁸ Interestingly, fibrillar assembly of functional amyloids is often driven by primary nucleation, whereas secondary processes only have small effects on the overall kinetics.⁹⁸ This reflects, to a certain extent, the importance of folded proteins for functional amyloid formation, rather than misfolding.⁵⁰

1.1.3 Structural Differences between Pathogenic and Functional Amyloids

Independent from the nature of action (pathological or functional), all amyloids share common properties of long filamentous structures typically assembled *via* a cross- β structure in the fibril core. Recent advances in cryoEM enable the comparison of pathogenic and functional amyloids on a molecular, structural level.⁹⁹ For example, polar residues, such as serine and glutamine, as well as glycine are more abundant in functional amyloids, offering flexible interfaces required for reversibility. In contrast, glutamate and lysine residues are more prevalent in pathological amyloids, while aliphatic residues are found both in pathological amyloids and biofilm-associated bacterial functional amyloids serving as scaffolds.

The impact of amyloid fibrils in physiological function suggests that the amino acid sequences of the corresponding monomeric proteins evolved towards an amyloidogenic structure, thus allowing tight control, reversibility and the avoidance of toxicity.⁵⁰ Furthermore, disease related amyloids often contain so-called frustrated segments forced into energetically unfavorable conformations.¹⁰⁰

An intriguing feature (so far only) of functional amyloids is the occurrence of cross- α fibrils with stacked α -helices, as first observed for bacterial PSM α 3 from *Staphylococcus aureus*.¹⁰¹ The helical motif in the fibril core was found to be important for the cytotoxic function of PSM α 3. Even more surprising,

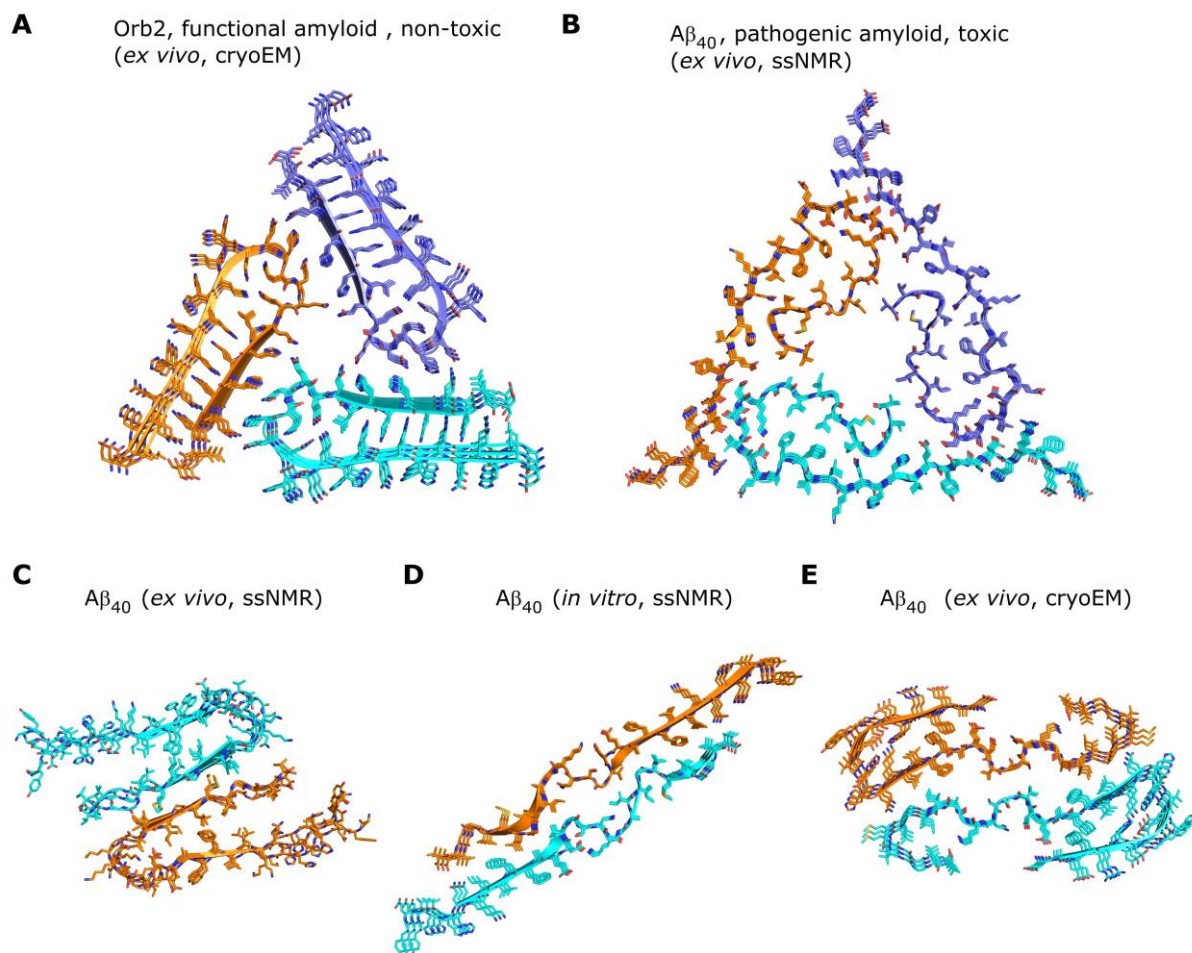


Figure 1.3: Comparison of reported fibril core structures of functional and pathological amyloids. **A** – Orb2 forms functional fibrils with a triangular hydrophilic core comprising three individual protein units (pdb: 6VPS,⁷³ cryoEM, *ex vivo* fibrils). **B** – A similar triangular architecture was found for pathological A β_{40} fibrils bearing a hydrophobic core (pdb: 2M4J,¹⁰² solid-state NMR (ssNMR), *in vitro* fibril formation from *ex vivo* fibrils as seeds). **C-E** – Essentially, in contrast to Orb2, A β_{40} fibrils display a strong polymorphism dependent on a variety of conditions. Three examples are given in panels C (pdb: 2LMN,¹⁰³ solid-state NMR, *in vitro*), D (pdb: 6W0O,¹⁰⁴ ssNMR, *in vitro* fibril formation from *ex vivo* fibrils as seeds) and E (pdb: 6SHS,¹⁰⁵ cryoEM, *ex vivo*). The segments are viewed along the fibril axis. Three consecutive β -stacks are shown. Each individual peptide unit is colored separately (same color is used for the two copies), nitrogens are colored in dark blue, hydrogens in red.

cross- α fibrils of *Uperoleia mjobergii* amphibian antimicrobial uperin 3.5 can be transformed to a cross- β architecture and *vice versa*.¹⁰⁶ This chameleon character is attributed to the regulation of the activity. Cross- α fibrils form at the surface of bacterial cells mediating cytotoxicity while the cross- β fibrils are inactive, thus possibly offering an additional storage function.

Non-functional, pathogenic amyloids are almost always found to display a high degree of polymorphism,¹⁰⁷ i.e. the same protein forms fibrils of different (core) structures, interfaces, number of composing protofilaments or filament symmetry which can be dependent on the experimental conditions or can exist simultaneously within the same sample.¹⁰⁸ The broad distribution of the conformational space associated with misfolding of natively folded proteins or of intrinsically disordered peptides (IDP) and the variability of their assembly is discussed as a biochemical basis for

fibril morphology, e.g. *via* the selection of conformational states for nucleation.¹⁰⁹ In contrast, functional amyloids are found to be monomorph under physiological conditions and, at least in the case of CsgA, also under harsh conditions.¹¹⁰ The already described membrane-associated Orb2 amyloids are a good example to demonstrate this characteristic difference between physiological and pathological fibrils.^{50,111} CryoEM structure determination of Orb2 fibrils required the extraction of material from appr. three million individual *D. melanogaster* flies, resulting in one (resolvable) structure (Figure 1.3A).⁷³ In contrast, A β ₄₀ fibrils, either assembled *in vitro* or extracted *ex vivo*, typically show a high level of polymorphism (Figure 1.3B-E). This demonstrates that physiological amyloids require one defined macromolecular structure in order to perform their function. The controlled fibril assembly seems to be a very important issue to ensure the correct structure since *in vitro* assembled Orb2 fibrils substantially differ from endogenous fibrils in terms of morphology, seeding capacity and biochemical activity.⁷³ Figure 1.3B displays a 3D structure of an A β ₄₀ fibril with three individual peptides in the fibril core similar to the functional fibril of Orb2 (Figure 1.3A). The most significant difference might be the contributing amino acid residues: While the A β ₄₀ fibril consists of hydrophobic steric zippers, lysine residues form the intramolecular and histidines the intermolecular (intersheet) interfaces of Orb2 fibrils, resulting in a polar core structure bearing the potential for easy reorganization.

1.2 The Mechanism of Amyloid Formation

1.2.1 Macroscopic Fibrillation as Network of Microscopic Processes

The assembly of amyloid fibrils is described as a nucleated polymerization of proteins.¹¹² To induce growth, the formation of a species of minimal size bearing growth-competent ends is essential, referred to as fibril nucleus. The fibril grows *via* the addition of new, in most cases, monomers. Experimentally monitoring the *de novo* growth of amyloid fibrils from a protein monomer solution will lead in most cases to a kinetic profile with a sigmoidal shape (Figure 1.4).¹¹³ A small fluorescent dye which is widely used for fibril detection is Thioflavin T (ThT) that shows increased fluorescence upon intercalation onto the fibril surface.¹¹⁴ The (schematic) profile is divided into three phases. In the lag phase, monomers are converted into nuclei capable of growing to (proto-) fibrils. Early fibrillar assembly occurs below the experimental detection limit.¹¹⁵ The following sigmoidal fast fibril replication and growth is referred to as growth phase. Finally, fibrillation turns into a plateau phase which is also called steady-state or thermodynamic equilibrium. A valuable parameter to compare fibrillation kinetics is the half time $t_{1/2}$. This parameter is defined as the time-point at which half of the maximum mass of amyloid fibrils is formed.¹¹³

For a detailed examination, the time evolution of each individual fibril species would need to be followed.¹¹⁶ However, tracking of each species is complex, especially since bulk methods like ThT detection monitor the overall gain of fibrillar material.¹¹⁴ A significant reduction of the complexity can be achieved by focusing on two parameters of the fibril length distribution at a given monomer concentration $c(t)$: the time dependent evolution of the number concentration $P(t)$ (referring to the number of fibrils, given in molar concentration in units of 1 M) and the mass concentration $M(t)$

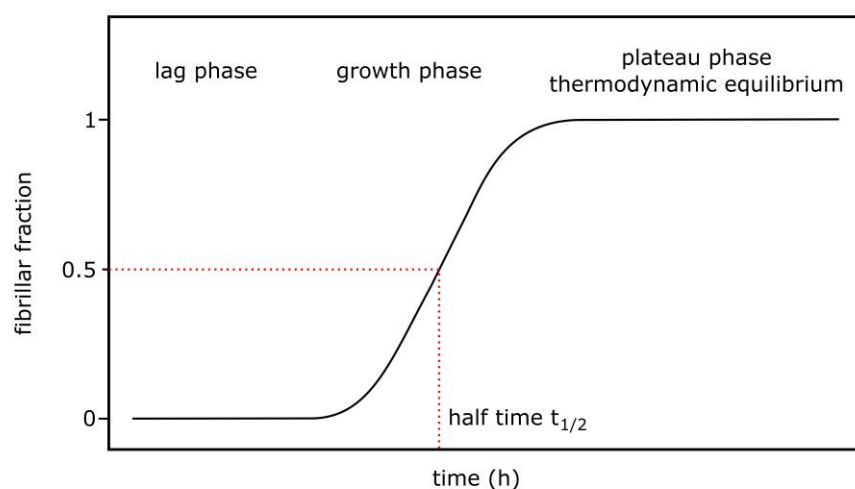


Figure 1.4: Schematic overall kinetic profile of amyloid self-assembly. The sigmoidal shape defines the three macroscopic phases, i.e. the lag, exponential growth and plateau phase. The time-point at which the fibrillar mass reaches 50 % of its plateau value is referred to as half-time $t_{1/2}$.

(referring to the monomer equivalent incorporated into fibrils, given in molar concentration in units of 1 M) of fibrils of any size.^{112,117,118}

Intensive research over the last decades revealed that the macroscopically observable sigmoidal fibrillation behavior originates from an intricate network of individual microscopic processes (Figure 1.5A).¹¹⁹ These individual processes are classified as processes affecting fibril mass M or fibril number P . The latter can further be sub-divided into monomer dependent primary and fibril dependent secondary (multiplication) processes. In the following, the individual processes as well as the corresponding rate equations will be introduced according to well-established descriptions.^{112,116,118}

- **Elongation** is considered to be the main contribution to the increase of fibril mass. The mechanism is typically understood as a ‘dock-and-lock’ process in which a monomer from solution attaches to a growth-competent end followed by a rearrangement step generating a new growth-competent end. At low concentrations, the monomer concentration dependent fast attachment step is rate-limiting, while the slower conversion step determines the rate at high concentrations. This leads to a saturation of the elongation process at high concentrations and shares high similarity with Michaelis-Menten like enzyme kinetics. Here, K_E describes the equilibrium constant at the half-maximal growth speed. The overall rate constant for elongation is k_+ .

$$\frac{dM}{dt} = \frac{2 k_+ c(t) P(t)}{1 + \frac{c(t)}{K_E}} \quad \text{Equation 1.1}$$

- **Primary nucleation** is the main process generating new fibrils in the lag phase of fibrillation. Primary nuclei are formed involving only peptides from bulk solution. The nucleus is defined to be smallest species offering growth competent ends. It is therefore thermodynamically unfavorable and is either rapidly dissociating or being elongated. Traditionally, primary nucleation is modeled as a single-step process with the rate constant k_n and the reaction order n_c though the exact molecular mechanism can involve several association and conversion steps. The associated increase of fibrillar mass due to primary nucleation is considered to be negligible.

$$\frac{dP}{dt} = k_n c(t)^{n_c} \quad \text{Equation 1.2}$$

- **Secondary nucleation** describes the formation of nuclei from monomers catalyzed by a present fibril surface. Thus, it only contributes to the overall fibrillation when a certain fibrillar mass has already been formed. In analogy to the mechanism described for elongation above, secondary nucleation can be considered as a two-step process involving a monomer concentration dependent attachment to the fibril surface and a subsequent rearrangement and detachment. Therefore, saturation can occur at high protein concentrations, where K_M is the equilibrium constant where dP/dt is half-maximal. The overall rate constant is k_2 with the corresponding reaction order n_2 .

$$\frac{dP}{dt} = \frac{k_2 M(t) c(t)^{n_2}}{\left(1 + \frac{c(t)}{K_M}\right)^{n_2}} \quad \text{Equation 1.3}$$

- **Fragmentation** creates new growth-competent ends originating from breakage of present fibrils e.g. due to shear forces and depends on the amount of fibrils. For simplicity, the fragmentation probability is assumed to be equal for each position of the fibril. The corresponding rate constant is k_- .

$$\frac{dP}{dt} = k_- M(t) \quad \text{Equation 1.4}$$

The rate constants (k_x) contribute to the overall kinetics as factors, whereas reaction orders (n_x) enter the equations as potencies and describe the dependence of dP/dt and dM/dt on the initial monomer concentration c_0 . The exact interplay of rates and reaction orders depending on the observed amyloidogenic system and the applied condition determines the overall (sigmoidal) shape of the macroscopic fibrillation profile. A simplified reaction network considering the evolution of $P(t)$ and $M(t)$ and their turnover by the microscopic processes is shown in Figure 1.5B.

The mechanism of fibril formation of an individual amyloidogenic system in terms of dominant microscopic processes often follows a well-established framework.^{120,121} Here, fibrillar growth is monitored for a broad range of initial concentrations. An extraction of the half-times with a subsequent plot of $\log(t_{1/2})$ vs. $\log(c_0)$ allows first insights into the dependence of fibril growth on the initial concentration, indicated by the scaling exponent γ .¹¹⁶ For many reported cases, this plot shows a linear scaling indicating a consistent mechanism throughout the concentration range probed, i.e. no change of the rate determining step (Figure 1.6A). The slope of γ can already hint towards dominant

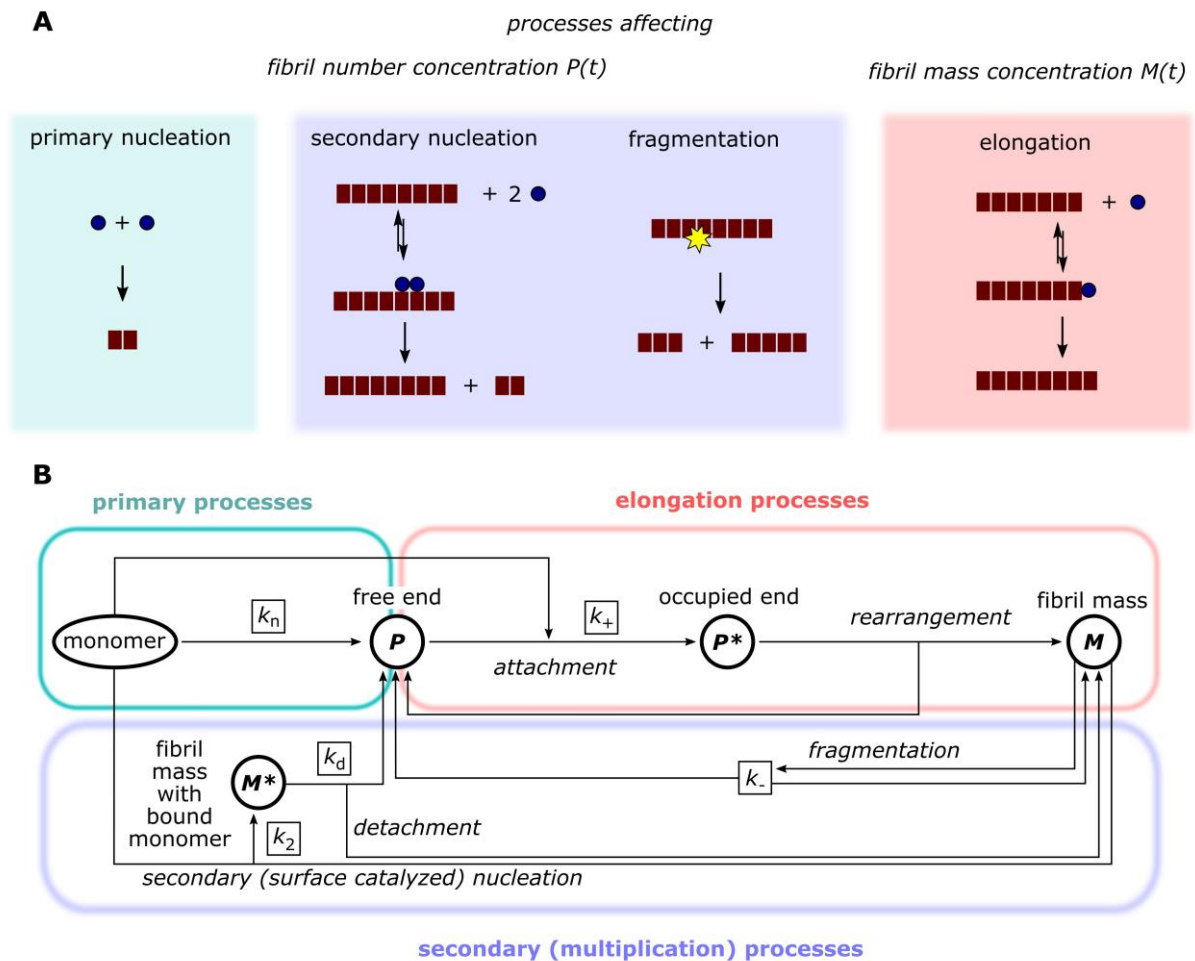


Figure 1.5: Individual microscopic processes involved in amyloid fibril formation. **A** – Schemes of the processes contributing to the increase of fibril number concentration $P(t)$ and fibril mass concentration $M(t)$. Monomers are represented by blue circles, fibrils by red rectangles. Secondary nucleation and elongation are displayed as multistep processes as described in the main text. **B** – Closed reaction network of the processes formulated as a Petri net with their contributions to $P(t)$ and $M(t)$ as the two only relevant entities for an effective kinetic description. A and B adapted from ref.¹¹⁶

processes and corresponding reaction orders.¹¹⁶ Exemplary, characteristic slopes of $\gamma = -0.5$ or $\gamma = -1.5$ can indicate fragmentation or secondary nucleation-driven fibrillation mechanisms for the specific case of $n_2 = 2$ ($\gamma = -(n_2 + 1) 2^{-1}$), respectively. In contrast, a non-linear scaling behavior can originate from saturation of serial processes (elongation or secondary nucleation as described above) with a positive curvature ($\Delta\gamma > 0$, Figure 1.6B) or from competition of two processes acting in parallel (two secondary processes or competition of primary with secondary nucleation) indicated by a negative curvature ($\Delta\gamma < 0$, Figure 1.6C).¹¹⁶ While saturation, typically occurring at high initial concentrations,¹²² as well as the competition of two secondary processes are well described in the literature,¹²³ a competition of the two main nucleation events (primary vs. secondary) remained obscure.¹²⁴ The rate constant k_n of primary nucleation is typically small compared to k_2 for secondary nucleation, normally by several orders of magnitude.¹²⁰ Consequently, the reaction order n_c (Equation 1.2) must be high compared to n_2 (Equation 1.3) for an effective competition of primary with secondary nucleation. This

has only been theoretically demonstrated.¹²⁵ Additionally, it has been shown that the formation of a primary nucleus involving many monomers most likely applies for peptides with a low β -sheet propensity.¹²⁶

The previous examples analyzed typical appearances of the $\log(t_{1/2})$ - $\log(c_0)$ -plot including linearity or curvature. Furthermore, inhibitory effects indicated by a positive slope (Figure 1.6D) were described e.g. for competition with off-pathway processes or “capping” effects at high concentrations.¹²⁷ Fibrillar growth independent from the total concentration have been reported for systems nucleating from micellar or liquid-liquid phase separated systems (Figure 1.6E).^{128,129}

The $\log(t_{1/2})$ - $\log(c_0)$ -plot only allows a first investigation of the concentration dependence of amyloid growth and a rough estimation of dominant processes. In order to learn more about elongation and the influence of multiplication processes for a distinct system, seeding experiments can help to elucidate the fibrillation mechanism.¹²² A seed, in this case, is a pre-formed fibril of the same peptide which is transferred to a new reaction solution and thus exposed to new monomers (Figure 1.7A). Monomers can attach to growth-competent ends and elongate the fibril, being referred to as templated growth (Figure 1.7B).¹³⁰ Additionally, secondary nucleation can occur catalyzed by the existing fibril surface. In principle, seeding can be performed homogeneously as described, or heterogeneously by using pre-formed fibrils from another peptide.¹³¹ In order to refer to the amount of seeds added, the concentration of monomer equivalents being incorporated into seed fibrils (in units of 1 M^{-1}) is often used.

For an appropriate application and interpretation of seeding experiments, the properties of the seed fibrils need to be considered.¹³² Depending on the specific peptide, fibrils can tend to be long or short, appear as individual filaments or clustered. Hence, the main parameter to describe the seed fibrils is the initial seed number concentration P_0 in relation to the mass concentration M_0 .^{132,133} Note that P_0 is

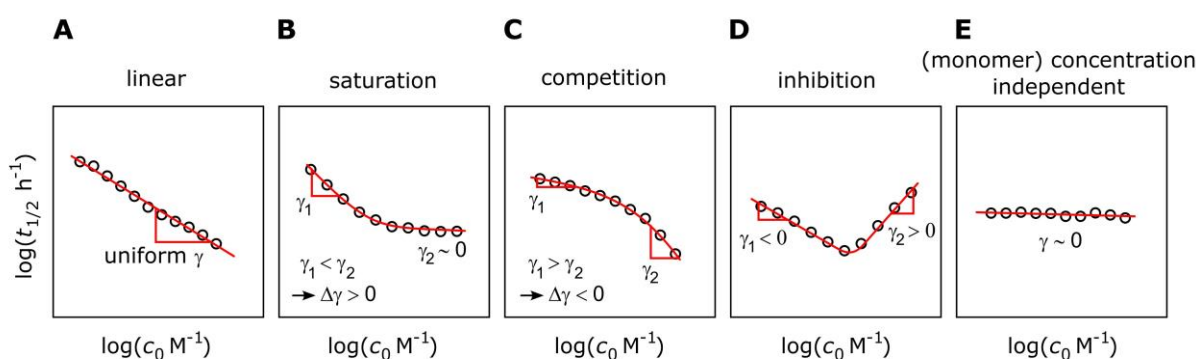


Figure 1.6: Possible cases of concentration dependences of fibril formation displayed as $\log(t_{1/2})$ - $\log(c_0)$ -plots for **A** – linear behavior, **B** – positive curvature ($\Delta\gamma > 0$) indicating saturation effects, **C** – negative curvature ($\Delta\gamma < 0$) typical for competing processes, **D** – inhibition of fibril formation indicated by a positive slope and **E** – (apparent) monomer concentration independent fibril growth. Artificial data points were used. A-C adapted from ref.¹¹⁶, D from ref.¹²⁷ and E from ref.¹²⁸

always several orders of magnitude smaller than M_0 since fibrils typically contain hundreds to thousands of monomers.¹³² According to the scientific question, it is required to expose either a high number of growth competent ends, or a high surface area. A control of the length distribution can be achieved e.g. by ultrasonication inducing breakage of fibrils (Figure 1.7C).¹³⁴

The general influence of multiplication processes on fibril growth can easily be investigated by a separate concentration dependent fibrillation experiment similar to the approach described above.¹²¹ Here, a low amount of pre-formed seeds is added, typically about 0.1 % of the respective monomer concentration, given in monomer equivalents.¹³⁵ The presence of seeds bypasses primary nucleation. Thus, a considerable reduction of the lag-phase, and therefore $t_{1/2}$, is a strong indicator for the involvement of multiplication processes (Figure 1.7D, red curve, and Figure 1.7E, left panel).^{121,135} This remodeling of the reaction network can lead to linearity of the $\log(t_{1/2})$ - $\log(c_0)$ -plot even for complex *de novo* behavior (Figure 1.7E, right panel).¹³⁶ Significantly increasing the seed concentration (typically 5 – 30 % of c_0) additionally makes secondary nucleation negligible resulting in a completely abolished lag phase with exponential-like growth that only reflects elongation (blue in Figure 1.7D).^{121,135} More generally, the first few time-points of seeded fibril growth (in the high-seeding regime) account for the elongation process.¹³⁷ They can either display an exponential-like curve shape for very high P_0 or an increasing slope, or even sigmoidal behavior, for a strong influence of secondary processes. In the latter case, P_0 is not sufficient that the early growth depends solely on elongation.

These considerations lead to the use of seeding experiments to investigate concentration effects on elongation and secondary nucleation. First, adding seeds with high P_0 compared to M_0 at a constant amount to increasing monomer concentrations (Equation 1.1) will allow (I) to investigate if there is a linear concentration dependence and (II) to extract the rate constant k_+ . A decrease of the slope (at high concentrations) indicates saturation of the elongation process.¹²² In contrast, an increasing slope indicates that elongation occurs *via* the addition of oligomeric species, rather than monomers.¹³⁷ This case has been demonstrated for the $\Delta N6$ variant of human microglobulin $\beta 2m$.¹³⁸ The extraction of k_+ requires an appropriate estimate of the fibril number P_0 , which is not trivial, but can be addressed by e.g. electron microscopy *via* the average dimension of the seed fibrils.¹³⁹ Second, a saturation of secondary nucleation indicated by a negative slope within the $\log(t_{1/2})$ - $\log(c_0)$ -plot can also be verified by a seeding experiment with constant P_0 and varying monomer concentrations.^{121,140} Here, a high surface area and relatively low number of growth-competent ends can assure that elongation of the seeds alone is not sufficient to significantly contribute to the overall fibrillation, rather than elongation of ends originating from multiplication processes. However, the described method only allows an estimate for the influence of secondary mechanisms rather than a determination of the corresponding rate constants.

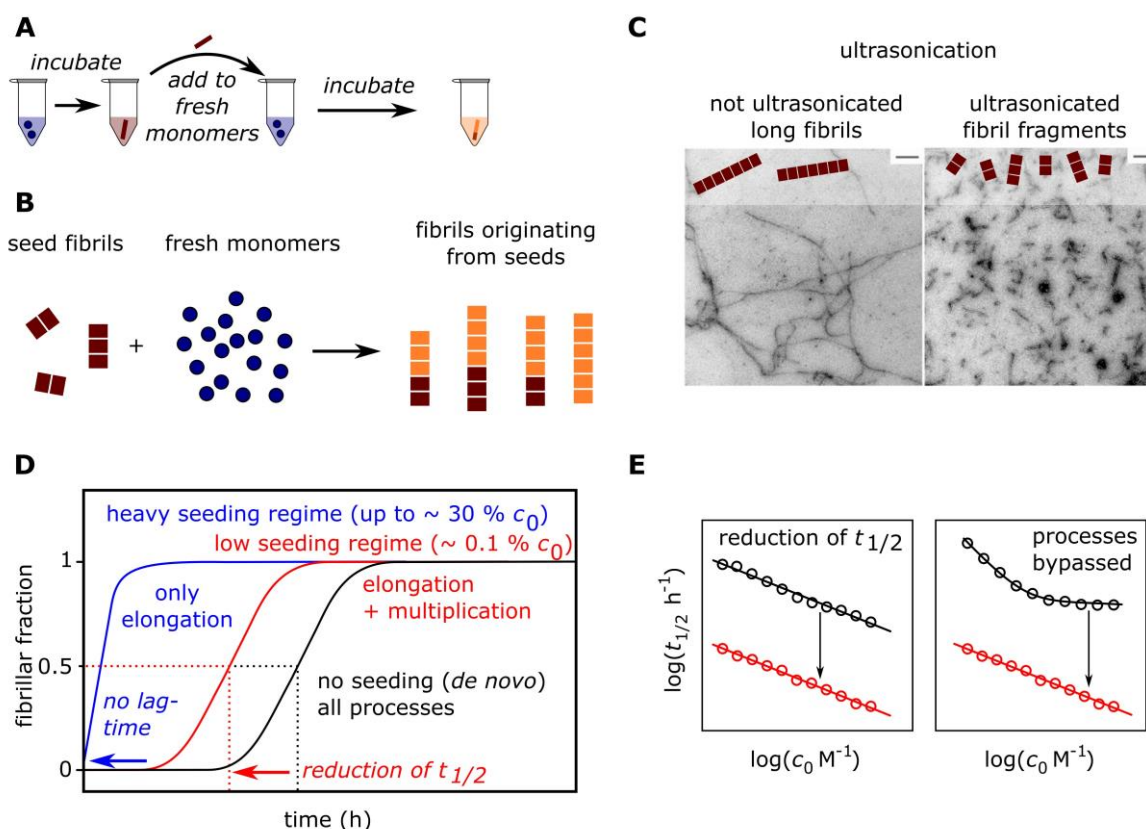


Figure 1.7: Principles of seeded fibril growth. **A** – Monomers (blue) are able to form fibrils from pre-formed fibril seeds (red) resulting in fibrils originating from these templates by elongation (red and orange) or secondary nucleation and elongation (only orange). **B** – The experimental scheme demonstrates that initially monomers are incubated to yield the seeds. These are subsequently added to a new solution of fresh monomers. Elongation and secondary nucleation result in a new fibril equilibrium. **C** – Ultrasonication can adjust the length distribution of the seeds by breakage of the initial fibrils. Short fibrils offer a high number of growth-competent ends P_0 for elongation, whereas long fibrils present a high surface area for secondary nucleation. **D** – Schematic influence of seed addition to the kinetics and the corresponding processes of fibril growth. In *de novo* fibrillogenesis (black, no seeds) all processes are active (compare Figure 1.4). Adding a low amount of seeds (red, appr. 0.1 % of c_0 , given in monomer equivalents) bypasses primary nucleation (in case secondary processes are active) resulting in a reduction of the lag-time. The presence of a high amount of seeds (blue, up to 30 % of c_0) bypasses elongation as well as secondary nucleation. As a consequence, only elongation significantly contributes to the fibrillation kinetics. **E** – Schematic $\log(t_{1/2})$ - $\log(c_0)$ -plots indicating the systematic reduction of $t_{1/2}$ in the case of a low-seeding regime. For curved plots (exemplary shown in the right panel), low seeding conditions typically lead to a linear behavior. Electron micrographs in C were taken from ref.¹⁴¹, plots in E (black) are identical to panels A and B of Figure 1.6. Artificial data points were used in panel E.

A more detailed determination of rate constants and reaction orders can be achieved by fitting concentration dependent kinetic fibrillation data to mathematical models with respect to the individual microscopic processes, including global fitting approaches.¹⁴² It becomes obvious that the mechanistic investigation of amyloid growth for a specific amyloidogenic peptide requires experimental data of high quality including reproducibility of replicates and between different sample batches. This can be achieved by a precise control of sample preparation and the conditions during fibril growth. Also, the quality of seeds determines the success of seeding experiments, requiring a reproducible protocol for seed preparation. The approaches discussed in this thesis are only valid for amyloid fibril formation displaying sigmoidal-shaped kinetics. Other forms or biphasic behavior might

occur due to weak control of conditions or represent an intrinsic property requiring other mathematical models.

1.2.2 The Role of Oligomers in Amyloid Growth

The assembly of monomers into oligomeric species is a fundamental requirement for amyloid fibril formation. In this context, oligomers are small, metastable associates of peptides or proteins observed during fibril growth with distinct morphologies from these mature fibrils.^{143,144} Direct, experimental observations of oligomers showed that their highest concentrations are reached during the early stages of the process, i.e. the lag time, being intermediates of the conversion of monomers into filaments.¹⁴⁵⁻¹⁴⁷

Depending on their contribution towards fibril formation, oligomers can be classified as “on-pathway” or “off-pathway”, although this simple binary discrimination is not trivial.¹⁴³ The latter do not directly contribute to fibril nucleation or growth and need to dissociate into monomers first and can thus even be inhibitors of fibril formation due to depletion of the available monomer or due to interference with other processes.^{148,149} On-pathway oligomers, in general, display at least a probability to be converted into fibrils, although despite being possibly prone for dissociation or side reactions.

For a mechanistic interpretation, oligomers are distinguished into fibrillar and non-fibrillar species.¹⁴³ “Fibrillar oligomers” are oligomers that can be elongated by, e.g., monomer addition but are too short to be identified as mature fibrils. The terminology “short colloidal filaments” might be a more accurate description for these species. This definition consequently requires the cross- β motif, as present in the mature fibrils. In contrast, “non-fibrillar” oligomers are much more heterogenous in terms of structure, size and persistence. Growth of these oligomer species is much slower compared to elongation of fibrils. Importantly, non-fibrillar oligomers can, given an on-pathway probability, be transformed to fibrillar oligomers and further into fibrils by a conformational conversion step.

Amyloid fibril formation implies a high energy barrier for primary nucleation depending on the pathway of nucleus formation.^{150,151} In principle, (on-pathway) oligomers can form cooperatively until the critical nucleus size is reached (Figure 1.8, left panel). The fate of the critical nucleus is determined by its propensity to either dissociate or grow towards a fibril. In analogy to classical nucleation theory, the nucleus formation is energetically highly unfavorable.¹⁵² Therefore, such oligomers are transient and challenging to be observed experimentally.¹⁴⁴ In contrast, oligomer formation can also represent a local minimum in the free energy landscape allowing accumulation of oligomeric species to a considerable degree (Figure 1.8, middle panel).^{153,154} The energy barrier towards nuclei formation in this case reflects the structural conversion towards the elongation-competent state. This is referred to

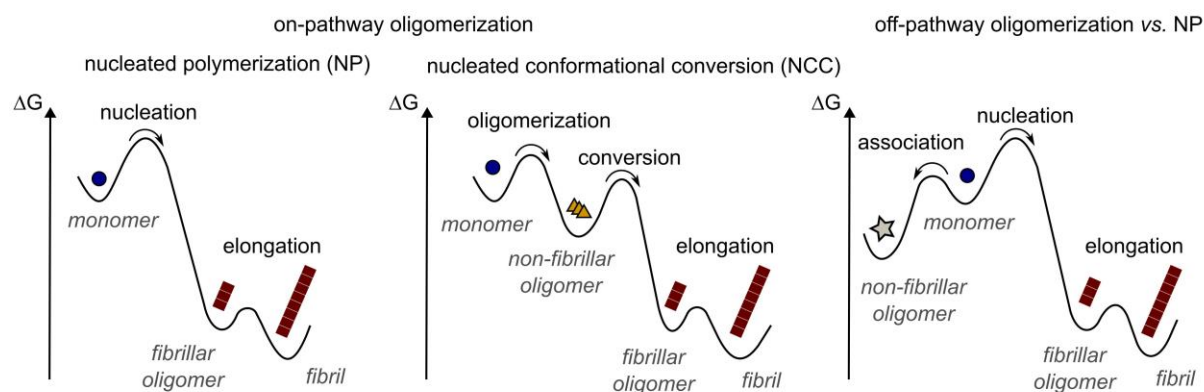


Figure 1.8: Simplified schematic Gibbs free energy landscapes for three scenarios of oligomer formation. On-pathway oligomerization is observed in nucleated polymerization (transient oligomer population, left panel) and in nucleated conformational conversion (conversion of stable oligomers, middle panel). Off-pathway oligomerization (right panel) can compete with on-pathway oligomerization. Monomers are shown as blue circles, fibrillar species as red rectangles. Non-fibrillar oligomers are indicated as orange triangles or grey stars. Adapted from ref.¹⁴⁴. Arrows mark the indicated direction of the processes.

as nucleated conformational conversion (NCC). Similar to NCC, off-pathway oligomers can also appear in a significant amount representing a local free energy minimum, in contrast not necessarily affecting the energy barrier for primary nucleation (Figure 1.8, right panel).¹⁴⁸

In general, the role of oligomers is diverse. They can contribute to fibril formation as intermediates for primary and secondary nucleation or as the unit being added to growth-competent ends during elongation. The latter case is rare but has been experimentally shown for the $\Delta N6$ variant of human microglobulin $\beta 2m$.^{138,155} Such direct roles classify oligomers as on-pathway oligomers. The network of oligomeric species in fibrillar assembly is often very complex. The seminal work of G.M. Clore and coworkers demonstrated the power of NMR spectroscopy to disentangle a prenucleation network of different on- and off-pathway oligomers for the Huntingtin Exon 1 protein involved in Huntington's disease.¹⁵⁶⁻¹⁵⁹ Importantly, for pathogenic amyloids oligomers more likely represent the toxic species rather than the mature fibrils, making them potential targets for anti-amyloid therapies.^{13,144,160}

1.2.3 Kinetic Descriptions of Nucleated Polymerization and Nucleated Conformational Conversion

The single-step nucleation description treats oligomers on-pathway to the fibril nucleus as fibrillar species already containing the required secondary structure (Figure 1.8, left panel). Necessarily, assembly size is considered as the only relevant degree of freedom. The nucleus is defined as the critical species from which elongation becomes more favorable than dissociation.

In order to kinetically describe the fibrillation reaction network (Figure 1.5B), a master equation approach can be employed.^{161,162} A master equation consists of coupled differential equations quantifying the population balance of relevant species in terms of reaction fluxes. The master equation is solved applying self-consistent approaches resulting in integrated rate laws. A master equation describing the single-step primary nucleation involving elongation and secondary nucleation is given by

$$\frac{\partial f(t,j)}{\partial t} = 2k_+c(t)f(t,j-1) - 2k_+c(t)f(t,j) + k_n c(t)^{n_c} \delta_{j,n_c} + k_2 c(t)^{n_2} M(t) \delta_{j,n_2} \quad \text{Equation 1.5}$$

where $f(t,j)$ denotes the concentration of j -sized fibrils.^{118,119,121,163,164} Conveniently, the focus is set only on the time evolution of the principal moments of fibril number concentration $P(t)$ and fibril mass concentration $M(t)$ with

$$P(t) = \sum_{j=\min(n_c, n_2)}^{\infty} f(t,j) \quad \text{Equation 1.6}$$

$$M(t) = \sum_{j=\min(n_c, n_2)}^{\infty} j f(t,j) \quad \text{Equation 1.7}$$

Summarizing over j and considering only elongation as the main dominant contribution to $M(t)$, the following simplified differential equations can be derived:^{118,119,121,163,164}

$$\frac{dP(t)}{dt} = k_n c(t)^{n_c} + k_2 c(t)^{n_2} M(t) \quad \text{Equation 1.8}$$

$$\frac{dM(t)}{dt} = 2k_+c(t)P(t) = -\frac{dc(t)}{dt} \quad \text{Equation 1.9}$$

In the absence of initial fibril seeds, an analytical solution applying self-consistent methods results in a single equation describing the time dependent increase of fibrillar mass from primary and secondary processes:^{118,164}

$$\frac{M(t)}{c_0} = 1 - \frac{c(t)}{c_0} = \frac{\frac{\lambda^2}{2\kappa^2} (e^{\kappa t} - 1)}{1 + \frac{\lambda^2}{2\kappa^2} (e^{\kappa t} - 1)} = 1 - \frac{1}{1 + \frac{\lambda^2}{2\kappa^2} (e^{\kappa t} - 1)} \quad \text{Equation 1.10}$$

The individual processes are summarized in the two parameters λ and κ and reflect the sum of primary and secondary processes, respectively. They are defined as

$$\lambda = (2 k_+ k_n c_0^{n_c})^{1/2} \quad \text{Equation 1.11}$$

$$\kappa = (2 k_+ k_2 c_0^{n_2+1})^{1/2} \quad \text{Equation 1.12}$$

Here, λ is the overall rate constant in the absence of any secondary processes as first developed by Oosawa^{112,165} and κ the analogous constant for multiplication processes.¹¹⁸ For a simple kinetic description of amyloid fibril growth using this traditional bulk model, Equation 1.10 is sufficient to discriminate the impact of primary and secondary processes.

However, this model is not sufficient to describe significant populations of oligomers, as demonstrated for A β ₄₂.¹⁴⁵ The multi-step mechanism of NCC involves an initial assembly step of non-fibrillar oligomers, i.e. that these oligomers can be structurally diverse and significantly different from the

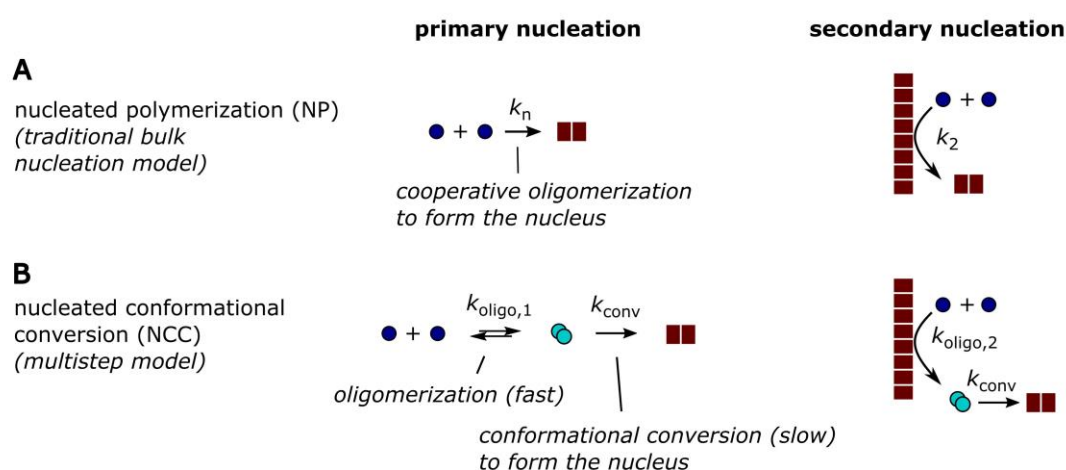


Figure 1.9: Simplified nucleation schemes according to the models of **A** – nucleated polymerization (NP) and **B** – nucleated conformational conversion (NCC, bottom) for primary (left) and secondary nucleation (right). In NP, the formation of the nucleus proceeds *via* the cooperative, consecutive growth of an oligomer until the critical nucleus size is reached and the elongation process starts to increase the fibrillar mass. Oligomers here are transient and have a high propensity to dissociate. In NCC, oligomers are formed that have a secondary structure distinct from the fibrillar state. These oligomers can accumulate to a significant degree and finally undergo a conformational conversion towards the fibrillar state to form the nucleus enabling the elongation process. The respective rate constants are indicated. The corresponding free energy landscapes are shown in Figure 1.8 (left and middle panel).

secondary structure of monomers incorporated into fibrils (Figure 1.8, middle panel, and Figure 1.9).¹⁶⁶⁻¹⁷⁰ An additional step necessary for nucleus formation is the structural conversion of oligomers into the elongation-competent fibril nucleus. Besides size, structure (β -sheet content in particular) is considered as a second degree of freedom.

A kinetic model including considerable oligomer accumulation has been developed by Michaels *et al.* (2020) and Dear *et al.* (2020) which will be introduced and referred to in the following section:^{145,171}

Oligomers ($O(t)$) able to convert into fibril nuclei and solely formed by association of free monomers are generated with the rate $O(t) = k_{oligo,1}c(t)^{n_{oligo,1}}$, oligomerization catalyzed by a fibril surface proceeds with $O(t) = k_{oligo,2}c(t)^{n_{oligo,2}}M(t)$. These oligomers finally convert to elongation-competent species, occurring with the rate $P(t) = k_{conv}c(t)^{n_{conv}}O(t)$. This extends the differential Equations 1.6 and 1.7 in the following way:

$$\frac{dO(t)}{dt} = k_{oligo,1}c(t)^{n_{oligo,1}} + k_{oligo,2}c(t)^{n_{oligo,2}} - k_{conv}c(t)^{n_{conv}}O(t) + k_dO(t) \quad \text{Equation 1.13}$$

$$\frac{dP(t)}{dt} = k_{conv}c(t)^{n_{conv}}O(t) \quad \text{Equation 1.14}$$

$$\frac{dM(t)}{dt} = 2k_+c(t)P(t) = -\frac{dc(t)}{dt} \quad \text{Equation 1.15}$$

where k_d is the dissociation rate of oligomers. In analogy to Equation 1.10, the time evolution of fibrillar mass can be expressed as

$$\frac{M(t)}{c_0} = \frac{\frac{M_0(t)}{c_0}}{1 + \frac{M_0(t)}{c_0}} \simeq \frac{\frac{\bar{\lambda}^3}{3\bar{\kappa}^3}(e^{\bar{\kappa}t} - 1)}{1 + \frac{\bar{\lambda}^3}{3\bar{\kappa}^3}(e^{\bar{\kappa}t} - 1)} = 1 - \frac{1}{1 + \frac{\bar{\lambda}^3}{3\bar{\kappa}^3}(e^{\bar{\kappa}t} - 1)} \quad \text{Equation 1.16}$$

$M_0(t)$ indicates a linearized solution of Equation 1.15 in the early time limit with $M_0(t) = \bar{\lambda}^3 3^{-1} \bar{\kappa}^{-1} (e^{\bar{\kappa}t} - 1)$. Equation 1.16 derives from a combination with the steady-state behavior $M(t=\infty) = c_0$. The parameters are defined as

$$\bar{\lambda} = \left(2 k_+ k_{oligo,1} k_{conv} c_0^{n_{oligo,1} + n_{conv}} \right)^{1/3} \quad \text{Equation 1.17}$$

$$\bar{\kappa} = \left(2 k_+ k_{oligo,2} k_{conv} c_0^{n_{oligo,2} + n_{conv} + 1} \right)^{1/3} \quad \text{Equation 1.18}$$

Note that λ and κ in Equation 1.10 are here replaced by $\bar{\lambda}$ and $\bar{\kappa}$. In principle, both equations are equivalent. Consequently, $\kappa/\bar{\kappa}$ as well as the prefactors must be equal. In Equation 1.16, the prefactor $\bar{\lambda}^3 3^{-1} \bar{\kappa}^{-3}$ can be interpreted as a critical mass of fibrillar material which is necessary to initiate the autocatalytic feedback loop of secondary nucleation.

The overall proliferation rate depends on the monomer concentration with $\bar{\kappa} \propto c_0^\gamma$. Thus, the scaling factor γ represents the arithmetic mean of the individual reaction orders for oligomer formation, conversion and elongation with

$$\gamma = \frac{n_{oligo,2} + n_{conv} + n_{elon}}{3} \quad \text{Equation 1.19}$$

For the case of elongation *via* monomer addition, $n_{elon} = 1$.

The single-step model treats nucleation as a process with assembly size as the only factor of freedom and therefore with only one relevant rate constant (k_n or k_2). Possible oligomers are assumed to be structurally identical to fibrils. This can be interpreted as a “nucleation-elongation” mechanism for primary and secondary processes. The corresponding reaction orders are directly related to physical nuclei sizes. In contrast, the multi-step model includes the formation of structurally diverse oligomers to a considerable amount ($k_{oligo,1}$, $k_{oligo,2}$). The reaction order ($n_{oligo,1}$, $n_{oligo,2}$) reflects the number of monomers to form the respective oligomer. An additional degree of freedom is represented by a structural conversion of the oligomers towards a, typically, β -sheet rich growth competent species (k_{conv}). A physical interpretation of the reaction order n_{conv} is given by the number of monomers in the oligomer that form the site of the first conversion step.

For an amyloidogenic system which is characterized by the accumulation of oligomeric species during nucleation, Equation 1.16 provides a powerful tool to disentangle primary ($\bar{\lambda}$) and secondary processes ($\bar{\kappa}$). In Figure 1.10A, the impact of a variation of the two parameters $\bar{\lambda}$ and $\bar{\kappa}$ is demonstrated. A

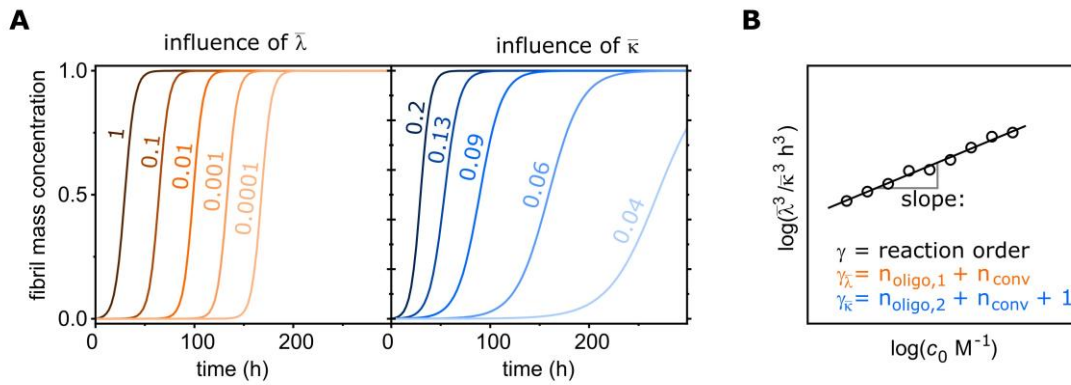


Figure 1.10: **A** – Influence of variations of the two parameters $\bar{\lambda}$ and $\bar{\kappa}$ of Equation 1.16 on the appearance of the time dependent fibril mass increase. The first curve in both graphs is calculated from Equation 1.16 with $\bar{\lambda} = 1 \text{ h}^{-1}$ and $\bar{\kappa} = 0.2 \text{ h}^{-1}$. A variation of $\bar{\lambda}$ leads to an increase of the lag-time and $t_{1/2}$ with no influence on the slope (left, $\bar{\lambda} = 1 \text{ h}^{-1}, 0.1 \text{ h}^{-1}, 0.01 \text{ h}^{-1}, 0.001 \text{ h}^{-1}, 0.0001 \text{ h}^{-1}$), whereas varying $\bar{\kappa}$ leads to a reduction of the slope and thus to an increase of $t_{1/2}$ (right, $\bar{\kappa} = 0.2 \text{ h}^{-1}, 0.13 \text{ h}^{-1}, 0.09 \text{ h}^{-1}, 0.06 \text{ h}^{-1}, 0.04 \text{ h}^{-1}$). **B** – Extracting $\bar{\lambda}$ and $\bar{\kappa}$ from concentration dependent fibrillation curves with a subsequent plot of $\log(\bar{\lambda}^3 / \bar{\kappa}^3)$ vs. $\log(c_0)$ allows the determination of the corresponding reaction orders from the slopes with $\gamma_{\bar{\lambda}} = n_{\text{oligo},1} + n_{\text{conv}}$ and $\gamma_{\bar{\kappa}} = n_{\text{oligo},2} + n_{\text{conv}} + 1$. Artificial data points were used in panel B.

systematic decrease of $\bar{\lambda}$ produces curves with identical slopes but increasing $t_{1/2}$, indicating a prolongation of the lag-phase. In contrast, a variation of $\bar{\kappa}$ leads to curves with a decreasing slope in the growth phase coupled with increasing $t_{1/2}$. Note that even small variations of $\bar{\kappa}$ display a substantial influence on the curves. As demonstrated in Figure 1.10A, a decrease by factor five shows a much higher impact than a decrease of $\bar{\lambda}$ by four orders of magnitude.

With this equation, concentration dependent fibrillation curves can be fitted either globally or individually. In the latter case, the two obtained parameters for each curve can be plotted as $\log(\bar{\lambda}^3 / \bar{\kappa}^3)$ vs. $\log(c_0)$. A linear slope of this plot gives the reaction orders $n_{\text{oligo},1} + n_{\text{conv}}$ for primary and $n_{\text{oligo},2} + n_{\text{conv}} + 1$ for secondary processes (Figure 1.10B)

1.2.4 The Critical Concentration of Amyloid Formation

In amyloid self-assembly, fibrillar mass increases towards a plateau phase. Intriguingly, fibrillar mass in the equilibrium is not equal to the initial concentration (in monomer equivalents) (Figure 1.11, left panel, blue).¹⁷² Analogously, the monomer concentration is decreasing until a constant remaining fraction of free monomer is left (red in the same Figure). This is connected to a phenomenon observed for nucleation: Models for amyloid growth are based on the concept of nucleated polymerization. In this concept, polymerization only occurs if the initial concentration of monomers exceeds a minimum level which is called the critical concentration c_{crit} .¹⁷²⁻¹⁷⁴ Figure 1.11 (right panel) demonstrates that below this level the monomer remains unconverted, even after infinite incubation time, i.e. the

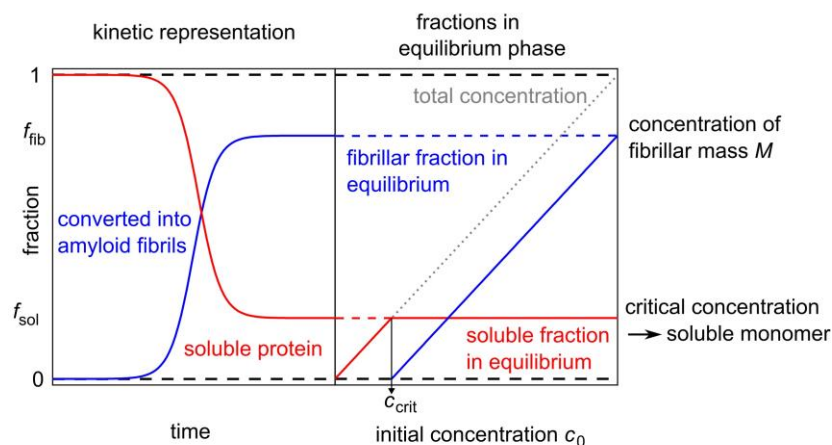
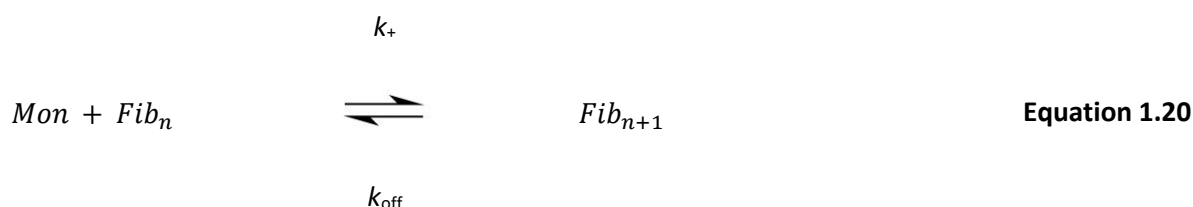


Figure 1.11: Concept of the critical concentration. The fraction of free, soluble protein decreases during fibril formation until only a small, residual proportion is left (left, red curve). Correspondingly, the fraction of fibrillar mass increases (blue curve). The residual free peptide fraction in thermodynamic equilibrium with fibrils is constant independent from the initial concentration (right, red curve), referred to as the critical concentration. Only the fraction of fibrillar mass increases with c_0 (right, blue curve). The grey dotted line represents the theoretical sum of the blue and red curve. An initial concentration below the critical concentration does not lead to fibril formation. The schematic graph in the left panel represents the highest c_0 displayed in the right panel.

concentration of soluble protein refers to the total protein concentration. In contrast, the solution becomes supersaturated if the protein concentration exceeds the minimum level. The protein is metastable and kinetically soluble.^{175,176} As a consequence, the protein is able to undergo nucleated conversion into growth-competent species with time and finally into amyloid fibrils. In the steady-state phase, or the thermodynamic equilibrium, monomers are in dynamic exchange with fibrils *via* association and dissociation. This requires the introduced certain fraction of free, soluble protein.¹⁷⁷ In Figure 1.11 (right panel) it is shown that this fraction is constant independent of the total protein concentration. Interestingly, this is equal to the critical concentration. The converted protein fraction increases with increasing total concentration, according to $c_0 = c_{\text{crit}} + M(t=\infty)$.

The critical concentration can be used to describe the Gibbs free energy of the overall fibrillation process.^{174,178} The elongation step of a growth-competent end can be described as a second-order reaction:



with *Mon* a monomer, *Fib_n* a fibril of the length *n*, k_+ the association rate constant (elongation) and k_{off} the fibril dissociation rate constant. In equilibrium, the dissociation constant K is given by

$$K = \frac{k_+}{k_{off}} = \frac{[Fib_{n+1}]}{[Mon][Fib_n]} \quad \text{Equation 1.21}$$

Due to its filamentous structure, the addition of a monomer does not change the number concentration of the fibril ($[Fib_{n+1}] = [Fib_n]$) eliminating both from the equation. Under equilibrium conditions, $[Mon]$ equals the critical concentration leading to the approximation

$$K \approx \frac{1}{[Mon]} = \frac{1}{c_{crit}} \quad \text{Equation 1.22}$$

The application of the Gibbs free energy law leads to

$$\Delta G^0 = -RT \ln\left(\frac{k_{on}}{k_{off}}\right) = -RT \ln(K) = -RT \ln\left(\frac{1 M}{c_{crit}}\right) \quad \text{Equation 1.23}$$

where R is the gas constant and T the temperature. A reference concentration is introduced, chosen to be 1 M for convenience. Essentially, this concept applies for homogenous nucleation.

1.3 The Parathyroid Hormone

The parathyroid hormone (PTH), produced in the parathyroid glands, is the antagonist of calcitonin and has an important role in the control of blood Ca^{2+} and phosphate homeostasis as well as in bone metabolism.¹⁷⁹ PTH is produced in the chief cells of the parathyroid glands as a pre-pro-hormone of 115 amino acids (Figure 1.12A).¹⁸⁰ The *N*-terminal 25 residues pre-sequence is co-translationally cleaved by a signal peptidase.¹⁸¹ The further post-translational processing in the Golgi apparatus is conducted by the cleavage of the pro-sequence by the pro-protein convertase furin.¹⁸² The physiological, mature PTH comprises 84 amino acids, referred to as PTH₈₄. Interestingly, only about 20 % of PTH is present in the active form, whereas 80 % remains as inactive fragments.¹⁸³ After processing, the peptide is subsequently stored in secretory granules until its release into the blood stream as reaction to a decrease of the serum Ca^{2+} level (Figure 1.12A).

However, an increase of the serum Ca^{2+} level, sensed by the Ca^{2+} sensitive receptor CaSR, downregulates mRNA transcription,^{184,185} inhibits the release and stimulates degradation of PTH₈₄ into C-terminal fragments.¹⁸⁶ In addition, (1 α ,25)-dihydroxyvitamin D (1,25-(OH)₂ D), representing the

active form of vitamin D, inhibits gene transcription through binding to the intracellular vitamin D receptor (VDR).¹⁸⁷ Furthermore, the osteocyte-derived fibroblast growth factor FGF23 which is involved in phosphate homeostasis, prevents mRNA transcription as well as peptide maturation by activating the FGF receptor FGFR1 and the coreceptor α -Klotho.¹⁸⁸

PTH₈₄ is the ligand of the membrane anchored receptor PTH1R in human and rodents,^{189,190} which is exposed on the surface of osteoblasts and stroma cells in the bones, as well as on apical and basolateral membranes of tubuli in kidney cells. PTH1R is a G protein coupled receptor (GPCR) class B with seven trans-membrane domains. However, only the *N*-terminal 34 residues are essential for receptor activation.¹⁹¹ Binding affinity is mediated by residues 15-34 *via* association with the *N*-terminal extracellular domain of PTH1R.¹⁹² Residues 1-9 interact with the transmembrane region and activate the receptor.¹⁹³ Receptor activation due to PTH binding further activates adenylyl cyclase protein kinase A (AC-PKA) and phospholipase C protein kinase C (PLC-PKC).¹⁹⁴ Additionally, PTH activates a second class of receptors (PTH2R) whose function remains largely unknown.¹⁹⁵

PTH₈₄ induces a decrease of the blood phosphate concentration by inhibiting renal phosphate absorption in the kidney,¹⁷⁹ as well as Ca²⁺ absorption (Figure 1.12B).¹⁹⁶ It additionally stimulates

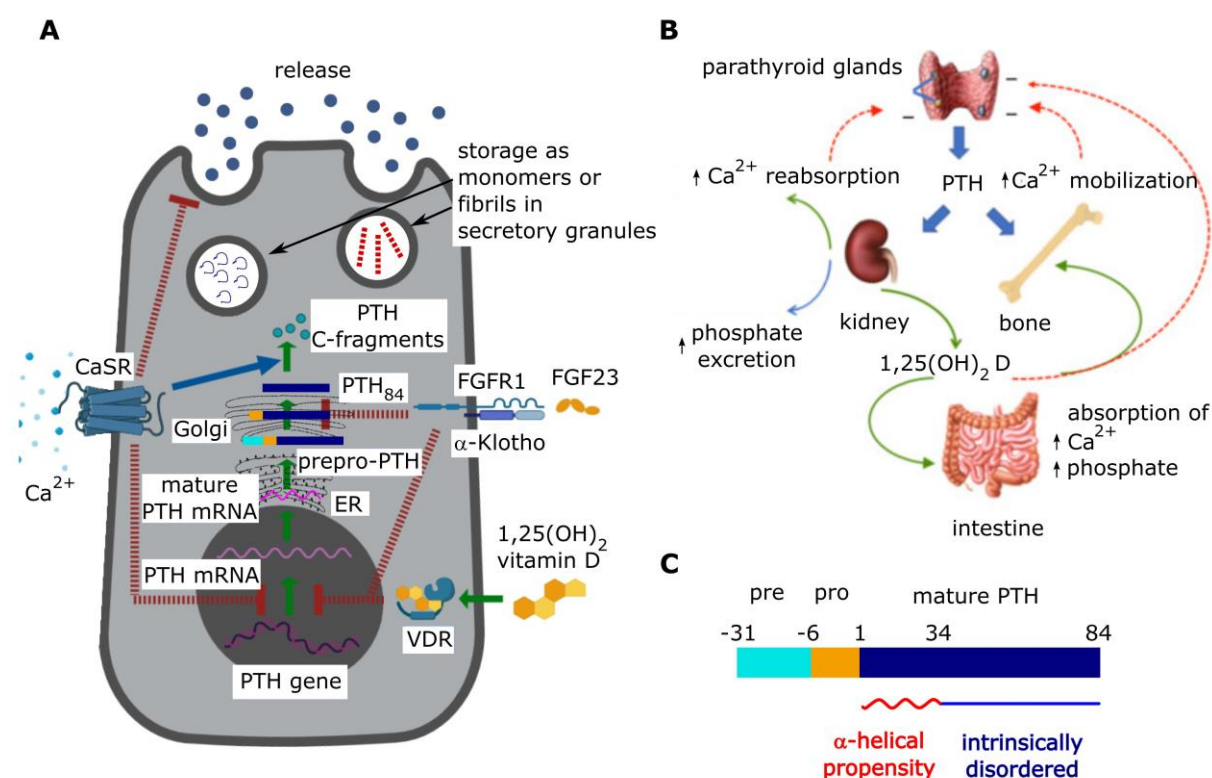


Figure 1.12: PTH₈₄ biosynthesis and action. **A** – Biosynthesis, processing in the Golgi apparatus and storage in secretory granules. The granule on the right indicates the hypothesis that PTH₈₄ is stored in the form of amyloid fibrils. **B** – Ca²⁺ and phosphate homeostasis. **C** – PTH is produced as a pre-pro-hormone. The 25-residues pre- and the 6-residues pro-sequence are cleaved during processing, leading to mature PTH₈₄. The numbers indicate the position in the amino acid sequence, the *N*-terminal serine residue of mature PTH₈₄ is referred to as position “1” for convenience. The *N*-terminal 34 residues of PTH₈₄ display an α -helical propensity, in contrast, the *C*-terminal 50 residues remain intrinsically disordered. The scheme in A is adapted from ref.¹⁹⁸, the scheme in B from ref.¹⁹⁹

hydroxylation of 25-hydroxyvitamin D into active (1 α ,25)-dihydroxyvitamin D, which in turn acts in the small intestines by increasing Ca²⁺ and phosphate absorption.¹⁹⁷

In contrast, the effect of PTH₈₄ on the bone metabolism determines the regulation of the calcium homeostasis (Figure 1.12B). The molecular composition of the bones is constantly rearranged in response to endocrine and exocrine signals.²⁰⁰ PTH₈₄ leads to changes of the gene expression levels in the PKA signal transduction pathway in osteoblasts. This leads to a gene expression of the *receptor activator of nuclear factor κ B ligand* (RANKL) and to an inhibition of osteoprotegerin (OPG).^{201,202} RANKL activates the osteoclasts due to binding of the receptor activator of NF- κ B (RANK). The ratio of RANKL and OPG controls the osteoclastogenesis.²⁰³ This leads to degradation of hydroxyle apatite from bones *via* complex mechanisms and thus to the release of Ca²⁺ and inorganic phosphate.¹⁹⁹

This effect on bones set the focus on PTH for the treatment of osteoporosis. Interestingly, it was shown that a continuous infusion of PTH leads to the expected catabolic response degrading the bones. In contrast, a periodic infusion leads to an anabolic response.²⁰⁴ In this pathway, the incorporation of Ca²⁺ increased the mineral density of the bone tissue. The exact mechanism is not fully understood. A regulation due to the activation of different sets of genes or different effects on the same set of genes by continuous or periodic PTH infusion are possible.²⁰⁵ Due to this dichotomous role, the N-terminal PTH fragment PTH₃₄ is used for the treatment of osteoporosis, known under the name teriparatide and has been distributed as Forteo[®]/Forsteo[®] since 1984.^{206,207} Many years later, in 2015, full-length PTH₈₄ was also approved as a drug and distributed as Natpara[®].²⁰⁸

As early as 1974 Anderson and Ewen showed that amyloid deposits are regularly found in healthy parathyroid glands (23 out of 50 cases with positive result, *post mortem* study).²⁰⁹ A significant trend with increasing age was indicated. Two years later, Kedar *et al.* reported that such deposits mainly contained PTH₈₄ and also showed *in vitro* fibril formation of the hormone.²¹⁰ A more detailed characterization of PTH₈₄ fibrils was published in 2015 by Balbach, Gopalswamy and coworkers.²¹¹ It was shown that PTH₈₄ could be converted into fibrils *in vitro* at high concentrations (10 mg ml⁻¹), high temperature (65 °C) and high pH (pH 9.0) within minutes of incubation time. The X-ray diffraction pattern was characteristic for a cross- β structure. Furthermore, residues 25-37 were identified to assemble within the fibril core. Compared to e.g. the A β peptide (with $c_{crit} = 0.9 \mu\text{M}$),¹⁷³ a high critical concentration of $74 \pm 25 \mu\text{M}$ was found by resolubilization of the fibrils, indicating a reversible fibrillation behavior of PTH₈₄. However, direct evidence for a physiological function of PTH₈₄ fibrils has not been reported until today. A role in peptide storage is suggested in analogy to peptide hormones from the pituitary glands.⁵⁵ At a molecular level, residues 1-34 of mature PTH₈₄ display a certain propensity to form α -helices, whereas the C-terminal 50 residues adopt no specific secondary structure, i.e. they are intrinsically disordered (Figure 1.12C).^{211,212}

1.4 Scientific Questions

When the projects presented in this thesis had been started, there was only a limited understanding of PTH₈₄ fibril formation. No detailed information about the general fibrillation mechanism and its individual sub-steps was available. Furthermore, a general deeper understanding of amyloid fibril formation at high peptide concentrations and under physiological conditions (pH, cellular effectors) was missing.

In addition, the critical concentration of amyloid formation was an under-investigated topic in the amyloid field. Only a few amyloidogenic peptides with a high critical concentration which is potentially analyzable by state-of-the-art techniques were known. The usually low (sub- μ M) critical concentrations are typically not considered to demand detailed understanding and investigation of the properties characterizing this phenomenon. PTH₈₄ offers the possibility to address this topic.

This thesis aims to shed light on the following physicochemical and biophysical questions from a biochemical perspective:

- What are the individual microscopic processes involved in PTH₈₄ amyloid fibril formation?
- Which of these processes is dominant and which is rate-limiting?
- What are the general characteristics of amyloid fibril formation at high peptide concentrations?
- What are the molecular characteristics of PTH₈₄ at the critical concentration for amyloid formation?
- What is the molecular structure of PTH₈₄ fibrils?
- What are the requirements for PTH₈₄ fibrillogenesis *in vivo*?
- Which experimental evidences classify PTH₈₄ as a functional amyloid?

The scientific findings are captured in three peer-reviewed publications which scaffold this cumulative doctoral thesis. Additional results to increase the understanding of different aspects of the hypotheses and conclusions are included in a separate chapter.



2 Publications and Results

This thesis is based on the following peer-reviewed publications:

- I. *A Competition of Secondary and Primary Nucleation Controls Amyloid Fibril Formation of the Parathyroid Hormone*

B. Voigt, M. Ott, J. Balbach
Macromol. Biosci. **2023**, e2200525
DOI: 10.1002/mabi.202200525

- II. *The Prenucleation Equilibrium of the Parathyroid Hormone Determines the Critical Aggregation Concentration and Amyloid Fibril Nucleation*

B. Voigt, T. Bhatia, J. Hesselbarth, M. Baumann, C. Schmidt, M. Ott, J. Balbach
ChemPhysChem **2023**, e202300439
DOI: 10.1002/cphc.202300439

- III. *Heparin promotes rapid fibrillation of the basic parathyroid hormone at physiological pH*

L.M. Lauth, B. Voigt, T. Bhatia, L. Machner, J. Balbach, M. Ott
FEBS Lett. **2022**, 596, 2928-2939
DOI: 10.1002/1873-3468.14455

2.1 Paper I: B. Voigt *et al.* (2023), A Competition of Secondary and Primary Nucleation Controls Amyloid Fibril Formation of the Parathyroid Hormone

Aims and Summary

In this paper, the molecular mechanism of amyloid fibril formation by the parathyroid hormone PTH₈₄ was investigated. The analysis of ThT monitored reaction kinetics revealed an intricate, concentration dependent network of individual monomer as well as fibril dependent processes. The subsequent analysis approach allowed to discriminate between the effective rates of primary and secondary processes. Two distinct rates were found for primary nucleation. The corresponding reaction orders indicate different concentration dependent primary nuclei precursors, i.e. a small, low-molecular weight oligomer at low concentrations (of the order of a di- to tetramer) and a high-molecular weight (HMW) oligomer at high concentrations (appr. a 9- to 16-mer). Most intriguingly, the consequence of this high dependence of primary processes on the total concentration is a competition of primary with secondary processes at high concentrations, which is the first experimentally reported case of this scenario according to the knowledge of the authors. Secondary nucleation, in contrast, was found to proceed *via* monomers. The same was found for elongation of existing fibrils. Both of these monomer dependent processes become inhibited at very high concentrations which was interpreted as reduced monomer availability due to oligomer formation. Interestingly, PTH₈₄ fibrils displayed a strong polymorphism, in terms of incorporated sub-filaments, depending on the initial concentration. Moreover, at high initial concentrations fibrils were found to form supramolecular clusters that eventually precipitate with an apparent rate constant independent from the monomer concentration. Last, the previously published critical concentration was confirmed and found to be independent of the initial monomer concentration, supporting the model of the critical monomer concentration for amyloid formation.

Contribution

The author of this thesis recombinantly produced the peptide (including a modification of the purification protocol to enhance data quality and reliability), prepared all samples for kinetics and imaging, planned and conducted all experiments, performed the (negative staining) electron microscopy imaging, analyzed the fibril nucleation kinetics (together with co-author Dr. Maria Ott) and kinetics of seeded fibril growth, interpreted the data with support from the co-authors, prepared all figures, wrote the complete manuscript draft and incorporated corrections from the co-authors.

Original Paper

The original paper is included on the following pages (pp. 32-42). The Supporting Information can be found in Appendix A.1.

A Competition of Secondary and Primary Nucleation Controls Amyloid Fibril Formation of the Parathyroid Hormone

Bruno Voigt, Maria Ott, and Jochen Balbach*

Functional amyloids belong to an increasing class of non-toxic biologic material, in contrast to the prominent disease-related amyloids. Herein, this work reports on the fibril formation of the parathyroid hormone PTH₈₄ as a representative candidate following the same generic principles of primary and secondary nucleation. Employing Thioflavin T monitored kinetics analyses and negative-staining transmission electron microscopy, an intricate, concentration dependent behavior of time dependent generation and morphologies of PTH₈₄ fibrils are found. While at low peptide concentrations, fibril formation is driven by surface catalyzed secondary nucleation, an increased amount of peptides cause a negative feedback on fibril elongation and secondary nucleation. Moreover, the source of primary nuclei is found to regulate the overall macroscopic fibrillation. As a consequence, the concentration dependent competition of primary versus secondary nucleation pathways is found to dominate the mechanism of fibril generation. This work is able to hypothesize an underlying monomer-oligomer equilibrium providing high-order species for primary nucleation and, additionally, negatively affecting the available monomer pool.

biological function. An important feature is the, at least partial, reversibility of fibril formation and thus a controlled monomer release. Among others, functional amyloids have implications in bacterial biofilm, human skin pigmentation, memory and peptide hormone storage.^[3–6] For the latter task, peptide hormones are synthesized as monomers, and subsequently stored in secretory granules. Upon release into the blood stream, monomers dissociate from fibril ends and can thus act on their targets.^[7–9] For β -endorphin it has been shown for example that a pH jump (from acidic granule into alkaline blood) in combination with a drop in peptide concentration due to dilution triggers the monomer release.^[10]

Tracking the kinetics of amyloid formation, for example, by the small organic dye Thioflavin T (ThT) monitoring the fibrillar mass, results in a sigmoidal shape build up curve when starting from peptide monomers. The time evolution comprises

a lag-phase, a growth phase and a stationary phase at which the system approaches an equilibrium state.^[11,12] Intensive work over the last decades revealed that this simple macroscopic behavior originates from an intricate network of different individual molecular mechanisms.^[13] These are typically classified into processes increasing the fibrillar mass M (elongation) and the number of fibrils P (**Figure 1**). The latter comprises primary (primary nucleation) and secondary events (secondary nucleation, fragmentation). The contribution of these individual microscopic pathways for a certain system and the respective rate constants defines the macroscopic curve shape as well as its dependence on the peptide concentration.^[14,15]

The parathyroid hormone is a peptide hormone acting in Ca²⁺ and phosphate homeostasis which gets produced by the parathyroid glands as a pre-pro-hormone of 115 amino acids.^[18,19] The 25 residue pre sequence is cleaved co-translationally, while the six residue pro-sequence is cleaved by the endopeptidase furin in the Golgi apparatus.^[20,21] The mature hormone, being referred to as PTH₈₄, comprises of 84 amino acids. The N-terminal 34 amino acids exhibit an α -helical propensity whereas the C-terminus remains intrinsically disordered.^[22,23] In previous in vitro studies we demonstrated that PTH₈₄ undergoes spontaneous fibrillar self-assembly at neutral and alkaline conditions

1. Introduction

Amyloid fibrils play key roles in disease and physiological function.^[1,2] An increasing number of so-called functional amyloids had been identified, for which the fibrillar state is not a pathological form of the corresponding protein but has its own

B. Voigt, J. Balbach
Institute of Physics
Martin Luther University Halle-Wittenberg
Betty-Heimann-Strasse 7, DE-06120 Halle, Germany
E-mail: jochen.balbach@physik.uni-halle.de

M. Ott
Institute of Biochemistry and Biotechnology
Martin Luther University Halle-Wittenberg
Kurt-Mothes-Strasse 3, DE-06120 Halle, Germany

 The ORCID identification number(s) for the author(s) of this article can be found under <https://doi.org/10.1002/mabi.202200525>

© 2023 The Authors. Macromolecular Bioscience published by Wiley-VCH GmbH. This is an open access article under the terms of the Creative Commons Attribution-NonCommercial-NoDerivs License, which permits use and distribution in any medium, provided the original work is properly cited, the use is non-commercial and no modifications or adaptations are made.

DOI: 10.1002/mabi.202200525

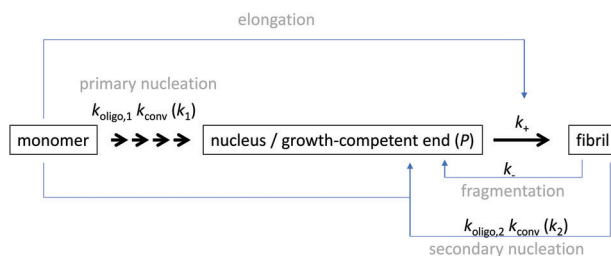


Figure 1. Simplified microscopic processes involved in macroscopic amyloid fibril formation.^[16] New fibrils (one fibril/seed is assumed to have two growth-competent ends, P) are generated by primary (primary nucleation – k_1) or secondary processes (secondary nucleation – k_2 , fragmentation – k_-). The increase of fibrillar mass M occurs mainly via elongation of growth-competent ends, k_+ , by the addition of, in most cases, monomers. The mass increase due to nucleation is typically neglected in the analysis. In this work, we use a three-step kinetic model treating k_1 as $k_{\text{oligo},1} k_{\text{conv}}$ and k_2 as $k_{\text{oligo},2} k_{\text{conv}}$ (see Experimental section).^[17]

(pH7.4 and pH9.0).^[22,24] Under physiological context, on the other hand, no spontaneous fibril formation is observed.^[25] Instead, glucose-amino-glycans (GAG), such as heparin, can act as a trigger molecule initializing amyloid fibril formation. The role of GAGs in assisting fibril formation is also known for other amyloidogenic peptides.^[6,26] Moreover, PTH₈₄ fibrils are the hypothesized storage form of the hormone in analogy to various peptide hormones from the pituitary gland.^[6,22,27]

This work was performed as part of project A12 of the Collaborative Research Center Transregio CRC-TRR 102 “Polymers under multiple constraints.” There, we focused on the polymer and biophysical properties of PTH₈₄ and polymer hybrid-molecules. The latter included covalent conjugates of synthetic polymers with PTH₈₄ or the Alzheimer peptide $A\beta_{1-40}$. PTH₈₄ conjugates showed a shroud-like polymer conformation and the polymer stimulated the nucleation process of the peptide hormone.^[24] A systematic variation of the physicochemical properties of the synthetic polymer allowed to elucidate how the molecular mass and hydrophilicity/hydrophobicity influenced the kinetics and morphology of amyloid fibrils of $A\beta_{1-40}$.^[28,29]

Further, we have engineered β -turn mimetic conjugates containing synthetic turn mimetic structures in the turn region of $A\beta_{40}$ and $A\beta_{16-35}$, replacing two amino acids in the turn-region G25 – K28.^[30] The structure of the turn mimic induces both, acceleration of fibrillation and the complete inhibition of fibrillation, confirming the importance of the turn region on the aggregation using either a bicyclic β -turn mimetic (BTD) or an artificial aromatic β -turn (TAA), while positions N27-K28 and V24-G25 showed only weaker or no inhibitory effects. A catalytic effect on the fibrillation or inhibition of native $A\beta_{40}$ was observed even when added in amounts down to a 1/10 ratio.

Using a reversibly photo-switchable group we could control the bioavailability of the fibrillating parathyroid hormone (PTH₁₋₈₄)-derived peptide.^[31] We have embedded the azobenzene derivative 3-[(4-aminomethyl)phenyl]diazanyl]benzoic acid (3,4'-AMPB) into the PTH-derived peptide PTH₂₅₋₃₇ to generate the artificial peptide AzoPTH₂₅₋₃₇, which can be reversibly photo-switched between its *cis* and *trans* forms. The *trans*-form of AzoPTH₂₅₋₃₇ is fibrillating similar to PTH₂₅₋₃₇, while the *cis*-form of AzoPTH₂₅₋₃₇ generates only amorphous aggregates. Fur-

thermore *cis*-AzoPTH₂₅₋₃₇ catalytically inhibits the fibrillation of PTH₂₅₋₃₇ in ratios down to 1/5, opening an approach to catalytically control fibrillation in vivo by an added photo-switchable peptide.^[31]

In the present work we report on a biophysical study aiming to investigate the spontaneous self-assembly of PTH₈₄ at neutral pH. Under these conditions, a long lag-phase ensured the concentration dependent investigations of fibril elongation and secondary processes since primary nucleation plays a minor role in this time regime.

2. Results and Discussion

2.1. PTH₈₄ Undergoes Spontaneous Amyloid Fibril Formation Only at Elevated Peptide Concentrations

One main key to elucidate the different mechanisms of fibril formation is the investigation of peptide concentration dependent fibril formation kinetics. For this purpose, we conducted aggregation experiments starting from freshly purified, monomeric PTH₈₄ at initial monomer concentrations c_0 ranging from 50 to 600 μM . The need of high peptide concentrations to obtain fibrils was already shown in previous studies and is closely linked to the reported critical concentration of $c_c = 74 \pm 25 \mu\text{M}$ for PTH₈₄.^[22,24] We obtained curves characteristic for amyloid fibril formation with a lag phase, a sigmoidal growth phase and a plateau phase at which the system approaches its thermodynamic equilibrium (Figure 2A). Interestingly and despite the high concentrations used, we found the lag times (time without significant fluorescence increase) with $t_{\text{lag}} > 50 \text{ h}$ to be very long compared to, for example, $A\beta_{40}$ ($t_{\text{lag}} < 10 \text{ h}$ for $c_0 < 10 \mu\text{M}$, depending on the exact conditions) followed by a relatively long growth phase.^[32] In addition, a notable feature of the fibrillation profiles is a double-sigmoidal character at low c_0 ($< 200 \mu\text{M}$, Figure 2A and Figure S1A, Supporting Information). We suspect that, at least, two distinguishable kinetic components with distinct rate constants contribute to the overall fibrillation curves.

However, for samples with c_0 above 200 μM the sigmoidal growth is followed by a decrease of the ThT fluorescence signal before finally reaching a plateau. Interestingly, the final fluorescence values are constant ($F_{\text{ThT}} = 8411 \pm 1904 \text{ a. u.}$), while the maximum signal revealed two linear regimes, with an intercept at 383 μM (Figure 2B). We suspect that these segments hint toward distinct fibril morphologies displaying unique ThT binding behavior. The mean of the final fluorescence overlaps with the maximum fluorescence at $c_0 = 230 \mu\text{M}$. Moreover, the fluorescence decrease can be described by a mono-exponential decay with a rate constant k_{dec} of $0.01 \pm 0.005 \text{ h}^{-1}$ (Equation (6)) without any dependence on c_0 (Figure 2D, inset). Hence, the decay results from a fibril dependent, rather than a monomer dependent, process, such as the assembly of fibrils into clusters. Images taken from the plate after 310 h incubation indeed proof the existence of precipitates large enough to lead to a turbid sample (Figure S1D, Supporting Information). Static light scattering experiments supported the presence of large particles by displaying an increase of the optical density at 600 nm (OD_{600} , Figure S1E,F, Supporting Information). Interestingly, we observed a shift of the maximum ThT absorbance toward higher wavelengths at high c_0 (Figure S1G, Supporting Information), indicating a change within the

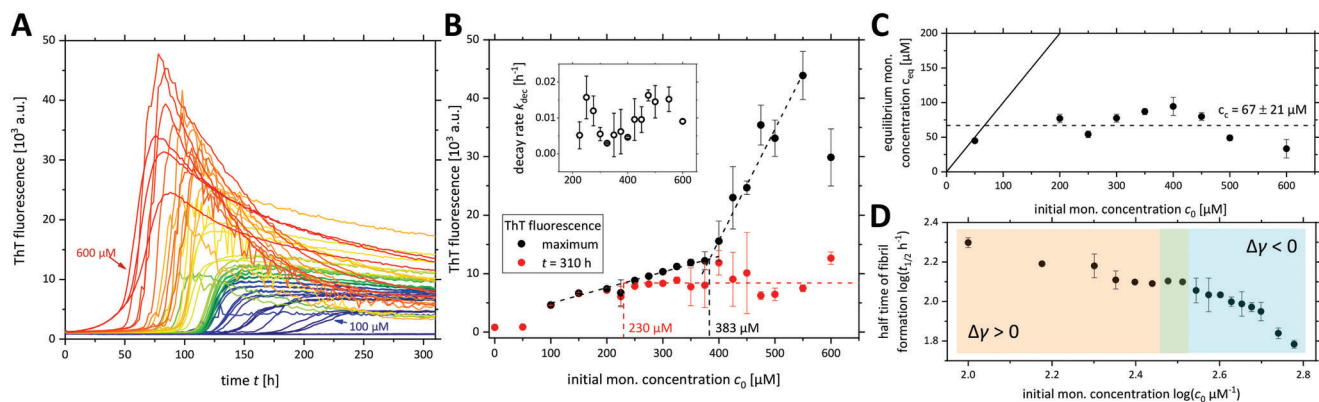


Figure 2. Amyloid fibril formation by PTH₈₄. A) ThT monitored fibrillation kinetics for the concentration range between 0 and 600 μM in steps of 25 or 50 μM . For 0 and 50 μM no ThT fluorescence increase was detected. All triplicates for each c_0 are shown. B) Average ThT fluorescence at the curve maximum (black) and at $t = 310$ h (red) with respect to c_0 . Black dashed lines mark the two linear regimes of the maximum fluorescence. The red dashed line indicates the average end-point fluorescence for $c_0 > 200$ μM . Inset: mono-exponential rate constant k_{dec} of the fluorescence decay after passing the maximum (Equation (6)). C) Equilibrium free monomer concentrations c_{eq} after 310 h. The critical concentration c_c (dashed line) was calculated as the mean of all c_{eq} (for $c_0 > 74$ μM).^[22] The solid line indicates the case of no fibril formation ($c_{\text{eq}} = c_0$). D) $\log(t_{1/2})$ - $\log(c_0)$ -plot of the half time of fibril formation ($t_{1/2}$). The shaded regions indicate positive (orange) and negative (cyan) curvature. All data points in B)–D) represent the mean and the standard deviation of three individual replicates.

molecular environment of the dye or a different binding behavior of ThT leading to distinct fluorescence quantum yields. We determined the concentration of free ThT after fibrillation (after centrifugation of the fibrils) which we found to be inversely proportional to c_0 (Figure S1H, Supporting Information), indicating that bound ThT sedimented together with the fibrils. Conversely, the ThT concentration in the control sample yielded only 35 μM . However, we checked the concentration at the beginning of the experiment (indicated by black dotted line). The decrease of detectable dye molecules could be due to micelle formation of ThT which precipitated during centrifugation.^[33] Another possibility would be self-quenching of ThT fluorescence due to an increase of the local dye concentrations leading to the observed fluorescence decrease (Figure 2B).^[34,35]

The critical concentration of amyloid formation, c_c , is a parameter reflecting the thermodynamic stability of amyloid fibrils.^[36] Therefore, we additionally measured the concentration of free PTH₈₄ monomers in equilibrium with fibrils after 310 h. The equilibrium free monomer concentration c_{eq} was consistently found to be 67 ± 21 μM , reflecting the critical concentration c_c (Figure 2C). This agrees with our previous studies as well as with the general concept of the critical concentration and monomer release from functional hormone fibrils.^[22,36]

An analysis of the times to half completion of fibrillation profiles (half times, $t_{1/2}$) is a powerful tool to obtain initial information on the dominating mechanisms as well as on corresponding reaction orders.^[16] The scaling exponent γ of a $\log(t_{1/2})$ - $\log(c_0)$ -plot can be extracted as a power law with $t_{1/2} \approx c_0^\gamma$. In general, a single consistently dominant mechanism is characterized by a linear scaling, while a competition between two processes typically results in a negative curvature ($\Delta\gamma < 0$). On the other hand, a positive curvature ($\Delta\gamma > 0$) indicates saturation effects, presumably of elongation or secondary nucleation. Here we analyzed the fibrillation kinetics until the maximum ThT fluorescence emission had reached. Interestingly, for PTH₈₄ at various initial monomer concentrations we found a positive as well as

a negative curvature of the corresponding half time plot (Figure 2D). This complex behavior has yet only been reported for the Tau_{304–380} fragment but it has not been further elucidated.^[37] The positive curvature dominates at $c_0 < 300$ μM , with a scaling exponent increasing from $\gamma \approx -0.5$ to $\gamma = 0$ (indicated by shaded orange region). This agrees with a saturation of the elongation process. The observed negative curvature at $c_0 > 300$ μM (shaded cyan region) denotes the entrance of a process generating additional growth-competent ends into the reaction network. In principle, primary and secondary nucleation need to be considered.

2.2. PTH₈₄ Fibrils Display a Strong Polymorphism

We further aimed to investigate the morphology of the fibrils at low (100 μM , Figure 3A), intermediate (300 μM , Figure 3B) and high c_0 (500 μM , Figure 3C) by negative staining transmission electron microscopy. The micrographs show curvilinear fibrils characteristic for PTH₈₄ as previously reported.^[22,24,25] The fibrils are up to several μm in length, only showing few shorter individual fibrils. Notably, PTH₈₄ fibrils exhibit a strong polymorphism. Fibrils can be found to be twisted or flat, with an irregular pitch length even in strongly twisted fibrils. Additionally, at 500 μM we found the fibrils to be clustered with only few individual fibrils (Figure 3C, upper panel). In a sample isolated 20 h after the fluorescence maximum was reached in the kinetic assay (Figure S1B, Supporting Information) as well as in a sample treated with probe-sonication (Figure S1C, Supporting Information) an essentially lower amount of these clusters is observed. Both samples exhibit the same macroscopic appearance as for 300 μM at the end-point (compare to Figure 3B). Taken together with the observed fluorescence decrease (Figure 2B), this supports the hypothesis of the formation of supramolecular fibril clusters with impaired ThT fluorescence. Thus, unclustered fibrils essentially contribute to the final ThT fluorescence signal. Since fibril

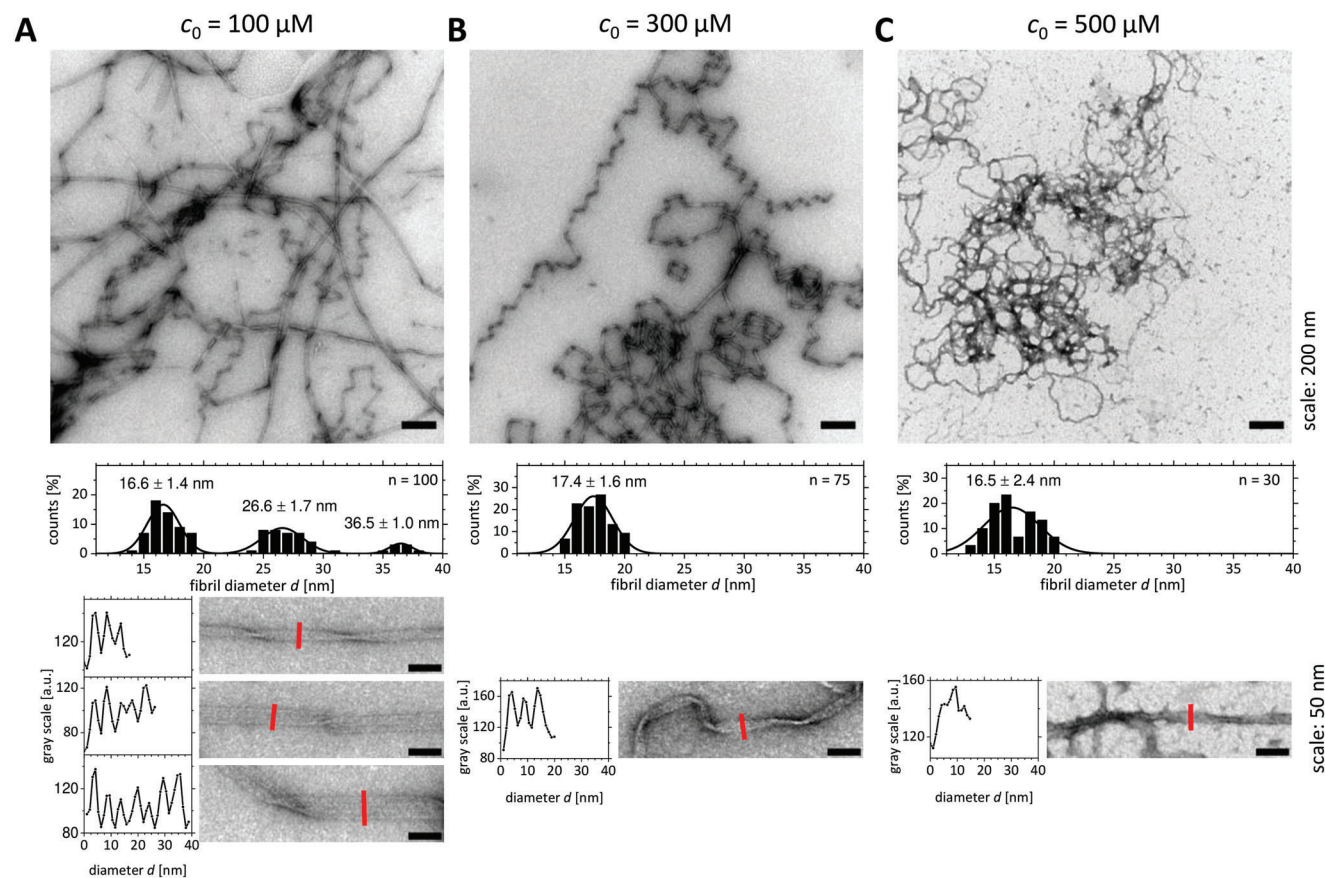


Figure 3. Electron Microscopy reveals polymorphism of PTH₈₄ fibrils. Fibril morphologies after 310 h incubation time have been characterized for A) $c_0 = 100 \mu\text{M}$, B) $c_0 = 300 \mu\text{M}$ and C) $c_0 = 500 \mu\text{M}$. Shown are representative electron micrographs (upper panel, scale bar = 200 nm), calculation of fibril diameters (middle panel) as well as fibril cross sections (lower panel, left – gray scale, right – representative individual fibril, scale bar = 50 nm, red solid lines indicate cross sections).

precipitation occurs above a threshold concentration of $c_0 = 230 \mu\text{M}$ (Figure 2B), we propose a maximum soluble fibril fraction of $230 - 67 \mu\text{M} = 163 \mu\text{M}$ (given in monomer equivalents converted into fibrils, with $c_c = 67 \mu\text{M}$ as the fraction of soluble monomers) in equilibrium with free monomers.

A more detailed analysis of the fibril dimension revealed a consistent diameter of $d_{300} = 17.4 \pm 1.6 \text{ nm}$ for $300 \mu\text{M}$ and of $d_{500} = 16.5 \pm 2.4 \text{ nm}$ for $500 \mu\text{M}$, whereas three different species with $d_{100,1} = 16.6 \pm 1.4 \text{ nm}$, $d_{100,2} = 26.6 \pm 1.7 \text{ nm}$ and $d_{100,3} = 36.5 \pm 1.0 \text{ nm}$ were found for $100 \mu\text{M}$ (Figure 3A–C, middle panels). An inspection of the cross sections shows that the fibrils consist of three ($d_{100,1}$, d_{300} , d_{500}), five ($d_{100,2}$), or seven ($d_{100,3}$) individual filamentous structures of about 5.5 nm width within a fibril (Figure 3A–C, bottom panels). The occurrence of three fibrillar sub-types gives rise to the assumption of different underlying kinetic rate constants of fibril formation, as observed for low c_0 (Figure S1A, Supporting Information). However, in a previous study using heparin as fibrillation trigger no polymorphism was observed.^[25] Heparin possibly favors the formation of only one morph which we also found for all probed c_0 . The morphology of fibrils present in vivo within the secretory granules is currently unknown but their characterization is part of our future work.

2.3. PTH₈₄ Fibril Formation is Dominated by Secondary Processes and Inhibition Effects

2.3.1. Light Seeding Demonstrates the Importance of Autocatalytic Self-replication

We further investigated whether secondary processes contribute to the macroscopic fibrillation behavior. Therefore, we repeated the experiment presented in Figure 2A with the addition of a low amount of pre-formed probe-sonicated seeds (0.2 % of c_0 , given in monomer equivalents) at time zero (Figure 4A, curves for all c_0 are shown in Figure S2A, Supporting Information). For seeded experiments, c_0 denotes the initial concentration of monomeric peptide to which pre-formed seeds are added. If secondary events (secondary nucleation or fragmentation) do not contribute to the overall time course no significant acceleration of fibrillation is expected for a given c_0 compared to the corresponding de novo experiment. Instead, we found a strong reduction of the lag times for all c_0 , underlying the importance of secondary events, and thus the autocatalytic self-propagation, for the fibrillation of PTH₈₄. Moreover, we found a linear scaling in the half-time plot with $\gamma = -0.75$, indicating that the saturation and competition effects, as observed for de novo fibrillation (Figure 2D),

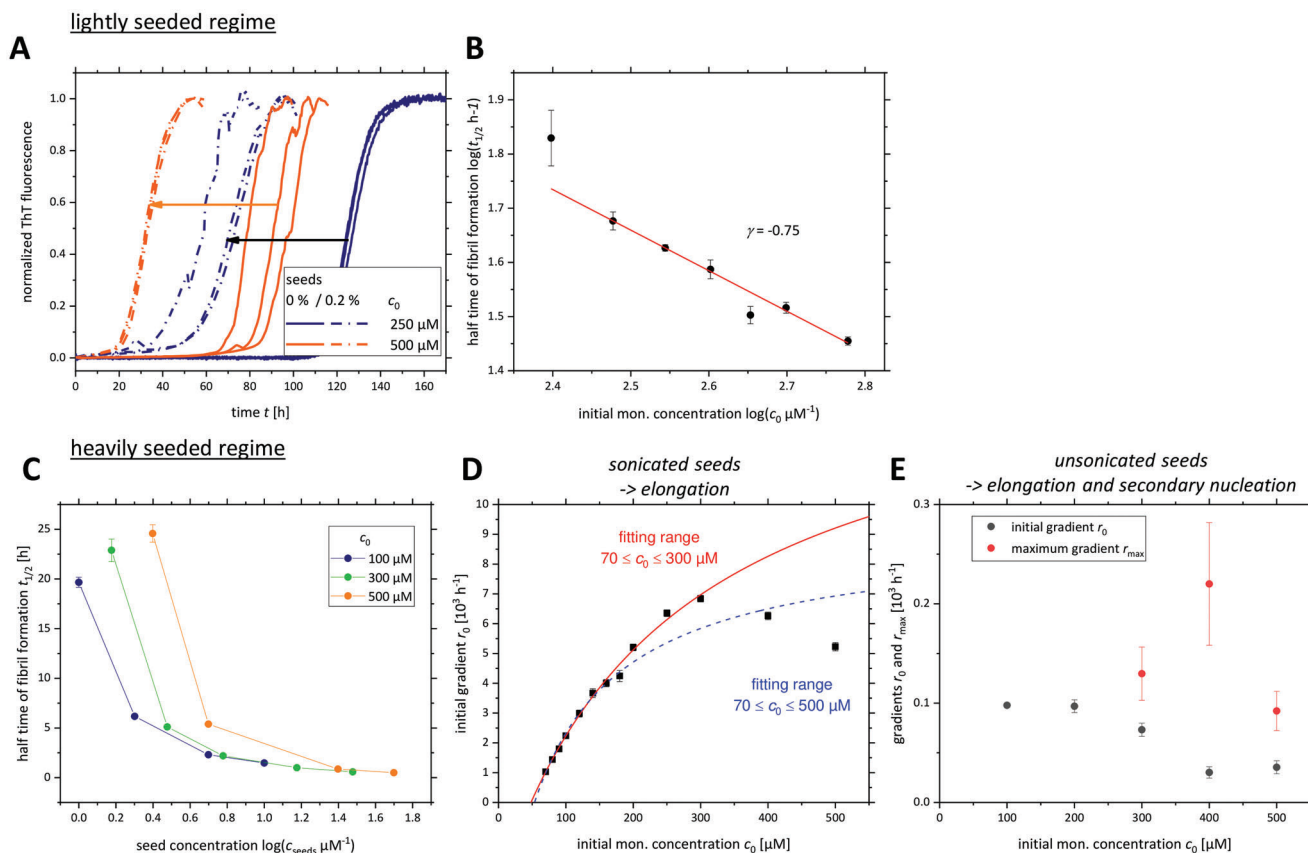


Figure 4. Seeding experiments reveal the importance of secondary processes as well as inhibition effects. A) Comparison of fibril formation de novo (solid lines) with the addition of 0.2 % seeds (given as monomer equivalents of c_0 , dotted lines) for $c_0 = 250$ and $500 \mu\text{M}$ (blue and orange). Arrows indicate the shift of the kinetic curves toward lower lag times. The data for de novo fibrillation are the same as presented in Figure 2A. B) $\log(t_{1/2})$ - $\log(c_0)$ -plot of the half times. The scaling factor was found to be $\gamma = -0.75$. Additional curves are shown in Figure S2A, Supporting Information. C) $t_{1/2}$ - $\log(c_0)$ -plot of PTH₈₄ at three different c_0 with different amounts of sonicated seeds added at time zero. Seed concentrations are given as monomer equivalents of c_0 . The solid lines connecting the data points are drawn to guide the eye. D) initial gradients r_0 at various c_0 supplemented with $25 \mu\text{M}$ sonicated seeds. The dashed blue and the solid red lines are fits according to Equation (2) in the c_0 ranges 70 – $500 \mu\text{M}$ or 70 – $300 \mu\text{M}$, respectively. E) initial (black) and maximum gradients (red) r_0 and r_{max} , respectively, of various c_0 supplemented with unsonicated seeds. For 100 and $200 \mu\text{M}$ no further fluorescence increase was found after the initial phase. All data points represent the mean and the standard deviation of three individual replicates.

are effectively bypassed (Figure 4B). With the addition of seeds, elongation and secondary nucleation directly proceed from these templates, whereas the relevance of primary nucleation becomes negligible.

2.3.2. Heavy Seeding Reveals that Elongation as well as Secondary Nucleation are Affected by High Peptide Concentrations

In order to evaluate if saturation of the elongation rate constant k_+ is responsible for the positive curvature of the halftime plot (Figure 2D), we performed additional seeding experiments (Figure 4C–E). In contrast to the presented data at very low c_{seed} , elongation of the existing seeds is the only significant contribution to the increase in fibrillar mass in the high seeding regime. This can be addressed as the linear initial gradient of the ThT signal r_0 at the first points of the time course. The dependence of r_0 from c_0 for a constant seed number concentration P_0 is given by

$$r_0 \sim \left. \frac{dM}{dt} \right|_{t \rightarrow 0} = 2 k_+ c_0 P_0 \quad (1)$$

with M the aggregate mass concentration and k_+ the rate constant of elongation.^[14] P_0 reflects the number of template fibrils in a seed sample, in contrast to c_{seed} which denotes the seed mass concentration. Since P_0 is a highly error-prone parameter, we do not aim to calculate k_+ . To determine the necessary seed mass concentration c_{seed} at which the high seeding regime can be expected we performed seeding experiments at increasing c_{seed} with three different monomer concentrations (with c_{seed} up to 10 % of c_0 , in monomer equivalents). Directly plotting the halftime of aggregation versus the logarithm of c_{seed} allows an estimation on the regime (Figure 4C and Figure S2B, Supporting Information). The high seeding regime is expected for a linear dependence with a small negative slope. We identified $c_{\text{seed}} = 25 \mu\text{M}$ to fulfill these requirements (at $\log(c_{\text{seed}}) = 1.4$ in Figure 4C). At lower seed concentrations, the non-linear nature of the plot proves the contribution of secondary processes. Interestingly, at a given c_{seed} in this range, we obtained a concentration dependent t_m , possibly indicating inhibitory effects at high c_0 .

In the next step, PTH₈₄ at varying monomer concentrations was supplemented at time zero with a constant seed mass

concentration of $c_{\text{seed}} = 25 \mu\text{M}$ (Figure 4D and Figure S2C, Supporting Information). We found a linear dependence of the initial gradient r_0 from c_0 for $c_0 \leq 200 \mu\text{M}$, indicative for monomers as the species required for elongation.^[38] The addition of oligomers to fibril ends would result in a polynomial-like dependence.^[39] However, with a maximum at $300 \mu\text{M}$ a further increase of c_0 even results in a decrease of r_0 . The data indicate that the rate constant of elongation, k_+ , is not proportional to c_0 , as predicted by the half-time plot (Figures 2D and 4C), and is written as \tilde{k}_+ . For the case of a saturation of the elongation process, Equation (1) needs to be extended to

$$r_0 = 2 \tilde{k}_+ c_0 P_0 = \frac{2 k_+ c_0}{1 + \frac{c_0}{K_E}} P_0 + \gamma_0 \quad (2)$$

in analogy to the Michaelis–Menten description of enzymatic reactions, with k_+ the true rate constant of elongation, K_E the concentration at which saturation effects occur and γ_0 an offset value introduced due to the high value of c_c below which no fibril formation occurs.^[40] In this case diffusion and binding of a monomer to a growth-competent end (“dock”) is the rate-determining step at low c_0 , whereas the slow structural conversion becomes limiting at high c_0 when basically all free ends are blocked by attached monomers (“lock”). A fit of the data to Equation (2) is shown in Figure 4D (blue dotted line). The fit only succeeds to represent the data at low c_0 but fails at high c_0 . However, a systematic decrease of r_0 at high c_0 is obvious from the experimental kinetic curves (Figure S2C, Supporting Information). We further confined the fitting range to the maximum value of r_0 (red solid line in Figure 4D) resulting in a valuable fit within this range. Interestingly, the model of saturated elongation reaches a limitation when applied to our data. We suspect that the elongation step at high c_0 is confined by an inhibition rather than by a true saturation effect.

Note that for this experiment the seeds have been probe-sonicated to break the fibrils into fragments and thus to increase the number of growth competent ends ($2 P_0$ in Equation (1) and (2), Figure S1C, Supporting Information). The same experiment can be conducted for untreated seeds displaying an essentially lower number of free ends compared to the fibril mass (Figure 4E and Figure S2D, Supporting Information). This allows conclusions on secondary processes. If secondary processes are active, the initial gradient r_0 is not equal to the maximum slope r_{max} . A relation of r_{max} to the time evolution of the fibril number concentration, predominantly reflecting secondary processes in the observed time regime, is given by

$$r_{\text{max}} \sim \frac{dP_t}{dt} \sim k_2 M_t c_0^{n_2} + 2 k_- P_t \quad (3)$$

where P_t and M_t are the fibril number and fibril mass concentration, respectively, k_2 and n_2 the rate constant and reaction order of secondary nucleation, respectively, according to the two-step bulk description, and k_- the rate constant of fragmentation.^[14,41,42] The contribution of primary nucleation is neglected in Equation (3). For the initial gradient we found a monomer dependence similar to the behavior described for probe-sonicated seeds. r_0 decreases for $c_0 > 200 \mu\text{M}$. Simultaneously, r_{max} increases, with a maximum at $c_0 = 400 \mu\text{M}$ and a decrease at $c_0 = 500 \mu\text{M}$.

Since r_{max} obviously depends on c_0 , we propose that secondary nucleation contributes to PTH₈₄ fibril formation, rather than monomer independent fragmentation (Equation (3)). Additionally, the data provide a hint toward a saturation or even an inhibition of secondary nucleation at high c_0 , in addition to the discussed effect on elongation.

2.4. Kinetics of PTH₈₄ Amyloid Formation Display a Complex Concentration Dependence

In order to gain a deeper understanding of the underlying mechanism of amyloid formation by PTH₈₄ we performed individual curve fittings to the increasing part of the ThT monitored fibrillation kinetics depicted in Figure 2A (Equation (6)) as described previously, thus revealing information about the effective rates of primary (λ) and secondary (κ) processes.^[25] The fits reproduce the data well, only at $c_0 = 600 \mu\text{M}$ (red curve) it is obvious that the applied simple model is not sufficient to describe the full curve (Figure 5A). Still, the parameters provide a solid trend. As mentioned before, the introduction of a second component contributing to the overall fibrillation kinetic is necessary to describe the data at c_0 below $200 \mu\text{M}$ (Equation (17)). Since the percentage of the second kinetic component approaches $< 5\%$ with increasing c_0 , and thus giving high errors of the fitting parameters, we only focused on the dominant first component (Figure S1A, Supporting Information inset). At c_0 below $250 \mu\text{M}$, λ exhibits a linear scaling, though the scattering of the data points did not allow a well-defined fit (Figure 5B). The visible trend agrees with a reaction order of $n_{\text{oligo},1} + n_{\text{conv}} \leq 4$ (Equation (9), reaction orders 2 (dotted orange line) and 4 (dashed orange line) are shown as theoretical examples). For higher c_0 the reaction order increases to $n_{\text{oligo},1} + n_{\text{conv}} = 18.5$. These data indicate that the species involved in primary nucleation changes from a low-order oligomer ($n_{\text{oligo},1} + n_{\text{conv}} \leq 4$) to a high-order oligomer ($n_{\text{oligo},1} + n_{\text{conv}} = 18.5$). Note that the reaction order denotes a combination of the respective reaction orders of oligomer formation and oligomer conversion, and thus does not reflect the exact number of monomers within a hypothetical oligomer. Nevertheless, it provides a clear trend. This, highly hypothetical, size of primary nuclei is consistent with a simulation study in which peptides with a low propensity to form β -sheets were found to have higher corresponding primary nuclei sizes of $n_1 > 2$ compared to, for example, $A\beta_{40}$.^[43] PTH₈₄ is known to exhibit an α -helical propensity at the N-terminus while the C-terminal region remains intrinsically disordered.^[22,23]

The importance of the air-water-interface (AWI), and thus the surface tension, is a mostly neglected but underappreciated factor in amyloid growth.^[44] The surface tension of a solution of insulin was shown to decrease if oligomers are present, but increased for a fibril-containing sample.^[45] In general, conformational and oligomerization effects at the AWI have been reported, for example, β -sheet containing dimer formation and induced polymorphism via alternative assembly pathways.^[44,46–48] For example, amphipathic helices display an inherent surface activity.^[49] For PTH₈₄ residues S17-V31 are reported to adopt such an amphipathic helical structure, which in the context of hormone activity is required for receptor activation.^[50] As a consequence, small oligomers of PTH₈₄ which are possibly formed and converted

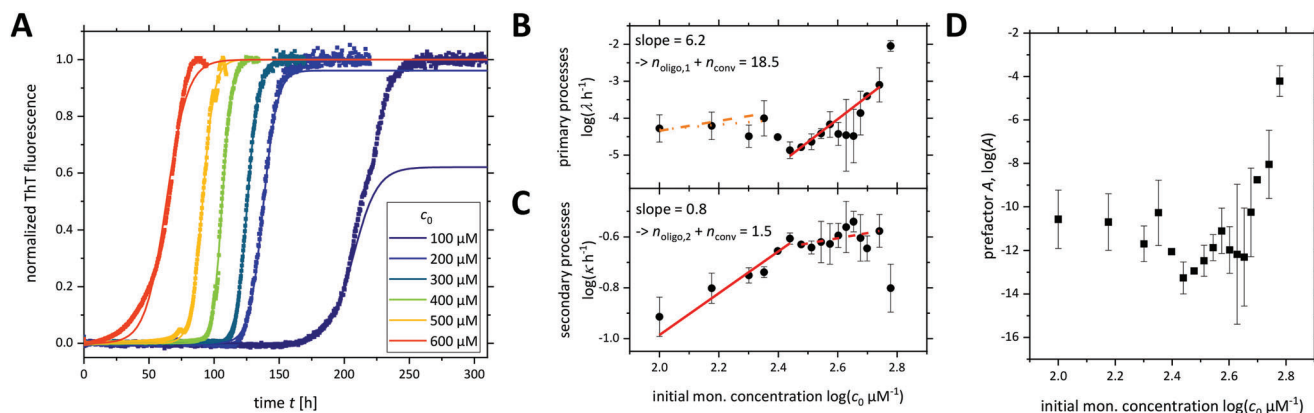


Figure 5. Individual curve fitting reveals insights into primary and secondary processes. The data shown in Figure 2A have been fitted according to Equation (7). A) Representative curves chosen from triplicate measurements (points) at six individual c_0 with the respective fits (solid lines) are shown. For 100 and 200 μM Equation (17) was used, introducing a second kinetic component. The fits and the data in the following panels are only given for the first component. The extracted parameters are B) λ , the sum of primary, C) κ , the sum of secondary processes and D) the kinetic prefactor A (Equation 8). In B–D) the parameters are presented as $\log(\text{parameter})\text{-}\log(c_0)$ -plots. Concentration ranges in panels B) and C) displaying a respective linear scaling are indicated with a solid red line corresponding to a power law fit with $\log(\lambda/\kappa) = \text{slope}_{\lambda/\kappa} \times \log(c_0) + \text{constant}_{\lambda/\kappa}$. All data points represent the mean and the standard deviation of three individual replicates. The orange lines in panel B) represent theoretical curves for $n_{\text{oligo},1} + n_{\text{conv}} = 2$ (dotted) and $n_{\text{oligo},1} + n_{\text{conv}} = 4$ (dashed).

to an elongation competent nucleus at low c_0 by adsorption of the amphipathic helix at the AWI via different pathways could be a considerable origin of the here observed polymorphism (Figure 3A).

For the investigation of κ we only took $c_0 \leq 275 \mu\text{M}$ into account considering the high statistical errors of the data points at higher c_0 and the inhibition effects at high c_0 (compare with Figure 4D,E), resulting in the reaction order $n_{\text{oligo},2} + n_{\text{conv}} = 1.5$ (Equation (10), Figure 5C). Equation (16) shows that this corresponds to the more frequently used bulk model with $n_2 = 0.7$, indicating a peptide monomer as the physical nucleus size required for secondary nucleation. Thus, we note that both elongation (Figure 4D) and secondary nucleation (Figures 4E and 5C), the microscopic processes requiring monomeric peptide, are inhibited at high c_0 . However, at 300 μM , a concentration at which the half-time scaling factor was found to approach $\gamma = 0$ (Figure 2D), the scaling of κ apparently becomes concentration independent. The definition of κ includes elongation (k_+) as well as secondary nucleation ($k_{\text{oligo},2}$, k_{conv}) (Equation (10)). The apparent saturation of κ might be an effect of the inhibition of one or both processes (see also Figure 4D,E). Interestingly, the high reaction order of λ obviously compensates the effect of k_+ on the c_0 dependence of λ . Nevertheless, the contribution of a high-order oligomer is evident. The high hypothesized order of an involved oligomer raises the question if this indicates a “core–shell” nanocrystal or a micelle- or droplet-like condensed state.^[51] Interestingly, for lysozyme, IAPP and α -synuclein it has been shown that nucleation from such states result in very weak dependences on c_0 which is in contrast to our data.^[48,52–54]

The significantly different reaction orders of primary and secondary nucleation, in combination with a negative curvature in the halftime plot, gives rise to the hypothesis that primary nucleation starts to compete with secondary processes at high c_0 to be the dominant mechanism of new fibril generation. To the best of our knowledge, this is the first experimental report of this specific case. An inspection of the prefactor A ($A = \lambda^3 3^{-1} \kappa^{-3}$, Equ-

ation (8)) illustrates this behavior. From this definition it follows that small values ($A < 0.33$ for $\lambda = \kappa$) or a negative trend indicate the dominance of secondary processes. At low c_0 , A is of the order 10^{-11} with a negative dependence on c_0 , highlighting the importance of secondary processes on the macroscopic fibrillation curves (Figure 4C). A dramatic increase of A of several orders of magnitude after passing a minimum at 275 μM indicates the competition of two microscopic mechanisms to be the dominant process for the creation of new growth-competent ends, P_0 , and thus the relevance of primary nucleation for high c_0 .

3. Conclusion

In this work we investigated amyloid fibril formation of PTH₈₄. Employing a simple kinetic analysis approach, we have been able to elucidate an intricate concentration-driven fibrillation network of a functional amyloid (Figure 6). We demonstrated a complex concentration dependent behavior including polymorphism, assembly of fibrils into clusters and inhibition effects. We found that at low c_0 (for $c_0 > c_c$) fibrils nucleate from small oligomeric peptide species. The variation of the fibril diameters agrees with the occurrence of, at least, two distinguishable kinetic components contributing to the overall fibrillation behavior. At low concentrations ($c_0 < 300 \mu\text{M}$), secondary nucleation is the dominant process for the creation of new fibrils. Upon increasing c_0 , the monomer consuming processes elongation and secondary nucleation become inhibited. In addition, the physical size of the primary nucleus dramatically increases, indicating a different underlying nucleation mechanism. We conclude that the nucleus originates from large on-pathway oligomers which are in equilibrium with monomers above a certain threshold concentration, the “critical oligomer concentration” (coc), reducing the effective monomer concentration. Thus, monomer availability becomes rate limiting for self-propagation (secondary nucleation) and the increase in fibrillar mass (elongation).

Equilibrium Free Monomer and ThT Concentrations: Fibrillation samples in the thermodynamic equilibrium were centrifuged at 16 100× g for 1 h at room temperature. The concentration of free peptide monomer in solution was determined at 280 nm ($\epsilon_{280} = 5500 \text{ M}^{-1} \text{ cm}^{-1}$) and of free ThT at 412 nm ($\epsilon_{412} = 36\,000 \text{ M}^{-1} \text{ cm}^{-1}$) by UV-vis spectroscopy.^[57,58] Since ThT contributes to the UV absorption at 280 nm, the peptide absorption was corrected using Equation (4)

$$OD_{280, \text{peptide}} = OD_{280} - OD_{412} \frac{OD_{280, \text{ref}}}{OD_{412, \text{ref}}} \quad (4)$$

where $OD_{280, \text{ref}}$ and $OD_{412, \text{ref}}$ are the corresponding absorption values of ThT in a reference sample without peptide. The molar concentrations were calculated with the law of Lambert-Beer. The baseline correction was conducted with pure buffer.

Seed Preparation: Seeds were prepared from a 500 μM fibrillation sample without ThT which reached the stationary phase. If not mentioned otherwise, fibrils were disrupted by probe-sonication (1 s pulse, 1 s pause, 12 × 10 % amplitude). Seeded assays were started within maximally 30 min after seed preparation.

Optical Density and Scattering: After completion of the kinetic assay, UV-vis spectra had subsequently been acquired for all replicates without removing the seal foil (FluoStar Omega, BMG Labtech; range 350–700 nm, data pitch 5 nm). For the characterization of the ThT absorbance the ratio of the optical density OD at 420 and 430 nm (OD_{420} / OD_{430}) was calculated. This work defined the observed turbidity of the samples to be the scattering intensity, that is, as the increase of OD_{600} of a respective sample compared to the control that only contained ThT:

$$\text{scattering} = OD_{600, \text{sample}} - OD_{600, \text{control}} \quad (5)$$

Kinetic Analyses: The fluorescence decay after passing a maximum value was fitted with a single exponential function

$$F = F_0 + Be^{-k_{\text{dec}}t} \quad (6)$$

with k_{dec} the exponential decay rate.

For the investigation of the mechanism of PTH₈₄ fibril formation a simple kinetic approach was employed as described previously.^[17,25,59] For a basic description of the sigmoidal curve shape the introduction of the parameters λ and κ reflecting the sum of primary and secondary events, respectively, results in the function

$$F_t = 1 - \frac{1}{1 + A(e^{\kappa t} - 1)} \quad (7)$$

with F the normalized ThT fluorescence and the parameters

$$A = \frac{\lambda^3}{3 \kappa^3} \quad (8)$$

$$\lambda = (2 k_+ k_{\text{oligo},1} k_{\text{conv}} c_0^{n_{\text{oligo},1} + n_{\text{conv}}})^{1/3} \quad (9)$$

$$\kappa = (2 k_+ k_{\text{oligo},2} k_{\text{conv}} c_0^{n_{\text{oligo},2} + n_{\text{conv}} + 1})^{1/3} \quad (10)$$

with $k_{\text{oligo},1/2}$ the rate constant of the formation of oligomers involved in primary or secondary nucleation, respectively, k_{conv} the rate constant of conversion, k_+ the rate constant of elongation via monomer addition, c_0 the initial peptide monomer concentration, $n_{\text{oligo},1/2}$ the reaction order of the formation of oligomers involved in primary or secondary nucleation, respectively, and n_{conv} the reaction order of oligomer conversion. The reaction orders can be extracted from the corresponding $\log(\lambda/\kappa)$ - $\log(c_0)$ -plots with the scaling factors.

$$\gamma_\lambda = \frac{n_{\text{oligo},1} + n_{\text{conv}}}{3} \quad (11)$$

$$\gamma_\kappa = \frac{n_{\text{oligo},2} + n_{\text{conv}} + 1}{3} \quad (12)$$

This approach explicitly takes nucleation via oligomeric species into account which is reflected by the cubic influence of λ and κ on the prefactor A and thus on the time scale. In this case nucleation is treated as a three-step process consisting of oligomer formation ($k_{\text{oligo},1/2}$), conversion of the oligomers into growth-competent species (k_{conv}) and elongation (k_+), with the respective reaction orders $n_{\text{oligo},1/2}$ and n_{conv} .

A connection to the more frequently used two-step description (nucleation coupled with elongation) with the bulk rate constants k_1 and k_2 and the corresponding bulk reaction orders n_1 and n_2 of primary and secondary nucleation, respectively, is given by:

$$k_1 = \frac{2}{3} \left(\frac{k_{\text{oligo},1}^3 k_{\text{conv}}^2}{2 k_+ k_{\text{oligo},2}} \right)^{1/3} \quad (13)$$

$$k_2 = \left(\frac{k_{\text{oligo},2} k_{\text{conv}}}{2 k_+} \right)^{1/3} \quad (14)$$

$$n_1 = n_{\text{oligo},1} - n_{\text{oligo},2} + n_2 \quad (15)$$

$$n_2 = \frac{2 n_{\text{oligo},2} + 2 n_{\text{conv}} - 1}{3} \quad (16)$$

For low concentrations, a second kinetic component was added to Equation (7), which leads to

$$F = F_{\text{tot}} - \frac{F_1}{1 + A_1(e^{\kappa_1 t} - 1)} + \frac{(F_{\text{tot}} - F_1)}{1 + A_2(e^{\kappa_2 t} - 1)} \quad (17)$$

with F_{tot} the total fluorescence signal, F_1 the fluorescence of component 1, $A_{1/2}$ and $\kappa_{1/2}$ the kinetic prefactor and the sum of secondary events for the first or the second component, respectively. The major kinetic component is indexed as "1."

Negative-Staining Electron Microscopy: The fibrillation samples were diluted 20-fold in buffer (50 mM Na₂HPO₄, 150 mM NaCl, pH7.4) and subsequently 5 μL were transferred to a 3 mm carbon/Formvar-coated copper grid. After 3 min incubation, the grids were blotted, washed with ddH₂O and blotted again. For negative staining, grids were incubated with 1 % uranyl acetate. After blotting, the grids were allowed to dry for 24 h on filter paper. Sample imaging was conducted on a Zeiss EM900 electron microscope with 80 kV acceleration voltage. The analyses of the fibril diameters as well as the cross-section gray-scale profiles were performed using ImageJ/Fiji software. The diameters were calculated based on the measurement of $n = 100$ ($c_0 = 100 \mu\text{M}$), $n = 75$ ($c_0 = 300 \mu\text{M}$), or $n = 30$ ($c_0 = 500 \mu\text{M}$) fibrils.

Supporting Information

Supporting Information is available from the Wiley Online Library or from the author.

Acknowledgements

The authors thank Gerd Hause for the access to the electron microscope, Ulrich Weininger and Malte Neudorf for valuable discussions and Monika Baumann, Marvin E.P. Umlandt and Florian Hennig for initial studies on the project. The work was funded by the German research foundation (DFG, project ID 189853844 – TRR 102 “polymers under multiple constraints”, TP A12, and project ID 391498659 – RTG 2467 “Intrinsically Disordered Proteins – Molecular Principles, Cellular Functions, and Diseases”, TP 2 and TP 11).

Open access funding enabled and organized by Projekt DEAL.

Conflict of Interest

The authors declare no conflict of interest.

Data Availability Statement

The data that support the findings of this study are available from the corresponding author upon reasonable request.

Keywords

amyloid fibrils, functional amyloids, parathyroid hormone

Received: November 30, 2022

Revised: January 27, 2023

Published online: March 9, 2023

- [1] F. Chiti, C. M. Dobson, *Annu. Rev. Biochem.* **2006**, *75*, 333.
- [2] D. Otzen, R. Riek, *Cold Spring Harb. Perspect. Biol.* **2019**, *11*, a033860.
- [3] M. R. Chapman, L. S. Robinson, J. S. Pinkner, R. Roth, J. Heuser, M. Hammar, S. Normark, S. J. Hultgren, *Science* **2002**, *295*, 851.
- [4] D. M. Fowler, A. V. Koulov, C. Alory-Jost, M. S. Marks, W. E. Balch, J. W. Kelly, *PLoS Biol.* **2006**, *4*, e6.
- [5] R. Hervas, M. J. Rau, Y. Park, W. Zhang, A. G. Murzin, J. A. J. Fitzpatrick, S. H. W. Scheres, K. Si, *Science* **2020**, *367*, 1230.
- [6] S. K. Maji, M. H. Perrin, M. R. Sawaya, S. Jessberger, K. Vadodaria, R. A. Rissman, P. S. Singru, K. P. R. Nilsson, R. Simon, D. Schubert, D. Eisenberg, J. Rivier, P. Sawchenko, W. Vale, R. Riek, *Science* **2009**, *325*, 328.
- [7] A. Anoop, S. Ranganathan, B. D. Dhaked, N. N. Jha, S. Pratihari, S. Ghosh, S. Sahay, S. Kumar, S. Das, M. Kombrabail, K. Agarwal, R. S. Jacob, P. Singru, P. Bhaumik, R. Padinhateeri, A. Kumar, S. K. Maji, *J. Biol. Chem.* **2014**, *289*, 16884.
- [8] R. S. Jacob, S. Das, S. Ghosh, A. Anoop, N. N. Jha, T. Khan, P. Singru, A. Kumar, S. K. Maji, *Sci. Rep.* **2016**, *6*, 23370.
- [9] S. K. Maji, D. Schubert, C. Rivier, S. Lee, J. E. Rivier, R. Riek, *PLoS Biol.* **2008**, *6*, e17.
- [10] N. Nespoitaya, J. Gath, K. Barylyuk, C. Seuring, B. H. Meier, R. Riek, *J. Am. Chem. Soc.* **2016**, *138*, 846.
- [11] K. C. Evans, E. P. Berger, C. G. Cho, K. H. Weisgraber, P. T. Lansbury, *Proc. Natl. Acad. Sci. U.S.A.* **1995**, *92*, 763.
- [12] L. Nielsen, R. Khurana, A. Coats, S. Frokjaer, J. Brange, S. Vyas, V. N. Uversky, A. L. Fink, *Biochemistry* **2001**, *40*, 6036.
- [13] T. C. T. Michaels, A. Šarić, J. Habchi, S. Chia, G. Meisl, M. Vendruscolo, C. M. Dobson, T. P. J. Knowles, *Annu. Rev. Phys. Chem.* **2018**, *69*, 273.
- [14] S. I. A. Cohen, M. Vendruscolo, M. E. Welland, C. M. Dobson, E. M. Terentjev, T. P. J. Knowles, *J. Chem. Phys.* **2011**, *135*, 065105.
- [15] F. Oosawa, M. Kasai, *J. Mol. Biol.* **1962**, *4*, 10.
- [16] G. Meisl, L. Rajah, S. A. I. Cohen, M. Pfammatter, A. Šarić, E. Hellstrand, A. K. Buell, A. Aguzzi, S. Linse, M. Vendruscolo, C. M. Dobson, T. P. J. Knowles, *Chem. Sci.* **2017**, *8*, 7087.
- [17] T. C. T. Michaels, A. Šarić, S. Curk, K. Bernfur, P. Arosio, G. Meisl, A. J. Dear, S. I. A. Cohen, C. M. Dobson, M. Vendruscolo, S. Linse, T. P. J. Knowles, *Nat. Chem.* **2020**, *12*, 445.
- [18] Z. Agus, L. Gardner, L. Beck, M. Goldberg, *Am. J. Physiol.* **1973**, *224*, 1143.
- [19] R. R. MacGregor, D. V. Cohn, *Clin. Orthop. Relat. Res.* **1978**, *137*, 244.
- [20] J. F. Habener, J. T. Potts, *N. Engl. J. Med.* **1978**, *299*, 580.
- [21] K. M. Wren, J. T. Potts, H. M. Kronenberg, *J. Biol. Chem.* **1988**, *263*, 19771.
- [22] M. Gopalswamy, A. Kumar, J. Adler, M. Baumann, M. Henze, S. T. Kumar, M. Fändrich, H. A. Scheidt, D. Huster, J. Balbach, *Biochim. Biophys. Acta* **2015**, *1854*, 249.
- [23] U. C. Marx, S. Austermann, P. Bayer, K. Adermann, A. Ejchart, H. Sticht, S. Walter, F. X. Schmid, R. Jaenicke, W. G. Forssmann, P. Röscher, *J. Biol. Chem.* **1995**, *270*, 15194.
- [24] Z. Evgrafova, B. Voigt, M. Baumann, M. Stephani, W. H. Binder, J. Balbach, *ChemPhysChem* **2019**, *20*, 236.
- [25] L. M. Lauth, B. Voigt, T. Bhatia, L. Machner, J. Balbach, M. Ott, *FEBS Lett.* **2022**, *596*, 2928.
- [26] J. S. Wall, T. Richey, A. Stuckey, R. Donnell, S. Macy, E. B. Martin, A. Williams, K. Higuchi, S. J. Kennel, *Proc. Natl. Acad. Sci. U.S.A.* **2011**, *108*, E586.
- [27] I. Kedar, M. Ravid, E. Sohar, *Isr. J. Med. Sci.* **1976**, *12*, 1137.
- [28] Z. Evgrafova, S. Rothmund, B. Voigt, G. Hause, J. Balbach, W. H. Binder, *Macromol. Rapid. Commun.* **2020**, *41*, 1900378.
- [29] Z. Evgrafova, B. Voigt, A. H. Roos, G. Hause, D. Hinderberger, J. Balbach, W. H. Binder, *Phys. Chem. Chem. Phys.* **2019**, *21*, 20999.
- [30] S. Deike, S. Rothmund, B. Voigt, S. Samantray, B. Strodel, W. H. Binder, *Bioorg. Chem.* **2020**, *101*, 104012.
- [31] A. Paschold, B. Voigt, G. Hause, T. Kohlmann, S. Rothmund, W. H. Binder, *Biomedicine* **2022**, *10*, 1512.
- [32] G. Meisl, X. Yang, E. Hellstrand, B. Frohm, J. B. Kirkegaard, S. I. A. Cohen, C. M. Dobson, S. Linse, T. P. J. Knowles, *Proc. Natl. Acad. Sci. U.S.A.* **2014**, *111*, 9384.
- [33] R. Khurana, C. Coleman, C. Ionescu-Zanetti, S. A. Carter, V. Krishna, R. K. Grover, R. Roy, S. Singh, *J. Struct. Biol.* **2005**, *151*, 229.
- [34] D. J. Lindberg, A. Wenger, E. Sundin, E. Wesén, F. Westerlund, E. K. Esbjörner, *Biochemistry* **2017**, *56*, 2170.
- [35] G. Sancataldo, S. Anselmo, V. Vetri, *Microsc. Res. Tech.* **2020**, *83*, 811.
- [36] J. D. Harper, P. T. Lansbury, *Annu. Rev. Biochem.* **1997**, *66*, 385.
- [37] D. C. Rodriguez Camargo, E. Sileikis, S. Chia, E. Axell, K. Bernfur, R. L. Cataldi, S. I. A. Cohen, G. Meisl, J. Habchi, T. P. J. Knowles, M. Vendruscolo, S. Linse, *ACS Chem. Neurosci.* **2021**, *12*, 4406.
- [38] A. K. Buell, *Biochem. J.* **2019**, *476*, 2677.
- [39] T. K. Karamanos, M. P. Jackson, A. N. Calabrese, S. C. Goodchild, E. E. Cawood, G. S. Thompson, A. P. Kalverda, E. W. Hewitt, S. E. Radford, *Elife* **2019**, *8*, e46574.
- [40] N. Lorenzen, S. I. A. Cohen, S. B. Nielsen, T. W. Herling, G. Christiansen, C. M. Dobson, T. P. J. Knowles, D. Otzen, *Biophys. J.* **2012**, *102*, 2167.
- [41] S. I. A. Cohen, M. Vendruscolo, C. M. Dobson, T. P. J. Knowles, *J. Chem. Phys.* **2011**, *135*, 065106.
- [42] S. Linse, *Curr. Opin. Struct. Biol.* **2021**, *70*, 87.
- [43] A. Šarić, T. C. T. Michaels, A. Zacccone, T. P. J. Knowles, D. Frenkel, *J. Chem. Phys.* **2016**, *145*, 211926.
- [44] L. Jean, C. F. Lee, C. Lee, M. Shaw, D. J. Vaux, *FASEB J.* **2010**, *24*, 309.
- [45] E. Kachooei, A. A. Moosavi-Movahedi, F. Khodaghali, H. Ramshini, F. Shaerzadeh, N. Sheibani, *PLoS One* **2012**, *7*, e41344.
- [46] E. Y. Chi, S. L. Frey, A. Winans, K. L. H. Lam, K. Kjaer, J. Majewski, K. Y. C. Lee, *Biophys. J.* **2010**, *98*, 2299.
- [47] F. Grigolato, P. Arosio, *Biophys. Chem.* **2021**, *270*, 106533.
- [48] Q. Han, F. Tao, Y. Xu, H. Su, F. Yang, V. Körstgens, P. Müller-Buschbaum, P. Yang, *Angew. Chem., Int. Ed.* **2020**, *59*, 20192.
- [49] L. Wang, D. Atkinson, D. M. Small, *J. Biol. Chem.* **2003**, *278*, 37480.
- [50] T. Dean, A. Khatri, Z. Potetinova, G. E. Willick, T. J. Gardella, *J. Biol. Chem.* **2006**, *281*, 32485.
- [51] F. Tao, Q. Han, K. Liu, P. Yang, *Angew. Chem., Int. Ed.* **2017**, *56*, 13440.
- [52] J. R. Brender, J. Krishnamoorthy, M. F. M. Sciacca, S. Vivekanandan, L. D'urso, J. Chen, C. La Rosa, A. Ramamoorthy, *J. Phys. Chem. B* **2015**, *119*, 2886.
- [53] S. T. Dada, M. C. Hardenberg, L. K. Mrugalla, M. O. McKeon, E. Klimont, T. C. T. Michaels, M. Vendruscolo, (Preprint) *bioRxiv*, <https://doi.org/10.1101/2021.09.26.461836>, submitted: 09, 2021.

- [54] S. B. Padrick, A. D. Miranker, *Biochemistry* **2002**, *41*, 4694.
- [55] E. Bosse-Doenecke, U. Weininger, M. Gopalswamy, J. Balbach, S. M. Knudsen, R. Rudolph, *Protein Expr. Purif.* **2008**, *58*, 114.
- [56] H. Levine, *Protein Sci.* **1993**, *2*, 404.
- [57] G. V. De Ferrari, W. D. Mallender, N. C. Inestrosa, T. L. Rosenberry, *J. Biol. Chem.* **2001**, *276*, 23282.
- [58] E. Gasteiger, C. Hoogland, A. Gattiker, S. Duvaud, M. R. Wilkins, R. D. Appel, A. Bairoch, in *The Proteomics Protocols Handbook*, Vol. 1 (Ed: J. M. Walker), Humana Press, Totowa (NJ), USA **2005**, p. 52.
- [59] A. J. Dear, T. C. T. Michaels, G. Meisl, D. Klenerman, S. Wu, S. Perrett, S. Linse, C. M. Dobson, T. P. J. Knowles, *Proc. Natl. Acad. Sci. U.S.A.* **2020**, *117*, 12087.

2.2 Paper II: B. Voigt *et al.* (2023), The Prenucleation Equilibrium of the Parathyroid Hormone Determines the Critical Aggregation Concentration and Amyloid Fibril Nucleation

Aims and Summary

Paper II addressed the critical monomer concentration as a generic thermodynamic aspect of amyloid fibril formation. The critical concentration of PTH₈₄ fibril formation has also already been reported e.g. in Paper I and Paper III. Here now, potential changes of the secondary structure or oligomeric states of PTH₈₄ related to the critical concentration were investigated. A multi-method approach, including optical and NMR spectroscopy, X-ray scattering, native mass spectrometry as well as single-molecule techniques, was applied to characterize the biophysical properties of PTH₈₄ dependent on the peptide concentration. Importantly, Paper II confirmed the oligomer hypothesis explaining the concentration dependent reaction order for primary nucleation as presented in Paper I. A complex prenucleation equilibrium, i.e. prior to fibril formation, was found, comprising distinct oligomers with different secondary structure compositions. PTH₈₄ was found to be solely monomeric with a helical propensity only at very low concentrations. With increasing concentration, a transition *via* a more disordered state towards a β -sheet enriched structure was evident. Most notable, a trimeric and a tetrameric species occurred only above the critical concentration. Both species relate well to small oligomers as precursors for primary nucleation at low concentrations as hypothesized in Paper I. The critical concentration was found to represent a lower cutoff for “productive” oligomer formation. Furthermore, the conformational and oligomeric state of the fraction of free peptide in thermodynamic equilibrium with fibrils adjusts to the prenucleation state at the critical concentration. Paper II thus extends the understanding of the critical concentration for amyloid formation in terms of consequences to the structure and oligomerization both before nucleation and in the presence of fibrils.

Contribution

The author of this thesis recombinantly produced the label-free and ¹⁵N isotope labelled peptide, prepared the samples (except for single-molecule fluorescence and native mass spectrometry), planned the experiments, conducted and analyzed circular dichroism, intrinsic fluorescence and all NMR spectroscopy experiments, interpreted the data with support from all co-authors, prepared 85 % of the figures, wrote 90 % of the manuscript and incorporated all corrections from the co-authors.

Original Paper

The original paper is included on the following pages (pp. 46-56). The Supporting Information can be found in Appendix A.2.

VIP Very Important Paper

The Prenucleation Equilibrium of the Parathyroid Hormone Determines the Critical Aggregation Concentration and Amyloid Fibril Nucleation

Bruno Voigt,^[a] Twinkle Bhatia,^[b] Julia Hesselbarth,^[c, d] Monika Baumann,^[a] Carla Schmidt,^[c, d] Maria Ott,^[b] and Jochen Balbach*^[a]

Nucleation and growth of amyloid fibrils were found to only occur in supersaturated solutions above a critical concentration (c_{crit}). The biophysical meaning of c_{crit} remained mostly obscure, since typical low values of c_{crit} in the sub- μM range hamper investigations of potential oligomeric states and their structure. Here, we investigate the parathyroid hormone PTH₈₄ as an example of a functional amyloid fibril forming peptide with a comparably high c_{crit} of $67 \pm 21 \mu\text{M}$. We describe a complex concentration dependent prenucleation ensemble of oligomers of different sizes and secondary structure compositions and highlight the occurrence of a trimer and tetramer at c_{crit} as possible precursors for primary fibril nucleation. Furthermore, the soluble state found in equilibrium with fibrils adopts to the prenucleation state present at c_{crit} . Our study sheds light onto early events of amyloid formation directly related to the critical concentration and underlines oligomer formation as a key

feature of fibril nucleation. Our results contribute to a deeper understanding of the determinants of supersaturated peptide solutions. In the current study we present a biophysical approach to investigate c_{crit} of amyloid fibril formation of PTH₈₄ in terms of secondary structure, cluster size and residue resolved intermolecular interactions during oligomer formation. Throughout the investigated range of concentrations (1 μM to 500 μM) we found different states of oligomerization with varying ability to contribute to primary fibril nucleation and with a concentration dependent equilibrium. In this context, we identified the previously described c_{crit} of PTH₈₄ to mark a minimum concentration for the formation of homo-trimers/tetramers. These investigations allowed us to characterize molecular interactions of various oligomeric states that are further converted into elongation competent fibril nuclei during the lag phase of a functional amyloid forming peptide.

Introduction

The capability of peptides and proteins to self-assemble into amyloid fibrils is typically associated with their role in neuro-

degenerative diseases (e.g. Alzheimer's and Parkinson's disease),^[1-4] injection amyloidosis (Diabetes type II)^[5] or systemic amyloidoses (e.g. antibody light chain amyloidosis).^[6] Additionally, so-called functional amyloids are involved in skin pigmentation,^[7] bacterial biofilm formation,^[8] memory^[9] or storage of peptide hormones.^[10] Amyloid fibrils assemble via a complex nucleation-dependent network of individual microscopic processes.^[11-12] The generation of new individual fibrils can occur via primary nucleation from bulk solution or via surface catalyzed secondary nucleation (Figure 1A).^[13-16] Elongation of existing fibrils via addition of new units increases the fibrillar mass.

Nucleation-dependent polymerization is a fundamental principle to describe the process of amyloid generation.^[17] In this concept, no assembly is observed below a certain minimum concentration, which is defined as the critical concentration (c_{crit}).^[17-19] The concentration of free peptide in the thermodynamic equilibrium with fibrils is also reflected by c_{crit} .^[20] This can be experimentally determined e.g. by sedimentation of the fibrils with a subsequent quantification of the soluble protein fraction or by diluting fibrils which, as a consequence, release monomers until c_{crit} is reached.^[21-23] Protein solutions exceeding c_{crit} are supersaturated, metastable and kinetically soluble.^[24-25] With time, the nucleated conversion into amyloid fibrils is a key feature of such metastable states.^[19] A crucial step for primary nucleation of an amyloid structure is the formation of

[a] B. Voigt, Dr. M. Baumann, Prof. Dr. J. Balbach
Martin Luther University Halle-Wittenberg
Institute of Physics
Betty-Heimann-Straße 7, 06120 Halle (Germany)
E-mail: jochen.balbach@physik.uni-halle.de

[b] T. Bhatia, Dr. M. Ott
Martin Luther University Halle-Wittenberg
Institute of Biochemistry and Biotechnology
Kurt-Mothes-Straße 3, 06120 Halle (Germany)

[c] J. Hesselbarth, Prof. Dr. C. Schmidt
present address: Johannes Gutenberg University Mainz
Institute of Chemistry – Biochemistry, Biocenter II
Hanns-Dieter-Hüsch-Weg 17, 55128 Mainz (Germany)

[d] J. Hesselbarth, Prof. Dr. C. Schmidt
Martin Luther University Halle-Wittenberg
Interdisciplinary Research Center HALOmEm, Institute of Biochemistry and Biotechnology
Kurt-Mothes-Straße 3a, 06120 Halle (Germany)

Supporting information for this article is available on the WWW under <https://doi.org/10.1002/cphc.202300439>

© 2023 The Authors. ChemPhysChem published by Wiley-VCH GmbH. This is an open access article under the terms of the Creative Commons Attribution Non-Commercial NoDerivs License, which permits use and distribution in any medium, provided the original work is properly cited, the use is non-commercial and no modifications or adaptations are made.

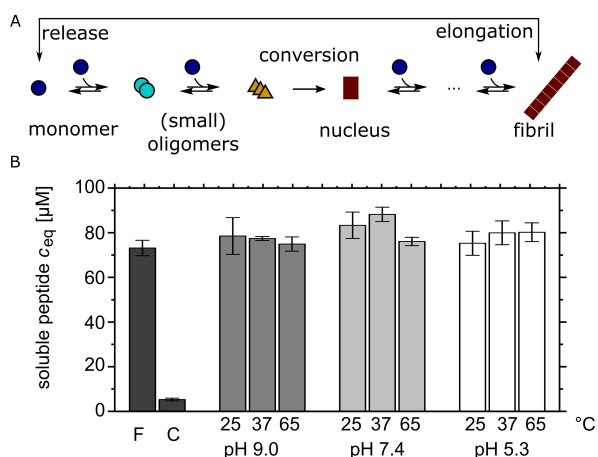


Figure 1. A – Simplified model of amyloid fibril growth involving oligomeric species for primary nucleation. B – Monomer release from pre-formed PTH₈₄ fibrils at 24 h in 50 mM sodium borate (pH 9.0), 50 mM sodium phosphate containing 150 mM sodium chloride (pH 7.4) or 10 mM Bis-Tris (pH 5.3). F: c_{eq} of the initial fibril sample, C: soluble peptide directly after resuspension of washed fibrils.

prefibrillar oligomers convertible into nuclei which finally grow to fibrils by monomer addition.^[26–27]

Oligomers in the context of amyloid self-assembly display a varying relevance to fibril formation.^[26] On-pathway oligomers are able to directly contribute to amyloid nucleation or growth, while off-pathway oligomers need to dissociate first. For example, the Huntingtin exon 1 protein htt^{ex1} and other constructs of this protein were found to be predominantly monomeric with transient populations of an off-pathway dimer as well as with an on-pathway dimer and tetramer preceding nucleation.^[28–29] In addition to this function as precursors for nucleation, oligomers have been found to be the species involved in fibril elongation e.g. for the truncation variant ΔN6 of human β_2 -microglobulin.^[30–32] So-called globular oligomers are also described to result in alternative pathways as precursors for the formation of curvilinear fibrils above a critical oligomer concentration (coc) for an artificial dimeric Amyloid β peptide (dimA β) and lysozyme, in contrast to rigid fibrils originating from nucleated polymerization below the coc.^[33–34]

Although there are many studies investigating oligomer formation during amyloid growth,^[26,35] only a few reports analyzed possible transitions of the secondary structure and oligomer sizes of a peptide at c_{crit} to investigate the influence of supersaturation on biophysical properties of peptides.^[36] In most cases c_{crit} is below experimental limits, e.g. in the pM to low μM range for A β ₄₀.^[24]

In this work we present an in vitro approach to biophysically characterize c_{crit} for amyloid fibril formation. For this purpose, we use the parathyroid hormone in its mature state bearing 84 residues (PTH₈₄).^[37] The hormone which acts in blood calcium and phosphate homeostasis is hypothesized to be stored in functional amyloid fibrils in secretory granules prior to its release into the blood stream.^[21,38] The N-terminal part of PTH₈₄ displays an α -helical propensity while the C-terminal part remains disordered.^[39–42] PTH₈₄ offers a reversible fibrillation

system with c_{crit} in a μM concentration range which is easily accessible by a variety of biophysical techniques.^[21–23] The secondary structure and oligomerization propensity of PTH₈₄ below, near and above c_{crit} are investigated at conditions at which the peptide self-assembles into fibrils to characterize potential transitions as a consequence of supersaturation. We show that the prenucleation state of PTH₈₄ comprises equilibria involving oligomers of different molecular weights dependent on the total concentration c_0 . Here, c_{crit} marks a transition from a monomer-dimer equilibrium ($c_0 < c_{crit}$) towards an equilibrium involving a trimeric and tetrameric state ($c_0 > c_{crit}$) which we suspect to contribute to primary nucleation. We additionally demonstrate that the monomer-dimer equilibrium persists in the presence of fibrils, thus revealing an important insight into the origin and role of c_{crit} and the early mechanism of amyloid formation.

Results

The Critical PTH₈₄ Concentration is not Affected by Buffer Conditions

The parathyroid hormone PTH₈₄ is able to self-assemble into amyloid-like fibrils with a reported c_{crit} of $67 \pm 21 \mu\text{M}$.^[21] To test whether c_{crit} depends on external factors, we performed monomer release assays from pre-formed fibrils (Figure 1B). For reversible assemblies, monomers are released from fibrils upon dilution until c_{crit} has been approached. Interestingly, independent from pH (pH 9.0, pH 7.4, pH 5.3), temperature (25 $^{\circ}\text{C}$ to 65 $^{\circ}\text{C}$) or buffer systems (phosphate, Bis-Tris, borate), the individually determined concentration of soluble peptide (c_{eq}) always increased to $79 \pm 4 \mu\text{M}$ after 24 h of incubation. This relates to a robust c_{crit} of PTH₈₄ that is unaffected by ample changes of the environment.

Furthermore, c_{crit} can be used as a measure of the Gibbs free energy for the overall fibrillation process with $\Delta G^0 = -RT \cdot \ln(1/Mc_{crit}^{-1}) = -23.8 \text{ kJ mol}^{-1}$ at 25 $^{\circ}\text{C}$.^[19,43] The high value of c_{crit} reflects the low thermodynamic stability of PTH₈₄ fibrils. For comparison, ΔG^0 of A β ₄₀ and h $\beta_2\text{m}$ is reported to be $-36.0 \text{ kJ mol}^{-1}$ and $-33.0 \text{ kJ mol}^{-1}$, corresponding to c_{crit} of 0.9 μM and 2.7 μM , respectively.^[18,44]

Biophysical PTH₈₄ Properties Depend on the Peptide Concentration

To characterize c_{crit} on the molecular level we examined the biophysical properties of PTH₈₄ in a broad concentration range below and above c_{crit} . In agreement with experimentally determined structures,^[40,42] AlphaFold 2.0 predicted an α -helix for residues E4-L37, an intrinsically disordered C-terminal part, and an additional α -helix for residues K72-A81 (Figure 2A).^[39,41] The latter α -helix was not experimentally observed.^[42] For a detailed analysis of possible c_0 effects on the structure we used the intrinsic W23 fluorescence ratio F_{350}/F_{320} as an indicator for spectral changes. Within the c_0 range probed, four different

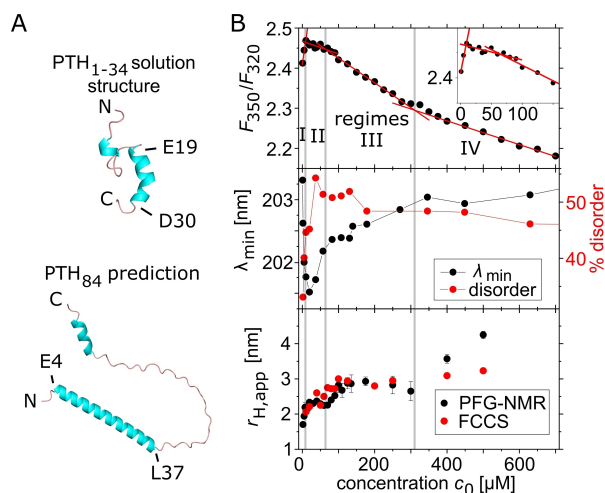


Figure 2. Structural and hydrodynamic properties of PTH₈₄ at various concentrations. **A** – cartoon sketch of PTH₁₋₃₄ (pdb-code 1zwa) (top) and AlphaFold 2.0 predicted structure of PTH₈₄ (bottom),^[39–41] **B** – intrinsic tryptophan fluorescence shown as the ratio F_{350}/F_{320} (upper panel). The red lines are linear fits to the respective data within the four regimes. The inset enlarges the range of low c_0 . Analysis of far-UV CD spectra (middle panel), shown are the wavelengths of the CD minimum $\lambda_{\min,1}$ around 202 nm (black) and the estimated content of disordered regions (red, deconvolution performed with BESTSEL). The apparent hydrodynamic radius $r_{H,app}$ (lower panel) was determined by PFG-NMR (black) and FCCS (red).

concentration regimes were identified (Figure 2B, upper panel): (a) $c_0 < 10 \mu\text{M}$ (regime I), (b) $10 \mu\text{M} < c_0 < 70 \mu\text{M}$ (regime II), (c) $70 < c_0 < 310 \mu\text{M}$ (regime III) and $c_0 > 310 \mu\text{M}$ (regime IV). Note that the transition between regimes II and III occurred at c_{crit} . The observed decrease of F_{350}/F_{320} for regimes II, III and IV indicates a shift of the maximum fluorescence $\lambda_{\text{em,max}}$ towards lower emission wavelengths (Figure S1A). This behavior refers to a decreased solvent accessibility of the W23 environment resulting either from intra- (conformational reorientation) or intermolecular interactions (oligomer formation). For regime I we found a positive slope indicating the opposing effect of a decreasing hydrophobicity of the W23 environment with c_0 .

The general appearance of the circular dichroism (CD) spectra displaying a dominant minimum at $\lambda_{\min,1} \approx 202 \text{ nm}$ and a minor minimum at $\lambda_{\min,2} \approx 220 \text{ nm}$ is indicative of an intrinsically disordered peptide with additional contributions from an α -helix (Figure S1B).^[21–22,42] In contrast, a CD spectrum calculated from the predicted structure (Figure S1B) shows the typical minima of α -helices at $\lambda_1 = 208 \text{ nm}$ and $\lambda_2 = 220 \text{ nm}$, indicating an overestimation of the α -helix content by AlphaFold 2.0.^[45] To monitor c_0 dependent effects, we used the evolution of the CD minimum wavelength $\lambda_{\min,1}$ as an indicator for disorder ($\lambda = 195 \text{ nm}$) and α -helical structure formation ($\lambda = 208 \text{ nm}$) (Figure 2B, middle panel). For regime I we found a shift of $\lambda_{\min,1}$ from 203.3 nm towards 201.7 nm with increasing c_0 . This small but notable systematic shift indicates an increase of disorder, which is supported by a BESTSEL analysis (red in the same Figure).^[46] Simultaneously, the apparent hydrodynamic radius $r_{H,app}$ increased from $1.7 \pm 0.1 \text{ nm}$ to $2.1 \pm 0.1 \text{ nm}$ as observed by pulsed field gradient (PFG)-NMR and fluorescence cross-correlation spectroscopy (FCCS) (Figure 2B, lower panel, and Fig-

ure S2). Interestingly, $r_{H,app}$ remained constant within regime II, while $\lambda_{\min,1}$ increased again towards 202.3 nm. Obviously, within regime II the structure of PTH₈₄ is affected by c_0 without an observable change in size. The major red shift of $\lambda_{\min,1}$ continued for regime III. Meanwhile, $r_{H,app}$ increased until $c_0 = 125 \mu\text{M}$ towards 2.9 nm, but remained constant for higher c_0 . In regime IV we observed a proceeding minor red shift of $\lambda_{\min,1}$ and a strong increase of $r_{H,app}$ to 4.2 nm or 3.5 nm as determined by PFG-NMR and FCCS, respectively. The BESTSEL analysis of the CD spectra for regimes II–IV revealed that the observed shift of $\lambda_{\min,1}$ indicates a slight decrease of disordered structure.

In summary, PTH₈₄ exhibits a compact state with a higher degree of secondary structure at low c_0 which becomes more extended with increasing c_0 , supported by an increased solvent accessibility of W23. The positive trend of Θ_{MRW} at $\lambda_{\min,1}$ (Figure S1B) suggests that PTH₈₄ evolves from an intrinsically disordered peptide (IDP) with α -helical propensity at low c_0 (regime I) towards an IDP with decreased helix propensity at high c_0 (regime IV). The trend of a strongly increasing ensemble $r_{H,app}$ indicates a monomer-oligomer equilibrium with different secondary structural compositions and transient species in fast dynamic exchange.^[30]

PTH₈₄ Monomers are in Equilibrium with Oligomers of Peptide Concentration Dependent Sizes

Next, we asked if the c_0 dependent increase of the ensemble $r_{H,app}$ occurs due to conformational changes resulting in an extended structure or due to oligomer formation. In order to reveal possible size distributions, we used small angle X-ray scattering (SAXS) with a subsequent ensemble optimization analysis (EOM, Figure 3A and Figure S3) to investigate the distributions of the radii of gyration (r_G) at $50 \mu\text{M}$ (regime II) and $500 \mu\text{M}$ (regime IV). The corresponding end-to-end distances (r_{ee}) were obtained by dual-color single-molecule fluorescence resonance energy transfer (smFRET, Figure 3B and Figure S4). For regime II, SAXS revealed two states with distinct, narrow distributions of r_G ($2.1 \pm 0.2 \text{ nm}$ and $2.8 \pm 0.2 \text{ nm}$) while only one r_{ee} distance (5.7 nm) was detected by smFRET. We suspect that both r_G states either display a monomeric and an oligomeric state while r_{ee} of the involved individual peptide chains remain unchanged or two conformational states that interconvert on a timescale $< 200 \mu\text{s}$. Exceeding c_{crit} the values of both r_G maxima increase ($2.4 \pm 0.2 \text{ nm}$ and $3.0 \pm 0.3 \text{ nm}$), indicating different dynamic equilibria for the probed c_0 regimes as well as a possible under-representation of monomers in the scattering intensity curves. Interestingly, smFRET experiments for regime IV also revealed two states. The r_{ee} of the dominant state increased only marginally with c_0 from 5.7 to 5.9 nm, while an additional, extended state with $r_{ee} = 7.5 \text{ nm}$ was found with 22% amplitude which was not detected by the EOM analysis.

Independently, we applied native mass spectrometry (MS) allowing the direct observation of oligomers. For regime I ($c_0 = 10 \mu\text{M}$), we obtained a charge state distribution corresponding to a molecular mass of 9424 g mol^{-1} (Figure 3C, upper panel, $M_{W,PTH84} = 9424.7 \text{ g mol}^{-1}$),^[47] revealing PTH₈₄ to be monomeric at

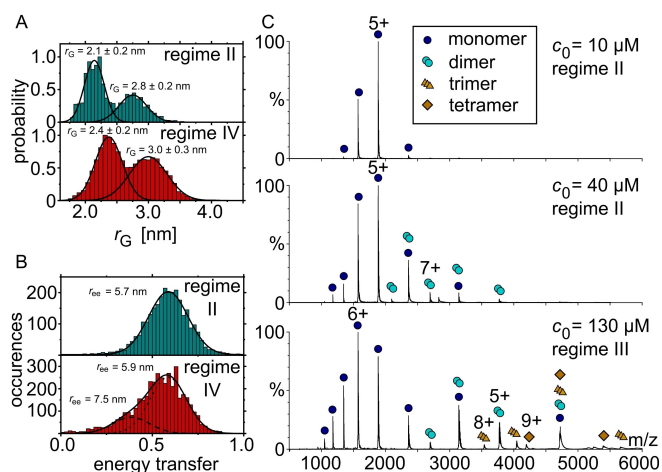


Figure 3. Analysis of PTH₈₄ oligomerization. **A** – EOM analysis of the X-ray scattering profiles for 50 μM (upper panel) and 500 μM (lower panel). **B** – smFRET determined energy transfer histograms for 50 μM (upper panel) and 500 μM (lower panel). **C** – native mass spectrometry of PTH₈₄ at 10 μM (upper panel), 40 μM (middle panel) and 130 μM (lower panel). The observed charge state distributions correspond to monomers (blue circles), dimers (cyan circles), trimers (orange triangles) and tetramers (orange squares). The respective molecular masses are given in the main text. After incubation, the buffer was exchanged to 200 mM $(\text{NH}_4)_2\text{CH}_3\text{COO}$ directly prior to the measurement.

low c_0 . However, at 40 μM (regime II) a second series of charge states was observed which can be assigned to an 18848 g mol^{-1} particle, equal to the molecular weight of a PTH₈₄ dimer (Figure 3C, middle panel). This was successfully confirmed by selecting the 7+ charge state of the dimer as a precursor for dissociation experiments (Figure S5). Thus, the two r_G states in SAXS-EOM in regime II refer to a PTH₈₄ monomer and a dimer. Further increasing c_0 (regime III) resulted in additional charge state series corresponding to a PTH₈₄ trimer (28280 g mol^{-1}) and tetramer (37754 g mol^{-1} , Figure 3C, lower panel).

Together, SAXS, smFRET and native MS confirmed that PTH₈₄ is solely monomeric only at regime I and exhibits a monomer-oligomer equilibrium at other regimes, with c_0 dependent cluster sizes. Most notably, above c_{crit} (regime III) additionally to dimeric PTH₈₄ a trimeric and a tetrameric species were observed by native MS. For regime IV, we suppose the formation of an oligomer of high molecular weight, supported by a strong increase of $r_{\text{H,app}}$ in this regime as well as a second extended r_{ee} state.

The N-terminus of PTH₈₄ Facilitates Oligomer Formation

Two-dimensional NMR spectroscopy allows to derive residue specific information about which segments of PTH₈₄ are involved in inter- and intramolecular interactions. The low dispersion within the proton dimension of cross-peaks in our c_0 dependent backbone ^1H - ^{15}N -fHSQC spectra (Figure 4A) agrees with a predominantly disordered peptide with transient α -helices.^[21,42,48] Notably, we observed a c_0 dependent perturbation of the chemical shift (CSP) or the detected signal intensity for many cross-peaks. Gradually shifting cross-peaks typically

indicate the co-existence of two or more distinct NMR detectable states in the fast chemical exchange regime on the sub-millisecond time scale.

For regime I we detected unspecific CSP for all residues (Figure 4B upper and middle panel, and Figure S6), while a significant decrease of intensity was only observed for residues L15-K27 which bear a basic RKK patch. Note that W23, sensing an increasing hydrophilicity of the environment (Figure 2B, upper panel), is in the same region. Additionally, the basic residues 50R-54K, which contain a second RKK patch, display a small but systematic intensity increase. In regimes II–IV, cross-peak intensity as well as CSP were most affected within the N-terminal region (residues S1-A42) of PTH₈₄ while little or no effect was detected for the disordered C-terminal region (R44-Q84). Interestingly, within regimes III and IV the CSP for V35-G38 increased compared to the other residues indicating a pronounced participation of this sequence in PTH₈₄ interactions.

Except for regime I, we observed additional minor cross-peaks in close proximity to the signals corresponding to V35, G38, and A39 (insets in Figure 4A). The occurrence of two distinct peaks indicated an additional equilibrium of states in the slow exchange limit. Since these minor cross-peaks were observed in a regime for which we found dimer formation, we attribute them to a dimeric state of PTH₈₄. All three residues are situated in a highly hydrophobic region of PTH₈₄ ($^3\text{FVALGAP}^{41}\text{LA}$), indicating that hydrophobic interactions are most probably involved in dimer formation. Additionally, the CSP of the corresponding major cross-peaks strongly modulated with c_0 , especially in regimes III and IV (Figure S6). This indicates that this peptide region senses, at least, two equilibria: one in the fast, the other in the slow exchange regime of the NMR chemical shift time scale. We suppose that hydrophobic interactions are also relevant for trimer/tetramer and high-order oligomer formation observed in regimes III and IV.

In order to analyze whether the intensity changes originate from differences of local dynamics or oligomer formation we determined the longitudinal (R_1) and transversal relaxation rates (R_2) at the different c_0 regimes. The R_2/R_1 ratio is sensitive to changes of the local peptide rotational correlation time τ_c on a nanosecond time scale and chemical exchange on a millisecond time scale. This is a valuable NMR parameter to reveal transient local structure formation especially of IDPs.^[49–50] In general, PTH₈₄ displayed a higher R_2/R_1 ratio for residues L7-G38 compared to other residues (Figure 4B, lower panel). This indicated a propensity for the formation of secondary structure in this region, in good agreement with reported structures.^[39–42] With increasing c_0 , R_2/R_1 strongly increased for regimes III and IV. We attribute this up to six-fold increase mainly to the formation of oligomers with a larger τ_c and to an additional exchange contribution (R_{ex}) to the transversal R_2 relaxation ($R_{2,\text{obs}} = R_2^0 + R_{\text{ex}}$). The latter arises from a fast interconversion of states on a millisecond time scale.^[51] Interestingly, no difference of R_2/R_1 was observed between $c_0 = 20 \mu\text{M}$ and 100 μM , although a strong decrease of the relative peak intensities was found. Again, residues L41-Q84 did not show c_0 effects on relaxation, indicating that this segment remains flexible in oligomeric PTH₈₄ states.

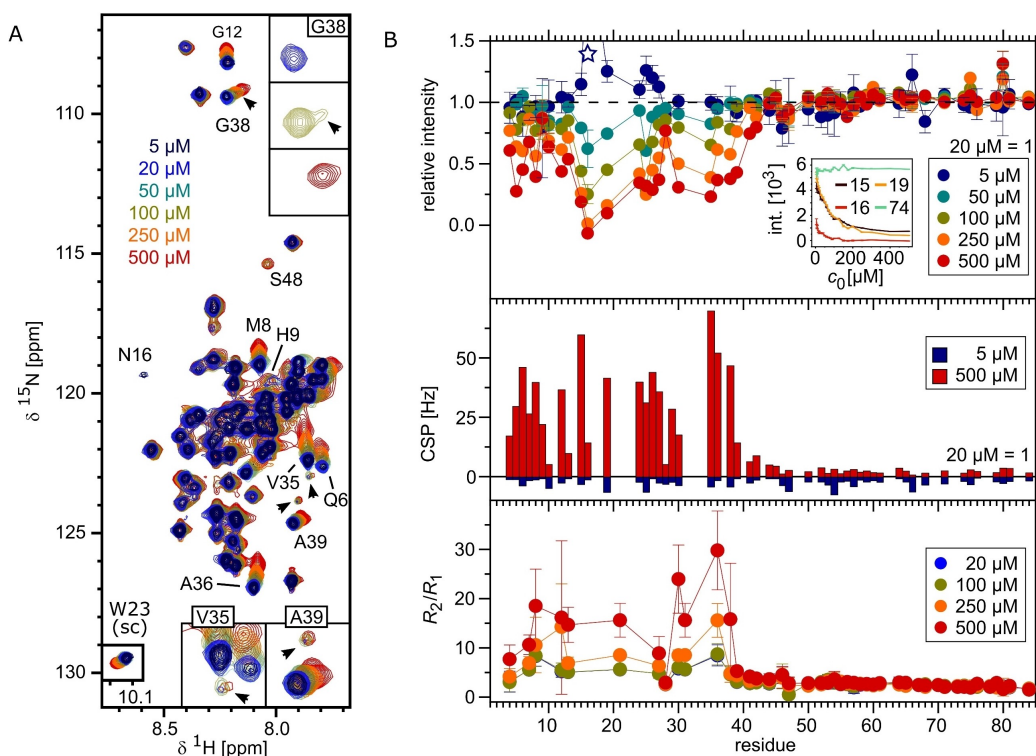


Figure 4. Concentration dependent NMR characterization of PTH₈₄. **A** – ¹H-¹⁵N-HSQC of ¹⁵N enriched PTH₈₄ at 5 μM, 20 μM, 50 μM, 100 μM, 250 μM and 500 μM. The assignments of selected cross-peaks with strong CSP are given. Additional cross-peaks for V35, G38 and A39 are indicated by black arrows (arrow for G38 points at additional cross-peak at 50 μM (blue-green)). The insets enlarge spectral regions near V35, G38 and A39 focusing on the additional minor cross-peaks. **B** – Relative intensities of cross-peaks at 5 μM, 100 μM, 250 μM and 500 μM (upper panel), CSP for 5 μM (displayed as negative values) and 500 μM compared to 20 μM (middle panel). The respective values for 20 μM are set to unity to compare changes for the monomer-related effects (regime I, $c_0 < 20 \mu\text{M}$) and additional effects from the oligomerization equilibrium (regimes II–IV, $c_0 > 20 \mu\text{M}$). Relaxation properties at 20 μM, 100 μM, 250 μM and 500 μM are displayed in the lower panel. R_2/R_1 ratios are almost identical for $c_0 = 20 \mu\text{M}$ and 100 μM. The inset in the upper panel displays absolute intensities (Equation 9) for L15, N16, E19 and D74. The relative intensity of N16 for 5 μM compared to 20 μM is 2.4 ± 0.8 , a high value which might be due to low absolute intensity of the N16 cross-peak (red in the inset). Adjacent residues L15 (dark red) and N19 (orange) show a similar intensity decrease with c_0 and follow the same trend in the relative intensity. We displayed the relative intensity data point of N16 with a star indicating a high value in the trend of nearby residues but with high uncertainty.

The Soluble Peptide in Equilibrium with Fibrils Adopts the Same State as Without Fibrils

Last, we asked if the soluble PTH₈₄ fraction in equilibrium with its fibrils is monomeric or adopts to the prenucleation state. For this purpose, we recorded ¹H-¹⁵N-fHSQC spectra of samples with ¹⁵N labeled PTH₈₄ (c_0 : 100 μM, 300 μM and 500 μM) before and after addition of 5% unlabeled PTH₈₄ fibrils (given in monomer equivalents) to induce seeded growth (Figure 5A). After 7 days of incubation c_{eq} was found to be 51.3 μM ($c_0 = 100 \mu\text{M}$), 69.2 μM ($c_0 = 300 \mu\text{M}$) and 52.2 μM ($c_0 = 500 \mu\text{M}$), in good agreement with c_{crit} (Figure 1B). We compared the chemical shift differences of the resulting cross peaks with the respective cross-peak positions obtained from a set of reference spectra without fibrils. The root mean square deviation (RMSD) was used to determine the pair of spectra with minimal CSP (Equation 10). Without fibrils, the RMSD values displayed minima at 100 μM, 300 μM and 500 μM, respectively, indicating that these spectra are most similar to the reference spectra acquired at the same c_0 as the samples (Figure 5A, closed circles, and Figure S7). In equilibrium with fibrils, we found minimum RMSD values at appr. 40 μM for all c_0 . Thus, the

resulting spectra in the presence of fibrils are most similar to the spectrum obtained from 40 μM PTH₈₄ without fibrils (Figure 5A, open circles), a concentration which agrees well with the obtained c_{eq} .

In order to learn more about the adaption of the free peptide to monomer consumption by fibril elongation, we investigated the evolution of the 2D fHSQC cross-peak pattern during seeded fibril growth at $c_0 = 250 \mu\text{M}$ (regime III) and 500 μM (regime IV) (Figure 5B). For all time points and for both c_0 , the RMSD minima closely corresponded to the concentration of the soluble peptide as determined by 1D ¹H NMR. We propose from these RMSD analyses and time-resolved NMR data that peptide consumption by fibril elongation does not lead to monomer depletion with a remaining oligomeric fraction. Instead, the dynamic equilibrium is readily re-established according to the available concentration of soluble peptide.

Finally, we analyzed the local backbone dynamics of the soluble state in equilibrium with fibrils (Figure S8). For residues L10-D30 we found a small and for residues A70-Q84 a very small but systematic increase of R_2/R_1 compared to the sample without fibrils. This increase indicates weak interactions of these

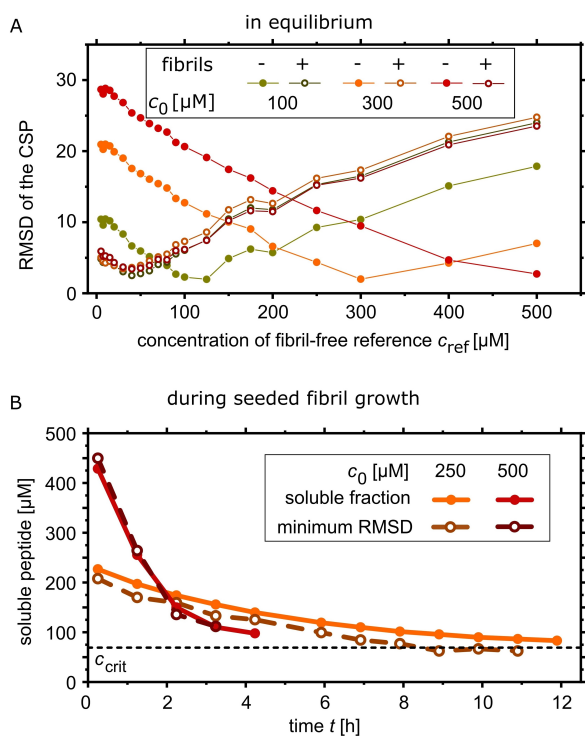


Figure 5. NMR characterization of PTH₈₄ in the presence of fibrils. **A** – RMSD of backbone chemical shifts in ¹H-¹⁵N-fHSQC spectra of samples with $c_0 = 100 \mu\text{M}$ (dark yellow), $300 \mu\text{M}$ (orange) and $500 \mu\text{M}$ (red) without (closed circles) and in equilibrium with fibrils (open circles) compared to reference spectra acquired in the absence of fibrils. **B** – 1D ¹H and 2D ¹H-¹⁵N-fHSQC detected seeded fibril growth at initial peptide concentrations of $250 \mu\text{M}$ (orange) and $500 \mu\text{M}$ (red). 1D ¹H intensity analysis to extract the concentration of free PTH₈₄ (closed circles) and the corresponding minimum RMSD of the CSP, compared to the prenucleation equilibrium (open circles) for each time point. The y-axis displays the concentration of the soluble peptide and the reference spectrum showing the lowest respective RMSD. For clarity, RMSD values are displayed in a darker color than the free peptide concentration. The black dashed line indicates the critical concentration c_{crit} .

sections of soluble PTH₈₄ with the fibrils at the fibril surface or growth-competent ends due to association and dissociation in equilibrium. Thus, slower local tumbling or chemical exchange increases transversal R_2 relaxation. This supports the hypothesis that fibrils do not induce additional conformational or oligomeric states.

Discussion

In the present work we investigated c_0 dependent secondary structure and the monomer-oligomer equilibrium of PTH₈₄ to biophysically characterize c_{crit} of amyloid formation. The identification of four c_0 regimes, characterized by distinct biophysical signatures with transition concentrations at $\sim 10 \mu\text{M}$, $\sim 70 \mu\text{M}$ and $\sim 310 \mu\text{M}$, was a remarkable finding of our study.

Many experimental reports of C-terminally truncated variants of PTH_{84r}, as well as structure prediction, consistently assign an α -helix for residues E4-L37 for the peptide monomer. A recent NMR study confirmed the helix propensity for PTH₈₄ at pH 5.3.^[42] At pH 7.4, we found PTH₈₄ to be solely monomeric

only at very low c_0 (regime I). An increase of c_0 within this regime resulted in an increase of structural disorder coupled to an expansion of the chain. Interestingly, only the backbone NMR intensities of residues L15-K27 were affected.

For regime II, PTH₈₄ is in equilibrium with its homo-dimeric form, as indicated by native MS and SAXS-EOM leading to NMR detectable changes in the N-terminal region (residues E4-G38). The fraction of dimeric species was not sufficient to significantly increase the ensemble r_{H} . Nevertheless, the overall content of secondary structure was again increased. The transition from regime II to regime III was characterized by the occurrence of an additional homo-trimer/tetramer and coincided with c_{crit} of PTH₈₄ fibrillation. In the high c_0 range, an additional state was observed with increased r_{H} (PFG-NMR and FCCS), higher r_{G} (SAXS-EOM) and larger r_{ee} (smFRET) compared to the lower c_0 regimes. Within the framework of our previous reported mechanism of PTH₈₄ fibril formation,^[23] we propose that the trimer or tetramer acts as precursor for primary nucleation at low c_0 ($< 310 \mu\text{M}$, regime III), since these oligomers only appeared above c_{crit} . The previously calculated reaction order for primary nucleation n_1 , being related to the physical nucleus size, of $2 \leq n_1 \leq 4$ supports such oligomer sizes.^[23] Interestingly, fibrillation was found to proceed with lag-times (t_{lag}) of approximately 175 h ($c_0 = 100 \mu\text{M}$) decreasing with increasing c_0 until fibrillation apparently becomes c_0 independent at $250 \mu\text{M}$ ($t_{\text{lag}} \approx 110$ h). Below c_{crit} (regime II), no fibril formation was observed. The high-order oligomer at regime IV, as previously hypothesized from kinetic experiments and supported by smFRET, FCCS and PFG-NMR in this work, is suspected to be the nucleation precursor at high c_0 ($> 310 \mu\text{M}$). For this c_0 regime we found a switch of the reaction order of primary nucleation towards $n_1 = 18.5$, enabling a competition with secondary nucleation.^[23] This led to a considerable reduction of the lag-time to about 60 h for $c_0 = 500 \mu\text{M}$ and further to ca. 20 h for $c_0 = 600 \mu\text{M}$. Importantly, in the current report we used an incubation time of 18 h to ensure an equilibrium between monomeric and oligomeric species.

Native MS revealed an equilibrium of PTH₈₄ monomers with oligomers of low molecular weight while only one corresponding r_{ee} fraction was found. From smFRET we suspect that peptides in monomers and small oligomers display comparable chain dimensions, but adopt a more extended conformation in high order oligomers (regime IV). Such extended conformational states were also found for the tau protein^[52] and α -synuclein^[53] within liquid-liquid phase separated solutions facilitating intermolecular cluster formation leading to amyloid fibril formation. Indeed, our CD analysis indicated a conformational reorientation with a decreasing α -helical propensity of the N-terminal region in the high c_0 regime.

Two-dimensional NMR spectroscopy allowed us to get to residue resolution and dynamic aspects of PTH₈₄ states. We not only found gradual CSP, indicating a fast, dynamic equilibrium between at least 2 states, but also additional cross-peaks for residues V35-A39, indicating a second, slow equilibrium in regimes II to IV. Our c_0 series probing the ensemble relaxation properties R_2/R_1 agree with a strongly decreased rotational correlation time τ_c as a consequence of oligomerization at high

c_0 as well as an exchange contribution R_{ex} due to fast equilibria. Interestingly, R_2/R_1 was almost identical for 20 μM (regime II) and 100 μM (regime III), consistent with the slow-exchange regime at which R_{ex} has only marginal effects on transversal relaxation. Note that $r_{H,app}$ (PFG-NMR) did also not change within regime II but CSPs were still observed. The additional cross-peaks for V35-A39, situated in a hydrophobic sequence, were detectable for regimes II to IV with a low signal intensity and even persisted in equilibrium with fibrils. We suspect that this refers to a dimeric species which is formed via weak hydrophobic interactions and is most probably non-productive for fibrillation. A similar network of sparsely populated productive dimers and tetramers as well as a non-productive dimer has also been described for the Huntington's disease related protein huntingtin (htt).^[29,54–55]

In our NMR-experiments, only little to no effects were observed for the disordered C-terminal part of PTH₈₄, while resonance intensity, CSP and relaxation were considerably affected within the N-terminal part. Under the neutral pH conditions used in this study, the major fraction of histidine residues is expected to be in the deprotonated state due to the side chain N–H pK_a value of 6.45.^[56–57] Of the 4 histidines of PTH₈₄ (H9, H14, H32, H63) only H9 displayed an assignable cross-peak with a low intensity at pH 7.4.^[58] In contrast, at pH 5.3 ($\text{pH} < pK_{a,HIS}$) all histidine residues were detectable.^[21,42] This fact hints towards a possible participation of histidine in such interactions. The response of both PTH₈₄ RKK patches as a consequence of c_0 increase within regime I, in which PTH₈₄ is monomeric but expanding, suggests contributions from these motifs. The helical parts are probably stabilized by weak intramolecular cation- π interactions of basic side chains with, e.g., histidine or π - π interactions involving histidine and arginine residues,^[59–62] also in the disordered part. The expansion of the chain coupled to the loss of secondary structure possibly occurs due to intermolecular transient interactions which further lead to oligomer formation.

We would like to highlight that soluble PTH₈₄ adopts the same monomer-dimer equilibrium after fibril formation as in the prenucleation state of appr. 40 μM (regime II), close to c_{crit} . This was not only observed for the thermodynamic equilibrium, but also during seeded fibril growth, indicating that the described oligomers are not static aggregates. The CSP of free, soluble PTH₈₄ readily adopted to the prenucleation situation at corresponding c_0 . Fibrils obviously do not affect the soluble state in terms of additional structure or oligomer formation. The small effect on R_2/R_1 ratios in equilibrium with fibrils for G12-V31 and A70-Q84 hint towards weak interactions of soluble peptides with the fibril surface, supporting our previous hypothesis.^[23] Monomer-fibril interactions are a common feature of amyloid systems and have been described in detail e.g. for A β_{40} .^[63–64]

To our knowledge, this is the first report of a c_0 dependent rapid oligomerization equilibrium of an aggregation-prone peptide specific for c_{crit} , which persists also in the presence of amyloid fibrils. The long lag-times agree with a very slow conversion step of the oligomers into fibril nuclei.^[23] We suppose that the considerably smaller lag-times for e.g. A β_{40}

indicate a slower oligomerization but a fast conversion rate which is possibly related to the toxicity of A β_{40} oligomers.^[65–66]

Experimental Section

Material. All chemicals were purchased from Sigma Aldrich or Carl Roth GmbH and used without further purification.

Recombinant Production of PTH₈₄ and sample preparation. The recombinant production of PTH₈₄ was conducted according to the previously published protocol.^[23] For 2D-NMR experiments, cells were grown in minimal salt medium with ¹⁵NH₄Cl as the only source of nitrogen.^[67] For single molecule techniques, double labelled Atto488-maleimide-cysteine-PTH₈₄-propargyl-glycine-Atto594-azid-OH was synthesized by the Core Unit Peptide Technologies of the University of Leipzig as published previously.^[22,68] Aliquots of the stock solution were allowed to thaw on ice, centrifuged (16000 g, 10 min, room temperature), diluted to the respective peptide concentration and supplemented with 150 mM NaCl for all analytical methods. The final buffer composition used for all experiments, if not stated otherwise, was 50 mM Na₂HPO₄, 150 mM NaCl, pH 7.4. All experiments have been conducted at 25 °C. For all experiments, the recombinantly produced PTH₈₄ was used. Synthetic PTH₈₄ double-labelled with fluorescent tags was additionally added for detection in single-molecule fluorescence techniques, as stated below.

Reversibility assay. Fibrils were grown by incubation of 700 μM PTH₈₄ in 50 mM Na-Borate, pH 9.0 for 18 h at 65 °C.^[21] After sedimentation (1 h, 16200 g), the supernatant was carefully removed, fibrils were resuspended in the same amount of Borate buffer, sedimented again and resuspended in borate buffer (pH 9.0), 50 mM Na₂HPO₄ (pH 7.4) or 10 mM BisTris, 300 mM Na₂SO₄ (pH 5.3) and incubated at 25 °C, 37 °C or 65 °C for 24 h. After sedimentation, the equilibrium monomer concentration within the supernatant was determined by UV/Vis spectroscopy on a J-650 spectrophotometer (Jasco International Co., Ltd., Tokyo, Japan).

CD spectroscopy. For estimating the overall amount of secondary structure, circular dichroism (CD) spectroscopy was used. In order to maintain a valuable signal-to-noise ratio, the detector tension (HT) and absorbance were kept below 600 V or 0.4, respectively. As a consequence, different cuvettes with different path lengths (d) were used: $d = 1$ mm ($c_0 < 20$ μM), $d = 0.1$ mm (20 $\mu\text{M} < c_0 < 150$ μM) and $d = 0.01$ mm ($c_0 > 150$ μM). For each sample 15 individual scans with a scanning speed of 50 nm/min and a bandwidth of 1 nm were accumulated on a J-815 spectropolarimeter (Jasco International Co., Ltd., Tokyo, Japan). The mean residue ellipticity, Θ_{MRE} , was calculated as

$$\Theta_{MRE} = \frac{\Theta}{10 c_0 d N_{aa}} \quad (1)$$

with Θ the measured ellipticity, c_0 protein concentration, d the path length and N_{aa} the number of residues within the peptide. A decomposition to extract information on structural content was performed by BESTSEL.^[46] Since PTH₈₄ is predominantly disordered, our analysis focuses on “other” structures which we interpret as unstructured content. A theoretical CD spectrum has been calculated from the AlphaFold 2.0 predicted three-dimensional structure of PTH₈₄ by using the PDBMD2CD server.^[69]

Intrinsic tryptophan fluorescence spectroscopy. Intrinsic PTH₈₄ W23 fluorescence was recorded ($\lambda_{exc} = 280$ nm, $\lambda_{em} = 290–550$ nm, scanning speed 50 nm/min) on a FP-6500 fluorescence spectrometer (Jasco International Co., Ltd., Tokyo, Japan). For analysis, the

fluorescence ratio F_{350}/F_{320} was used. As a consequence of the high peptide concentrations used, the fluorescence intensity at only one emission frequency is possibly biased due to primary inner filter effects, whereas the ratio monitors concentration dependent changes with respect to the spectral form. In the absence of changes to the spectral shape the trend of this ratio is expected to be linear. Whereas intermolecular quenching effects of W23 possibly contribute to spectral changes, intramolecular effects due to F34 should be negligible.

Native mass spectrometry (native MS). Using a mass spectrometer modified for transmission of high masses,^[70] proteins and complexes thereof are transferred intact into the gas phase by preserving non-covalent interactions. Thus, the oligomeric state can directly be observed.^[71] The storage buffer of 20 μL PTH₈₄ was exchanged to 200 mM ammonium acetate using Micro Bio-Spin 6 gel filtration columns (BioRad). 4 μL of 10–130 μM PTH₈₄ were loaded into gold-coated glass capillaries prepared in-house^[72] and directly introduced into a Waters Micromass Q-ToF Ultima mass spectrometer modified for transmission of high masses.^[70] For data acquisition the following parameters were used: capillary voltage 1.3–1.7 kV, sample cone voltage 80 V, RF lense voltage 80 V, collision voltage 20–50 V. Mass spectra were processed using MassLynx 4.1 software (Waters) and were externally calibrated using 100 mg/ml caesium iodide solution. Mass spectra were assigned using MassLynx 4.1 and Massign software (version 11/14/2014).^[73]

Single molecule fluorescence spectroscopy. Single-molecule fluorescence experiments were conducted on a home-built confocal microscope equipped with a pulsed fiber laser (FemtoFiber pro TVIS, Toptica Photonics AG, Graefelfing, Germany) operating at 488 nm and a repetition rate of 80 MHz, with the pulses being synchronized with a diode-based laser (LDH P–C–485B, Picoquant GmbH, Berlin, Germany) operating at 485 nm and 20 MHz. A single-mode fiber (LMA-8, NKT Photonics, Birkerød, Denmark) was used for spatial filtering and a 60X microscope objective (UPlanApo 60x/1.20W, Olympus, Tokyo, Japan) for excitation and fluorescence light collection. Dichroic beam splitters (Di01-R405/488/594–25x36, Semrock Inc./IDEX Corp., Lake Forest, IL, U.S.A., ZT594rdc, Chroma Technology Corp., Bellows Falls, VT, U.S.A) and a polarizing beam splitter (CVI Laser Optics, Albuquerque, NM, U.S.A.) were used to split the emission light and to guide it onto single-photon avalanche diodes (SPCM-AQRH-14-TR, Excelitas Technologies Corp., Mississauga, Canada) with their active areas serving as confocal pinholes. Spectral filters allowed to set the spectral range for the donor channel (LP496, BP25/50) and the acceptor channel (LP615, BP629/56), all filters were purchased from Semrock Inc (IDEX Corp., Lake Forest, IL, U.S.A.). Pulses from the detectors were fed into a TCSPC board (MultiHarp 150, Picoquant GmbH, Berlin, Germany) operating in the time-tagged time-resolved mode with 80 ps time resolution.

Single-molecule FRET (smFRET). Single-molecule FRET measurements were performed with 50–100 μM of Fmoc-synthesized doubly-labeled PTH₈₄ in the presence of recombinantly produced PTH₈₄ within the range of 10 μM to 500 μM . For burst experiments, a pulsed-interleaved excitation scheme was used with the donor molecule being excited with 80 MHz and 50 μW and the acceptor with 20 MHz and 10 μW . Detected photons were sorted by their arrival times with respect to a synchronization signal of 20 MHz for assignment to the respective excitation sources. Fluorescence bursts were identified using two threshold criteria, one threshold for the integrated emission after donor excitation and one for the acceptor emission after direct excitation of the acceptor to select for molecules bearing both a donor and acceptor, respectively. The first threshold was applied to a sliding density average of 10 adjacent photons detected by either of the two detection channels to avoid time binning. All consecutive photons above this threshold

were combined into one burst and the minimum number of photons per burst was set to 100. Counted photons of each detector channel were corrected for background counts, quantum yields of fluorescence, and quantum efficiency of detection (including collection efficiency, filter transmission, spectral cross talk and detector efficiency). Averaging owing to conformational flexibility during transit through the focus was taken into consideration in the calculation of distances from energy transfer histograms using the integral

$$\langle E \rangle = \int P(r_{ee})E(r_{ee})dr_{ee}, \quad (2)$$

where $E(r_{ee}) = 1/(1 + (r_{ee}/R_0)^6)$ is the distance dependence of the energy transfer with R_0 the characteristic Förster distance of 5.8 nm and $P(r_{ee})$ an excluded-volume probability distribution of the end-to-end distance approximated by the Gaussian-chain description:^[74]

$$P(r_{ee}) = \left(\frac{3}{2\pi N b^2} \right)^{3/2} e^{-\frac{3r_{ee}^2}{2N b^2}} \quad (3)$$

where N is the sum of the number of amino acids between the dye labels and the apparent length of the dye linker in terms of b , and b the distance between two C $_{\alpha}$ -atoms, found as 0.38 nm.^[75] The parameter r_{ee} can be used as a measure for the conformational space of a disordered chain (e.g. swollen, collapsed). For the high concentration, 4185 bursts were collected in total, while for the low concentration regime, individual energy transfer histograms of the samples with 40 μM , 50 μM , 60 μM and 70 μM were accumulated to obtain one plot (2835 bursts in total). A 2D analysis of the FRET efficiency and stoichiometry S was used to ensure that the displayed energy transfer values truly result from the energy transfer between donor and acceptor molecules, since molecules carrying a donor only would also apparently lead to low energy transfer values.^[76] This photon distribution analysis is shown in Figure S4.

Fluorescence cross correlation spectroscopy (FCCS). The characteristic decay time of the translational diffusion was determined from the cross-correlation functions of the donor and the acceptor channel, $G(\tau)$, using the fitting function:

$$G(\tau) = \frac{1}{N} \left[1 - T + T \exp\left(-\frac{\tau}{\tau_T}\right) \right] \left(1 + \left(\frac{\tau}{\tau_D}\right)^a \right)^{-1} * \left(1 + S^2 \left(\frac{\tau}{\tau_D}\right)^a \right)^{-1/2} \quad (4)$$

where S and a are system parameters describing the shape of the focal volume, N is the average number of labeled molecules in the focal volume, and τ_D the average dwell time in the focus volume, being related to the inverse translational diffusion coefficient, D . Triplet blinking was parameterized by the triplet fraction, T , and triplet time, τ_T . The hydrodynamic radius, r_h was determined using the Stokes-Einstein equation with:

$$D = \frac{k_B T}{6\pi\eta r_h}, \quad (5)$$

where k_B is the Boltzmann constant, T the absolute temperature and η the viscosity of the solvent.^[77] $G(\tau)$ was normalized with

respect to the average number of molecules in the focus volume, $G_n(t) = G(\tau) \times N$. The reference measurements were conducted with Atto488 and Atto594.

Small angle X-ray scattering (SAXS). X-ray scattering experiments were performed in transmission mode using a SAXSLAB laboratory setup (Retro-F) equipped with an AXO micro-focus X-ray source. The AXO multilayer X-ray optic (AXO Dresden GmbH, Dresden, Germany) was used as a monochromator for Cu- K_{α} radiation ($\lambda = 0.154$ nm). A two-dimensional detector (PILATUS3 R 300 K; DECTRIS, Baden, Switzerland) was used to record the 2D scattering patterns.

SAXS experiments were conducted using refillable capillaries with an outer diameter of 1 mm (BioSAS JSP stage, SAXSLAB/Xenocs, France). The intensities were angular-averaged and plotted versus the scattering angle q . The measurements were performed at room temperature and corrected for background, transmission and sample geometry. The measurement times were set to 6 h. Subsequent EOM analysis of the scattering intensities were conducted to reveal the most probable distributions of the radius of gyration, $p(r_g)$, and the end-to-end distances, $p(R_{ee})$ for 50 μM and 500 μM of PTH₈₄.^[78–79]

Pulsed-Field-Gradient (PFG) NMR spectroscopy. The diffusion coefficient at different peptide concentrations was determined via PFG-NMR on the basis of proton spectra on a 600 MHz Bruker Avance III spectrometer. The gradient strength G was incremented in 26 steps from 2% to 98% of the maximum gradient $G_{\text{max}} = 0.53$ T/m. The intensity for each gradient increment was integrated in the area 0.5 ppm–2.5 ppm. This resulting intensity decay was analyzed using the Stejskal-Tanner equation

$$\frac{I}{I_0} = e^{-D \gamma^2 \sigma^2 G^2 \delta^2 (\Delta - \frac{\delta}{2})} \quad (6)$$

where D is the diffusion coefficient, γ the gyromagnetic ratio of protons, σ the gradient shape factor ($2/\pi$ for the sine bell shape used in this work), G the gradient strength, δ the gradient length (6 ms) and Δ the diffusion time (100 ms).^[80] The data were compared to the diffusion of the internal chemical shift reference substance DSS and converted to apparent hydrodynamic radii $r_{\text{H,app}}$ as

$$r_{\text{H,app,PTH}} = \frac{D_{\text{DSS}} r_{\text{H,DSS}}}{D_{\text{app,PTH}}} \quad (7)$$

In an additional, similar experiment the r_{H} of DSS was calculated to be 0.339 nm, using 1,4-Dioxan ($r_{\text{H}} = 0.212$ nm) as a reference substance.^[81] The obtained $r_{\text{H,app}}$ do not reflect a distinct state, but represents an average of the full ensemble of possible states within the sample. Hence, we only use it as a parameter indicating trends for the hydrodynamic properties.

Chemical shift perturbation (CSP) and signal intensity. ^1H - ^{15}N -fHSQC spectra were acquired at different PTH₈₄ concentrations on an 800 MHz Bruker Avance III spectrometer. The previously reported assignment of the cross-peaks was used.^[58] The number of scans as a parameter to improve the signal-to-noise ratio was adjusted according to the sample concentration while the receiver gain was kept constant for all samples. Acquired spectra were processed using NMRPipe^[82] and analyzed with PINT.^[83–84] The change of the position of the cross peaks in ^1H - ^{15}N -fHSQC spectra are expressed as the combined chemical shift $\Delta\delta$ and calculated as

$$\Delta\delta(^1\text{H}, ^{15}\text{N}) = \sqrt{(\delta^1\text{H})^2 + (\delta^{15}\text{N})^2} \quad (8)$$

with $\delta^1\text{H}$ and $\delta^{15}\text{N}$ the chemical shift difference between two spectra, given in Hz, in the direct and indirect dimension, respectively. For the analysis of the intensities of the cross peaks the signal intensity I was corrected for experimental details by

$$I = \frac{I_{\text{exp}}}{ns c_0} \quad (9)$$

where I_{exp} is the experimental intensity of a distinct cross-peak, ns the number of scans accumulated to acquire the ^1H - ^{15}N -HSQC spectrum and c_0 the molar sample concentration. The samples contained 10% (v/v) D₂O and 0.01 mg/ml DSS as a reference substance for the chemical shift.

The absolute intensity of a cross-peak in an ^1H - ^{15}N -fHSQC spectrum depends on many experimental and protein specific factors and therefore a direct quantification of protein populations is complex.^[85] However, the change of relative intensities within a concentration series mostly results from differences in the transversal relaxation rate (R_2) due to changes of the local dynamics, the rotational correlation time or chemical exchange.^[86–87] Therefore, the evolution of the cross-peak intensities as well as the CSP allows valuable insights to characterize the concentration dependence of PTH₈₄ ^1H - ^{15}N -fHSQC spectra. Due to slow tumbling of peptides incorporated into fibrils leading to broadening of cross-peaks beyond detection, only free, soluble peptides are expected to contribute to the acquired signal.

NMR relaxation experiments. The longitudinal (R_1) and transversal (R_2) relaxation rates were determined as pseudo-3D spectra on the basis of ^1H - ^{15}N -fHSQC spectra as read-out on an 800 MHz Bruker Avance III spectrometer.^[49] The respective rates were extracted from the mono-exponential decay over 8 points (0 ms–1000 ms for R_1 ; 0 ms–192 ms for R_2) of recovery time. Relaxation experiments were conducted for samples containing 20 μM , 100 μM , 250 μM and 500 μM ^{15}N -labelled PTH₈₄. Due to the reduced sensitivity of NMR relaxation experiments compared to ^1H - ^{15}N -fHSQC, it was not possible to acquire reliable relaxation data for regime I to compare with the purely monomeric state. To analyze the relaxation properties of soluble PTH₈₄ in equilibrium with fibrils, a 100 μM ^{15}N labelled sample was incubated with 5% pre-formed unlabeled seeds for 20 h prior to the measurement.

CSP-RMSD analysis. ^1H - ^{15}N -fHSQC spectra of samples containing 100 μM , 250 μM or 500 μM ^{15}N -PTH₈₄ were acquired before and 7 days after addition of 5% unlabeled pre-formed seeds (given in monomer equivalents). The incubation time of 7 days was chosen to ensure that the system reached the thermodynamic equilibrium. Directly prior to the measurement, the samples were carefully mixed to resuspend settled fibrils. The chemical shift differences $\Delta\delta$ between these sample spectra and a set of fibril-free reference spectra in a range of $5 \mu\text{M} < c_0 < 500 \mu\text{M}$ were used to compare the soluble state in the presence of fibrils with the prenucleation equilibrium. As a measure for the overall CSP between a sample and each reference spectrum we then calculated the root mean square deviation (RMSD) for each pair of spectra as

$$\text{RMSD} = \sqrt{\frac{(\Delta\delta_1)^2 + (\Delta\delta_2)^2 + \dots + (\Delta\delta_n)^2}{n}} \quad (10)$$

This experiment allows to study the soluble peptide fraction also in the presence of fibrils, as the signal width of ^{15}N labelled PTH₈₄ eventually incorporated into fibrils would broaden beyond detection due to slow tumbling. In order to obtain information about the time dependence, we added 10% unlabeled pre-formed seeds at time zero (directly before spectra acquisition) and repeated the

acquisition of ^1H spectra to monitor the concentration of NMR detectable, soluble PTH₈₄ and ^1H - ^{15}N -fHSQC spectra to follow the time dependence of the CSP for two samples with $c_0 = 250 \mu\text{M}$ and $500 \mu\text{M}$. For each time point, the RMSD values of the CSP between the sample spectra and the fibril-free reference spectra have been conducted as stated above. The integrals from 2.4 ppm to 0 ppm from the ^1H spectra were used to estimate the overall concentration of soluble peptide.

Acknowledgements

We acknowledge funding from the Federal Ministry for Education and Research (BMBF, 03Z22HN22), the European Regional Development Funds (EFRE, ZS/2016/04/78115 and for the support of the NMR infrastructure), the MLU Halle-Wittenberg, the JGU Mainz and the German research foundation (DFG, project ID 189853844 – TRR 102 “polymers under multiple constraints”, TP A12 and TP B12, and project ID 391498659 – RTG 2467 “Intrinsically Disordered Proteins – Molecular Principles, Cellular Functions, and Diseases”, TP 1, TP 2 and TP 11). The authors thank Jakob Schneider for initial studies on the project, Sven Rothemund for the synthesis of Atto488/Atto594 labelled PTH₈₄ as well as Malte Neudorf, Ulrich Weininger and Stefan Gröger for valuable discussions. Open Access funding enabled and organized by Projekt DEAL.

Conflict of Interests

The authors declare no conflict of interest.

Data Availability Statement

The data that support the findings of this study are available from the corresponding author upon reasonable request.

Keywords: biophysics · functional amyloids · peptide hormone · nucleation · critical concentration

- [1] F. Chiti, C. M. Dobson, *Annu. Rev. Biochem.* **2006**, *75*, 333–366.
- [2] J. T. Jarrett, P. T. Lansbury Jr., *Cell* **1993**, *73*, 1055–1058.
- [3] P. T. Lansbury, H. A. Lashuel, *Nature* **2006**, *443*, 774–779.
- [4] J. D. Sipe, M. D. Benson, J. N. Buxbaum, S. Ikeda, G. Merlini, M. J. Saraiva, P. Westermark, *Amyloid* **2012**, *19*, 167–170.
- [5] Y. Shikama, J. Kitazawa, N. Yagihashi, O. Uehara, Y. Murata, N. Yajima, R. Wada, S. Yagihashi, *Intern. Med.* **2010**, *49*, 397–401.
- [6] J. N. Buxbaum, J. V. Chuba, G. C. Hellman, A. Solomon, G. R. Gallo, *Ann. Intern. Med.* **1990**, *112*, 455–464.
- [7] D. M. Fowler, A. V. Koulov, C. Alory-Jost, M. S. Marks, W. E. Balch, J. W. Kelly, *PLoS Biol.* **2006**, *4*, e6.
- [8] M. R. Chapman, L. S. Robinson, J. S. Pinkner, R. Roth, J. Heuser, M. Hammar, S. Normark, S. J. Hultgren, *Science* **2002**, *295*, 851–855.
- [9] R. Hervas, M. J. Rau, Y. Park, W. Zhang, A. G. Murzin, J. A. J. Fitzpatrick, S. H. W. Scheres, K. Si, *Science* **2020**, *367*, 1230–1234.
- [10] S. K. Maji, M. H. Perrin, M. R. Sawaya, S. Jessberger, K. Vadodaria, R. A. Rissman, P. S. Singru, K. P. Nilsson, R. Simon, D. Schubert, D. Eisenberg, J. Rivier, P. Sawchenko, W. Vale, R. Riek, *Science* **2009**, *325*, 328–332.
- [11] K. C. Evans, E. P. Berger, C. G. Cho, K. H. Weisgraber, P. T. Lansbury Jr., *Proc. Natl. Acad. Sci. USA* **1995**, *92*, 763–767.
- [12] L. Nielsen, R. Khurana, A. Coats, S. Frokjaer, J. Brange, S. Vyas, V. N. Uversky, A. L. Fink, *Biochemistry* **2001**, *40*, 6036–6046.
- [13] S. I. Cohen, M. Vendruscolo, M. E. Welland, C. M. Dobson, E. M. Terentjev, T. P. Knowles, *J. Chem. Phys.* **2011**, *135*, 065105.
- [14] T. C. T. Michaels, A. Šarić, J. Habchi, S. Chia, G. Meisl, M. Vendruscolo, C. M. Dobson, T. P. J. Knowles, *Annu. Rev. Phys. Chem.* **2018**, *69*, 273–298.
- [15] M. Törnquist, T. C. T. Michaels, K. Sanagavarapu, X. Yang, G. Meisl, S. I. A. Cohen, T. P. J. Knowles, S. Linse, *Chem. Commun.* **2018**, *54*, 8667–8684.
- [16] M. Törnquist, S. Linse, *Angew. Chem. Int. Ed.* **2021**, *60*, 24008–24011.
- [17] J. D. Harper, P. T. Lansbury Jr., *Annu. Rev. Biochem.* **1997**, *66*, 385–407.
- [18] B. O’Nuallain, S. Shivaprasad, I. Kheterpal, R. Wetzel, *Biochemistry* **2005**, *44*, 12709–12718.
- [19] R. Wetzel, *Acc. Chem. Res.* **2006**, *39*, 671–679.
- [20] R. Crespo, F. A. Rocha, A. M. Damas, P. M. Martins, *J. Biol. Chem.* **2012**, *287*, 30585–30594.
- [21] M. Gopalswamy, A. Kumar, J. Adler, M. Baumann, M. Henze, S. T. Kumar, M. Fändrich, H. A. Scheidt, D. Huster, J. Balbach, *Biochim. Biophys. Acta* **2015**, *1854*, 249–257.
- [22] L. M. Lauth, B. Voigt, T. Bhatia, L. Machner, J. Balbach, M. Ott, *FEBS Lett.* **2022**, *596*, 2928–2939.
- [23] B. Voigt, M. Ott, J. Balbach, *Macromol. Biosci.* **2023**, e2200525.
- [24] A. J. Baldwin, T. P. Knowles, G. G. Tartaglia, A. W. Fitzpatrick, G. L. Devlin, S. L. Shammah, C. A. Waudby, M. F. Mossuto, S. Meehan, S. L. Gras, J. Christodoulou, S. J. Anthony-Cahill, P. D. Barker, M. Vendruscolo, C. M. Dobson, *J. Am. Chem. Soc.* **2011**, *133*, 14160–14163.
- [25] M. So, D. Hall, Y. Goto, *Curr. Opin. Struct. Biol.* **2016**, *36*, 32–39.
- [26] A. J. Dear, G. Meisl, A. Šarić, T. C. T. Michaels, M. Kjaergaard, S. Linse, T. P. J. Knowles, *Chem. Sci.* **2020**, *11*, 6236–6247.
- [27] G. A. Garcia, S. I. Cohen, C. M. Dobson, T. P. Knowles, *Phys. Rev. E* **2014**, *89*, 032712.
- [28] A. Ceccon, V. Tugarinov, R. Ghirlando, G. M. Clore, *Proc. Natl. Acad. Sci. USA* **2020**, *117*, 5844–5852.
- [29] S. A. Kotler, V. Tugarinov, T. Schmidt, A. Ceccon, D. S. Libich, R. Ghirlando, C. D. Schwieters, G. M. Clore, *Proc. Natl. Acad. Sci. USA* **2019**, *116*, 3562–3571.
- [30] T. K. Karamanos, M. P. Jackson, A. N. Calabrese, S. C. Goodchild, E. E. Cawood, G. S. Thompson, A. P. Kalverda, E. W. Hewitt, S. E. Radford, *eLife* **2019**, *8*, e46574.
- [31] Z. Hall, C. Schmidt, A. Politis, *J. Biol. Chem.* **2016**, *291*, 4626–4637.
- [32] E. Rennella, T. Cutuili, P. Schanda, I. Ayala, F. Gabel, V. Forge, A. Corazza, G. Esposito, B. Brutscher, *J. Mol. Biol.* **2013**, *425*, 2722–2736.
- [33] F. Hasecke, T. Miti, C. Perez, J. Barton, D. Schölzel, L. Gremer, C. S. R. Grüning, G. Matthews, G. Meisl, T. P. J. Knowles, D. Willbold, P. Neudecker, H. Heise, G. Ullah, W. Hoyer, M. Muschol, *Chem. Sci.* **2018**, *9*, 5937–5948.
- [34] C. Perez, T. Miti, F. Hasecke, G. Meisl, W. Hoyer, M. Muschol, G. Ullah, *J. Phys. Chem. B* **2019**, *123*, 5678–5689.
- [35] P. H. Nguyen, A. Ramamoorthy, B. R. Sahoo, J. Zheng, P. Faller, J. E. Straub, L. Dominguez, J. E. Shea, N. V. Dokholyan, A. De Simone, B. Ma, R. Nussinov, S. Najafi, S. T. Ngo, A. Loquet, M. Chiricotto, P. Ganguly, J. McCarty, M. S. Li, C. Hall, Y. Wang, Y. Miller, S. Melchionna, B. Habenstein, S. Timr, J. Chen, B. Hnath, B. Strodel, R. Kayed, S. Lesné, G. Wei, F. Sterpone, A. J. Doig, P. Derreumaux, *Chem. Rev.* **2021**, *121*, 2545–2647.
- [36] U. I. Gerling, M. S. Miettinen, B. Koksche, *ChemPhysChem* **2015**, *16*, 108–114.
- [37] J. F. Habener, M. Rosenblatt, J. T. Potts Jr., *Physiol. Rev.* **1984**, *64*, 985–1053.
- [38] T. J. Anderson, S. W. Ewen, *J. Clin. Pathol.* **1974**, *27*, 656–663.
- [39] J. Jumper, R. Evans, A. Pritzel, T. Green, M. Figurnov, O. Ronneberger, K. Tunyasuvunakool, R. Bates, A. Židek, A. Potapenko, A. Bridgland, C. Meyer, S. A. A. Kohli, A. J. Ballard, A. Cowie, B. Romera-Paredes, S. Nikolov, R. Jain, J. Adler, T. Back, S. Petersen, D. Reiman, E. Clancy, M. Zielinski, M. Steinegger, M. Pacholska, T. Berghammer, S. Bodenstein, D. Silver, O. Vinyals, A. W. Senior, K. Kavukcuoglu, P. Kohli, D. Hassabis, *Nature* **2021**, *596*, 583–589.
- [40] U. C. Marx, K. Adermann, P. Bayer, W. G. Forstmann, P. Rösch, *Biochem. Biophys. Res. Commun.* **2000**, *267*, 213–220.
- [41] M. Varadi, S. Anyango, M. Deshpande, S. Nair, C. Natassia, G. Yordanova, D. Yuan, O. Strope, G. Wood, A. Laydon, A. Židek, T. Green, K. Tunyasuvunakool, S. Petersen, J. Jumper, E. Clancy, R. Green, A. Vora, M. Lutfi, M. Figurnov, A. Cowie, N. Hobbs, P. Kohli, G. Kleywegt, E. Birney, D. Hassabis, S. Velankar, *Nucleic Acids Res.* **2022**, *50*, D439–D444.

- [42] S. Sachan, C. G. Moya, B. Voigt, M. Köhn, J. Balbach, *FEBS Lett.* **2023**, *597*, 995–1006.
- [43] K. Hasegawa, K. Ono, M. Yamada, H. Naiki, *Biochemistry* **2002**, *41*, 13489–13498.
- [44] C. L. Pashley, E. W. Hewitt, S. E. Radford, *J. Mol. Biol.* **2016**, *428*, 631–643.
- [45] T. R. Alderson, I. Pritišanac, A. M. Moses, J. D. Forman-Kay, **2022**, bioRxiv preprint DOI: 10.1101/2022.02.18.481080.
- [46] A. Micsonai, F. Wien, L. Kerna, Y. H. Lee, Y. Goto, M. Réfrégiers, J. Kardos, *Proc. Natl. Acad. Sci. USA* **2015**, *112*, E3095–E3103.
- [47] E. Gasteiger, C. Hoogland, A. Gattiker, S. Duvaud, M. R. Wilkins, R. D. Appel, A. Bairoch, in *The Proteomics Protocols Handbook* (Ed.: J. M. Walker), Humana Press, Totowa, NJ, **2005**, pp. 571–607.
- [48] H. J. Dyson, P. E. Wright, *Nat. Struct. Biol.* **1998**, *5 Suppl*, 499–503.
- [49] T. Gruber, M. Lewitzky, L. Machner, U. Weininger, S. M. Feller, J. Balbach, *J. Mol. Biol.* **2022**, *434*, 167407.
- [50] N. Tjandra, S. E. Feller, R. W. Pastor, A. Bax, *J. Am. Chem. Soc.* **1995**, *117*, 12562–12566.
- [51] A. G. Palmer, 3rd, *Curr. Opin. Struct. Biol.* **1997**, *7*, 732–737.
- [52] J. Wen, L. Hong, G. Krainer, Q. Q. Yao, T. P. J. Knowles, S. Wu, S. Perrett, *J. Am. Chem. Soc.* **2021**, *143*, 13056–13064.
- [53] D. Ubbiali, M. Fratini, L. Piersimoni, C. H. Ihling, M. Kipping, I. Heilmann, C. Iacobucci, A. Sinz, *Angew. Chem. Int. Ed.* **2022**, *61*, e202205726.
- [54] A. Ceccon, V. Tugarinov, G. M. Clore, *J. Phys. Chem. Lett.* **2020**, *11*, 5643–5648.
- [55] A. Ceccon, V. Tugarinov, F. Torricella, G. M. Clore, *Proc. Natl. Acad. Sci. USA* **2022**, *119*, e2207690119.
- [56] G. Platzer, M. Okon, L. P. McIntosh, *J. Biomol. NMR* **2014**, *60*, 109–129.
- [57] H. N. Raum, U. Weininger, *ChemBioChem* **2019**, *20*, 922–930.
- [58] Z. Evgrafova, B. Voigt, M. Baumann, M. Stephani, W. H. Binder, J. Balbach, *ChemPhysChem* **2019**, *20*, 236–240.
- [59] J. Heyda, P. E. Mason, P. Jungwirth, *J. Phys. Chem. B* **2010**, *114*, 8744–8749.
- [60] K. Kumar, S. M. Woo, T. Siu, W. A. Cortopassi, F. Duarte, R. S. Paton, *Chem. Sci.* **2018**, *9*, 2655–2665.
- [61] S. M. Liao, Q. S. Du, J. Z. Meng, Z. W. Pang, R. B. Huang, *Chem. Cent. J.* **2013**, *7*, 44.
- [62] R. M. Vernon, P. A. Chong, B. Tsang, T. H. Kim, A. Bah, P. Farber, H. Lin, J. D. Forman-Kay, *eLife* **2018**, *7*, e31486.
- [63] N. L. Fawzi, D. S. Libich, J. Ying, V. Tugarinov, G. M. Clore, *Angew. Chem. Int. Ed.* **2014**, *53*, 10345–10349.
- [64] N. L. Fawzi, J. Ying, R. Ghirlando, D. A. Torchia, G. M. Clore, *Nature* **2011**, *480*, 268–272.
- [65] S. De Sio, J. Waegeler, T. Bhatia, B. Voigt, H. Lilie, M. Ott, *Macromol. Biosci.* **2023**, e2200527.
- [66] Y. R. Huang, R. T. Liu, *Int. J. Mol. Sci.* **2020**, *21*, 447.
- [67] C. Piotrowski, C. H. Ihling, A. Sinz, *Methods* **2015**, *89*, 121–127.
- [68] J. Wägele, S. De Sio, B. Voigt, J. Balbach, M. Ott, *Biophys. J.* **2019**, *116*, 227–238.
- [69] E. D. Drew, R. W. Janes, *Nucleic Acids Res.* **2020**, *48*, W17–W24.
- [70] F. Sobott, H. Hernández, M. G. McCammon, M. A. Tito, C. V. Robinson, *Anal. Chem.* **2002**, *74*, 1402–1407.
- [71] J. L. Benesch, B. T. Ruotolo, D. A. Simmons, C. V. Robinson, *Chem. Rev.* **2007**, *107*, 3544–3567.
- [72] H. Hernández, C. V. Robinson, *Nat. Protoc.* **2007**, *2*, 715–726.
- [73] N. Morgner, C. V. Robinson, *Anal. Chem.* **2012**, *84*, 2939–2948.
- [74] M. Doi, S. F. Edwards, *The theory of polymer dynamics*, The Clarendon Press, Oxford University Press, New York, **1986**.
- [75] H. Hofmann, A. Soranno, A. Borgia, K. Gast, D. Nettels, B. Schuler, *Proc. Natl. Acad. Sci. USA* **2012**, *109*, 16155–16160.
- [76] B. Hellenkamp, S. Schmid, O. Doroshenko, O. Opanasyuk, R. Kühnemuth, S. Rezaei Adariani, B. Ambrose, M. Aznauryan, A. Barth, V. Birkedal, M. E. Bowen, H. Chen, T. Cordes, T. Eilert, C. Fijen, C. Gebhardt, M. Götz, G. Gouridis, E. Gratton, T. Ha, P. Hao, C. A. Hanke, A. Hartmann, J. Hendrix, L. L. Hildebrandt, V. Hirschfeld, J. Hohlbein, B. Hua, C. G. Hübner, E. Kallis, A. N. Kapanidis, J. Y. Kim, G. Krainer, D. C. Lamb, N. K. Lee, E. A. Lemke, B. Levesque, M. Levitus, J. J. McCann, N. Naredi-Rainer, D. Nettels, T. Ngo, R. Qiu, N. C. Robb, C. Röcker, H. Sanabria, M. Schlierf, T. Schröder, B. Schuler, H. Seidel, L. Streit, J. Thurn, P. Tinnefeld, S. Tyagi, N. Vandenberk, A. M. Vera, K. R. Weninger, B. Wunsch, I. S. Yanez-Orozco, J. Michaelis, C. A. M. Seidel, T. D. Craggs, T. Hugel, *Nat. Methods* **2018**, *15*, 669–676.
- [77] C. C. Miller, J. Walker, *Proc. Math. Phys. Eng. Sci.* **1924**, *106*, 724–749.
- [78] A. Sagar, C. M. Jeffries, M. V. Petoukhov, D. I. Svergun, P. Bernadó, *J. Chem. Theory Comput.* **2021**, *17*, 2014–2021.
- [79] G. Tria, H. D. Mertens, M. Kachala, D. I. Svergun, *IUCrJ* **2015**, *2*, 207–217.
- [80] E. O. Stejskal, J. E. Tanner, *J. Chem. Phys.* **1965**, *42*, 288–292.
- [81] D. K. Wilkins, S. B. Grimshaw, V. Receveur, C. M. Dobson, J. A. Jones, L. J. Smith, *Biochemistry* **1999**, *38*, 16424–16431.
- [82] F. Delaglio, S. Grzesiek, G. W. Vuister, G. Zhu, J. Pfeifer, A. Bax, *J. Biomol. NMR* **1995**, *6*, 277–293.
- [83] A. Ahlner, M. Carlsson, B.-H. Jonsson, P. Lundström, *J. Biomol. NMR* **2013**, *56*, 191–202.
- [84] M. Niklasson, R. Otten, A. Ahlner, C. Andresen, J. Schlaginitweit, K. Petzold, P. Lundström, *J. Biomol. NMR* **2017**, *69*, 93–99.
- [85] M. Dreydoppel, J. Balbach, U. Weininger, *J. Biomol. NMR* **2022**, *76*, 3–15.
- [86] W. Becker, K. C. Bhattiprolu, N. Gubensäk, K. Zangger, *ChemPhysChem* **2018**, *19*, 895–906.
- [87] J. Jeener, B. H. Meier, P. Bachmann, R. R. Ernst, *J. Chem. Phys.* **1979**, *71*, 4546–4553.

Manuscript received: June 22, 2023
Revised manuscript received: July 18, 2023
Accepted manuscript online: July 21, 2023
Version of record online: ■■■, ■■■

2.3 Paper III: L.M. Lauth *et al.* (2022), Heparin promotes rapid fibrillation of the basic parathyroid hormone at physiological pH

Aims and Summary

The focus of Paper III was set towards *in vivo* like conditions of PTH₈₄ fibrillation. PTH₈₄ is stored in secretory granules prior to release into the blood stream. These granules contain a low pH-value of appr. pH 5.5. The fibrillation of PTH₈₄ alone and in the presence of heparin was investigated. Interaction studies revealed heparin-PTH₈₄ binding with a sub- μ M dissociation constant and a maximum stoichiometry of 1:11 (heparin:PTH₈₄). The critical molar ratio for interaction was found to be 1:10 (heparin-PTH₈₄). Two-dimensional NMR spectroscopy showed that PTH₈₄-heparin interaction is facilitated by the *N*-terminal region. *De novo* fibril formation for PTH₈₄ alone did not occur at acidic pH. The addition of heparin led to rapid fibril growth within several hours. Heparin influenced primary as well as secondary processes of PTH₈₄ fibrillation in a non-linear concentration dependent manner. This indicated the structural conversion of PTH₈₄ into growth-competent fibrillar species to be the main driving force of heparin action. Paper III underlined the importance of glycosaminoglycans present in secretory granules, such as heparin, as potential candidates to induce and assist the formation of functional amyloid fibrils. This had been demonstrated for other peptide hormones from the pituitary glands and now for PTH₈₄ as well.

Contribution

The author of this thesis recombinantly produced the ¹⁵N isotope labelled peptide (100 %), supported planning and conducting the fibrillation experiments (50 %), prepared and conducted the electron microscopy imaging (100 %), planned and conducted the NMR spectroscopy characterization (90 %), supported interpreting the data, prepared one figure and reviewed the manuscript during all stages of preparation.

Original Paper

The original paper is included on the following pages (pp. 60-71). The Supporting Information can be found in Appendix A.3.

RESEARCH LETTER

Heparin promotes rapid fibrillation of the basic parathyroid hormone at physiological pH

 Luca M. Lauth¹ , Bruno Voigt² , Twinkle Bhatia¹, Lisa Machner³, Jochen Balbach²  and Maria Ott² 
¹ Department of Biochemistry and Biotechnology, Martin-Luther-University Halle-Wittenberg, Germany

² Department of Biophysics, Martin-Luther-University Halle-Wittenberg, Germany

³ Department of Molecular Medicine, Martin-Luther-University Halle-Wittenberg, Germany

Correspondence

L. M. Lauth and M. Ott, Department of Biochemistry and Biotechnology, Martin-Luther-University Halle-Wittenberg, Halle, Germany

Tel: +49 (0)345 5 524 946

E-mail: luca.lauth@bct.uni-halle.de (LML); maria.ott@bct.uni-halle.de (MO)

(Received 19 March 2022, revised 14 June 2022, accepted 9 July 2022)

doi:10.1002/1873-3468.14455

Edited by Barry Halliwell

In acidic secretory granules of mammalian cells, peptide hormones including the parathyroid hormone are presumably stored in the form of functional amyloid fibrils. Mature PTH, however, is considerably positively charged in acidic environments, a condition known to impede unassisted self-aggregation into fibrils. Here, we studied the role of the polyanion heparin on promoting fibril formation of PTH. Employing ITC, CD spectroscopy, NMR, SAXS, and fluorescence-based assays, we could demonstrate that heparin binds PTH with submicromolar affinity and facilitates its conversion into fibrillar seeds, enabling rapid formation of amyloid fibrils under acidic conditions. In the absence of heparin, PTH remained in a soluble monomeric state. We suspect that heparin-like surfaces are required *in vivo* to convert PTH efficiently into fibrillar deposits.

Keywords: acidic pH; amyloid fibrillation; functional amyloids; heparin interaction; intrinsically disordered proteins; parathyroid hormone

The parathyroid hormone (PTH) is a peptide hormone expressed in parathyroid chief cells that binds the PTH-specific G protein-coupled receptors PTH1R and PTH2R to regulate serum calcium ion and phosphate levels [1–4]. Like any peptide hormone, PTH needs to be secreted from the producing cells to enable its access to the target structures *via* the blood stream [5] (Fig. 1A). For that purpose, peptide hormones are generally destined to pass the secretory pathway. Importantly, the organelles that constitute the secretory pathway get continuously acidified as they approach the state of secretion [6]. The resulting pH gradient across the secretory pathway is implicated in regulating events of post-translational modifications and sorting of cargo proteins. Moreover, the decrease in pH is accompanied by the formation of amyloid

fibrils, which is the presumed storage form of peptide hormones inside secretory granules [7–9]. Interestingly, many peptide hormones yield an isoelectric point (pI) close to the acidic pH of approx. 5.5 as found in the trans-Golgi network and secretory granules. Consequently, these proteins are less soluble at low pH while displaying an enhanced propensity to aggregate, for example, into amyloid fibrils [8,10–12]. Indeed, many of these peptide hormones spontaneously fibrillate also *in vitro* at pH 5.5 [7].

Mature PTH (C-terminal 84 amino acids, from now on referred to as PTH₁₋₈₄), however, has a calculated pI value of 8.9 and harbors four histidine residues with a pK_A value of approximately 6.2. As a result, the net charge of PTH₁₋₈₄ increases significantly under acidifying conditions: While the net charge at pH 7.4 is

Abbreviations

b, length of a Kuhn segment; CD, circular dichroism; GAG, glycosaminoglycan; ITC, isothermal titration calorimetry; κ , rate of secondary nucleation and growth; *L*, contour length; PTH, parathyroid hormone; R_c , cross-sectional radius; R_g , radius of gyration; SAXS, small-angle X-ray scattering; TEM, transmission electron microscopy; ThT, Thioflavin T; WAXS, wide-angle X-ray scattering; λ , rate of primary nucleation and growth.

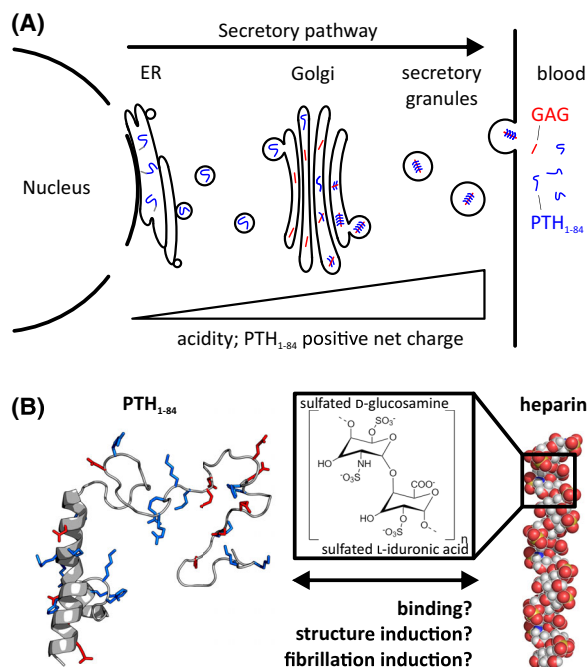


Fig. 1. Research hypothesis based on cellular transport of basic PTH₁₋₈₄ and fibrillation in acidic environments. (A) Illustration of the PTH (blue) passing through the secretory pathway. The pH gradient across the secretory pathway leads to a continuous increase in positive net charge of PTH₁₋₈₄. PTH₁₋₈₄ fibrils are found in acidic secretory granules [9]. GAGs (red) are abundant in the secretory pathway [17,18]. We hypothesize that GAGs interact with PTH₁₋₈₄ and induce its fibrillation. (B) Cartoon representation of PTH₁₋₈₄ based on the PDB entry 1ZWA and a C-terminal disordered region. Charged residues are highlighted in blue (positive) and red (negative). The linear polyanionic heparin consists of repeating sulfated D-glucosamines and L-iduronic acid monosaccharides (black box).

approximately +1.4, it is raised to +5.9 at pH 5.5 [13]. Since PTH₁₋₈₄ is a protein with high structural disorder (Fig. 1B) [14], an increased repulsion between like-charged residues should lead to more extended conformations and enhanced mutual repulsion. Hence, the inherent predisposition for amyloid-prone conformations and the formation of initial amyloid seeds should be affected [15]. Indeed, *in vitro* screening of different buffer conditions revealed that amyloid fibrils form preferably at basic conditions, close to the pI of PTH₁₋₈₄ [14]. This finding contrasts *in vivo* observations of amyloid fibril generation in acidic secretory granules of parathyroid chief cells [9]. Hence, under physiological conditions, fibril formation of PTH₁₋₈₄ requires additional factors to occur. In this study, we tested the hypothesis of a polyanion-assisted fibrillation of PTH₁₋₈₄ by the use of heparin (Fig. 1B), an important and widely used member of the glycosaminoglycan (GAG) family [16]. GAGs are linear

polyanionic polysaccharides that are abundant in the secretory pathway [17,18] and known components of amyloid deposits [19]. Notably, the seminal work of Maji and coworkers in 2009 identified GAGs to be essential for *in vivo* fibrillation of numerous peptides and protein hormones found in secretory granules [7]. To our best knowledge, this aspect has not yet been investigated for the parathyroid system with its hormone PTH₁₋₈₄.

With the help of *in vitro* experiments, we could demonstrate that heparin does not only efficiently bind PTH₁₋₈₄, but also increases its ordered secondary structure content and induces rapid fibrillation even at low physiological pH. Moreover, fibrils formed in the presence of heparin were still capable to release monomeric peptides, a typical characteristic of functional amyloid fibrils. In the absence of heparin, PTH₁₋₈₄ was not able to form fibrils.

Material and methods

Material

PTH₁₋₈₄ was synthesized by the Core Unit Peptide Technologies of the University Leipzig using microwave-assisted solid-phase peptide synthesis (CEM GmbH, Kamp-Lintfurt, Germany) based on Fmoc-strategy. For long peptides as PTH₁₋₈₄, the incorporation of selected pseudoproline leads to products usable for the challenging purification steps after the cleavage from the resin. The successful synthesis of PTH₁₋₈₄ was verified by mass spectrometry. Unfractionated porcine intestinal heparin with an average molecular weight of 20 kDa was sourced from Carl Roth (Carl Roth GmbH, Karlsruhe, Germany). The heparin sulfate analog fondaparinux (pentasaccharide) was sourced from Merck (Merck KGaA, Darmstadt, Germany). Other chemicals were reagent grade and sourced from Sigma-Aldrich (Sigma-Aldrich Chemie GmbH, Schnellendorf, Germany) if not stated otherwise.

Methods

Sample preparation

Lyophilized PTH₁₋₈₄ was dissolved in citrate buffer (20 mM, pH 5.5) or sodium phosphate buffer (50 mM, pH 7.4) and its concentration adjusted *via* UV absorbance at 280 nm ($\epsilon = 5500 \text{ M}^{-1} \cdot \text{cm}^{-1}$). Heparin or fondaparinux were weighed in and dissolved in the same buffer. Desired heparin concentrations were prepared according to its average mass of 20 kDa.

Circular dichroism spectroscopy

UV circular dichroism (CD) measurements were carried out on a Jasco J-810 spectrophotometer (Jasco Deutschland

GmbH, Pfungstadt, Germany) using a 0.01 cm pathlength quartz cuvette (Hellma GmbH & Co. KG, Müllheim, Germany). The PTH₁₋₈₄ concentration was adjusted to 0.1 mM in citrate buffer (20 mM, pH 5.5) or sodium phosphate buffer (50 mM, pH 7.4). Heparin-containing samples were set to a final molar ratio of 1 : 10 (heparin : PTH₁₋₈₄) and incubated for 1 h at 20 °C. As the amplitude of the CD signal of heparin was much smaller compared with PTH₁₋₈₄, we corrected the CD spectra of the solution containing PTH₁₋₈₄ and heparin for eventual heparin contributions by adding equal heparin concentrations in the reference buffer. The exposure time was set to 50 nm·min⁻¹, and spectra were obtained from averaging 64 subsequent measurements at 20 °C after subtracting the reference buffer spectrum.

NMR spectroscopy

2D 1H-15 N HSQC spectra of 100 μM 15 N labeled PTH₁₋₈₄ were recorded on a Bruker Ascend 500 MHz spectrometer at pH 5.5 and 25 °C in the absence and presence of 100 μM fondaparinux. Chemical shift assignments were performed by standard triple resonance experiments based on the published values [20].

Isothermal titration calorimetry

Calorimetric measurements were performed using a Micro-Cal iTC200 (Malvern Panalytical Ltd, Malvern, UK) calorimeter at 25 °C and 750 r.p.m stirring. Titrations of a 125 μM heparin solution into a 150 μM PTH₁₋₈₄ solution, both citrate buffer (20 mM, pH 5.5), were analyzed. The titration regime included an initial 0.5 μL injection and subsequent 39 × 1 μL injections with a time interval of 300 s. The reference cell contained citrate buffer (20 mM, pH 5.5). Thermograms were integrated using NITPIC software (version 1.3.0) [21]. Data fitting was performed using CHASM software with the built-in one-site model and optional use of multi-site models [22].

Wide-angle and small-angle X-ray scattering

All X-ray scattering experiments were performed in transmission mode using a SAXSLAB laboratory setup (Retro-F) equipped with an AXO microfocus X-ray source. The AXO multilayer X-ray optic (AXO Dresden GmbH, Dresden, Germany) was used as a monochromator for Cu-K_α radiation (λ = 0.154 nm). A two-dimensional detector (PILATUS3 R 300 K; DECTRIS, Baden, Switzerland) was used to record the 2D scattering patterns. For wide-angle X-ray scattering (WAXS) experiments, fibrils were formed in citrate buffer (20 mM, pH 5.5) in the presence of heparin (1 : 10 molar ratio). The fibril suspension was ultracentrifuged (200 000 × g, 10 min) and the thus obtained pellet transferred into a ring-shaped aluminum holder (2 mm thick and with a central hole of 1.5 mm diameter) and left

to dry overnight. The scattering measurements were performed at room temperature in vacuum.

Small-angle X-ray scattering (SAXS) experiments were conducted using refillable capillaries with an outer diameter of 1 mm (BioSAS JSP stage, SAXSLAB/Xenocs SAS, Grenoble, France). The intensities were angular-averaged and plotted versus the scattering angle q . The measurements were performed in citrate buffer (20 mM, pH 5.5), at room temperature and corrected for background, transmission and sample geometry. The measurement times of pure heparin and PTH₁₋₈₄ solutions were 10 h. For the time-dependent series of the mixed solution, 12 consecutive measurements of 2 h each were taken. Due to the lower scattering contrast of heparin and, consequently, the need to measure at higher concentrations, we performed experiments at two concentrations (100 μM and 1 mM) with subsequent extrapolation to zero concentration [23]. The data analysis for all measurements included at first the determination of the radius of gyration, R_g , using the Guinier approximation with $\ln(I(q)) \approx R_g^2/3 \cdot q^2$ for the low q -range, $qR_g < 1.3$. Secondly, the intermediate q -range was fitted to access the shapes of the scatterers using suitable form factor descriptions, $P(q)$. For the scattering of PTH₁₋₈₄, a linear polymer model (Debye function) was used [24]:

$$P(q) = \phi(\Delta\rho)^2 2V_c \left(e^{(qR_g)^2} + (qR_g)^2 - 1 \right) / (qR_g)^4, \quad (1)$$

where V_c is the chain's volume of occupation, $\Delta\rho$ the scattering contrast, and ϕ the volume fraction.

For solutions of heparin and heparin with PTH₁₋₈₄, a description of a semiflexible chain, as introduced by Pedersen and Schurtenberger [25,26], gave the best fitting result. The main fitting parameters are the so-called Kuhn length, b , reflecting the stiffness of the chain, the chain's cross-sectional radius, R_c , and the contour length, L , describing the total length of the chain. To strengthen the uniqueness of the description, the parameters were matched with results from other analyses techniques: R_c was additionally derived from the Guinier relation $\ln(I(q)) \cdot q \approx R_{c,g}^2/2 \cdot q^2$ for the q -range $1.5 < qR_{c,g} < 2.1$ with $R_c = \sqrt{2}R_{c,g}$ and found to be concentration independent. The parameter b was determined by the minimum of the plot $I(q) \cdot q^2$ versus q via the relation $b \approx 4.6/q^*$ and subsequent extrapolation to zero concentration [27]. The contour length, L , was also determined by extrapolation, using the concentration-dependent scattering intensities $I(q)$ and $I(q)q$ with $q \rightarrow 0$ [23].

Thioflavin T assay

Thioflavin T (ThT) assays were carried out on a FLUOstar Omega (BMG Labtech GmbH, Ortenberg, Germany) reader using Greiner 96 F-bottom (non-binding) well plates

(Greiner Bio-One GmbH, Frickenhausen, Germany). All experiments were performed at 37 °C. Every 300 s, the ThT fluorescence was monitored at 480 nm with excitation at 450 nm. Samples were shaken with 300 r.p.m for 150 s prior to each excitation. The final sample volume was set to 150 μ L with final concentrations of 150 μ M PTH_{1–84} and 50 μ M ThT in citrate buffer (20 mM, pH 5.5) or sodium phosphate buffer (50 mM, pH 7.4). A series of heparin concentrations (0, 3, 7.5, 15, 30, 150, and 600 μ M) was tested to assess its role in PTH_{1–84} fibrillation. All measurements were done in triplicate with subsequent averaging of the ThT intensities.

Recent molecular rate kinetic descriptions of fibrillar growth enable to disentangle two main fibrillation processes [28]. While primary nucleation describes the generation of structured nuclei in the absence of fibrils, secondary pathways address the generation of nuclei on fibrillar surfaces. Both processes affect the time dependence of the fibrillar growth in a different way and hence, their contributions to the total increase in fluorescence, $\Delta F(t)$, can be analyzed using the function

$$\Delta F(t) = \left(1 - \frac{1}{\frac{\lambda^3}{3\kappa^3} (e^{\kappa t} - 1) + 1} \right) \Delta F_{\text{pl}} \quad (2)$$

where ΔF_{pl} describes the plateau of the fluorescence assay. λ and κ are the rate constants of nucleation and growth for primary and secondary processes, respectively. λ and κ comprise the individual microscopic rates of oligomerization, k_{o1} and k_{o2} , respectively, the rate of conversion of the unstructured oligomers into seeds, k_c , as well as the rate of elongation *via* monomer addition k_+ [29,30]:

$$\lambda = (2k_{o1}k_c k_+ m^{n1})^{1/3}, \kappa = (2k_{o2}k_c k_+ m^{n2+1})^{1/3} \quad (3)$$

The parameter m displays the total mass of the monomers and $n1$ and $n2$ the sizes of the nuclei for each process. In this context, λ would also include heterogeneous seeding, as it might be induced by surfaces.

Transmission electron microscopy

5 μ L of a 20 times dilution of the respective fibrillated sample was transferred to a 200 mesh Formvar/Carbon coated Cu grid (Plano GmbH, Wetzlar, Germany). After 3 min of waiting time, the grids were first cleaned in water for 3×10 s and then negatively stained with 1 percent (w/v) uranyl acetate for a further 60 s. Transmission electron microscopy (TEM) images were taken with an electron microscope (EM 900; Carl Zeiss AG, Oberkochen, Germany) at 80 kV acceleration voltage.

Determination of the critical concentration

PTH_{1–84} fibrils (1 mL of 150 μ M PTH_{1–84} monomer) were formed in the presence of heparin (1 : 10 molar ratio) in pH 5.5 (20 mM citrate) or pH 7.4 (50 mM sodium

phosphate) buffer at 37 °C and 350 r.p.m agitation for 3 h. The chosen incubation time ensured completion of fibril formation. Fibrils were pelleted *via* ultracentrifugation at 200 000 \times g for 10 min. The PTH_{1–84} concentration of the supernatant fraction was determined using UV spectroscopy and taken as the critical concentration, c^* .

Monomer release assay

Fibril pellets were obtained as mentioned above, resuspended in 100 μ L pH 7.4 buffer (50 mM sodium phosphate, 5% mannitol), and subjected to dialysis through 20 k MWCO Slide-A-Lyzer Mini dialysis devices (Fisher Scientific GmbH, Schwerte, Germany) against 1 mL pH 7.4 buffer (50 mM sodium phosphate, 5% mannitol). The protein concentration outside of the dialysis device was determined using UV spectroscopy at several time points.

Results and discussion

Binding of PTH_{1–84} to heparin

Thermodynamics of the interaction

Binding thermodynamics can provide a comprehensive view of the various types of molecular interactions that drive biomolecular association. The thermodynamic feature of the heparin-PTH_{1–84} binding was accessed using isothermal titration calorimetry (ITC), which detects the heat absorbed or released along the reaction coordinate. The resulting binding isotherm, as shown in Fig. 2A, can be used to determine the enthalpy, Gibbs free energy as well as stoichiometry of binding. Using a model description of independent identical binding sites, we found the equilibrium constant of dissociation, K_D , to be (213 ± 29) nM and the stoichiometry of binding to be $n = 0.09 \pm 0.01$ corresponding to 11 PTH_{1–84} molecules per heparin molecule. The negative isotherms generated by the interaction of PTH_{1–84} with heparin correspond to an exothermic binding event with a Gibbs free energy change, ΔG , of (-38.0 ± 0.3) kJ·mol⁻¹. The changes in enthalpy, ΔH , and entropy, ΔS are (-72.5 ± 1.0) kJ·mol⁻¹ and (0.89 ± 0.01) kJ mol⁻¹·K⁻¹, respectively. The here determined Gibbs free energy change is in very good agreement with a previously published value of -37 kJ·mol⁻¹ of Kamerzell et al. [31], who used unfractionated heparin with an average mass of 12–16 kDa compared with the larger 20 kDa heparin used in this study. While the different sizes of heparin did not seem to alter ΔG , we found the stoichiometry of binding to scale linearly with the size of the heparin molecules. While heparin molecules of the size of 20 kDa (this study) revealed a binding ratio of about 11 proteins per heparin molecule, Kamerzell et al. found in their experiments that

one 12–16 kDa heparin molecule can bind about 8 PTH₁₋₈₄ molecules. Hence, assuming an average mass of a disaccharide unit of 533 Da, one protein binds roughly 3 disaccharide units of heparin. This finding supports the beads on a string model, as previously suggested in the context of other heparin-protein systems [32,33]. Notably, a minor enthalpic deviation of about 20 kJ·mol⁻¹ is apparent at low ligand (heparin) concentrations and could be explained by a second binding process of a higher affinity but smaller exothermic enthalpy [22]. Multi-site approaches, however, yielded a high fitting error and could not be applied.

Induction of secondary structure

Circular dichroism spectroscopy was used to compare the relative secondary structure content of PTH₁₋₈₄ in citrate buffer (20 mM, pH 5.5) in the absence and presence of heparin (see Fig. 2B). In its unbound state, PTH₁₋₈₄ gave rise to a CD spectrum with pronounced negative ellipticities close to 200 nm and a shallow minimum around 222 nm. This characteristic is typical for intrinsically disordered proteins with contributions from transient α -helices [34] and matches structural data of several PTH constructs obtained *via* X-ray crystallography and nuclear magnetic resonance spectroscopy [35–37]. In the presence of heparin, a very different CD spectrum was obtained with a loss of negative ellipticity around 200 nm and significantly stronger contribution of negative ellipticity in the range spanning 210–230 nm. Since irregular peptide structures show relatively low optical activity in the latter wavelength range, the CD spectrum suggests an increase in ordered secondary structure elements of PTH₁₋₈₄ that is governed by the interaction with heparin. The CD spectrum analysis tool BeStSel [38] revealed an enhanced α -helical content in the presence of heparin (12% without heparin, 33% with heparin) accompanied by a decrease in β -strand content (25% without heparin, 13% with heparin, see Fig. S1). Comparing pH 7.4 to pH 5.5, a similar structural content of PTH₁₋₈₄ was found, but the change in secondary structure upon heparin binding was less pronounced for pH 7.4. Based on these results it can be concluded that the polyanion heparin does not only bind PTH₁₋₈₄ at low pH, while presumably screening its positive charges, but importantly also induce a change in the ordered secondary structure content.

Size and shape of heparin-PTH₁₋₈₄ associates

Small-angle X-ray scattering experiments allow to study sizes, shapes, and mutual interactions of dissolved particles and are used to investigate the

molecular arrangement of PTH₁₋₈₄ with heparin. Figure 2C displays absolute scattering intensities of solutions of PTH₁₋₈₄ and heparin (1 : 10 molar ratio), prior and after mixing. The scattering intensity profile of PTH₁₋₈₄ (black data set of Fig. 2C) agreed with the simple polymer model of a flexible chain as given by Eq. 1, yielding a radius of gyration, R_g , of (2.9 ± 0.5) nm. The applicability of this model depicts the disordered feature of the protein. In contrast to PTH₁₋₈₄, the shape of the heparin molecules (gray dataset) could be described by a semiflexible chain with a Kuhn length, b , of (19.2 ± 0.7) nm and a contour length, L , of approx. 30 nm, in agreement with literature values [23,27]. While L describes the average length of the heparin backbone, b reflects the length scale of the chain's stiffness. The radius of the chain's cross-section, R_c , is (0.45 ± 0.03) nm. Immediately after the addition of PTH₁₋₈₄, the scattering intensity of the heparin solution increased by two orders of magnitude (see the red data set of Fig. 2C). Again, according to the model of a semiflexible chain, a reasonable agreement could be achieved, without changing b or L of the aforementioned description (red line in Fig. 2C). Only the cross-section of the chain increased significantly from $R_c = (0.45 \pm 0.03)$ nm to (5.3 ± 0.2) nm, supporting the earlier mentioned beads on a string model as sketched in Fig. 2D.

With time, the scattering intensities of the described chains displayed a slightly increased scattering intensity at low q values, eventually reaching a plateau after 22 h (see colored data sets in Fig. 2C). The exponent of the arising power-law dependence, $I(q) \sim q^D$, can be interpreted as the dimension, D , of a mass fractal. We found D to be 2.04, characteristic for a diffusion-limited aggregation with a preferred growth at the tips and thus reduced branching [39]. This slow and preferably linear growth of PTH₁₋₈₄-heparin constructs can be taken as a first indication for a process of fibrillar growth.

Fibrillation properties

Since PTH₁₋₈₄ needs to undergo at least a partial conformational transition from α -helices to β -strands to form cross- β -structured amyloid fibrils [14], we monitored the growth process using the structure-sensitive fluorescent dye Thioflavin T that binds to β -sheet surfaces along motifs formed by cross- β strand ladders (see Fig. 3A). In the absence of heparin, the ThT fluorescence remained at a low level throughout the measurement indicating that any potential buildup of fibrils was below the detection limit. Even after 70 h of incubation at an elevated temperature of 37 °C and

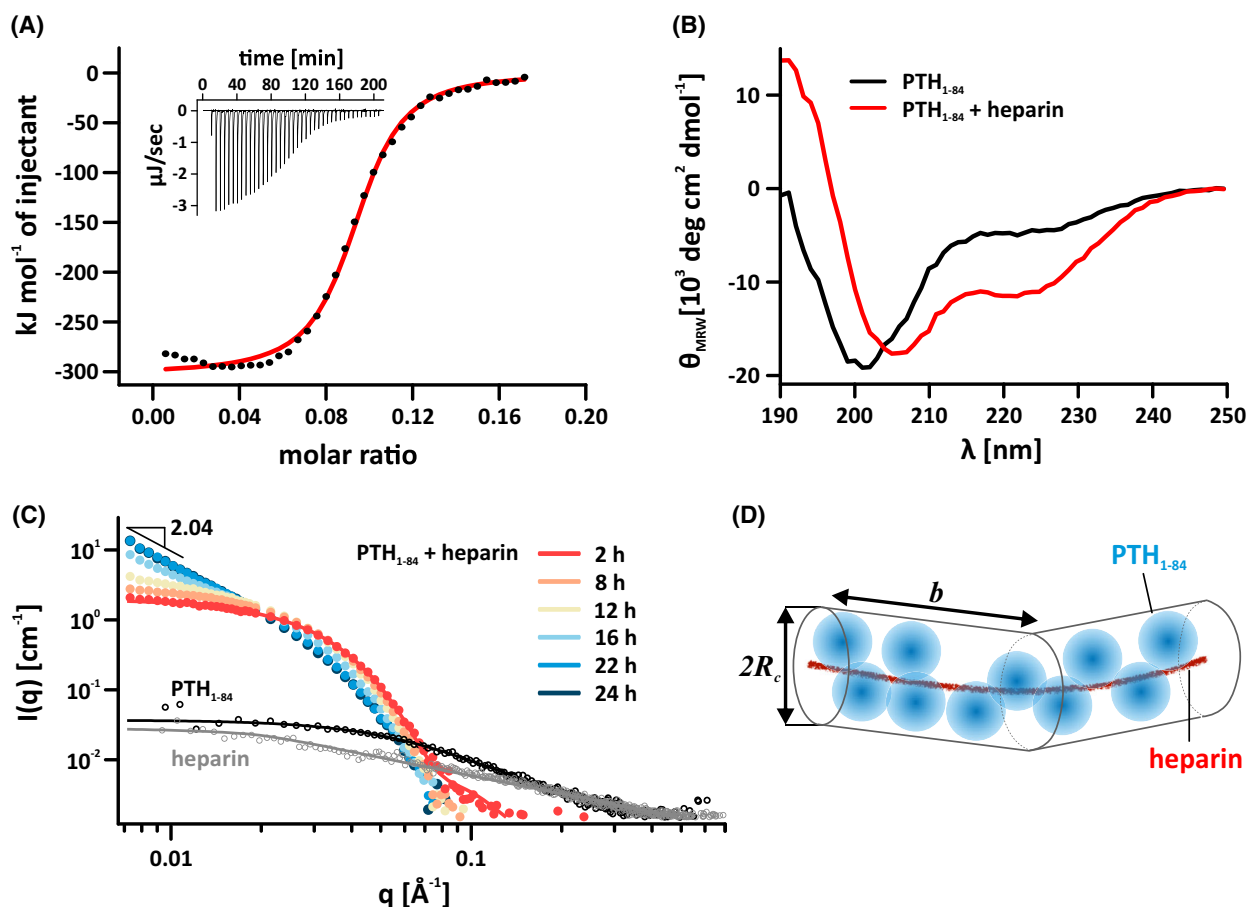


Fig. 2. Heparin binds PTH₁₋₈₄ and induces structure and aggregation. (A) Isothermal titration calorimetric data of PTH₁₋₈₄ with heparin as displayed by the integrated heat plot (dots) together with a single-site ligand-binding model fit (red line). The x-axis gives the molar ratio of heparin versus PTH₁₋₈₄. Inset: The raw titration data of the heat resulting from each injection of heparin into the PTH₁₋₈₄ solution. (B) CD spectrum of 100 μM PTH₁₋₈₄ in the absence (black) and presence of heparin (1 : 10 molar ratio heparin : PTH₁₋₈₄, red line). The latter was corrected for heparin contributions. (C) SAXS intensities of heparin (gray symbols), PTH₁₋₈₄ (black symbols) and a 1 : 10 molar ratio heparin : PTH₁₋₈₄ solution at different times after mixing (red to blue symbols). Lines represent adapted linear chain model functions and are described in the text. (D) Scheme of the initial PTH₁₋₈₄ binding to a single heparin molecule, as described by the model of a semiflexible linear chain (red data set in C). All measurements were performed in citrate buffer (20 mM, pH 5.5).

with orbital shaking, the fluorescence level remained virtually unchanged. Subsequent centrifugation of the sample did not yield a noticeable precipitate, suggesting that PTH₁₋₈₄ remained in its soluble, monomeric state. Conversely, PTH₁₋₈₄ rapidly formed fibrils when heparin was present with ThT plateau intensities that initially increased with heparin concentration and eventually saturated (Fig. 3C, top graph). The latter could be evidence for possible binding of heparin to the fibrillar surfaces as it was observed for fibrils of the amyloid beta peptide [40].

Notably, the initial lag phase was passing a minimum value of 0.6 h at heparin concentrations of 15 μM and 30 μM (1 : 10 and 1 : 5 ratio of heparin: PTH₁₋₈₄) indicative for a more complex interplay of

aggregation processes than simple seeding. Seeding would solely lead to a concentration-dependent decrease in the lag times [41].

To infer more information regarding the dominating processes of fibrillation, we analyzed the data with respect to the total rates of primary and secondary fibrillation pathways, λ and κ, as given by Eq. 2. The fitting results are displayed in the normalized data set of Fig. 3B and the derived values of λ and κ are given in Fig. 3C, bottom graph. While λ reflects the generation of structured nuclei in the absence of fibrils, κ addresses the generation of nuclei on the surface of the growing fibrillar phase. It is important to mention that both rates comprise not only their specific microscopic rates of nucleation but also the more general rate of

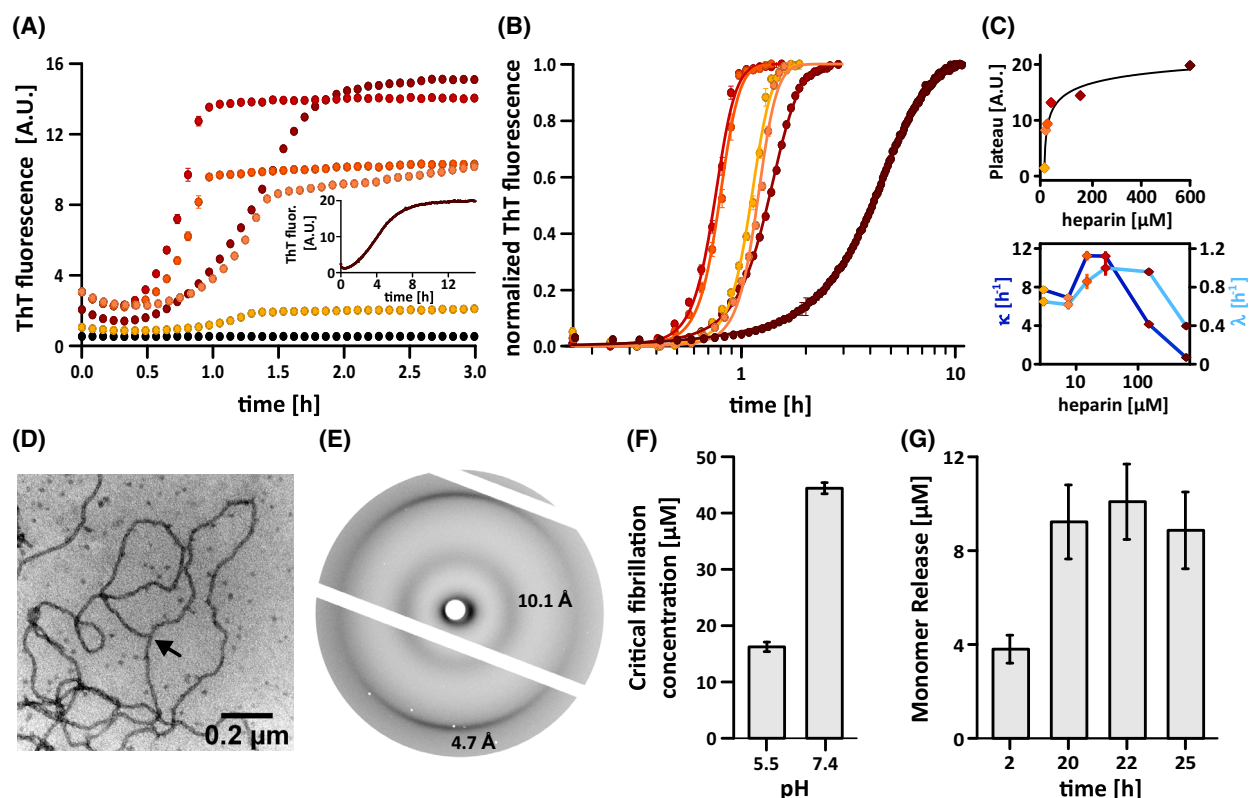


Fig. 3. Heparin induces rapid PTH₁₋₈₄ fibrillation. (A) ThT fluorescence was used to monitor fibrillation of PTH₁₋₈₄ (150 μM, 37 °C, 300 r.p.m orbital shaking) at several heparin concentrations [black—no heparin; yellow—3 μM; light orange—7.5 μM; orange—15 μM; red—30 μM; dark red—150 μM; purple (inset)—600 μM]. Solely in the presence of heparin, the ThT fluorescence increased significantly over time reaching plateau values that were depending on heparin concentration (see C top graph). Data points were averaged from triplicates and shown with standard deviation error bars. (B) Normalization of the ThT fluorescence (symbols) and subsequent fitting using Eq. 2 (lines) yielded heparin-dependent nucleation and growth rates λ (primary fibrillation pathways) and κ (secondary fibrillation pathways). (C) The plateau intensities (top graph) and λ and κ values (bottom graph) were dependent on heparin concentration. (D) Transmission electron microscope images of PTH₁₋₈₄ fibrils displayed a curvilinear structure with fibrillar branching (arrow). (E) X-ray diffraction of PTH₁₋₈₄ fibrils formed in the presence of heparin at pH 5.5. Reflections at 4.7 Å and 10.1 Å were consistent with a cross-β structure. (F) At pH 5.5, the critical concentration for fibril formation is reduced compared with pH 7.4. Fibrillation was induced with 1 : 10 molar ratio heparin:PTH₁₋₈₄. Data points were averaged from triplicates with standard deviation error bars shown. (G) PTH₁₋₈₄ fibrils formed in the presence of heparin at pH 5.5 release monomers in a time-dependent manner. Data points were averaged from triplicates with standard deviation error bars shown.

fibrillar growth *via* monomer addition (see Eq. 3). For concentrations below the critical molar ratio of 1 : 10 (heparin : PTH₁₋₈₄), one can expect that not all of the PTH₁₋₈₄ molecules are bound to heparin. For low concentrations (up to 7.5 μM, 1 : 20 ratio), we found both rates to not depend on heparin concentration. Higher heparin concentrations caused both rates to increase until a plateau of about 150% of their initial values was reached. The significant increase of κ implies that heterogeneous seeding, meaning that heparin molecules act as seeds on their own, cannot be the leading mechanism by which heparin induces fibrillation. Heterogeneous seeding would affect λ only and, hence, lead to an increase in the so-called nucleation-to-growth factor $\lambda^3/3\kappa^3$ of Eq. 2. This factor was not only small,

indicative for reactions in which the nucleation step is rate-limiting [42], but also independent from the heparin concentration with, for example, $(2.0 \pm 0.2) \cdot 10^{-4}$ for the 1 : 50 molar ratio and $(1.5 \pm 0.3) \cdot 10^{-4}$ for the 1 : 10 molar ratio (heparin : PTH₁₋₈₄). Hence, the experimental determined increase in the overall rate could either originate from an increased rate of structural conversion into seeds, or fibrillar growth (k_c or k_+ of Eq. 3). If the latter would be true, λ and κ should be still enhanced at higher heparin concentrations, at which most of the PTH₁₋₈₄ molecules are bound to heparin. However, at heparin concentrations above the critical molar ratio of 1 : 10, we observed a plateau of λ and κ followed by a decrease (see Fig. 3C), meaning that heparin-bound PTH₁₋₈₄ can form primary and

secondary seeds but cannot contribute to the fibrillar growth as growth seems to require unbound PTH₁₋₈₄-molecules. Hence, the leading mechanism of heparin at high and low concentrations is the structural conversion of bound PTH₁₋₈₄ into amyloid-prone seeds. The morphology and structure of the mature PTH₁₋₈₄ fibrils were confirmed by electron microscopy (Fig. 3D) and X-ray diffraction (Fig. 3E). The TEM images displayed long and slightly curved fibrils of about 16 nm thickness. Branching was very rarely observed, which agrees well with the fractal dimension from the scattering experiments. WAXS experiments confirmed the cross- β sheet structure of the fibrils with characteristic reflections at 4.7 Å and 10.1 Å (Fig. 3E) [14].

The interactions of heparin/GAG with proteins are known to be dominated by electrostatics [43]. Since the charge state of PTH₁₋₈₄ is sensitive toward changes in the physiological pH range, we asked if variations in pH conditions influence fibrillation efficiency. We incubated PTH₁₋₈₄ and heparin at 37 °C for 3 h in buffers adjusted to pH 5.5 or pH 7.4 and pelleted the fibrillar content *via* ultracentrifugation (more details in material and methods). As a control, by omitting the incubation, we could confirm that heparin-PTH₁₋₈₄ complexes formed immediately after mixing could not be pelleted by ultracentrifugation, indicating that fibrils formed after 3 h are the main species pelleted. The remaining protein concentration in the supernatant should approximate the critical concentration for fibril formation assuming basic thermodynamic principles [42]. Following the described procedure, we found the critical concentrations for fibril formation, c^* , to be about 2.6-fold higher at pH 7.4 compared with pH 5.5 (Fig. 3F). This finding would imply that the conversion of monomers into fibrils is more efficient at low pH. In order to validate this finding, we additionally compared the plateau intensities of the ThT assays. Based on the crystallization model of Finke and Watzky [42], plateau values of ThT assays, ΔF_{pl} , are not only directly correlated to the fibrillar mass but also to the supersaturation of the solution, $\sigma = (c - c^*)/c^*$ [42]. These considerations lead to the equation:

$$c_{\text{pH}7.4}^*/c_{\text{pH}5.5}^* \approx c/c_{\text{pH}5.5}^* - \left(\Delta F_{\text{pl}}^{\text{pH}7.4} / \Delta F_{\text{pl}}^{\text{pH}5.5} \right) \left(c/c_{\text{pH}5.5}^* - 1 \right),$$

where c is the total protein concentration of the experiment. Using the experimentally derived value $c_{\text{pH}5.5}^*$ of 17 μM and the independently obtained ThT plateau intensities of the PTH₁₋₈₄ fibrillation (see Fig. S2), these considerations would lead to a ratio $c_{\text{pH}7.4}^*/c_{\text{pH}5.5}^*$ of 3.2. This value is slightly larger than from the above-mentioned ultracentrifugation experiments, but in the same range. The difference could originate, for

example, from surface charges that are present at low pH and modify the interaction of ThT with fibrils [44]. Possible pH-dependent spectral changes in ThT were considered by control measurements. Surprisingly, the obtained ratio of the critical concentrations would be equivalent to just a small additional gain in free energy of $\Delta(\Delta G) \approx 2.6 - 2.8 \text{ kJ}\cdot\text{mol}^{-1}$ according to the relation $\Delta(\Delta G) = -RT \ln(c_{7.4}^*/c_{5.5}^*)$. Hence, lowering the pH leads to a small, but significant change in ΔG compared with the total gain of free energy for amyloid fibrillation that is about 30–50 $\text{kJ}\cdot\text{mol}^{-1}$ [45].

The described pH dependence points to a mainly charge-driven interaction of heparin with PTH₁₋₈₄ that is modulated by the protonation state of the four histidine residues within the peptide chain. Due to their unique pK_{A} value close to the physiological pH ($\text{pH} \approx 6.2$), histidine side chains are mainly protonated at pH 5.5 while unprotonated at pH 7.4. Therefore, histidines display a pH-dependent switch-like property that is key in many biochemical processes including pH sensoric function [46,47]. This switch-like property has previously been identified to modulate protein–GAG interactions [48].

However, even accounting for protonated histidines, PTH₁₋₈₄ lacks a classical heparin-binding consensus sequence (XBBXB and XBBBXXB, where B is a basic residue and X is a hydrophobic residue) [49]. Importantly though, heparin-binding proteins lacking these particular amino acid sequences are well known [50]. They may instead bind heparin through a structurally similar binding motif, in which the involved residues are spatially close but may be distant in the primary sequence [50]. This binding modality seems particularly intriguing in the case of the largely disordered PTH₁₋₈₄, which might dynamically adopt a high-affinity heparin-binding state with particular amino acids arranged in a structural heparin-binding motif. At low pH, this structural binding motif might be partially formed by protonated histidines within PTH₁₋₈₄, while being interrupted when histidines are unprotonated at neutral pH. Similarly, it has already been reported that seemingly minute differences in the sequence of peptides can have significant effects on the GAG-mediated fibril formation [51].

To get a more detailed view on the binding sites of PTH₁₋₈₄ for GAGs, we recorded a residue resolved 2D NMR experiment in the presence and absence of fondaparinux (Fig. S3). Fondaparinux is a pentameric heparin sulfate analog with a well-defined molecular weight of 1728 Da and suitable in size for NMR spectroscopy [52]. We observed binding within the first 40 residues, which contain H10, K13, H14, R20, R25,

K26, K27, and H32 with the latter four residues contributing to the fibrillar core [14]. Additionally, the positive stretch R52, K53, and K54 reported binding. Along this line, our data indicate that PTH_{1–84} fibrillation in the presence of heparin does not only overcome fibrillation retarding side chain protonation due to charge repulsion, but results even in a remarkably higher fibrillation efficiency compared with neutral pH.

Monomer release of PTH_{1–84} fibrils

Functional amyloid fibrils typically are reversible structures capable of releasing monomers in solution [53–56]. Various structures of PTH and related peptides in complex with their target receptor PTH1R show a protrusion of the ligand deep into a tight cavity of the receptor [57–59]. Hence, it is likely that monomeric PTH_{1–84} is required for receptor stimulation. We tested whether PTH_{1–84} fibrils formed at pH 5.5 in the presence of heparin-released monomers in a neutral pH buffer. We used a dialysis approach with a cutoff filter of 20 k MWCO to let PTH_{1–84} monomers pass the membrane and dialyzed against buffer adjusted to pH 7.4 to resemble the blood pH (see Method section). Under these conditions, we found the PTH_{1–84} monomer concentration outside of the dialysis membrane increasing over time (Fig. 3F), suggesting a time-dependent monomer release. This is in accordance with similar functional amyloid [53,60] and confirms an earlier report by Gopalswamy et al., [14] who found PTH_{1–84} fibrils to release monomers in a similar manner.

In summary, a major goal of our *in vitro* experiments was to mimic two key environmental properties that may affect the fibrillation of PTH_{1–84} in the cellular context (Fig. 1A): We adjusted the pH to a moderately acidic value (pH 5.5) to approximate the conditions in which PTH_{1–84} fibrils are supposed to form *in vivo*. We combined the low pH conditions with the addition of heparin, as the Golgi apparatus is the major site for the synthesis of GAGs. The use of the GAG heparin allowed us to study the effect of a polyanionic linear macromolecule that is in close resemblance of what PTH_{1–84} might interact with during intracellular transport.

Under the conditions tested, we found that the largely intrinsically disordered PTH_{1–84} binds with a sub-micromolar affinity to heparin and heparin is indispensable for rapid PTH_{1–84} fibril formation. Strikingly, binding to heparin changed not only the ordered secondary structure content and induced fibrillation, but enabled even more efficient fibrillation at low pH

compared with neutral pH. Notably, the mean β -strand content as determined by CD spectroscopy did not correlate with individual seeding capabilities (comparison of PTH_{1–84} free and bound to heparin at low pH) nor fibrillation efficiencies (comparison of PTH_{1–84} fibrillation with heparin at high and low pH) for heparin-PTH_{1–84} associates. This finding underscores the importance of heparin or equivalent polyanionic structures and their interactions during protein assembly.

The enhanced kinetic of fibrillation in the presence of heparin is consistent with the potentially short lifetime of the peptide hormone in the cells as indicated by previously conducted pulse-chase experiments that show a cellular secretion of PTH_{1–84} as soon as 30 min after its translation [61,62]. This is in line with the general properties of functional amyloids, which need to form more rapidly compared with disease-associated fibrils [63]. Mechanistically, heparin forms a semiflexible chain assembly decorated with several PTH_{1–84} molecules, which induces fibril formation by enhancing primary and secondary nucleation pathways likewise. The heparin-assisted fibrillar growth at low pH further suggests that PTH_{1–84} fibril formation might follow a similar mechanism in the cellular context possibly relying on endogenous GAGs or glycosylated proteins. This is further supported by earlier studies which revealed that PTH_{1–84} is co-stored and co-secreted with proteoglycans [62,64]. The high efficiency of fibril formation as indicated by a reduced critical fibrillation concentration at the lower pH suggests that the polyanion-driven PTH_{1–84} fibrillation is enhanced under pH conditions present in later stages of the secretory pathway, for example, the trans-Golgi network and secretory granules. The pH sensitivity of this process might have a regulating function for sorting and further transport of PTH_{1–84}. A regulatory role of the GAG-assisted formation of functional amyloid fibrils in the secretory pathway was previously proposed [7].

Acknowledgements

The authors acknowledge funding by the German Science Foundation (DFG) under Project No. 391498659 (RTG 2467) and Project No. 189853844 (CRC TRR 102). The authors thank for the kind experimental support of Stephan M. Feller of the Institute of Molecular Medicine of the Martin-Luther University Halle-Wittenberg (ITC) and of Thomas Thurn-Albrecht of the Institute of Physics of the Martin-Luther University Halle-Wittenberg (SAXS).

Author contributions

MO and LL designed the research and wrote the manuscript. LL performed the majority of the experimental work and data analysis, NMR and TEM experiments were performed and analyzed by BV, SAXS experiments were conducted by TB, LM provided the expertise for ITC experiments. MO and JB supervised experiments, data analysis and discussion. All authors reviewed the results and approved the final version of the manuscript.

Data accessibility

Data are available on request from the authors.

References

- Habener JF, Rosenblatt M, Potts JTT. Parathyroid hormone: biochemical aspects of biosynthesis, secretion, action, and metabolism. *Physiol Rev.* 1984;**64**:985–1053.
- Usdin TB. The PTH2 receptor and TIP39: a new peptide–receptor system. *Trends Pharmacol Sci.* 2000;**21**:128–30.
- Jüppner H, Abou-Samra A-B, Freeman M, Kong XF, Schipani E, Richards J, et al. A G protein-linked receptor for parathyroid hormone and parathyroid hormone-related peptide. *Science.* 1991;**254**:1024–6.
- Gensure RC, Gardella TJ, Jüppner H. Parathyroid hormone and parathyroid hormone-related peptide, and their receptors. *Biochem Biophys Res Commun.* 2005;**328**:666–78.
- Michael DJ, Cai H, Xiong W, Ouyang J, Chow RH. Mechanisms of peptide hormone secretion. *Trends Endocrinol Metab.* 2006;**17**:408–15.
- Paroutis P, Touret N, Grinstein S. The pH of the secretory pathway: measurement, determinants, and regulation. *Physiology.* 2004;**19**:207–15.
- Maji SK, Perrin MH, Sawaya MR, Jessberger S, Vadodaria K, Rissman RA, et al. Functional amyloids as natural storage of peptide hormones in pituitary secretory granules. *Science.* 2009;**325**:328–32.
- Dannies PS. Prolactin and growth hormone aggregates in secretory granules: the need to understand the structure of the aggregate. *Endocr Rev.* 2012;**33**:254–70.
- Anderson TJ, Ewen SWB. Amyloid in normal and pathological parathyroid glands. *J Clin Pathol.* 1974;**27**:656–63.
- Furukawa K, Aguirre C, So M, Sasahara K, Miyanoiri Y, Sakurai K, et al. Isoelectric point-amyloid formation of α -synuclein extends the generality of the solubility and supersaturation-limited mechanism. *Curr Res Struct Biol.* 2020;**2**:35–44.
- Nespoovitaya N, Gath J, Barylyuk K, Seuring C, Meier BH, Riek R. Dynamic assembly and disassembly of functional β -endorphin amyloid fibrils. *J Am Chem Soc.* 2016;**138**:846–56.
- Marek PJ, Patsalo V, Green DF, Raleigh DP. Ionic strength effects on amyloid formation by amylin are a complicated interplay among Debye screening, ion selectivity, and Hofmeister effects. *Biochemistry.* 2012;**51**:8478–90.
- Calculated using the Protein Tool protpi. [cited 2021 May 8]. Available from: <https://www.protpi.ch/Calculator/ProteinTool>
- Gopalswamy M, Kumar A, Adler J, Baumann M, Henze M, Kumar ST, et al. Structural characterization of amyloid fibrils from the human parathyroid hormone. *Biochim Biophys Acta.* 2015;**1854**:249–57.
- Priyadarshini M, Bano B. Conformational changes during amyloid fibril formation of pancreatic thiol proteinase inhibitor: effect of copper and zinc. *Mol Biol Rep.* 2012;**39**:2945–55.
- Lima M, Rudd T, Yates E. New applications of heparin and other glycosaminoglycans. *Molecules.* 2017;**22**:749.
- Dick G, Akslen-Hoel LK, Grøndahl F, Kjos I, Prydz K. Proteoglycan synthesis and golgi organization in polarized epithelial cells. *J Histochem Cytochem.* 2012;**60**:926–35.
- Prydz K. Determinants of glycosaminoglycan (GAG) structure. *Biomolecules.* 2015;**5**:2003–22.
- Wall JS, Richey T, Stuckey A, Donnell R, Macy S, Martin EB, et al. In vivo molecular imaging of peripheral amyloidosis using heparin-binding peptides. *Proc Natl Acad Sci U S A.* 2011;**108**:E586–94.
- Kumar A, Gopalswamy M, Wishart C, Henze M, Eschen-Lippold L, Donnelly D, et al. N-terminal phosphorylation of parathyroid hormone (PTH) abolishes its receptor activity. *ACS Chem Biol.* 2014;**9**:2465–70.
- Keller S, Vargas C, Zhao H, Piszczek G, Brautigam CA, Schuck P. High-precision isothermal titration calorimetry with automated peak-shape analysis. *Anal Chem.* 2012;**84**:5066–73.
- Le VH, Buscaglia R, Chaires JB, Lewis EA. Modeling complex equilibria in isothermal titration calorimetry experiments: thermodynamic parameters estimation for a three-binding-site model. *Anal Biochem.* 2013;**434**:233–41.
- Pavlov G, Finet S, Tatarenko K, Korneeva E, Ebel C. Conformation of heparin studied with macromolecular hydrodynamic methods and X-ray scattering. *Eur Biophys J.* 2003;**32**:437–49.
- Roe RJ. Methods of X-ray and neutron scattering in polymer science. New York: Oxford University Press; 2000.
- Pedersen JS, Schurtenberger P. Scattering functions of semiflexible polymers with and without excluded volume effects. *Macromolecules.* 1996;**29**:7602–12.

- 26 Chen W-R, Butler PD, Magid LJ. Incorporating Intermicellar interactions in the fitting of SANS data from cationic wormlike micelles. *Langmuir*. 2006;**22**:6539–48.
- 27 Khorramian B, Stivala S. Small-angle x-ray scattering of high- and low-affinity heparin. *Arch Biochem Biophys*. 1986;**247**:384–92.
- 28 Meisl G, Rajah L, Cohen SAI, Pfammatter M, Šarić A, Hellstrand E, et al. Scaling behaviour and rate-determining steps in filamentous self-assembly. *Chem Sci*. 2017;**8**:7087–97.
- 29 Michaels TCT, Šarić A, Curk S, Bernfur K, Arosio P, Meisl G, et al. Dynamics of oligomer populations formed during the aggregation of Alzheimer's A β 42 peptide. *Nat Chem*. 2020;**12**:445–51.
- 30 Dear AJ, Michaels TCT, Meisl G, Klenerman D, Wu S, Perrett S, et al. Kinetic diversity of amyloid oligomers. *Proc Natl Acad Sci U S A*. 2020;**117**:12087–94.
- 31 Kamerzell TJ, Joshi SB, Mcclean D, Peplinskie L, Toney K, Papac D, et al. Parathyroid hormone is a heparin/polyanion binding protein: binding energetics and structure modification. *Protein Sci*. 2007;**16**:1193–203.
- 32 Venkataraman G, Sasisekharan V, Herr AB, Ornitz DM, Waksman G, Cooney CL, et al. Preferential self-association of basic fibroblast growth factor is stabilized by heparin during receptor dimerization and activation. *Proc Natl Acad Sci U S A*. 1996;**93**:845–50.
- 33 Kuschert GSV, Coulin F, Power CA, Proudfoot AEI, Hubbard RE, Hoogewerf AJ, et al. Glycosaminoglycans interact selectively with chemokines and modulate receptor binding and cellular responses. *Biochemistry*. 1999;**38**:12959–68.
- 34 Kelly SM, Jess TJ, Price NC. How to study proteins by circular dichroism. *Biochim Biophys Acta*. 2005;**1751**:119–39.
- 35 Chen Z, Xu P, Barbier J-R, Willick G, Ni F. Solution structure of the osteogenic 1–31 fragment of the human parathyroid hormone. *Biochemistry*. 2000;**39**:12766–77.
- 36 Marx UC, Adermann K, Bayer P, Forssmann W-G, Rösch P. Solution structures of human parathyroid hormone fragments hPTH(1–34) and hPTH(1–39) and bovine parathyroid hormone fragment bPTH(1–37). *Biochem Biophys Res Commun*. 2000;**267**:213–20.
- 37 Jin L, Briggs SL, Chandrasekhar S, Chirgadze NY, Clawson DK, Schevitz RW, et al. Crystal structure of human parathyroid hormone 1–34 at 0.9-Å resolution. *J Biol Chem*. 2000;**275**:27238–44.
- 38 Micsonai A, Bulyáki E, Kardos J. BeStSel: from secondary structure analysis to protein fold prediction by circular dichroism spectroscopy. *Methods Mol Biol*. 2021;**2199**:175–89.
- 39 Nicolás-Carlock JR, Carrillo-Estrada JL. A universal dimensionality function for the fractal dimensions of Laplacian growth. *Sci Rep*. 2019;**9**:1120.
- 40 Madine J, Pandya MJ, Hicks MR, Rodger A, Yates EA, Radford SE, et al. Site-specific identification of an A β fibril-heparin interaction site by using solid-state NMR spectroscopy. *Angew Chem Int Ed*. 2012;**51**:13140–3.
- 41 Cukalevski R, Yang X, Meisl G, Weininger U, Bernfur K, Frohm B, et al. The A β 40 and A β 42 peptides self-assemble into separate homomolecular fibrils in binary mixtures but cross-react during primary nucleation. *Chem Sci*. 2015;**6**:4215–33.
- 42 Crespo R, Rocha FA, Damas AM, Martins PM. A generic crystallization-like model that describes the kinetics of amyloid fibril formation. *J Biol Chem*. 2012;**287**:30585–94.
- 43 Lander AD. Targeting the glycosaminoglycan-binding sites on proteins. *Chem Biol*. 1994;**1**:73–8.
- 44 Arad E, Green H, Jelinek R, Rapaport H. Revisiting thioflavin T (ThT) fluorescence as a marker of protein fibrillation – the prominent role of electrostatic interactions. *J Colloid Interface Sci*. 2020;**573**:87–95.
- 45 Baldwin AJ, Knowles TPJ, Tartaglia GG, Fitzpatrick AW, Devlin GL, Shamma SL, et al. Metastability of native proteins and the phenomenon of amyloid formation. *J Am Chem Soc*. 2011;**133**:14160–3.
- 46 Mideros-Mora C, Miguel-Romero L, Felipe-Ruiz A, Casino P, Marina A. Revisiting the pH-gated conformational switch on the activities of HisKA-family histidine kinases. *Nat Commun*. 2020;**11**:769.
- 47 Wu W, Celma CC, Kerviel A, Roy P. Mapping the pH sensors critical for host cell entry by a complex nonenveloped virus. *J Virol*. 2019;**93**:e01897–18.
- 48 Elimova E, Kisilevsky R, Ancsin JB. Heparan sulfate promotes the aggregation of HDL-associated serum amyloid a: evidence for a proamyloidogenic histidine molecular switch. *FASEB J*. 2009;**23**:3436–48.
- 49 Cardin AD, Weintraub HJ. Molecular modeling of protein-glycosaminoglycan interactions. *Arteriosclerosis*. 1989;**9**:21–32.
- 50 Muñoz EM, Linhardt RJ. Heparin-binding domains in vascular biology. *Arterioscler Thromb Vasc Biol*. 2004;**24**:1549–57.
- 51 Jha NN, Anoop A, Ranganathan S, Mohite GM, Padinhateeri R, Maji SK. Characterization of amyloid formation by glucagon-like peptides: role of basic residues in heparin-mediated aggregation. *Biochemistry*. 2013;**52**:8800–10.
- 52 Gao Q, Yang J-Y, Moremen KW, Flanagan JG, Prestegard JH. Structural characterization of a heparan sulfate pentamer interacting with LAR-Ig1-2. *Biochemistry*. 2018;**57**:2189–99.
- 53 Jackson MP, Hewitt EW. Why are functional amyloids non-toxic in humans? *Biomolecules*. 2017;**7**:71.
- 54 Jacob RS, Das S, Ghosh S, Anoop A, Jha NN, Khan T, et al. Amyloid formation of growth hormone in presence of zinc: relevance to its storage in secretory granules. *Sci Rep*. 2016;**6**:23370.

- 55 Anoop A, Ranganathan S, Dhaked BD, Jha NN, Pratihari S, Ghosh S, et al. Elucidating the role of disulfide bond on amyloid formation and fibril reversibility of Somatostatin-14. *J Biol Chem*. 2014;**289**:16884–903.
- 56 Maji SK, Schubert D, Rivier C, Lee S, Rivier JE, Riek R. Amyloid as a depot for the formulation of long-acting drugs. *PLoS Biol*. 2008;**6**:e17.
- 57 Zhao L-H, Ma S, Sutkeviciute I, Shen DD, Zhou XE, de Waal PW, et al. Structure and dynamics of the active human parathyroid hormone receptor-1. *Science*. 2019;**364**:148–53.
- 58 Pioszak AA, Xu HE. Molecular recognition of parathyroid hormone by its G protein-coupled receptor. *Proc Natl Acad Sci U S A*. 2008;**105**:5034–9.
- 59 Pioszak AA, Parker NR, Gardella TJ, Xu HE. Structural basis for parathyroid hormone-related protein binding to the parathyroid hormone receptor and Design of Conformation-selective Peptides. *J Biol Chem*. 2009;**284**:28382–91.
- 60 Chatterjee D, Jacob RS, Ray S, Navalkar A, Singh N, Sengupta S, et al. Co-aggregation and secondary nucleation in the life cycle of human prolactin/galanin functional amyloids. *Elife*. 2022;**11**:e73835.
- 61 Habener JF, Amherdt M, Ravazzola M, Orci L. Parathyroid hormone biosynthesis. Correlation of conversion of biosynthetic precursors with intracellular protein migration as determined by electron microscope autoradiography. *J Cell Biol*. 1979;**80**:715–31.
- 62 Muresan Z, Macgregor RR. The release of parathyroid hormone and the exocytosis of a proteoglycan are modulated by extracellular Ca²⁺ in a similar manner. *Mol Biol Cell*. 1994;**5**:725–37.
- 63 Otzen D, Riek R. Functional amyloids. *Cold Spring Harb Perspect Biol*. 2019;**11**:a033860.
- 64 Gorr SU, Hamilton JW, Cohn DV. Sulfated secreted forms of bovine and porcine parathyroid chromogranin a (secretory protein-I). *J Biol Chem*. 1991;**266**:5780–4.

Supporting information

Additional supporting information may be found online in the Supporting Information section at the end of the article.

Fig. S1. Buffer effect on circular dichroism spectra of PTH_{1–84} in absence and presence of heparin (1 : 10 molar ratio heparin : PTH_{1–84}).

Fig. S2. Buffer effect on ThT curves of PTH_{1–84} in presence of heparin (1 : 10 molar ratio heparin : PTH_{1–84}).

Fig. S3. NMR detected interaction of PTH_{1–84} with fondaparinux.

2.4 Additional Results Extending the Findings of Papers I-III

2.4.1 General Remarks

This section contains results that are not peer-reviewed and have not been published at the time of submission of this thesis. The section is intended to present additional findings for a more detailed investigation of single aspects of the topics from Papers I-III. The here applied methods follow those presented in the papers and are referred to in the respective chapters. Variations and additional methods are indicated and described.

In Paper II, four PTH₈₄ concentration regimes were identified with distinct biophysical properties. The regimes are summarized in Table 2.1 and Figure 2.1A. If appropriate, PTH₈₄ concentrations are contextualized referring to these regimes. The results of the mechanistic investigation of PTH₈₄ fibril formation (Paper I) are shown in Figure 2.1B in the form of a petri net (see also Figure 1.5B).

Table 2.1: Summary of the PTH₈₄ concentration regimes identified in Paper II.

regime	c_0 range	observation
I	$c_0 < 10 \mu\text{M}$	monomeric, chain expands with increasing c_0
II	$10 \mu\text{M} < c_0 < 70 \mu\text{M}$	two monomer-dimer equilibria, one in the fast and one in the slow exchange regime (referring to the NMR time scale)
III	$70 \mu\text{M} < c_0 < 300 \mu\text{M}$	additional trimers and tetramers, which are precursors for primary nucleation
IV	$c_0 > 300 \mu\text{M}$	additional high molecular weight (HMW) oligomers as precursors for primary nucleation at high c_0

This section addresses the open scientific questions:

- Is it possible to characterize the residual structure of the PTH₈₄ monomer? (Chapter 2.4.2)
- Do destabilizing conditions influence c_{crit} ? (Chapter 2.4.3)
- What is the impact of non-productive dimers on fibril formation? (Chapter 2.4.3)
- In the model of c_{crit} , no net growth occurs for $c_0 < c_{\text{crit}}$. Does it apply for PTH₈₄? (Chapter 2.4.3)
- What is the rate-limiting process? Is it possible to quantify k_+ ? (Chapter 2.4.3)
- What is the molecular structure of PTH₈₄ fibrils? (Chapter 2.4.4)
- Is a prenucleation equilibrium evident for near-physiological conditions? (Chapter 2.4.5)
- What is the impact of near-physiological conditions on fibril morphology? (Chapter 2.4.5)

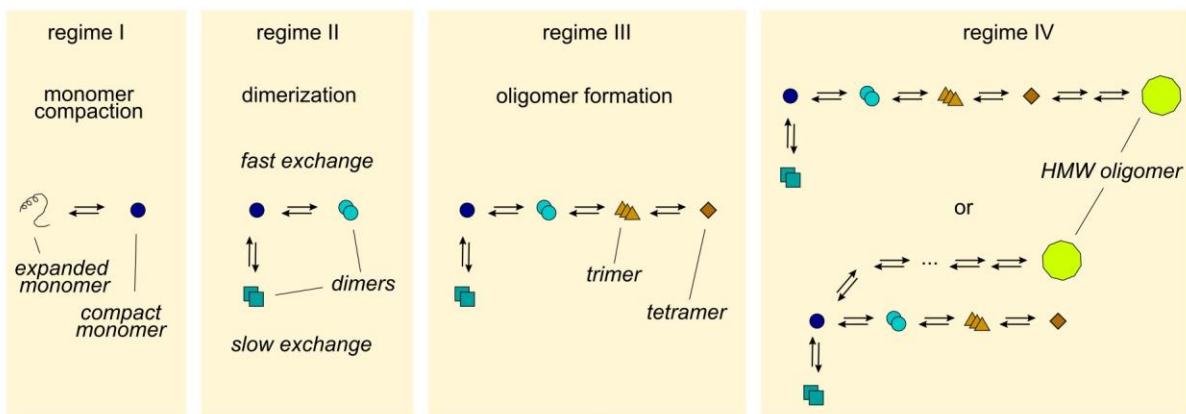
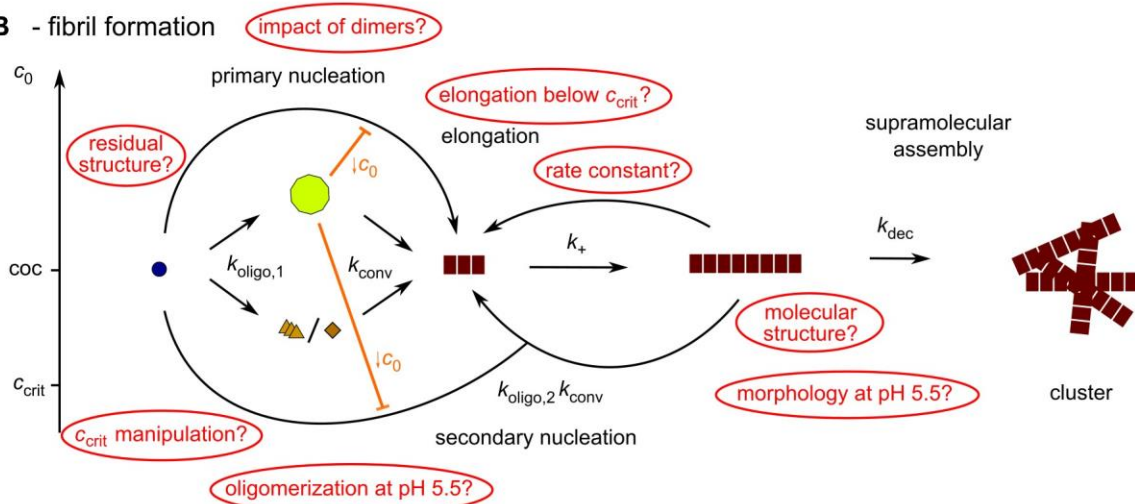
A - prenucleation equilibrium**B - fibril formation**

Figure 2.1: Summary of the investigation of the mechanism of PTH₈₄ fibril formation, as described in the papers, and resulting open questions. **A** – Prenucleation equilibrium (Paper II). Shown are the directly or indirectly observed PTH₈₄ species and the corresponding equilibria for each of the identified regimes (Table 2.1). The dimer in the slow exchange regime (cyan squares) is non-productive for primary nucleation, while the other pathway (fast exchange dimer-trimer-tetramer) is productive. In regime IV it remained unclear whether the HMW oligomer is formed from the tetramer or *via* a separate pathway e.g. starting from the monomer. **B** – Simplified mechanism of fibril formation in the form of a petri net showing the reaction fluxes without including all individual species and their equilibria. The individual processes and the corresponding rate constants are indicated. The y-axis (c_0) is shown to discriminate the oligomer species as nucleation precursors for regimes III ($c_0 < coc$) and IV ($c_0 > coc$). The axis has no impact for the position of the arrows corresponding to elongation or secondary nucleation. The open questions are labelled in red and are situated at their relevant positions.

2.4.2 Effects of Denaturing and α -Helix Inducing Agents on the Structure of Free PTH₈₄

In addition to the acquirement of CD spectra in dependence of the PTH₈₄ concentration (presented in Paper II - Figures 2 and S1), the evolution of the spectra in response to increasing amounts of the denaturing agent urea and the α -helix inducing 2,2,2-Trifluoroethanol (TFE) was investigated. The general methodology followed the details described in Paper II. Urea concentration was adjusted using

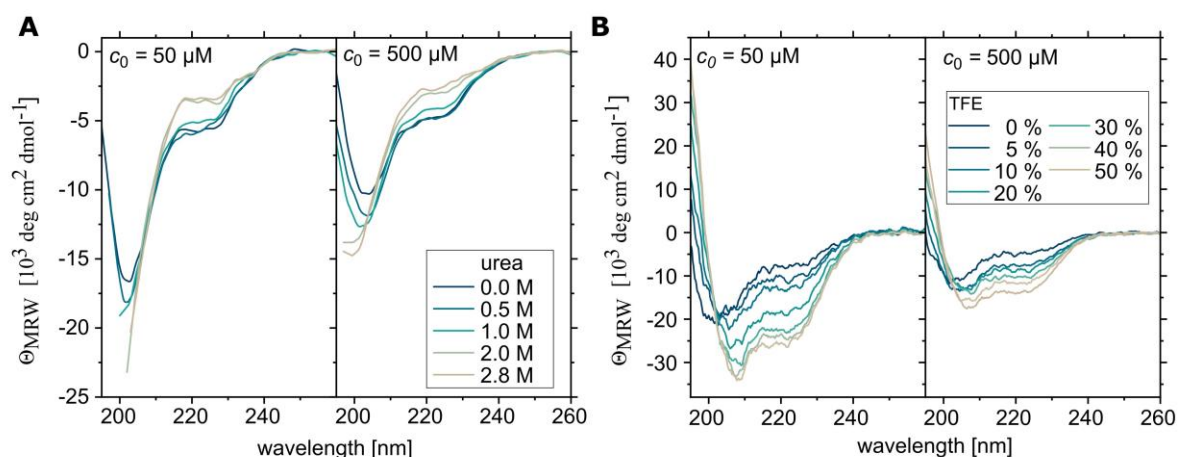


Figure 2.2: CD spectra monitoring the effect of **A** – urea and **B** – TFE on PTH₈₄ secondary structural ensemble at 50 μM (regime II) and 500 μM (regime IV). All experiments were conducted at 25 $^{\circ}\text{C}$ in buffer containing 50 mM Na_2HPO_4 , 150 mM NaCl, pH 7.4 with or without urea or TFE, respectively.

a stock solution (8 M urea in buffer) and was determined for each sample by refractometry using Equation A.1.

The addition of urea as a denaturation agent led to a shift of λ_{min} towards lower wavelengths, a decrease of Θ_{MRW} at 203 nm and an increase of Θ_{MRW} at 222 nm both at c_0 of 50 μM (regime II) and 500 μM (regime IV, Figure 2.2A). These data indicated a decrease of secondary structural content, i.e. denaturation, revealing that PTH₈₄ exhibits residual secondary structure at both regimes. Furthermore, TFE, which is known to induce α -helical structures in peptides,²¹³ was added to PTH₈₄ solutions of the same respective c_0 . These spectra displayed minima at 208 (50 μM) or 207 nm (500 μM) and a second minimum at 222 nm, indicative for α -helix formation (Figure 2.2B). While the transitions at both c_0 displayed a cooperative character, an isodichroic point was only found for regime II at 202.6 nm, which indicated a two-state process. In contrast to the trend towards more negative values of Θ_{MRW} in response to TFE, the positive scaling of Θ_{MRW} at 203 nm and the constant Θ_{MRW} at 222 nm with increasing c_0 indicated that the c_0 induced structural transition of PTH₈₄ proceeded from an intrinsically disordered peptide (IDP) with α -helical propensity at low (regime I) to a more β -sheet enriched structure at high c_0 (regime IV). In both cases, denaturation and α -helix induction, a stronger effect at regime II was observed. It can be suspected that the structure formed at high c_0 is more resistant, regarding the amplitude, towards external factors affecting the secondary structure.

A more detailed investigation of the urea mediated transition of the PTH₈₄ structural ensemble at both regimes by CD spectroscopy is shown in Appendix A, Figure A1. In general, a clear transition was not observed. The scattering of the data points at low urea concentration does not allow to distinguish if a baseline for a native state is present or if PTH₈₄ already unfolds at those mild conditions. A defined baseline would be typically observed for folded proteins, which supports the hypothesis that PTH₈₄ does not display a stable three-dimensional structure. Instead, the residual structure uncooperatively

unfolded towards a disordered state. This state produced a baseline at high urea concentrations, indicated by the solid lines in Figure A1. The respective urea concentration at which the baseline is reached can be considered for a qualitative analysis. At 500 μM PTH₈₄, the end of the transition occurs at a lower urea concentration (1.1 M urea compared to 2.0 M urea at 50 μM PTH₈₄), indicating that both regimes displayed different contents of secondary structure with a unique response to urea. Note that no quantitative information for changes of the thermodynamic stability or the cooperativity of unfolding could be extracted.

Considering the conclusions from Paper II, the situation at both regimes is complex due to different monomer-oligomer equilibria at 50 μM (monomer-dimer) and 500 μM (HMW oligomer). Obviously, the contribution of the HMW oligomer to the ensemble stability, in terms of urea resistance, is decreased compared to the dimer leading to an unfolding transition at lower urea concentrations. Intriguingly, the overall signal change in CD (specifically Θ_{MRW} at 203 nm) is higher at low PTH₈₄ concentrations (Figure 2.2A). In summary, this suggests an incomplete dissociation of HMW oligomers triggered by unfolding observed at 500 μM PTH₈₄.

2.4.3 Fibril Elongation of PTH₈₄

Effects of Urea on Seeded Fibril Growth and the Critical Concentration

In Paper I - Figure 4, the initial gradient of fibrillar growth as a function of PTH₈₄ concentration was investigated. At low concentrations, a linear dependence was observed, while an apparent inhibition occurred at high c_0 due to oligomerization induced monomer depletion. To further investigate this behavior, the dependence of the initial gradient on urea as a denaturing agent was analyzed for regimes III and IV. Urea mediated oligomer dissociation should lead to a higher availability of monomers for the elongation process.

Seeding experiments were conducted as described in Paper I, at three different PTH₈₄ concentrations ($c_0 = 100 \mu\text{M}$, 300 μM and 500 μM) with the addition of 5 % seeds (given in monomer equivalents) and increasing amounts of urea. The urea stock solution ($c = 8 \text{ M}$) was prepared in buffer directly before usage. The urea concentration in each sample was determined by refractometry applying Equation A.1. Note that the experiment was designed to investigate the elongation process. The seeding conditions are chosen to bypass nucleation events. More details as well as the raw kinetic data are given in Appendix A.4 (including Figure A2).

The addition of urea to seeded samples from regime IV led to an increase of the initial gradients r_0 (Figure 2.3A, extracted from ThT fluorescence data displayed in Figure A.2A). Both samples (300 μM

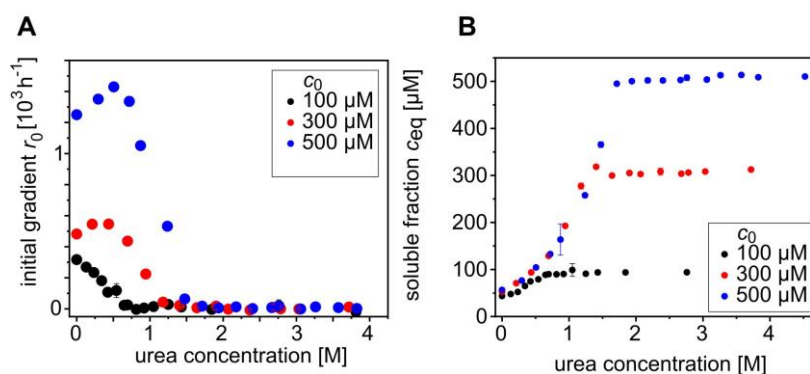


Figure 2.3: Effects of urea on elongation and c_{crit} of PTH₈₄. **A** – Plot of the extracted initial gradients r_0 , determined from the raw data presented in Figure A.2A. **B** – Concentrations of the soluble PTH₈₄ fraction in equilibrium c_{eq} as a function of the urea concentration. All measurements were performed in triplicates. The data points and error bars represent the arithmetic means of triplicate measurements with the standard deviations as error bars. All experiments were conducted at 25 °C in buffer containing 50 mM Na₂HPO₄, 150 mM NaCl, pH 7.4.

and 500 μM) displayed the highest r_0 at around 0.5 M urea. This indicated that at these PTH₈₄ concentrations the elongation process (attachment and/or conversion step) is favored compared to the standard buffer conditions. At 100 μM urea did not induce this effect, suggesting it to be specific for the HMW oligomers at regime IV. Furthermore, the overall rate is not affected for 100 μM , as visible in the normalized data (Figure A.2B).

Furthermore, the soluble fraction in equilibrium with fibrils was determined for each sample following the method described in Paper I. The concentrations of free, unconsumed monomers for each initial PTH₈₄ concentration in dependence of each urea concentration is shown in Figure 2.3B. Urea led to an increase of the soluble peptide fractions until the initial monomer concentrations are reached. In the transition ranges, the soluble fractions at the respective urea concentrations were independent from the initial concentrations c_0 . Considering that c_{crit} is defined by the occurrence of a trimeric or tetrameric oligomer at the transition between regimes II and III (Paper II), the experiment indicated that urea induced a shift of this cut-off concentration towards a higher value. Note that the urea concentration ranges (0–1.5 M for kinetics and 0–1.6 M for c_{eq}) match the range for the CD monitored structural transition, supporting this hypothesis.

In the seeding kinetics, urea did not affect the rate of elongation for 100 μM PTH₈₄ (Figure A.2B, left panel) besides its effect on the soluble fraction in equilibrium. Consequently, no denaturation of residual structure seemed to be mandatory for the incorporation into fibrils, even though urea displayed a stronger overall effect at a low than at a high PTH₈₄ concentration (Figure 2.2A). In contrast, urea facilitated elongation at 300 μM and 500 μM PTH₈₄, indicating that a destabilization of HMW oligomers enabled a higher fraction of monomers available for elongation.

The analysis of the urea dependence of the soluble fractions can also be used to determine the free energy of the elongation process in addition to the estimation described by Equation 1.20 to 1.23.¹⁷⁵

More details, the fits and the extracted parameters are given in Appendix A.4 (including Figure A2, Equation A2 and Table A.1). In general, the here determined Gibbs free energy of $\Delta G_{el}^0 = -22.6 \pm 0.2 \text{ kJ mol}^{-1}$ ($c_0 = 100 \mu\text{M}$) agrees with the value reported in Paper II, indicating the comparability of the two methods.

Evidence of a Second Kinetic Phase in Seeded Fibril Growth at Low Concentrations

Seeded fibril growth investigated in Paper I - Figure 4 focused on the initial gradients in the high-seeding regime and therefore on the time-scale for which elongation is the only relevant process contributing to the increase of fibrillar mass. However, the subsequent theoretical “static plateau” was not found. In order to systematically clarify if this relates to a possible two-phase fibrillation process, as found for *de novo* fibrillation (Paper I - Figure 2 and S1), the data were re-investigated. For a more detailed analysis of elongation effects, fibril growth needs to be analyzed as the increase of fibrillar mass dM/dt . Details are given in Appendix A.4 (including Figure A.3). Figure 2.4A shows seeded fibril growth for $c_0 \leq 140 \mu\text{M}$. It is clearly visible that the initial growth is followed by a second, slower phase. This requires a close inspection of the soluble peptide fraction present at the end of the “burst” growth. If all monomers (in terms of $c_0 - c_{crit}$) would have been consumed in the initial growth, the free monomer concentrations should always equal the critical concentration. In contrast, an excessive soluble fraction is observed with a maximum at $c_0 = 120 \mu\text{M}$, with about $80 \mu\text{M}$ free peptide (Figure 2.4B).

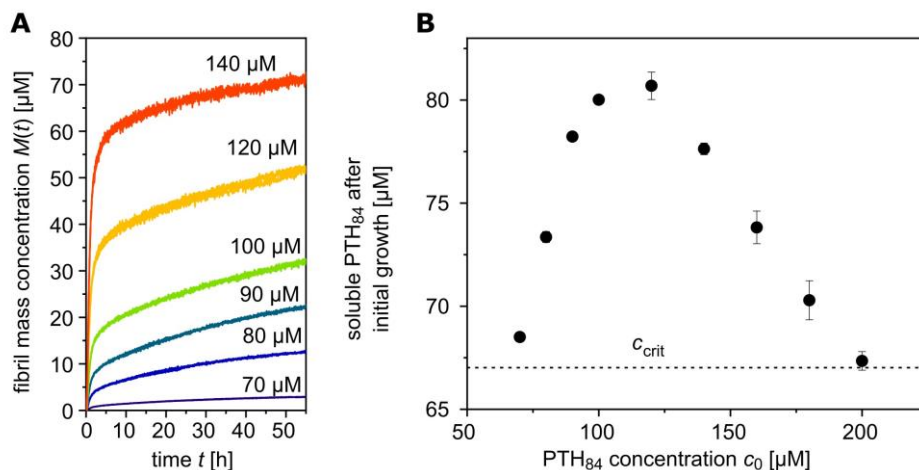


Figure 2.4: Increase of fibril mass $M(t)$ during seeded fibril growth and effects of fibril elongation at low concentrations. **A** – Enlarged representation for $c_0 \leq 140 \mu\text{M}$. A further increase of fibril mass after the initial “burst” is clearly visible, referred to as late-stage gradients dM/dt . **B** – Soluble PTH₈₄ fraction at the intersection time-points. The dashed line marks c_{crit} . All measurements were performed in triplicates. Data points and error bars represent the arithmetic means and the corresponding standard deviation. All experiments were conducted at $25 \text{ }^\circ\text{C}$ in buffer containing $50 \text{ mM Na}_2\text{HPO}_4$, 150 mM NaCl , $\text{pH } 7.4$.

This might originate from a considerable fraction of dimers, as reported for $c_0 > 10 \mu\text{M}$ (Paper II). PTH₈₄ present as monomers can be directly incorporated into seed fibrils, while dimers need to dissociate first. The slow growth for $t > 10 \text{ h}$ was associated with a low dissociation rate of the dimers. The maximum soluble peptide after initial growth at $120 \mu\text{M}$ possibly indicated the highest dimer fraction at this concentration. The effect occurred within concentration regime III ($70 \mu\text{M} \leq c_0 \leq 300 \mu\text{M}$, Paper II), for which additional trimer/tetramer formation was observed. However, the decrease of excess soluble PTH₈₄ after the maximum at $120 \mu\text{M}$ excluded the possibility that this behavior originated from such oligomers. The transition of the small oligomers to HMW oligomers occurred in regime IV at $c_0 \geq 300 \mu\text{M}$.

The ThT fluorescence at the intersection time-points was analyzed in the primary data sets (as shown in Paper I). Figure A.3E interestingly demonstrated a linear dependence on c_0 , which agrees well with an equilibrium of monomers with a dimer in slow exchange. The late-stage fluorescence decrease at higher c_0 (Figure A.3A) can be attributed to fibril clustering and precipitation, as described for *de novo* fibril formation of PTH₈₄ above $230 \mu\text{M}$ (Paper I - Figure 2 and 3).

Approximation of the Elongation Rate Constant

The investigation of fibrillation kinetics conducted in Paper I does not allow a direct extraction of the individual rate constants for oligomerization $k_{\text{oligo}1/2}$, oligomer conversion k_{conv} or elongation k_+ . Compared to e.g. A β (hours), PTH₈₄ fibril formation occurred on the time scale of several days. In order to derive insights into the overall rate-limiting step, k_+ was approximated using a method described by Meisl *et al.* (2014).¹³⁹ This method is based on the initial gradient $dM/dt|_0$ of heavily seeded kinetics reflecting the product $2 k_+ P_0$ (Equation 1.1). The latter itself needs to be approximated by the average seed fibril volume, analyzed by TEM.

In heavily seeded fibrillation experiments, fibril growth predominantly occurs *via* elongation of the pre-formed seeds while primary nucleation and multiplication processes can be neglected. The initial gradients $dM/dt|_0$ from the data shown in Figure A.3A were extracted using the same data points as in Paper I (for r_0) and are shown in Figure 2.5A. Intriguingly, the low-concentration data ($c_0 < 150 \mu\text{M}$) exhibited a sub-linear behavior which typically indicated that oligomers are incorporated in the elongation step rather than monomers. This would be in contrast to the findings of Paper I. However, in this concentration range two kinetic phases were observed, as described above (Figure 2.4), one of which is attributed to slow dimer dissociation. A dimer in slow exchange would consequently cause a reduction of the effective monomer concentration. Correcting c_0 considering this issue resulted in the

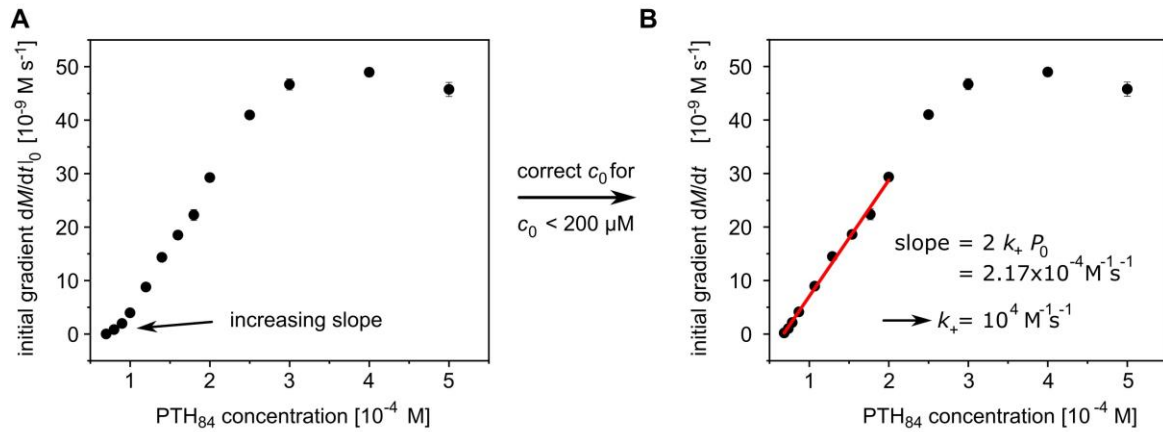


Figure 2.5: Increase of fibril mass $M(t)$ during seeded fibril growth. **A** – Extracted initial gradients $dM/dt|_0$ obtained from linear fits of the data presented in Figure A.3A. **B** – Extracted initial gradients $dM/dt|_0$ plotted vs. initial PTH₈₄ corrected for the effective concentration (see also Figure 2.4). The slope of a linear fit in the c_0 range with no saturation (red solid line) yields $2 k_+ P_0$. Measurements were performed in triplicates. Data points and error bars in B reflect the arithmetic means with the standard deviation. All experiments were conducted at 25 °C in buffer containing 50 mM Na₂HPO₄, 150 mM NaCl, pH 7.4.

plot shown in Figure 2.5B displaying a linear behavior before saturation occurred. This confirmed the interpretation presented in Paper I. The slope of the linear segment is given by $2 k_+ P_0 = 2.17 \times 10^{-4} \text{M}^{-1} \text{s}^{-1}$ (according to Equation 1.1 without saturation). Note that in the analysis using ThT fluorescence units (Paper I), the sub-linear effect was not observed, supporting the linear scaling of ThT fluorescence with c_0 shown in Figure A.3E.

The analysis of the average seed fibril volume by TEM as well as the approximation of P_0 and k_+ are described in detail in Appendix A.4 (including Figure A.4 and Equations A.3 to A.8). A broad length distribution was found (Figure A.4C), resulting in a high uncertainty of the derived k_+ . Considering the geometry of one subfilament, the found average height ($H = 5.92 \pm 0.68$ nm, Figure A.4D) closely corresponded to the diameter of ca. 5.5 nm reported in Paper I - Figure 3, indicating a cylindrical form. A rate constant k_+ of about $10^4 \text{M}^{-1} \text{s}^{-1}$ has been calculated. This value should be considered as a rough approximation due to the broad length distribution leading to a high uncertainty of P_0 . Considering the time scale of PTH₈₄ fibril formation, k_+ is surprisingly high and only one order of magnitude smaller than k_+ of e.g. A β_{40} ($k_+ = 3 \times 10^5 \text{M}^{-1} \text{s}^{-1}$).¹³⁹ More generally, it falls in the range reported for disease related ($10^2 < k_+ < 10^7$) and functional amyloids ($10^3 < k_+ < 10^6$).¹³⁷ Consequently, k_+ most likely does not represent the rate-limiting step.

Fibril Growth Behavior Below the Critical Concentration

In Paper I, the initial gradient r_0 of seeded fibril growth for a sample slightly exceeding c_{crit} (i.e., $c_0 = 70 \mu\text{M}$) was found to considerably differ from “zero” (Paper I - Figure 4D). Typically, no net growth

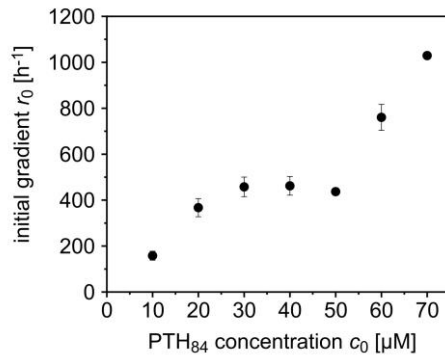


Figure 2.6: Fibril growth below the critical concentration. The initial gradient r_0 , extracted from the raw data, is plotted vs. c_0 . All measurements were performed in triplicates. Data points and error bars represent the arithmetic means and the corresponding standard deviation. All experiments were conducted at 25 °C in buffer containing 50 mM Na₂HPO₄, 150 mM NaCl, pH 7.4.

should occur at $c_0 = c_{\text{crit}}$ and, in contrast to growth, overall dissociation for $c_0 < c_{\text{crit}}$.¹³⁷ In the case of PTH₈₄, extrapolation by a fit to a model of saturated elongation predicted that no net growth will occur for $c_0 \approx 50$ μM, in agreement with c_{crit} . To test this hypothesis, the experiment was repeated with $10 \mu\text{M} \leq c_0 \leq 70 \mu\text{M}$ in analogy to the method described in Paper I (25 μM seeds, given in monomer equivalents). The results are shown in Figure 2.6.

In contrast to the model of the critical concentration, i.e. that fibrils will completely dissociate if $c_0 < c_{\text{crit}}$, fibril growth was observed for all samples. Interestingly, the initial gradient displayed a local plateau for $30 \mu\text{M} < c_0 < 50 \mu\text{M}$ but scaled again with the monomer concentration with higher c_0 . This plateau covered concentration regime II which has been defined in Paper II ($10 \mu\text{M} < c_0 < 70 \mu\text{M}$) supporting an inhibitory effect of the dimeric species on fibril elongation by monomer addition. The further increase of r_0 near c_{crit} hinted towards a decrease of the dimer impact due to a shift of the monomer-oligomer equilibrium towards a trimeric species (regime III, $c_0 > 70 \mu\text{M}$).

2.4.4 Structural Aspects of PTH₈₄ Fibrils

In Paper I, the predominant macroscopic morphology of PTH₈₄ fibrils was shown to consist of three adjacent subfilaments in diameter and one in height. A comparison of the subfilament diameters (Chapter 2.4.3) revealed a cylindrical structure. So far, detailed information about the molecular organization of the fibrils is missing. The following section aims to gain new insights. Additional details are provided in Appendix A.4 (including Figures A.5 to A.8 and Table A.2).

The PTH₈₄ segment incorporated into the fibril core has been reported to be formed of R25-L37, determined by enzymatic digestion of solvent accessible residues.²¹¹ The probability of PTH₈₄ to form steric zippers has been analyzed using the zipperDB online server which processes the primary sequence (Figure 2.7A).²¹⁴ The analysis is based on comparisons of hexapeptides with a sequence of sup35 known to form steric zippers. With this method, PTH₈₄ residues S1-Q6, S3-M8, N10-L15, G12-S17, K26-V31, H32-L37 and A73-L78 were identified to display a propensity to form amyloids as a steric

zipper. Two of these hexapeptides matched the previously identified core segment indicating a significance of steric zippers for PTH₈₄ fibrils. The hits in the *N*- and *C*-terminal regions potentially indicated additional peptide regions to be involved in nucleation or elongation. Note that the hydrophobic segment V35-P43 was excluded from the analysis since proline containing hexapeptides cannot be processed by the algorithm. Additionally, the β -turn propensity for PTH₈₄ was analyzed (window size: 5 residues).^{215,216} For the fibril core fragment, three segments displayed a score > 1, namely K26-D30, Q29-N33 and D30-F34 (Figure A.8A). Besides steric zippers, LARKS form a second class of fibril core conformations. However, the prediction server larksDB, in analogy to zipperDB, was not accessible at the time of submission of this thesis.³⁸ Aromatic residues are required for the formation of LARKS, making PTH₈₄ W23 and F34 potential candidates to be involved in such a fibril core conformation.

The described prediction tools in combination with previous reports suggested that the PTH₈₄ fibril core consists of β -strands connected by a β -turn allowing the organization as steric zippers. For a more detailed analysis, experimental evidence is necessary. Therefore, the molecular structure of PTH₈₄ fibrils was to be determined by using cryoEM. The power of this method is undoubtedly the possibility to obtain structural models from a few individual fibrils and to differentiate between different polymorphs.^{105,217} The (preliminary) results presented in this section were obtained in close cooperation with the cryoEM research group of the Center for Innovation Competence HALOmem (Halle (Saale)) under the supervision of Jun.-Prof. Dr. Panagiotis Kastiris. Grid preparation, blotting and vitrification was conducted by Dr. Fotios Kyrilis, image acquisition by Dr. Farzad Hamdi and data analysis by Dr. Ioannis Skalidis. The author of this thesis was responsible for fibril sample preparation and TEM screening.

An important requirement for cryoEM is a sample with separated, individual fibrils displaying a periodic structure. Since PTH₈₄ fibrils grown *de novo* from monomeric solution are very heterogeneous (Paper I), different methods for sample preparation were tested. Details as well as challenges during the acquisition of the first datasets are provided in Appendix A.4. In summary, the use of fibrils grown at pH 7.4 from pre-formed seeds, with a subsequent sonication step and quiescent incubation prior to the transfer onto the EM grid was chosen to be the most promising preparation method (Figure 2.7B). The cryoEM micrographs, acquired on a Glacios 200 keV Cryo-transmission electron microscope following a published methodology,²¹⁸ showed that the fibrils survive the blotting and vitrification procedure without a modification of the morphology (Figure A.6A and B and Figure A.8B). Promising 2D classes demonstrated the particle picking from the sub-filaments (Figure A.8C). Helical reconstruction from the 2D classes revealed a preliminary low-resolution structural model of PTH₈₄

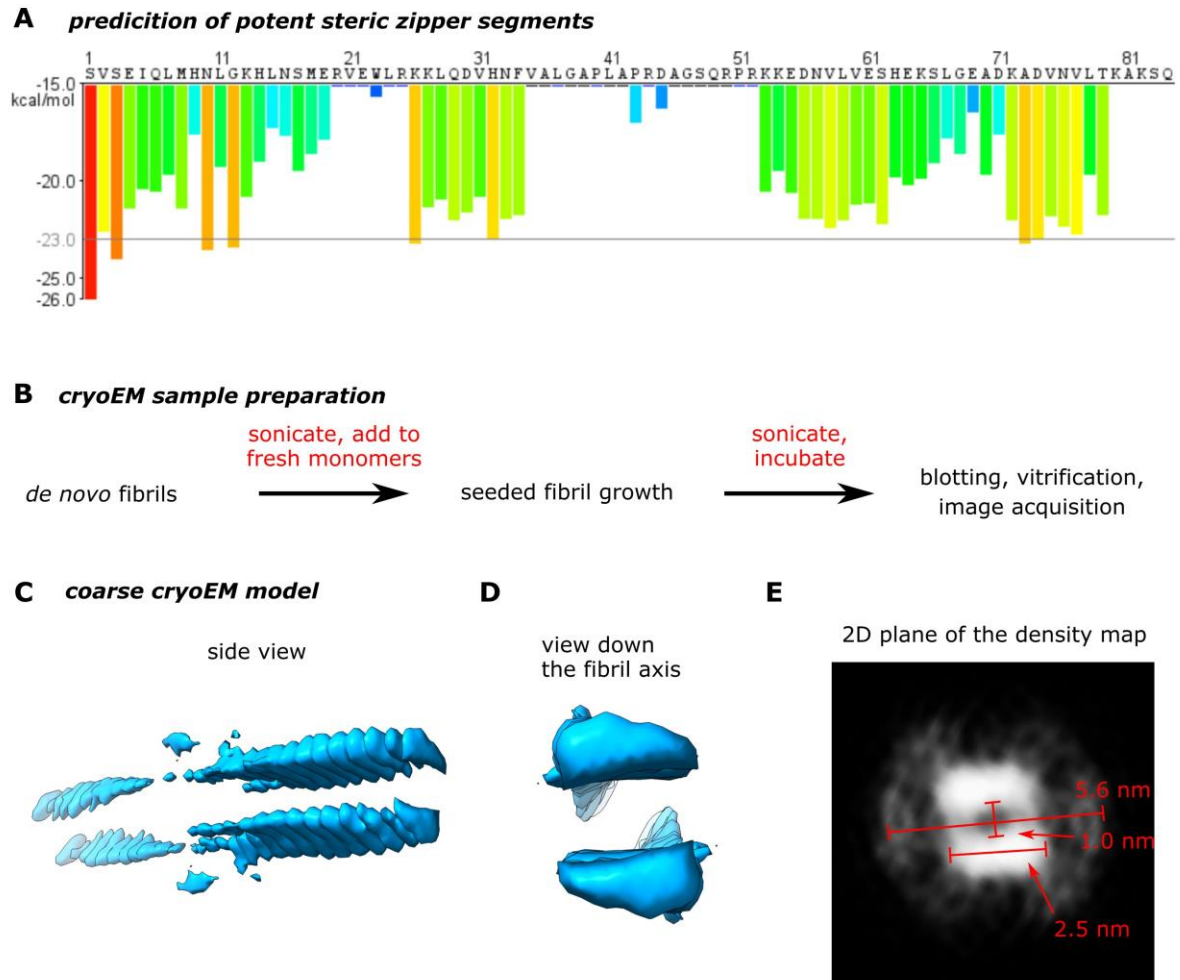


Figure 2.7: Prediction and preliminary PTH₈₄ structure determination by cryoEM. **A** – Result of the zipperDB fibrillation propensity analysis. The calculation is based on structural comparisons of hexapeptides (without prolines) to the sup35 NNQQNY sequence forming amyloid fibrils with steric zipper structures. The y-axis is the result of the energetic fit, evaluated by a Rosetta based algorithm. An energy threshold of $-23 \text{ kcal mol}^{-1}$ indicates a propensity for steric zipper formation. Each bar represents the calculation for one hexapeptide starting at the respective position. The color code indicates the gradient from low (blue) to medium (green) and high energy (red). **B** – Workflow of fibril sample preparation. Seeded fibrils are sonicated prior to the transfer onto the EM grid. **C** – Side view of a structural model reconstructed from cryoEM images. Despite the low resolution, the cross- β structure with hints for a steric zipper-like repetitive motif is evident. **D** – The same model viewed down the fibril axis. A twist is recognizable which possibly represents a bias from helical reconstruction. **E** – Representative 2D plane of the structural model. The two dense regions span 2.5 nm in diameter and represent the segments fixed and incorporated into a steric zipper. The labelled spacing of the segments of 1 nm indicates the interstrand distance obtained from X-ray diffraction.²¹¹ The dense regions are surrounded by a diffuse halo with a total diameter of about 5.5 nm. Fibril growth and sample preparation was conducted at 25 °C in buffer containing 50 mM Na₂HPO₄, 150 mM NaCl, pH 7.4.

fibrils (Figure 2.7C and D). The typical periodic cross- β motif could already be seen in this coarse model. A twist of the fibril was also indicated despite the lack of evidence from other experiments. Consequently, this could also be an artifact from the helical reconstruction requiring the input of a helical pitch. Nevertheless, a cross- β structure agrees with previously published CD data.²¹¹ Two dimensional planes of the density map revealed that the two strands are both 2.5 nm in diameter with a distance of 1 nm (Figure 2.7E). They further reveal a circular halo around the dense segments

spanning 5.6 nm, matching the reported thickness of a subfilament (Paper I). A detailed discussion is presented in Chapter 3.2.

It is important to understand that the obtained model represents a preliminary result which has to be verified and improved by further experiments as well as cycles of data acquisition and analysis.

2.4.5 PTH₈₄ Concentration Dependent Structure and Oligomerization at Acidic pH and the Influence of Heparin on Fibril Morphology

Investigation of the Oligomer Equilibrium at Acidic pH

The speed of PTH₈₄ fibril formation was found to be very high at basic pH but decreased with decreasing pH (Papers I and III). At near-physiological conditions (pH 5.5), *de novo* fibrillogenesis was not observed due to the absence of primary nucleation events (Paper III). In contrast, nucleation at neutral pH (pH 7.4) was found to be modulated by the occurrence of specific oligomeric states as nucleation precursors (Papers I and II). In order to understand this behavior, the oligomerization propensity at pH 5.5 was investigated employing CD and fluorescence, as well as pulsed field gradient (PFG) and two-dimensional (2D) NMR spectroscopy. All experiments were conducted with recombinantly produced ¹⁵N enriched PTH₈₄ according to the methods presented in Paper II in 20 mM Na-citrate buffer (pH 5.5, as used in Paper III).

With fluorescence spectroscopy only marginal changes were detected. The spectra did not show visible differences (Figure 2.8A) while the intensity ratio $F_{350} F_{320}^{-1}$, which remained constant for $20 \mu\text{M} \leq c_0 \leq 400 \mu\text{M}$, revealed a weak trend of a shift towards lower wavelengths, indicating an increase of hydrophobicity of the W23 environment (Figure 2.8B upper panel). Note that the decrease of the intensity ratio at pH 7.4 was about 2.5 units (Paper II) compared to the 0.08 units at acidic pH. Similarly, only slight visible changes were observed in the CD spectra (Figure 2.8C), the wavelength of the minimum around 201 nm only increased by 0.6 nm (compared to 1.5 nm at pH 7.4, Paper II) indicating a certain propensity for secondary structure at high concentrations (Figure 2.8B, middle panel). Additionally, the same shift of the wavelength was observed for 20 μM . The estimated content of disordered structure remained constant at around 50 % with an exception for 20 μM with 55 %.²¹⁹ In the same manner, a constant apparent hydrodynamic radius $r_{H,app}$ was observed for $20 \mu\text{M} \leq c_0 \leq 250 \mu\text{M}$ as determined by PFG-NMR (Figure 2.8B, lower panel) which increased at higher concentrations to a value corresponding to the monomer-dimer equilibrium at pH 7.4 (Paper II). The CD observed position of the minimum wavelength at 20 μM , considering that no such trends were visible in other data, might be an artifact of the measurement.

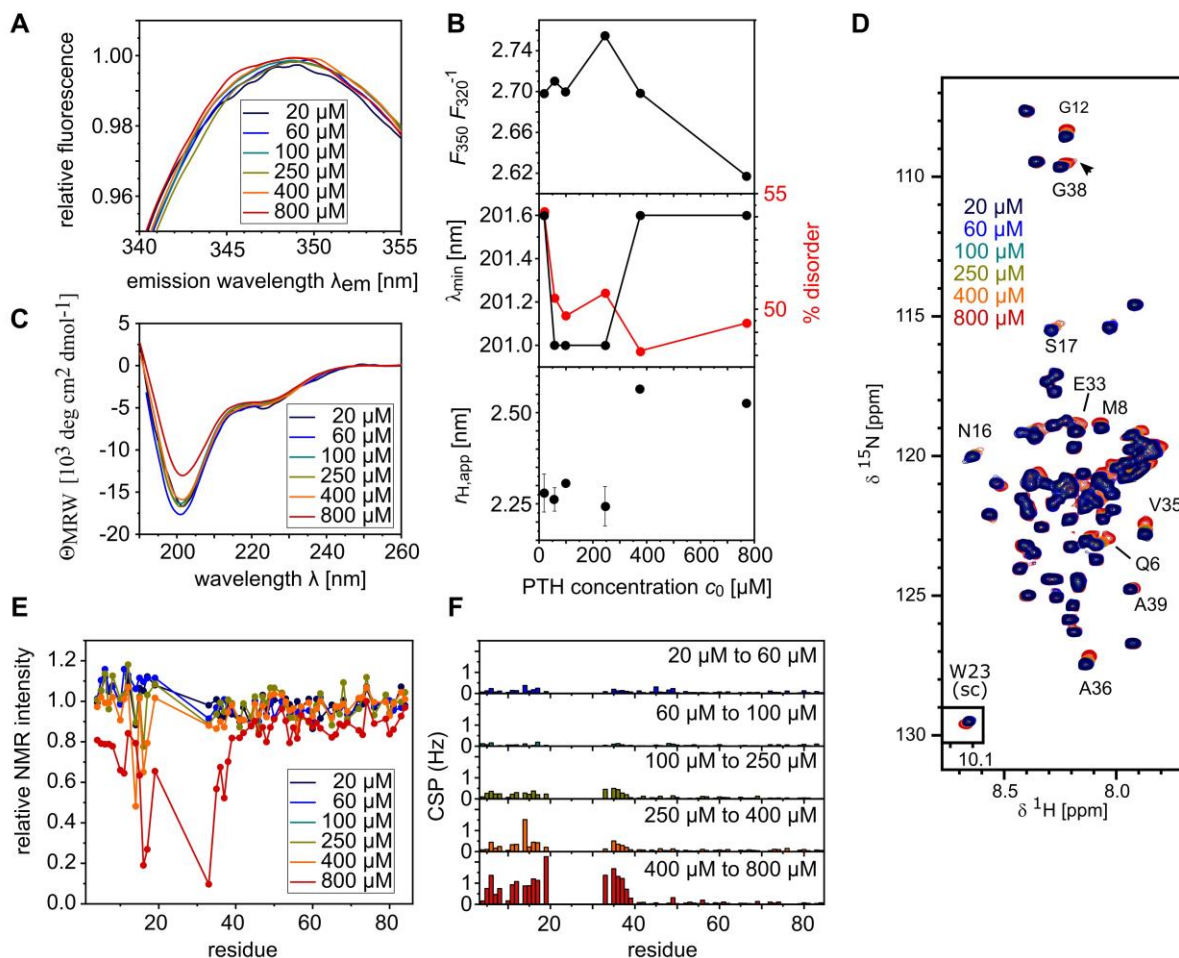


Figure 2.8: Analysis of the concentration dependence of PTH₈₄ at pH 5.5. **A** – W23 fluorescence emission spectra ($\lambda_{\text{exc}} = 280 \text{ nm}$). The respective highest value was set to the value “1”. **B** – CD spectra displayed as mean residue ellipticity Θ_{MRW} . **C** – Results of the analysis of W23 fluorescence shown as the intensity ratio $F_{350} F_{320}^{-1}$ (upper panel), of CD presented as λ_{min} the position of the minimum around 201 nm and the extracted content of disordered structure (middle panel) as well as of PFG-NMR revealing the apparent hydrodynamic radius $r_{\text{H,app}}$ (lower panel). **D** – Overlay of ^1H - ^{15}N -HSQC spectra at different concentrations. Corresponding residues for cross-peaks showing a high chemical shift perturbation (CSP) are indicated. **E** – Relative intensity of the cross-peaks as compared to the intensity at $c_0 = 20 \mu\text{M}$. **F** – CSP shown as the difference between the consecutive analyzed concentrations, given in Hz. The experiments were conducted at 25 °C in buffer containing 20 mM Na-citrate, pH 5.5.

In addition, ^1H - ^{15}N -HSQC spectra were acquired, representing a fingerprint of the peptide backbone in response to changes of the concentration (Figure 2.8D). In general, the HSQC spectra were slightly more dispersed than at pH 7.4 (Paper II - Figure 4). Similar to the corresponding experiment at neutral pH, linear perturbations of the chemical shifts (CSP) were observed indicating an equilibrium of species in the fast exchange regime. Additionally, the cross-peak for G38 displayed a weak shoulder for 800 μM revealing a second equilibrium in the slow exchange regime. The relative intensity (compared to the smallest concentration of 20 μM) was decreased in the *N*-terminal region for the highest concentration (Figure 2.8E). A closer inspection revealed that this applies for residues E4-G12 and E19-Q84. In contrast, residues H14-S17 showed a decreased relative intensity already at 250 μM . This shared a high

similarity with the intensity analysis at very low concentrations ($< 20 \mu\text{M}$) at pH 7.4 (Paper II) related to an expansion of the monomer chain enabling dimer formation at higher c_0 . Potentially, the same effect is observed here at significantly higher concentrations. Considerable CSP were observed in the *N*-terminal region above $100 \mu\text{M}$ (Figure 2.8F) with a similar pattern as found for the monomer-dimer equilibrium at pH 7.4 (regime II in Paper II). Note that the division into five concentration ranges does not imply any model for regimes and is only meant to compare the analyzed data points.

In summary, the investigated biophysical characteristics were constant for concentrations from $20 \mu\text{M}$ to $250 \mu\text{M}$. At higher concentrations, an increased ensemble $r_{\text{H,app}}$ indicated a monomer-dimer equilibrium coupled to an increased structure propensity and hydrophobicity of possible interfaces. Moreover, 2D-NMR revealed effects at $250 \mu\text{M}$ similar to those observed for the increase of monomer chain dimensions. This was interestingly not observed with other techniques which possibly originates from the fact that those effects are rather small or only affect a small fraction of the peptide. The results at high concentrations support the hypothesis of a monomer-dimer equilibrium.

Effect of Acidic Conditions and Heparin on Fibril Morphology

In Paper III, the influence of heparin, as a representative for GAGs, on the fibril formation of PTH₈₄ was investigated. Now, electron microscopy images acquired for the analysis of heparin induced fibrils during the experimental work for Paper III have been re-investigated focusing on the fibril morphology (Figure 2.9). Importantly, the images have been acquired from samples with recombinantly produced PTH₈₄ according to the methods shown in Paper III.

In contrast to their appearance at neutral pH (Paper I - Figure 3), fibrils at near-physiological conditions were predominantly straight and seemed to be more rigid (Figure 2.9A-F). Moreover, they displayed a periodic twist, i.e. a 360° turn of the fibril around its axis. At neutral pH the twists were mostly linked to a change of the filament orientation on the grid (Paper I - Figure 3). The average diameter of $17.2 \pm 2.1 \text{ nm}$ corresponded to the one obtained in Paper I containing three subfilaments (Figure 2.9G). Only a small number of fibrils were found with a higher diameter. Interestingly, these were slightly thinner than their counterparts at neutral pH. Additionally, single fibrils or segments displayed curvature or a twist similar to pH 7.4 conditions. In summary, fibrils at pH 5.5 in the presence of heparin were predominantly straight and homogenous in their appearance, or unimorph.

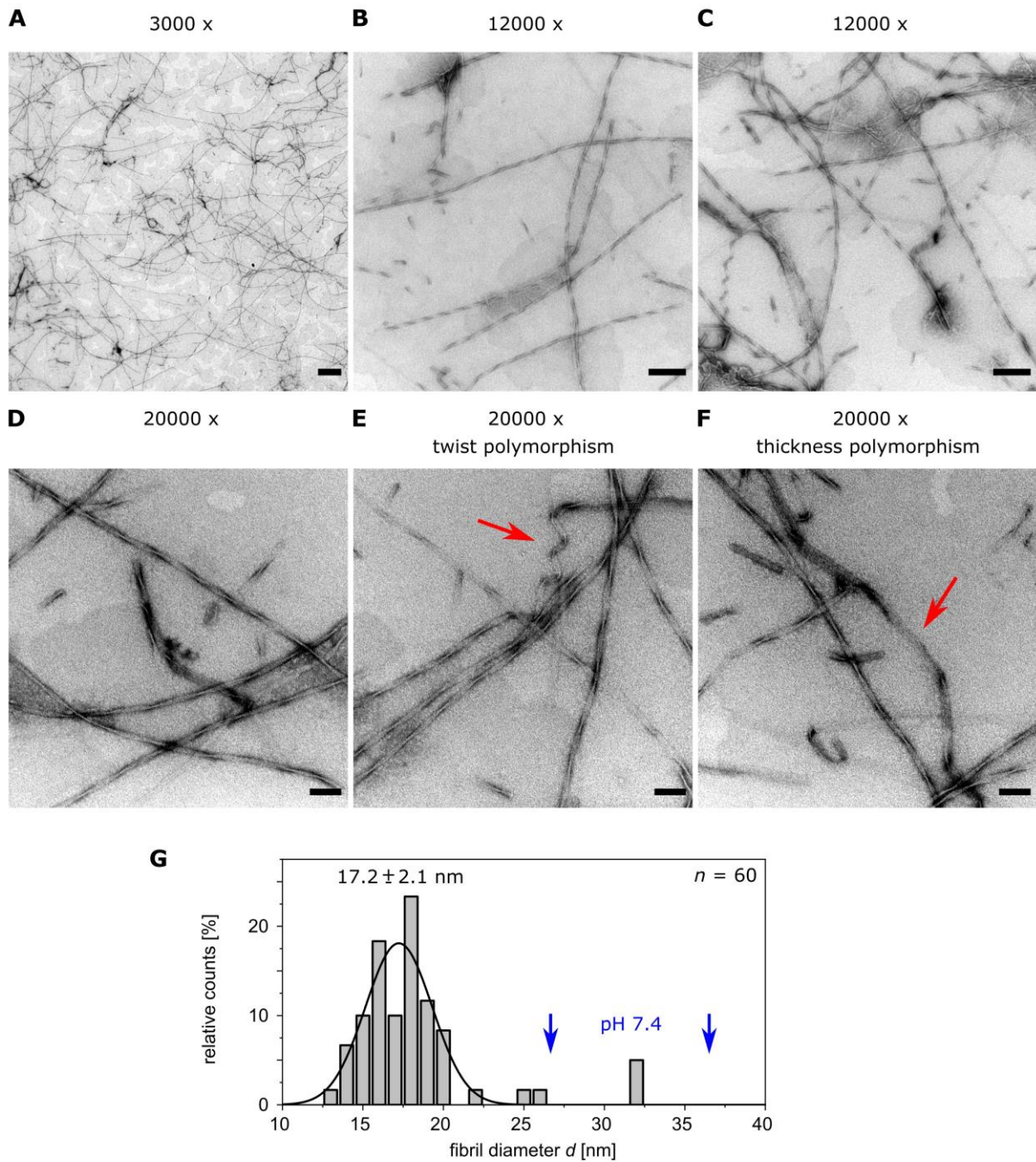


Figure 2.9: Electron micrographs acquired for PTH₈₄ samples after fibril formation at pH 5.5 in the presence of heparin at a magnification of **A** – 3000 x, **B** and **C** – 12000 x and **D-F** – 20000 x. Panels E and F show examples for polymorphism of the twist and fibril width, respectively (labelled with red arrows). **G** – Analysis of the fibril diameter, obtained from the measurement of 60 individual fibrils. The blue arrows in G indicate the diameters for fibrils with 5 and 7 subfilaments (at pH 7.4 shown in Paper I). The scale bar in A corresponds to 1000 nm, in B and C to 250 nm and in D-F to 100 nm. The experiments were conducted at 25 °C in buffer containing 20 mM Na-citrate, pH 5.5.



3 Comprehensive Discussion

3.1 The Mechanism of Amyloid Fibril Formation by PTH₈₄ at Neutral pH

This thesis focused on the investigation of amyloid fibril formation by the hormone PTH₈₄, which is hypothesized to have a physiological function during secretion. The fibrillogenesis has been investigated in molecular detail from the perspective of fibril nucleation and elongation as well as from prenucleation events. Both revealed intriguing mechanistic details and a high dependence on the initial monomer concentration.

For the kinetic investigation presented in Paper I, a mechanistic model based on NCC was chosen considering nucleation as the conversion of non-fibrillar to fibrillar oligomers (Figures 1.8 and 1.9). Fibril formation of PTH₈₄ exhibits two distinct regimes for its dependence on the monomer concentration (for a graphical representation, see also Figure 2.1 or Figure 3.4). In the lower range ($c_0 < 300 \mu\text{M}$), secondary nucleation was found to proceed with a reaction order of $n_{\text{oligo},2} + n_{\text{conv}} = 1.5$ (Paper I - Figure 5) which can, in physical terms, be interpreted as a secondary nucleus of the size of a monomer. A similar determination for primary nucleation was not possible due to the scatter of the data points. This might originate from the two-phase behavior at low c_0 and uncertainties of the corresponding fits regarding the ratio of the two phases. However, a reaction order of $2 \leq (n_{\text{oligo},1} + n_{\text{conv}}) \leq 4$ is able to reproduce the data indicating a small oligomer, such as a dimer to tetramer, to be the precursor for primary nucleation. This agrees well with the investigation of the prenucleation state of PTH₈₄ shown in Paper II. In the corresponding concentration range $100 \mu\text{M} \leq c_0 < 300 \mu\text{M}$, referred to as regime III, a trimeric as well as a tetrameric oligomer was detected by mass spectrometry in addition to monomers and dimers which already occurred at $c_0 < 70 \mu\text{M}$ (Paper II - Figure 3). This close correlation of the kinetics with the prenucleation data led to the conclusion that the observed non-fibrillar oligomers can be converted to fibrillar oligomers displaying the fibril nuclei (Figure 3.1A). The occurrence of these oligomers only above the critical concentration strongly supports this hypothesis. Moreover, the indicated accumulation of oligomers prior to the conversion step towards nuclei approves the NCC model used for the kinetic analysis.

At concentrations above appr. $250 \mu\text{M}$, the $\log(t_{1/2})$ - $\log(c_0)$ -plot shows a positive curvature ($\Delta\gamma > 0$) which hints towards a saturation effect (Paper I - Figure 2). Indeed, strongly seeded kinetic experiments with fragmented seeds revealed a decrease of the initial gradient r_0 for this concentration, indicating a saturation of the elongation process (Paper I - Figure 4). Simultaneously, the described linear scaling of $\bar{\kappa}$ turns into a range with minimal slope, indicating that secondary processes are also affected at high c_0 (Paper I - Figure 5). This was verified by seeding experiments for which unsonicated,

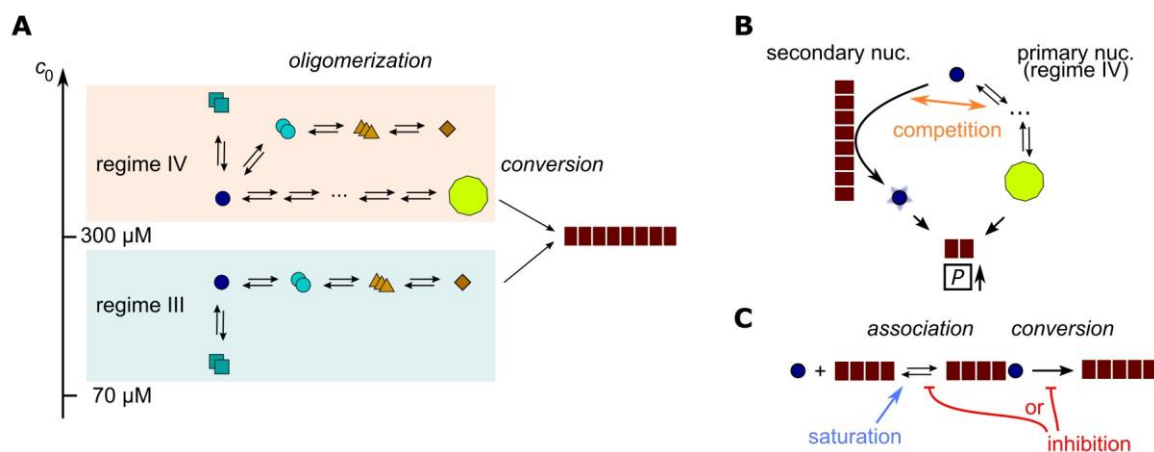


Figure 3.1: Details of individual processes and their interactions. **A** – Origin of the precursors for primary nucleation at regime III (bottom) and regime IV (top). For simplicity, only one of the two possible pathways for the formation of HMW oligomers is shown. **B** – Primary and secondary nucleation compete for monomers and therefore to be the main process to increase the fibril number P at high c_0 . **C** – Differences between saturation and inhibition of the elongation process. In the case of saturation, the equilibrium of the association step is shifted towards the bound “lock” state at high c_0 , while inhibition includes a direct negative interference with one of the two sub-steps. The symbols were used as defined in Figure 2.1.

long seeds were used. The maximum gradient also decreased at high concentrations (Paper I - Figure 4). Interestingly, for $c_0 > 325 \mu\text{M}$ the $\log(t_{1/2})$ - $\log(c_0)$ -plot followed a negative curvature ($\Delta\gamma < 0$) indicating a competition between processes (Paper I - Figure 2). This was accompanied by a significant increase of the reaction order of primary processes towards $n_{\text{oligo},1} + n_{\text{conv}} = 18.5$, i.e. an HMW oligomer (Figure 3.1A and Paper I - Figure 5). This indeed agrees well with the prenucleation state analyzed in Paper II. For high concentrations with $c_0 > 300 \mu\text{M}$ (regime IV), such a large assembly state was evident (Paper II - Figure 2). Even a stretched conformation of monomers within the oligomer was observed in smFRET (Paper II - Figure 3). In principle, the HMW oligomer could be the product of further monomer addition to tetramers or represents a separate equilibrium with monomers (indicated in Figure 2.1A, right). While the evidence of a stretched conformation would favor the second hypothesis, additional experiments are required to confirm this. In physical terms, the HMW oligomer is converted into fibril nuclei at high peptide concentrations instead of the trimer/tetramer.

The positive scaling of the kinetic prefactor A ($A = \bar{\lambda}^3 3^{-1} \bar{\kappa}^{-3}$) demonstrates that fibril formation of PTH₈₄ is driven by primary nucleation at high concentrations (Paper I - Figure 5). Since elongation and secondary nucleation, as the two processes consuming monomeric PTH₈₄, are affected by HMW oligomers, it is suggested that the formation of such oligomers decreases the available monomer pool. This also enables the kinetic competition between primary and secondary nucleation at high c_0 (Figure 3.1B). Oligomer dependent primary nucleation is facilitated compared to monomer dependent secondary nucleation as a result of limited monomer availability. Inhibition in this case does consequently not refer to a direct effect or suppression of a specific process by oligomers, as observed

for $A\beta_{40}$ and $A\beta_{42}$,²²⁰ but to the decrease of available monomer reducing the effective c_0 . For elongation, this inhibition affects the initial gradient but does not suppress a further increase of the gradient before the equilibrium is reached (Paper I - Figure S1). Note that the applied methods do not allow to distinguish if this is the result of oligomer dissociation or of secondary nucleation which can typically occur in seeded fibril growth. However, the acquired data in general do not allow a detailed differentiation between saturation or inhibition of the elongation process (Figure 3.1C). Possibly both apply for PTH₈₄ fibril formation at high concentrations.

In *de novo* as well as in seeded fibril growth, a second kinetic phase was evident at low concentrations. (Figure 2.4 and Paper I - Figure 1 and S2). In the seeding data this effect was observed for $c_0 < 200 \mu\text{M}$, with a maximum at $120 \mu\text{M}$ (Figure 2.4). A closer investigation of fibril mass increase $M(t)$ revealed that the corresponding soluble peptide fraction at the end of the initial growth considerably exceeded c_{crit} . The combination with the results from the prenucleation state suggests the hypothesis that the increased soluble fraction is associated to a relatively high population of a dimeric species with small dissociation rate constant. The initial gradient represents rapid monomer consumption by elongation while additional monomers obtained from slow dimer dissociation are incorporated in the late-stage gradient. Intriguingly, the initial gradient $dM/dt|_0$ (extracted from fibril mass increase, Figure 2.5A) plotted vs. c_0 follows a sub-linear behavior while a linear slope was observed for r_0 (extracted from raw fluorescence data, Paper I - Figure 4). A sublinear plot would indicate that an oligomeric species, forming at high c_0 , is incorporated into fibrils in the elongation step rather than a monomer.^{137,138} Considering the high influence of the dimer at low concentrations and therefore implementing a correction for the effective c_0 , $dM/dt|_0$ again shows a linear behavior (Figure 2.5B). This finally supports the hypothesis of a monomeric unit for elongation. In *de novo* fibril formation, the second kinetic component displayed the highest ratio at $100 \mu\text{M}$ and was rarely abundant for $c_0 \geq 200 \mu\text{M}$ (Paper I - Figure S2). An analysis according to the formalism used in Paper I (Equation 1.16 of this thesis) did not result in convincing data, which has been assigned to the low ratio. A distinct second primary nucleation process at low concentrations was discussed in Paper I to be the origin of this minor component. In principle, the high similarity of the observed effects and c_0 ranges strongly suggest that the second phase in *de novo* fibrillogenesis also relates to the slow dissociation of a dimeric species. The denaturant urea was found to induce a conformational transition of PTH₈₄ (Figure 2.2A and A.1). CD spectroscopy was employed to monitor this transition. While a baseline for high urea concentrations and therefore for the denatured state was found, no clear baseline was indicated for the native state at low urea concentrations. This supports the hypothesis from Paper II that PTH₈₄ only bears a transient rather than a stable, ordered structure at the analyzed conditions. The urea concentration range was shifted towards lower concentrations for higher c_0 of PTH₈₄, indicating that either the peptide structure or the oligomers are less resistant to urea at higher c_0 . Interestingly, the

overall effect was stronger for 50 μM (regime II, dimers) compared to 500 μM (regime IV, HMW oligomers). Perhaps, the secondary structure of HMW oligomers is more likely destabilized than secondary structure of the monomer, but HMW oligomers display a denatured state which is distinct from a denatured monomer. Additionally, HMW oligomers seem to be more resistant towards α -helix inducing TFE, pointing into the same direction. Moreover, urea displayed a differentiated effect on PTH₈₄ fibril elongation (Figure 2.3). Urea facilitated dissociation of HMW oligomers at 300 μM and 500 μM PTH₈₄ resulting in an increased initial gradient r_0 for low urea concentrations. For 100 μM , this effect was not observed. This either indicates that urea is not able to dissociate the dimer, that the dissociation does not significantly contribute to the kinetics or that no destabilization of the secondary structure of the PTH₈₄ monomer is required for elongation. Consequently, the expanded monomeric structure (regime I/II) might be able to directly contribute to elongation. This agrees with the finding that urea displays a stronger effect at lower than at high concentrations (Figure 2.2).

The RMSD analysis of backbone NMR chemical shift perturbations showed that the soluble fractions of all samples ($c_0 = 100 \mu\text{M}$, 300 μM and 500 μM) in equilibrium with fibrils adopt the same state as a fibril-free sample with $c_0 = 40 \mu\text{M}$, i.e. below c_{crit} (Figure 3.2 and Paper II - Figure 5). The long incubation time of seven days obviously allowed the dimer (for the 100 μM sample) to dissociate towards equilibrium. The time-tracked RMSD analysis for $c_0 = 250 \mu\text{M}$ and 500 μM revealed a rapid adoption of the soluble fraction to the corresponding fibril-free prenucleation conditions, confirming that a dimer fraction (in terms of slow dimer dissociation) does not contribute to the kinetics for these concentrations. Note that the urea analysis showed that this effect is only observable for $c_0 \leq 200 \mu\text{M}$ (Figures 2.3 and A.3). Consequently, the RMSD analysis supports the dimer dissociation hypothesis for low concentrations. The interpretation suggested that peptide consumption for elongation does not lead to monomer depletion resulting in a remaining oligomer fraction that is slowly dissociating

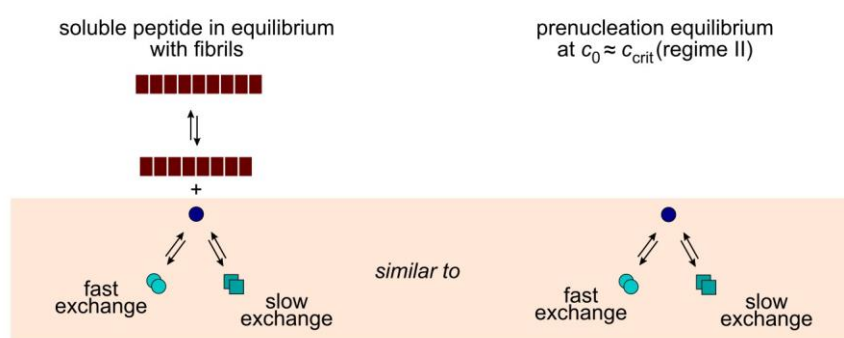


Figure 3.2: Representation of the analogy between the thermodynamic equilibrium in the presence of fibrils (left) and the prenucleation equilibrium at regime II ($c_0 < c_{\text{crit}}$, right). Fibrils are in equilibrium with monomers which subsequently form a second equilibrium with dimers both in fast and slow chemical exchange (referring to the chemical shift NMR time-scale). The same equilibrium of monomers and two different dimers is evident for the fibril-free state below c_{crit} . The symbols were used as defined in Figure 2.1.

(Paper II). Instead, the equilibrium rapidly readjusts according to the available free peptide concentration. The opposite case of monomer depletion and a subsequent slow dimer dissociation applies only for $c_0 \leq 200 \mu\text{M}$ (Figure 2.4). Secondly, inhibition of elongation due to a reduction of the effective monomer concentration by HMW oligomers at high c_0 (Figure 2.5 and Paper I - Figure 4) implies that the fraction of these oligomers must be high compared to the dimer fraction at low c_0 . It is advised to conduct the time-tracked RMSD analysis for a sample with $c_0 < 200 \mu\text{M}$, e.g. $100 \mu\text{M}$ or $150 \mu\text{M}$, to support this hypothesis. The applied methodology in Paper II did not allow this experiment due to low signal intensity and therefore unreliable peak picking.

The observation of fibril net growth in a seeded experiment below c_{crit} was a remarkable finding of this thesis (Figure 2.6 and Figure 3.3). According to the model of the critical concentration, this condition should lead to the dissociation of the fibril.¹³⁷ Due to typically very low critical concentrations for other amyloidogenic peptides, this phenomenon has only been reported for α -synuclein.²²¹ The authors argue that the term “critical concentration c_{crit} ” in general refers to primary nucleation only. An additional critical concentration for elongation is consequently decoupled from, and in this case lower than, the critical concentration of nucleation. The α -synuclein fibrils grown from seeds below c_{crit} were found to be morphologically distinct from those above c_{crit} .²²¹ Furthermore, after an increase for very low concentrations, r_0 for PTH₈₄ remained constant for $30 \mu\text{M} \leq c_0 \leq 50 \mu\text{M}$. For this range (regime II), dimer formation was found (Paper II - Figure 3). For $c_0 > 50 \mu\text{M}$, r_0 again increased (Figure 2.6). The high similarity with the above-described phenomenon for $70 \mu\text{M} \leq c_0 \leq 200 \mu\text{M}$ (Figure 2.4) suggests that the dimer again interferes with elongation by reducing the effective c_0 (Figure 3.3). Extrapolating for $c_0 < 30 \mu\text{M}$ suggests that the critical concentration for elongation is below $5 \mu\text{M}$ and therefore considerably lower than the more general c_{crit} (Figure 2.6). The following speculation might offer an interpretation for the case of PTH₈₄: *De novo* fibril formation occurs *via* nucleation from oligomers that are only formed above c_{crit} . The critical concentration is therefore determined by this monomer-oligomer equilibrium which persists in the soluble peptide fraction. Below c_{crit} , PTH₈₄ is only subject to a monomer-dimer equilibrium not allowing primary nucleation. The presence of seed fibrils bypasses nucleation. As a consequence, the monomer-fibril equilibrium is shifted in favor of fibrils. This would imply an increase of the soluble fraction until it remains constant for $c_0 \geq c_{\text{crit}}$ with an equilibrium constant equal to the prenucleation equilibrium for a fibril-free sample at c_{crit} . In other words, the concept of the critical concentration (referring to nucleation) in terms of a minimum concentration or threshold would only apply for the case $c_0 > c_{\text{crit}}$. For a seeded reaction with $c_0 < c_{\text{crit}}$, the monomer fibril equilibrium adjusts according to a monomer-fibril equilibrium constant and is therefore characterized by a certain monomer-fibril ratio. To support this hypothesis, a determination of the soluble fractions after seeded growth for $c_0 < c_{\text{crit}}$ will be necessary.

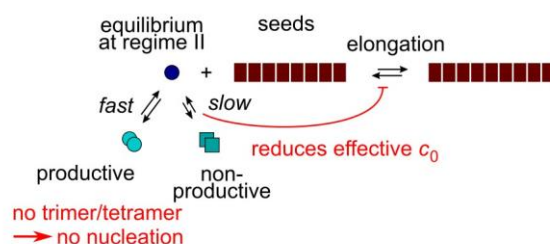


Figure 3.3: Representation of seeded fibril growth at concentrations below c_{crit} . The formation of dimeric species in equilibrium with monomers reduce the effective c_0 and consequently negatively affect the elongation process (indicated by red line). Simultaneously, no primary nucleation can occur due to the absence of trimeric/tetrameric nucleation precursors. For simplicity, elongation is depicted as one step. The symbols were used as defined in Figure 2.1.

In general, the soluble fraction displays two equilibria: (I) the monomer-fibril equilibrium and (II) the monomer-dimer (-trimer/tetramer) equilibrium (Figure 3.2, left). HMW oligomers are not included here due to the concentration of the soluble fraction of about 70 μM . Note that seeding in general does not change the soluble peptide concentration in equilibrium with fibrils (Figure 2.3B, $c_0 \geq c_{crit}$, for 0 M urea). However, fibril net growth below c_{crit} , even at 10 μM which is below the dimer and trimer thresholds, additionally supports the hypothesis of elongation *via* monomer addition.

The Gibbs free energy for PTH₈₄ fibril formation in equilibrium has been independently determined from c_{crit} (Paper II, $\Delta G^0 = -23.8 \text{ kJ mol}^{-1}$) and from the urea dependence of the soluble fraction (Table A.1, $\Delta G_{el}^0 = -22.6 \text{ kJ mol}^{-1}$ for $c_0 = 100 \mu\text{M}$) Moreover, PTH₈₄ fibril elongation displays one of the lowest thermodynamic stabilities among a variety of analyzed amyloidogenic proteins and peptides (range: $-13.7 \geq \Delta G_{el}^0 \geq -65.0 \text{ kJ mol}^{-1}$).¹⁷⁵ The free energy per residue, $\Delta G_{el}^0 N_{aa}^{-1} = -0.27 \text{ kJ mol}^{-1}$, is exceptionally low and even matches stabilities calculated for folded proteins of similar sizes with an average $\Delta G^0 N_{aa}^{-1}$ of about $-0.25 \text{ kJ mol}^{-1}$. For comparison, bovine PI3-SH3 with a comparable chain length of 86 residues displays a considerably higher free energy than the native proteins with $\Delta G^0 N_{aa}^{-1} = -0.44 \text{ kJ mol}^{-1}$.¹⁷⁵ The low Gibbs free energy corresponds to the high critical concentration of PTH₈₄.

PTH₈₄ *de novo* fibril formation was found to occur very slowly with lag-times of several days (Paper I - Figure 1). In addition, very high peptide concentrations are needed for nucleation. In principle, the rate constants for elongation k_+ , primary nucleation $k_{oligo,1}k_{conv}$, secondary nucleation $k_{oligo,2}k_{conv}$ or fragmentation k can be rate-limiting. The presented approach to determine the elongation rate constant k_+ offers a good but coarse approximation based on the mean fibril length (Figure 2.5 and A.4, Equations A.3 to A.8). However, the rate constant can only mirror an average value. Amyloid formation tends to be complex, even elongation is reported to occur in an asymmetric, polarized manner.²²² Importantly, the approximated elongation rate constant of $10^4 \text{ M}^{-1} \text{ s}^{-1}$ is comparable to those reported for other functional or pathogenic amyloid systems.¹³⁷ Fibrils grow relatively fast once the process is initiated by nucleation. This would also exclude secondary processes

to be considered since these were found to be kinetically relevant for fibril formation. Therefore, the long lag-times put primary nucleation with a very small $k_{\text{oligo},1}k_{\text{conv}}$ into the focus. Since oligomers are detectable for conditions corresponding to the early lag-time and are found to be in fast chemical exchange with monomers, $k_{\text{oligo},1}$ is suspected to be relatively large. Consequently, the conversion of oligomers into elongation competent nuclei must occur with a very small rate constant k_{conv} representing the rate-limiting step. Amyloid fibril formation of PTH₈₄ has been shown to occur at 65 °C with short (minutes)²¹¹ and at 37 °C with long lag-times (hours to days, Paper I - Figure 1). The oligomer populations, as observed in Paper II, can interestingly already be detected at room temperature. The structural conversion is potentially limited by a high activation energy barrier which explains the strong temperature dependence.

The kinetic analysis in Paper I - Figure 5 followed a single-curve approach rather than a global analysis. In PTH₈₄ *de novo* fibrillogenesis, the maximum ThT fluorescence intensity did not entirely scale linearly with the concentration (Paper I - Figure 1). Instead, two linear ranges were found, additionally indicated by a shift of the absorption wavelength at high PTH₈₄ concentrations (Paper I - Figure S1). Possibly, ThT displays different binding affinities for the individual fibril morphologies resulting in different fluorescence intensity distributions at different PTH₈₄ concentrations.²²³ Therefore, PTH₈₄ as an amyloidogenic system is not suitable for a global analysis of fibrillation curves with e.g. Amylofit used predominantly for pathogenic systems since this would require a linear ThT fluorescence dependence.¹⁴² Importantly, the mechanistic analysis by individual curve fitting is still allowed since fitting of $\bar{\lambda}$ and $\bar{\kappa}$ was only conducted in the respective linear ranges of the parameters (Paper I - Figure 5). For $\bar{\lambda}$, this partly involved data points from both fluorescence intensity segments. However, excluding those data points would slightly increase the slope of the linear fit, and therefore $n_{\text{oligo},1} + n_{\text{conv}}$, with no dramatic consequences for the interpretation of the reaction order as HMW oligomers representing the primary nucleation precursors. Additionally, global analysis tools like Amylofit are most powerful for a consistent mechanistic behavior. PTH₈₄ fibril formation instead displays several saturation or inhibition events which provokes overparameterization impeding a reliable global fitting result.¹³⁶

Taken together, the presented results draw a conclusive picture of PTH₈₄ amyloid fibril formation at neutral pH (Figure 3.4). The fibrillation behavior is determined by equilibria, in terms of conformational and oligomer states, occurring in solution without fibrils. The critical concentration marks a minimum concentration for the occurrence of trimers/tetramers. Below c_{crit} , dimers are evident. At high concentrations, HMW oligomers are formed. These states are consecutively formed and are in fast exchange, as observed in 2D-NMR and time-tracked RMSD experiments. Fibril nucleation proceeds *via* structural conversion of oligomers present at the respective concentrations into growth-competent

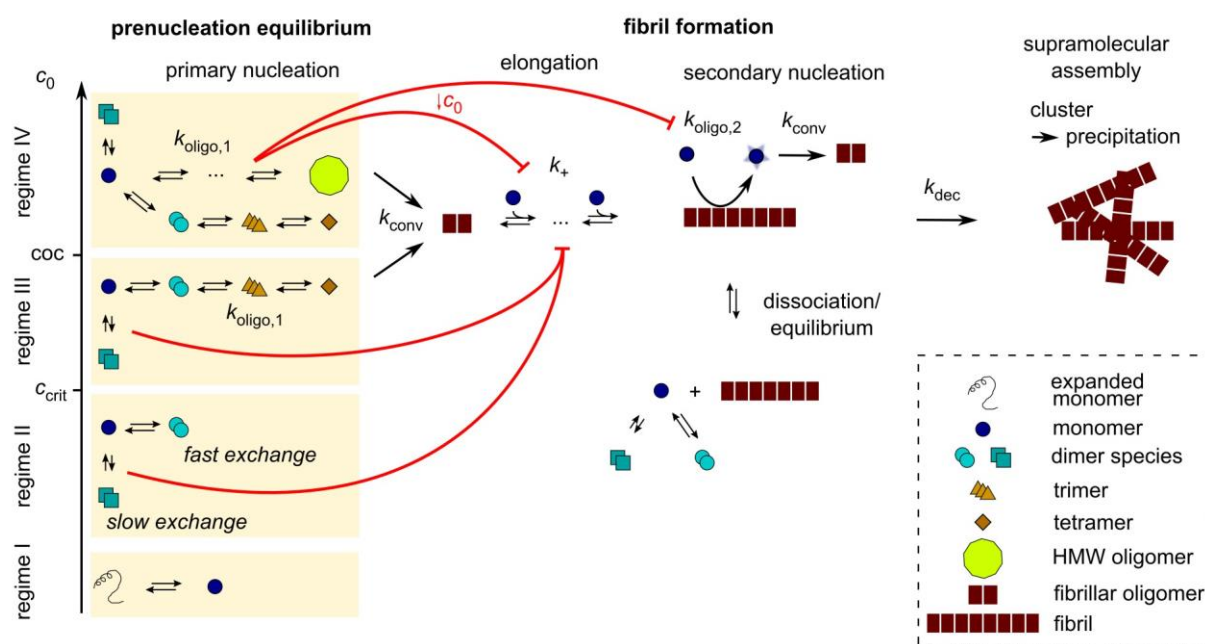


Figure 3.4: Summary of the presented findings concerning the molecular mechanism of PTH₈₄ fibril formation. The prenucleation equilibria at the four identified regimes are shown on the left with their respective influences on fibril formation processes. Negative effects of reduced monomer availability on elongation and secondary nucleation are indicated by red lines. For simplicity, elongation is depicted as one step and only one possible pathway for the formation of HMW oligomers at regime IV is shown.

species. The oligomers negatively affect the available monomer pool, thus leading to apparent inhibition effects of monomer consuming processes such as elongation and secondary nucleation. Furthermore, the occurrence of a dimer with a small dissociation rate constant supports the finding of additional cross-peaks, i.e. an additional state in slow dynamic exchange, in the 2D ¹H-¹⁵N-HSQC NMR data. If the dimer would be productive and on-pathway, i.e. the precursor for trimers and HMW oligomers, the slow dimer dissociation would be ubiquitously observed in all experiments. This implies that two distinct dimeric states are in equilibrium with monomers. The productive dimer is in fast exchange and grows to trimers/tetramers, agreeing with the linear CSPs in regime II (as well as regimes III and IV). The non-productive, off-pathway dimer in contrast is evident for regimes II to IV ($c_0 > 10 \mu\text{M}$) and displays its highest abundance at around $120 \mu\text{M}$.

3.2 PTH₈₄ Fibril Formation at Physiological-Like Conditions and Considerations on PTH₈₄ as a Functional Amyloid

PTH₈₄ amyloid fibril formation at physiological-like conditions was the main focus of Paper III. Most importantly, PTH₈₄ fibrillogenesis was suppressed when incubated alone and was only observed in the presence of a GAG (heparin). The influence of heparin has been attributed to the modulation of k_{conv} , the rate constant of conversion from non-fibrillar to fibrillar oligomers. Since an influence on the oligomerization rate constant $k_{\text{oligo},1}$ could be excluded, the hypothesis was suggested that PTH₈₄ is subject to a monomer-oligomer equilibrium that is either independent from pH (similar to the one presented in Paper II) or pH dependent with unique regimes and populations. A biophysical characterization (Figure 2.8) revealed the formation of a homo-dimer at high concentrations ($c_0 > 250 \mu\text{M}$), but did not indicate oligomerization or structural changes at lower concentrations ($20 \mu\text{M} \leq c_0 \leq 250 \mu\text{M}$). Indeed, analogous effects on NMR chemical shifts and cross-peak intensities in ^1H - ^{15}N -HSQC spectra as presented in Figure 2.8D-F have been previously observed at similar conditions and attributed to the formation of a PTH₈₄ homo-dimer,²²⁴ but were not further investigated. In contrast, four concentration regimes (two below, two above c_{crit}) have been observed at pH 7.4 (Paper II). Interestingly, the interplay of acidic conditions with heparin decreased c_{crit} of PTH₈₄ fibril formation to about $16 \mu\text{M}$ (Paper III - Figure 3), a concentration which was not covered by the experiments shown in Figure 2.8. This supports the second theory: Acidic conditions possibly favor an altered monomer-oligomer equilibrium for which $16 \mu\text{M}$ marks the occurrence of a (transient) nucleus precursor whose conversion is catalyzed by heparin (Figure 3.5A). Significant oligomer populations are only accumulated at very high concentrations. In principle, the combination with the results from Paper II enables an alternative view: Assuming the same equilibrium constants as for pH 7.4 but with transient oligomer populations that do not display an observable effect on the ensemble behavior, the effect of heparin might be the conversion of dimers (occurring below c_{crit} at pH 7.4) into fibrillar oligomers (Figure 3.5B). Note that the transition from regime I to regime II, and therefore dimer formation, occurred around $10 \mu\text{M}$ (Paper II - Figure 2). Since the data acquired for Figure 2.8 only cover the range $20 \mu\text{M} \leq c_0 \leq 800 \mu\text{M}$, the origin of the decreased critical concentration at acidic pH will remain an open question. The strong interaction of PTH₈₄ with heparin and its role for nucleation suggests that the GAG binds oligomeric states for the further catalysis of conversion (indicated in Figure 3.5). In order to confirm or disprove the two hypotheses, further experiments are required. It is suggested to systematically follow the approach presented in Paper I using various concentrations of heparin.

Interestingly, PTH₈₄ nucleation is favored with increasing pH,²²⁵ while the opposing effect is evident for

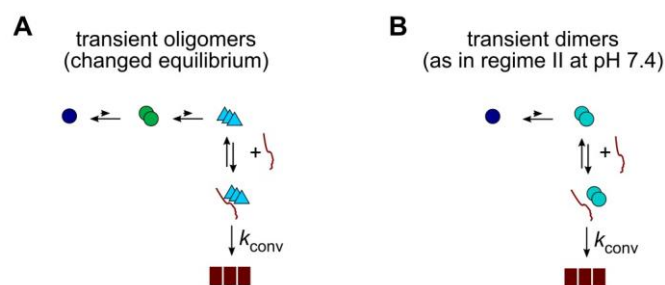


Figure 3.5: Models of PTH₈₄ fibril formation at physiological-like conditions. **A** – The oligomer equilibrium is changed compared to neutral conditions. The oligomeric states are already formed at lower c_0 , compared to pH 7.4. The coloring of the oligomers indicate that they potentially differ from those at neutral conditions from a structural perspective. **B** – The oligomers are transient but principally follow the regimes observed at pH 7.4 (at least regime II). In this case, heparin potentially enables the conversion of dimers into fibrillar oligomers. The symbols were used as defined in Figure 2.1. The GAG is indicated by a dark red line.

e.g. A β ₄₀.²²⁶ The isoelectric point (pI), the pH value at which the peptide net charge is “zero”, of PTH₈₄ is pI 9.1, and of A β ₄₀ pI 5.3,²¹⁶ i.e. at opposing pH ranges. Therefore, the effect for both can be seen in the context of the reduction of electrostatic repulsion near the pI. The histidines in A β ₄₀ seem to play an additive role for the net charge: At acidic pH, the histidines are protonated. For PTH₈₄, the deprotonation of histidines potentially marks an important requirement for oligomer formation and nucleation (Paper II). This illustrates the various roles of histidines in peptides and proteins, especially in amyloid formation.

Fibrils of PTH₈₄ are hypothesized to be the storage form of the hormone as functional amyloids in secretory granules of parathyroid chief cells.²¹¹ To the current date, clear evidence is missing. The following section aims to summarize the reported indications (Table 3.1). Amyloid fibrils have been extracted from pathological as well as from healthy parathyroid glands suggesting that the fibrils are not exclusively related to disease.²⁰⁹ Furthermore, functional amyloids undergo strong control mechanisms.⁵⁰ Physiological fibril formation of PTH₈₄ might occur in the Golgi apparatus after processing with subsequent storage in secretory granules. These compartments display an acidic pH value of about pH 5.5.⁸² Under these conditions, no *de novo* fibril formation of PTH₈₄ is observed (Paper III) preventing uncontrolled fibril formation. Even at neutral pH, as in other cell compartments, fibril formation tends to be very slow (Paper I). GAGs present in the Golgi apparatus can serve as inductors for fibril formation, as demonstrated for heparin in Paper III in analogy to hormones from the pituitary glands.⁵⁵ This can assure that fibril formation occurs at the correct location. Moreover, the presence of heparin led to rapid fibril growth within hours controlled *via* the oligomer conversion rate k_{conv} . The accumulation of potentially toxic oligomeric species is therefore effectively suppressed. No significant degree of oligomerization was observed at pH 5.5 at physiologically relevant concentrations. In contrast, considerable populations of oligomers are observed in the lag-time at

Table 3.1: Indications of functional amyloids and experimental evidence for PTH₈₄.

Indication	PTH ₈₄
role in function	fibrils no connection to disease, ²⁰⁹ proposed storage function ^{55,211}
control of fibril formation	at <i>in vivo</i> -like conditions: no fibril formation alone, presence of a helper molecule mandatory (Paper III), fast fibril growth (Paper III), no (or only transient) oligomer populations (Figure 2.8)
monomorphism	polymorphous fibrils under neutral and high pH conditions ²¹¹ (Paper I), monomorphous fibrils at <i>in vivo</i> -like conditions (Paper III)
monomer release	fibrils able to release monomers ^{211,227} (Papers II and III)

neutral pH. It remains an open question if PTH₈₄ can display toxicity towards human cells. The toxic intermediates of A β fibrillogenesis (all variants) are thermodynamically stable and isolatable,^{228,229} whereas PTH₈₄ oligomers rapidly exchange with monomers and are therefore sensitive for local concentration gradients.

Another feature of functional amyloids is monomorphism. At pH 5.5 in the presence of heparin PTH₈₄ fibrils are considerably less curvilinear than at pH 7.4, they even appear to be rigid-like as A β ₄₀ fibrils. They also display a regular twist and only isolated cases of polymorphism (referring to different twisting and thickness). The situation *in vivo* might be even more homogenous, as reported for memory-associated Orb2 fibrils.⁷³

Last, the release of monomers from fibrils is an important requirement for the proposed storage function. Most likely, the release is triggered by dilution, which occurs due to the secretion of fibrils from secretory granules into the blood stream. The potential of PTH₈₄ fibrils to release monomers has been demonstrated in Paper II, Paper III as well as elsewhere,^{211,227} and is closely related to the low thermodynamic stability of the fibrils (i.e. the high c_{crit}). Interestingly, the interplay of acidic conditions with heparin decreases c_{crit} of PTH₈₄ fibril formation to about 16 μ M (Paper III - Figure 3). As a consequence, the pH shift during hormone secretion additionally favors fibril dissociation by increasing the critical concentration below which PTH₈₄ is soluble. The low thermodynamic stability, especially when related to the chain length (Table A.1 and Paper II), suggests that PTH₈₄ is not evolutionary designed to form fibrils “on its own”. The strong modulation of kinetics, fibril morphology and the critical concentration point into the same direction. This might be interpreted as evidence for the classification as a functional amyloid with assisted, controlled fibril formation in the physiological context.

3.3 The Morphology and Molecular Structure of PTH₈₄ Fibrils

The fibrils formed *in vitro* by PTH₈₄ at neutral pH appear to be very long and curvilinear, displaying an unregular twist which differs between individual fibrils but also within the same fibril (Paper I - Figure 3). In addition to this form of polymorphism, the diameter distribution is heterogenous, the predominant morph measures 16.6 ± 1.4 nm in width. The average height was determined as 5.9 ± 0.7 nm, characterizing the mature fibrils as flat filaments (Figure A.4). Moreover, mature fibrils constitute of individual subfilaments (or protofibrils, three for the dominant morph) with an average diameter of about 5.5 nm (Paper I - Figure 3). The combination with the height suggests a cylindrical form of the subfilaments (Figure 3.6A). However, no experimental evidence was found for twisting of the subfilaments in addition to the unregular twist of the whole fibrils. This should be verified by additional methods, e.g. atomic force microscopy.

A previously reported CD analysis of PTH₈₄ fibrils indicated a cross- β structure for the fibril core sequence.²¹¹ In the same study, the 13-residue fragment R25-L37 was identified as the solvent-inaccessible fibril core incorporated sequence by enzymatic digestion. Assuming a linear stretch of this fragment and a contour length per residue of 0.4 ± 0.02 nm,²³⁰ the theoretical diameter of this sequence is given by 13×0.4 nm = 5.2 nm, agreeing with the average fibril subfilament width of 5.5 nm. This would support a structure of two PTH₈₄ monomers mated *via* side chain interactions constituting one subfilament (Figure 3.6B). Preliminary results from structure determination by cryoEM suggest a different view. Two dense regions were reconstructed surrounded by a halo (Figure 2.7E). Both display a diameter of about 2.5 nm and a spacing of about 1 nm, the latter agreeing

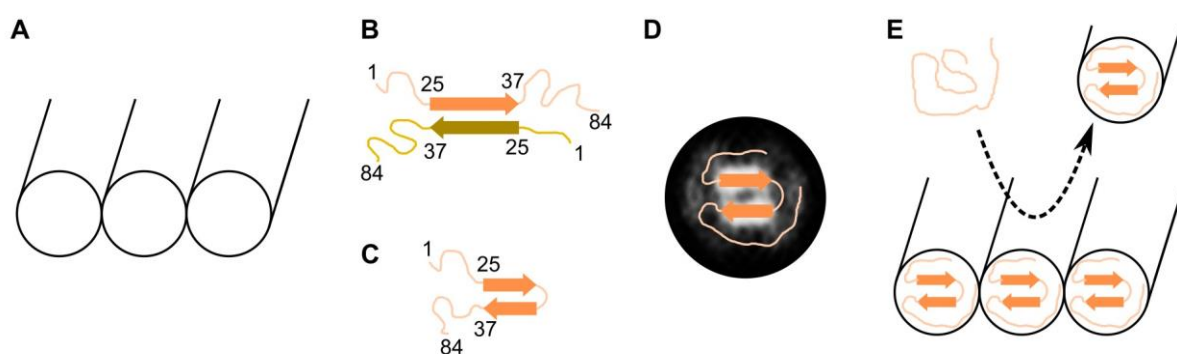


Figure 3.6: Structural models of PTH₈₄ fibrils. **A** – The dominant fibril morph comprises three individual filaments (protofibrils) forming a flat fibril. **B** – Representation of a molecular model containing two individual peptides in the fibril core. **C** – Representation of a structural model with a single peptide forming the fibril core. **D** – Projection of the model from panel C onto the experimental cryoEM model (Figure 2.7). **E** – Projection of the model from panel C onto the cylindrical fibril representation from panel A. A model for secondary nucleation is included. Note that the arrows indicating the β -strands do not represent the peptide orientation. Side chains are aligned in the paper plane, whereas backbone hydrogen bonds are perpendicular to the paper plane (see Figure 1.1 for clarity).

with the X-ray diffraction pattern.²¹¹ Assuming the above-mentioned contour length, the dense regions comprise six to seven residues. Additionally, a β -turn analysis revealed a turn-propensity for segments K26-D30 and Q29-N33 (Figure A.7A).^{215,216} Considering the latter combined with the two segments with a high propensity to form steric zippers (K26-V31 and H32-L37, Figure 2.7A), the fibril core alternatively can consist of one chain with two β -strands connected by a β -turn and stabilized by interstrand side-chain interactions (Figure 3.6C). This suggestion also offers an interpretation for the additional space, indicated by the diffuse halo, which is probably filled by the *N*- and/or *C*-terminal tails (Figure 3.6D). Therefore, the subfilaments would attach to each other *via* intermolecular side chain interactions of the tails. For final evidence, the cryoEM derived model needs to be improved towards side chain resolution. This will require further engineering of the sample preparation conditions. However, this hypothesis is in good agreement with the calculation of the elongation unit and of the secondary nucleus of the size of a monomer (Paper I). One monomer is converted to an elongation-competent state *via* surface catalysis, initiating one subfilament (Figure 3.6E), which either attaches to another subfilament or recruits monomers for subsequent secondary nucleation.

The fibrils of PTH₈₄ grown homogeneously at neutral and high pH appear to be curvilinear (Paper I - Figure 3).²¹¹ They are rather long and assemble with long lag times. In contrast, “typical” curvilinear fibrils display either a short or no lag time,²³¹ attributed to their fast nucleation *via* globular oligomers,^{43,49} and are short in size with a lack of ordered structural organization. Moreover, they mostly occur for proteins with a globular fold in their native state leading to the hypothesis that their sequences are optimized for such structures.²³¹ Another feature of curvilinear fibrils seems to be the occurrence of at least two fibrillation/aggregation prone regions (APR, determined by experiment or prediction). In addition, highly hydrophobic regions adjacent to an APR or separating two APRs (inter-APR) were found to facilitate curvilinearity.²³¹ Isolated APRs, lacking the flanking sequences, mostly form straight long fibrils. In PTH₈₄, the experimentally determined fibril core (K25-L37) indeed overlaps with a highly hydrophobic region (F34-P43, Figure 3.7). Furthermore, multiple steric zipper prone regions, which are assumed to indicate additional potential APRs, have been predicted (Figure 2.7A) in good agreement with the above-mentioned requirements. Indeed, the fragments PTH₃₄ and the core fragment PTH₂₅₋₃₇ lacking the hydrophobic sequence and the disordered C-terminus both form short, straight fibrils.^{232,233} In contrast, PTH₈₄ fibrils are very long (up to several μm) and display a long lag

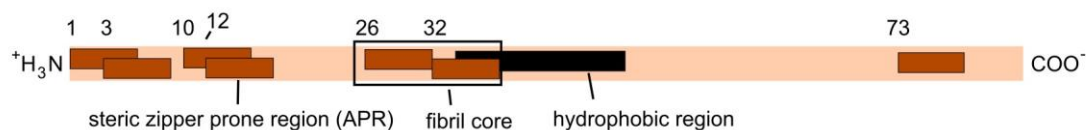


Figure 3.7: Sequence determinants for curvilinear fibrils found in PTH₈₄. The PTH₈₄ sequence is shown in light brown, steric zipper (aggregation) prone regions (APR) in dark red, a strongly hydrophobic region in black and the PTH₈₄ fibril core sequence as a black rectangle.

time in their growth kinetics (Paper I - Figure 2 and 3). Moreover, the curvilinear appearance is only observed if PTH₈₄ is incubated alone, together with heparin under near-physiological conditions they are considerably more rigid (Figure 2.9).

These considerations lead to the hypothesis that PTH₈₄ fibrils only appear to be curvilinear if fibril formation occurs without control mechanisms (Figure 3.8A, left). The exposure to near-physiological conditions (pH 5.5 and a GAG) leads to a single morph of straight fibrils without changing the diameter and the number of constituting subfilaments (Figure 2.9 and Figure 3.8A, right). The basic RKK patch at the *N*-terminal part of the core segment might serve as heparin attachment site (Paper III - Figure S3). Consequently, heparin seems to introduce structural stability by aligning lysine and/or arginine residues along the fibril axis and possibly a strain facilitating the regular twist (Figure 3.8B). Importantly, heparin most likely does not significantly influence the thermodynamic stability since fibrils are still able to release monomers. The “curliness” of PTH₈₄ fibrils grown under other conditions might therefore be associated to the absence of such stabilizing agents. In the case of β -endorphin heparin was identified as a structural component,²³⁴ the 3D structure of the fibrils later revealed exposed lysine residues aligning along the fibril axis serving as binding sites for the GAG.²³⁵ When grown without heparin, the fibrils displayed polymorphism.⁸⁸ The similarity of the two cases supports the hypothesis that PTH₈₄ does not form “traditional” curvilinear fibrils and that curliness is prevented by the GAG. Furthermore, the role of heparin in PTH₈₄ fibril formation is extended from monomer binding and oligomer conversion to the interaction with the fibril.

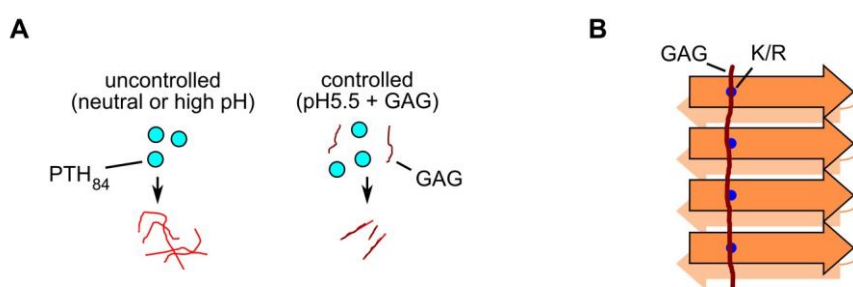


Figure 3.8: Model of the influence of conditions and control mechanisms on PTH₈₄ fibril morphology. **A** – In the absence of control mechanisms (neutral or high pH), curvilinear fibrils are formed (left), while straight fibrils dominate when physiological control mechanisms (pH 5.5 and a GAG) are present (right). **B** – The GAG might scaffold the fibrils by aligning positively charged residues. The GAG is indicated by dark red lines, the soluble PTH₈₄ by cyan circles, fibrils by red lines, positively charged residues by blue circles.

3.4 Consequences of the Results on the Interpretation of Other Experiments

Last, the results acquired and presented in this thesis imply direct consequences for the interpretation of (biophysical) investigations of PTH₈₄. Paper II, Paper III and chapter 2.4.5 of this thesis demonstrated that PTH₈₄ exhibits distinct biophysical properties referring to conformation and oligomerization which depend on the peptide concentration as well as on pH. For most experimental indications it needs to be considered that the full ensemble is affected rather than only monomeric peptide. Special care is required for NMR experiments. For 2D HSQC based investigations, a high signal intensity, good signal-to-noise ratio and a high cross-peak dispersion enable a satisfying analysis. Therefore, the conditions need to be adapted. In the case of PTH₈₄, this was acquired by a low pH value, i.e. pH 5.3.²¹¹ Acidic conditions lead in most cases to an increased signal-to-noise ratio due to a reduction of the exchange between amide protons and water. Importantly, PTH₈₄ at pH 5.3 is not equivalent to e.g. pH 7.4 in terms of structure propensity and oligomeric state. The pH change can induce considerable shifts of the corresponding equilibria. For example, ligand binding studies monitored by ¹H-¹⁵N-HSQC spectra almost always affect intensity and the chemical shift of cross-peaks corresponding to *N*-terminal residues.^{211,224,225,236,237} According to the results presented in this thesis, this more likely indicates a shift of equilibria rather than direct binding events, or the former as a consequence of and in addition to the latter. Additionally, experiments conducted at different peptide concentrations might lead to different results.

In summary, the experimental conditions, including concentration, can exhibit a high influence on protein structure and oligomerization. Changes or differences of conditions should be carefully reviewed if they affect those parameters. This should be a central requirement for biochemical and biophysical studies on proteins in general.

4 Summary

Amyloid fibrils are found in almost all aspects of life and are not necessarily associated with neurotoxic effects as in Alzheimer's or Parkinson's disease. Exemplary, fibrils can perform functional tasks, including the storage of peptide hormones in secretory granules. Such a function has been shown for a variety of peptide hormones from the pituitary gland and is postulated for the parathyroid hormone PTH₈₄ in close analogy. In this dissertation, amyloid fibril formation of PTH₈₄ was investigated with respect to its molecular mechanism at neutral pH. The analysis was conducted with respect to the involved nucleation and growth processes, as well as the prenucleation equilibrium in the absence of fibrils. A complex network of individual processes was identified, which is additionally influenced by peptide concentration-dependent oligomers. The main contribution of the latter seems to be a decrease of the effective concentration of PTH₈₄ monomers, which can directly participate in elongation and secondary nucleation. At low total concentrations, a slowly dissociating dimer has the greatest effect and a high molecular weight oligomer at high concentrations. The latter also enables a special case of competition of the dominant primary and secondary nucleation processes, which has been described here for the first time in this form. Furthermore, a novelty provided by this dissertation was an analysis of the soluble peptide in equilibrium with fibrils. It was possible to reveal that the same monomer-oligomer relationship as found in fibril-free samples at corresponding concentrations also characterize the thermodynamic monomer-fibril equilibrium.

Another focus of this work was the investigation of PTH₈₄ fibril formation under conditions that mimic the physiological environment during storage. These include a slightly acidic pH of pH 5.3. PTH₈₄ alone does not form fibrils under these conditions. An analysis revealed that the oligomers required for nucleation are absent or only transiently present, i.e., below the detector limits. Interestingly, addition of the negatively charged glycosaminoglycan heparin, which is also localized in secretory granules, leads to rapid fibril formation within hours. The effect of heparin can be attributed to the acceleration of the conversion of non-fibrillar to fibrillar oligomers. This interaction is localized to the *N*-terminal region as well as a central basic sequence. Furthermore, heparin causes a change in fibril morphology towards straight, more rigid fibrils. In contrast to neutral pH conditions, these are homogeneous in their macroscopic appearance.

The present work provides important approaches for the evaluation and interpretation of the mechanism of fibril formation, on the one hand at high peptide concentrations and on the other hand of complex mechanism networks. Furthermore, important insights into the critical concentration as a threshold for certain oligomers, which can induce the formation of amyloid fibrils by a structural transformation, could be obtained. These may contribute to a better understanding of metastable

supersaturated peptide and protein solutions. In addition, this work provides a contribution to the classification of PTH₈₄ as a functional amyloid.

5 Zusammenfassung

Amyloide Fibrillen kommen in nahezu allen Bereichen des Lebens vor und stehen dabei nicht zwangsweise mit einer neurotoxischen Wirkung wie bei der Alzheimer'schen oder Parkinson'schen Krankheit in Verbindung. Fibrillen können ganz im Gegenteil funktionale Aufgaben wahrnehmen, wie z.B. die Speicherung von Peptidhormonen in sekretorischen Granulae. Eine solche Funktion wurde für eine Vielzahl von Peptidhormonen aus der Hypophyse gezeigt, ein analoges Beispiel wird für das Parathormon PTH₈₄ aus der Nebenschilddrüse postuliert. In dieser Dissertation wurde die Fibrillenbildung von PTH₈₄ hinsichtlich des molekularen Mechanismus bei neutralem pH-Wert untersucht. Dies erfolgte sowohl im Hinblick auf die beteiligten Keimbildungs- und Wachstumsprozesse, als auch auf das vorgeschaltete Gleichgewicht des Peptidmonomers mit Oligomeren in Abwesenheit von Fibrillen. Ein komplexes Netzwerk individueller Prozesse konnte identifiziert werden, welches zusätzlich durch jene peptidkonzentrationsabhängigen Oligomere beeinflusst wird. Diese scheinen dabei hauptsächlich eine Verringerung der effektiven Konzentration an PTH₈₄-Monomeren, welche direkt an Elongation und Sekundärnukleation teilnehmen können, zu bewirken. Bei niedrigen Gesamtkonzentrationen hat ein langsam dissoziierendes Dimer, bei hohen Konzentrationen ein großes Oligomer mit hohem Molekulargewicht den größten Effekt. Letzteres ermöglicht zudem einen Spezialfall der Kompetition der dominanten keimbildenden Prozesse, welcher in dieser Form hier erstmals beschrieben wurde. Ein zusätzliches neuartiges Ergebnis entstand aus der Analyse des Zustands löslichen Peptids im Gleichgewicht mit Fibrillen. Es konnte gezeigt werden, dass ebenjene Monomer-Oligomer-Wechselwirkungen, welche in Abwesenheit von Fibrillen eine Rolle spielen, auch charakteristisch für das thermodynamische Gleichgewicht mit Fibrillen sind.

Ein weiterer Schwerpunkt dieser Arbeit war die Untersuchung der Fibrillenbildung des PTH₈₄ unter Bedingungen, welche der physiologischen Umgebung während der Speicherung nachempfunden sind. Diese beinhalten unter anderem einen leicht sauren pH-Wert von pH 5,3. PTH₈₄ allein bildet unter diesen Umständen keine Fibrillen. Eine Analyse ergab, dass die zur Keimbildung benötigten Oligomere nicht oder nur transient, also unterhalb der Detektorgrenzen, vorhanden sind. Interessanterweise führt die Zugabe des negativ geladenen Glykosaminoglykans Heparin, welches ebenfalls in sekretorischen Granulae lokalisiert ist, zu einer schnellen Fibrillenbildung innerhalb von Stunden. Der Effekt von Heparin lässt sich dabei auf die Beschleunigung der Umwandlung nicht-fibrillärer zu fibrillären Oligomeren zurückführen. Diese Wechselwirkung ist auf den N-terminalen Bereich sowie eine zentrale basische Sequenz lokal begrenzt. Weiterhin bewirkt Heparin eine Änderung der Fibrillenmorphologie hin zu geraden, eher starren Fibrillen. Diese sind, im Gegensatz zu neutralen pH-Bedingungen, homogen in ihrem makroskopischen Erscheinungsbild.

Die vorliegende Arbeit liefert wichtige Ansätze für die Auswertung und Interpretation des Mechanismus der Fibrillenbildung einerseits bei hohen Peptidkonzentrationen und andererseits von komplexen Mechanismusnetzwerken. Weiterhin konnten wichtige Einblicke in die kritische Konzentration als Schwellenwert für bestimmte Oligomere, welche durch eine strukturelle Umwandlung die Bildung amyloider Fibrillen induzieren können, erzielt werden. Diese können zu einem besseren Verständnis metastabiler, übersättigter Peptid- und Proteinlösungen beitragen. Zudem liefert diese Arbeit einen Beitrag zur Klassifizierung von PTH₈₄ als funktionales Amyloid.

6 References

- 1 Alzheimer, A. Über eine eigenartige Erkrankung der Hirnrinde. *All. Z. Psychiatr.* **1907**, *64*, 146-148.
- 2 Astbury, W. T.; Dickinson, S.; Bailey, K. The X-ray interpretation of denaturation and the structure of the seed globulins. *Biochem. J.* **1935**, *29*, 2351-2360.2351. DOI: 10.1042/bj0292351.
- 3 Astbury, W. T.; Woods, H. J. X-Ray Studies of the Structure of Hair, Wool, and Related Fibres. II. The Molecular Structure and Elastic Properties of Hair Keratin. *Philos. Trans. Royal Soc. A* **1934**, *232*, 333-394.
- 4 Eanes, E. D.; Glenner, G. G. X-ray diffraction studies on amyloid filaments. *J. Histochem. Cytochem.* **1968**, *16*, 673-677. DOI: 10.1177/16.11.673.
- 5 Ruska, E.; Knoll, M. Die magnetische Sammelpule für schnelle Elektronenstrahlen. *Z. Tech. Phys.* **1932**, *78*, 318-339.
- 6 Cohen, A. S.; Calkins, E. Electron Microscopic Observations on a Fibrous Component in Amyloid of Diverse Origins. *Nature* **1959**, *183*, 1202-1203. DOI: 10.1038/1831202a0.
- 7 Kidd, M. Paired helical filaments in electron microscopy of Alzheimer's disease. *Nature* **1963**, *197*, 192-193. DOI: 10.1038/197192b0.
- 8 Terry, R. D. The Fine Structure of Neurofibrillary Tangles in Alzheimer's Disease. *J. Neuropathol. Exp. Neurol.* **1963**, *22*, 629-642. DOI: 10.1097/00005072-196310000-00005.
- 9 Hardy, J.; Allsop, D. Amyloid deposition as the central event in the aetiology of Alzheimer's disease. *Trends Pharmacol. Sci.* **1991**, *12*, 383-388. DOI: 10.1016/0165-6147(91)90609-v.
- 10 Selkoe, D. J. The molecular pathology of Alzheimer's disease. *Neuron* **1991**, *6*, 487-498. DOI: 10.1016/0896-6273(91)90052-2.
- 11 Cappai, R.; White, A. R. Amyloid beta. *Int. J. Biochem. Cell Biol.* **1999**, *31*, 885-889. DOI: 10.1016/s1357-2725(99)00027-8.
- 12 O'Brien, R. J.; Wong, P. C. Amyloid precursor protein processing and Alzheimer's disease. *Annu. Rev. Neurosci.* **2011**, *34*, 185-204. DOI: 10.1146/annurev-neuro-061010-113613.
- 13 Benilova, I.; Karran, E.; De Strooper, B. The toxic A β oligomer and Alzheimer's disease: an emperor in need of clothes. *Nat. Neurosci.* **2012**, *15*, 349-357. DOI: 10.1038/nn.3028.
- 14 Colvin, M. T.; Silvers, R.; Ni, Q. Z.; Can, T. V.; Sergeev, I.; Rosay, M.; Donovan, K. J.; Michael, B.; Wall, J.; Linse, S.; Griffin, R. G. Atomic Resolution Structure of Monomorphic A β 42 Amyloid Fibrils. *J. Am. Chem. Soc.* **2016**, *138*, 9663-9674. DOI: 10.1021/jacs.6b05129.
- 15 Wälti, M. A.; Ravotti, F.; Arai, H.; Glabe, C. G.; Wall, J. S.; Böckmann, A.; Güntert, P.; Meier, B. H.; Riek, R. Atomic-resolution structure of a disease-relevant A β (1-42) amyloid fibril. *Proc. Natl. Acad. Sci. U.S.A.* **2016**, *113*, E4976-E4984. DOI: 10.1073/pnas.1600749113.
- 16 Fitzpatrick, A. W. P.; Falcon, B.; He, S.; Murzin, A. G.; Murshudov, G.; Garringer, H. J.; Crowther, R. A.; Ghetti, B.; Goedert, M.; Scheres, S. H. W. Cryo-EM structures of tau filaments from Alzheimer's disease. *Nature* **2017**, *547*, 185-190. DOI: 10.1038/nature23002.
- 17 Picken, M. M. The Pathology of Amyloidosis in Classification: A Review. *Acta Haematol.* **2020**, *143*, 322-334. DOI: 10.1159/000506696.
- 18 Spillantini, M. G.; Schmidt, M. L.; Lee, V. M. Y.; Trojanowski, J. Q.; Jakes, R.; Goedert, M. α -Synuclein in Lewy bodies. *Nature* **1997**, *388*, 839-840. DOI: 10.1038/42166.
- 19 Götz, J.; Halliday, G.; Nisbet, R. M. Molecular Pathogenesis of the Tauopathies. *Annu. Rev. Pathol.* **2019**, *14*, 239-261. DOI: 10.1146/annurev-pathmechdis-012418-012936.
- 20 Chen, C.; Ding, X.; Akram, N.; Xue, S.; Luo, S. Z. Fused in Sarcoma: Properties, Self-Assembly and Correlation with Neurodegenerative Diseases. *Molecules* **2019**, *24*. DOI: 10.3390/molecules24081622.
- 21 Kwiatkowski, T. J. J.; Bosco, D. A.; Leclerc, A. L.; Tamrazian, E.; Vanderburg, C. R.; Russ, C.; Davis, A.; Gilchrist, J.; Kasarskis, E. J.; Munsat, T.; Valdmanis, P.; Rouleau, G. A.; Hosler, B. A.; Cortelli, P.; de Jong, P. J.; Yoshinaga, Y.; Haines, J. L.; Pericak-Vance, M. A.; Yan, J.; Ticozzi, N.; Siddique,

- T.; McKenna-Yasek, D.; Sapp, P. C.; Horvitz, H. R.; Landers, J. E.; Brown, R. H. J. Mutations in the FUS/TLS gene on chromosome 16 cause familial amyotrophic lateral sclerosis. *Science* **2009**, *323*, 1205-1208. DOI: 10.1126/science.1166066.
- 22 Benditt, E. P.; Eriksen, N. Chemical classes of amyloid substance. *Am. J. Pathol.* **1971**, *65*, 231-252.
- 23 Levin, M.; Franklin, E. C.; Frangione, B.; Pras, M. The amino acid sequence of a major nonimmunoglobulin component of some amyloid fibrils. *J. Clin. Invest.* **1972**, *51*, 2773-2776. DOI: 10.1172/jci107098.
- 24 Benditt, E. P.; Eriksen, N.; Hermodson, M. A.; Ericsson, L. H. The major proteins of human and monkey amyloid substance: Common properties including unusual N-terminal amino acid sequences. *FEBS Lett.* **1971**, *19*, 169-173. DOI: 10.1016/0014-5793(71)80506-9.
- 25 Glenner, G. G.; Terry, W.; Harada, M.; Isersky, C.; Page, D. Amyloid fibril proteins: proof of homology with immunoglobulin light chains by sequence analyses. *Science* **1971**, *172*, 1150-1151. DOI: 10.1126/science.172.3988.1150.
- 26 Koike, H.; Katsuno, M. Transthyretin Amyloidosis: Update on the Clinical Spectrum, Pathogenesis, and Disease-Modifying Therapies. *Neurol. Ther.* **2020**, *9*, 317-333. DOI: 10.1007/s40120-020-00210-7.
- 27 Jadoul, M.; Garbar, C.; Noël, H.; Sennesael, J.; Vanholder, R.; Bernaert, P.; Rorive, G.; Hanique, G.; van Ypersele de Strihou, C. Histological prevalence of beta 2-microglobulin amyloidosis in hemodialysis: a prospective post-mortem study. *Kidney Int.* **1997**, *51*, 1928-1932. DOI: 10.1038/ki.1997.262.
- 28 Störkel, S.; Schneider, H. M.; Müntefering, H.; Kashiwagi, S. Iatrogenic, insulin-dependent, local amyloidosis. *Lab. Invest.* **1983**, *48*, 108-111.
- 29 Westermark, P. Amyloid and polypeptide hormones: What is their interrelationship? *Amyloid* **1994**, *1*, 47-60. DOI: 10.3109/13506129409148624.
- 30 Sieber, P.; Riniker, B.; Brugger, M.; Kamber, B.; Rittel, W. Menschliches Calcitonin. VI. Die Synthese von Calcitonin M. *Helv. Chim. Acta* **1970**, *53*, 2135-2150. DOI: 10.1002/hlca.19700530826.
- 31 Westermark, P.; Engström, U.; Johnson, K. H.; Westermark, G. T.; Betsholtz, C. Islet amyloid polypeptide: pinpointing amino acid residues linked to amyloid fibril formation. *Proc. Natl. Acad. Sci. U.S.A.* **1990**, *87*, 5036-5040. DOI: 10.1073/pnas.87.13.5036.
- 32 Johansson, B.; Wernstedt, C.; Westermark, P. Atrial natriuretic peptide deposited as atrial amyloid fibrils. *Biochem. Biophys. Res. Commun.* **1987**, *148*, 1087-1092. DOI: 10.1016/s0006-291x(87)80243-7.
- 33 Westermark, P.; Eriksson, L.; Engström, U.; Eneström, S.; Sletten, K. Prolactin-derived amyloid in the aging pituitary gland. *Am. J. Pathol.* **1997**, *150*, 67-73.
- 34 Geddes, A. J.; Parker, K. D.; Atkins, E. D. T.; Beighton, E. "Cross- β " conformation in proteins. *J. Mol. Biol.* **1968**, *32*, 343-358. DOI: 10.1016/0022-2836(68)90014-4.
- 35 Sunde, M.; Blake, C. The Structure of Amyloid Fibrils by Electron Microscopy and X-Ray Diffraction. In *Advances in Protein Chemistry*, Richards, F. M., Eisenberg, D. S., Kim, P. S. Eds.; Vol. 50; Academic Press, 1997; pp 123-159.
- 36 Sawaya, M. R.; Sambashivan, S.; Nelson, R.; Ivanova, M. I.; Sievers, S. A.; Apostol, M. I.; Thompson, M. J.; Balbirnie, M.; Wiltzius, J. J. W.; McFarlane, H. T.; Madsen, A. Ø.; Riek, C.; Eisenberg, D. Atomic structures of amyloid cross- β spines reveal varied steric zippers. *Nature* **2007**, *447*, 453-457. DOI: 10.1038/nature05695.
- 37 Eisenberg, D. S.; Sawaya, M. R. Structural Studies of Amyloid Proteins at the Molecular Level. *Annu. Rev. Biochem.* **2017**, *86*, 69-95. DOI: 10.1146/annurev-biochem-061516-045104.
- 38 Hughes, M. P.; Sawaya, M. R.; Boyer, D. R.; Goldschmidt, L.; Rodriguez, J. A.; Cascio, D.; Chong, L.; Gonen, T.; Eisenberg, D. S. Atomic structures of low-complexity protein segments reveal kinked β sheets that assemble networks. *Science* **2018**, *359*, 698-701. DOI: 10.1126/science.aan6398.

- 39 Chou, K.-C.; Pottle, M.; Némethy, G.; Ueda, y.; Scheraga, H. A. Structure of β -sheets: Origin of the right-handed twist and of the increased stability of antiparallel over parallel sheets. *J. Mol. Biol.* **1982**, *162*, 89-112. DOI: 10.1016/0022-2836(82)90163-2.
- 40 Sunde, M.; Serpell, L. C.; Bartlam, M.; Fraser, P. E.; Pepys, M. B.; Blake, C. C. F. Common core structure of amyloid fibrils by synchrotron X-ray diffraction. *J. Mol. Biol.* **1997**, *273*, 729-739. DOI: 10.1006/jmbi.1997.1348.
- 41 Kodali, R.; Wetzel, R. Polymorphism in the intermediates and products of amyloid assembly. *Curr. Opin. Struct. Biol.* **2007**, *17*, 48-57. DOI: 10.1016/j.sbi.2007.01.007.
- 42 Hill, S. E.; Robinson, J.; Matthews, G.; Muschol, M. Amyloid protofibrils of lysozyme nucleate and grow via oligomer fusion. *Biophys. J.* **2009**, *96*, 3781-3790. DOI: 10.1016/j.bpj.2009.01.044.
- 43 Miti, T.; Mulaj, M.; Schmit, J. D.; Muschol, M. Stable, Metastable, and Kinetically Trapped Amyloid Aggregate Phases. *Biomacromolecules* **2015**, *16*, 326-335. DOI: 10.1021/bm501521r.
- 44 Hill, S. E.; Miti, T.; Richmond, T.; Muschol, M. Spatial extent of charge repulsion regulates assembly pathways for lysozyme amyloid fibrils. *PLoS One* **2011**, *6*, e18171. DOI: 10.1371/journal.pone.0018171.
- 45 Sawaya, M. R.; Sambashivan, S.; Nelson, R.; Ivanova, M. I.; Sievers, S. A.; Apostol, M. I.; Thompson, M. J.; Balbirnie, M.; Wiltzius, J. J.; McFarlane, H. T.; Madsen, A. Ø.; Riek, C.; Eisenberg, D. Atomic structures of amyloid cross-beta spines reveal varied steric zippers. *Nature* **2007**, *447*, 453-457. DOI: 10.1038/nature05695.
- 46 Gremer, L.; Schölzel, D.; Schenk, C.; Reinartz, E.; Labahn, J.; Ravelli, R. B. G.; Tusche, M.; Lopez-Iglesias, C.; Hoyer, W.; Heise, H.; Willbold, D.; Schröder, G. F. Fibril structure of amyloid- β (1-42) by cryo-electron microscopy. *Science* **2017**, *358*, 116-119. DOI: 10.1126/science.aao2825.
- 47 Dapson, R. W. Amyloid from a histochemical perspective. A review of the structure, properties and types of amyloid, and a proposed staining mechanism for Congo red staining. *Biotech. Histochem.* **2018**, *93*, 543-556. DOI: 10.1080/10520295.2018.1528385.
- 48 Ruzafa, D.; Morel, B.; Varela, L.; Azuaga, A. I.; Conejero-Lara, F. Characterization of oligomers of heterogeneous size as precursors of amyloid fibril nucleation of an SH3 domain: an experimental kinetics study. *PLoS One* **2012**, *7*, e49690. DOI: 10.1371/journal.pone.0049690.
- 49 Hasecke, F.; Miti, T.; Perez, C.; Barton, J.; Schölzel, D.; Gremer, L.; Grüning, C. S. R.; Matthews, G.; Meisl, G.; Knowles, T. P. J.; Willbold, D.; Neudecker, P.; Heise, H.; Ullah, G.; Hoyer, W.; Muschol, M. Origin of metastable oligomers and their effects on amyloid fibril self-assembly. *Chem. Sci.* **2018**, *9*, 5937-5948, 10.1039/C8SC01479E. DOI: 10.1039/C8SC01479E.
- 50 Otzen, D.; Riek, R. Functional Amyloids. *Cold Spring Harb. Perspect. Biol.* **2019**, *11*. DOI: 10.1101/cshperspect.a033860.
- 51 Larsen, P.; Nielsen, J. L.; Dueholm, M. S.; Wetzel, R.; Otzen, D.; Nielsen, P. H. Amyloid adhesins are abundant in natural biofilms. *Environ. Microbiol.* **2007**, *9*, 3077-3090. DOI: 10.1111/j.1462-2920.2007.01418.x.
- 52 Greenwald, J.; Kwiatkowski, W.; Riek, R. Peptide Amyloids in the Origin of Life. *J. Mol. Biol.* **2018**, *430*, 3735-3750. DOI: 10.1016/j.jmb.2018.05.046.
- 53 Greenwald, J.; Riek, R. On the possible amyloid origin of protein folds. *J. Mol. Biol.* **2012**, *421*, 417-426. DOI: 10.1016/j.jmb.2012.04.015.
- 54 Maury, C. P. J. Amyloid and the origin of life: self-replicating catalytic amyloids as prebiotic informational and protometabolic entities. *Cell. Mol. Life Sci.* **2018**, *75*, 1499-1507. DOI: 10.1007/s00018-018-2797-9.
- 55 Maji, S. K.; Perrin, M. H.; Sawaya, M. R.; Jessberger, S.; Vadodaria, K.; Rissman, R. A.; Singru, P. S.; Nilsson, K. P.; Simon, R.; Schubert, D.; Eisenberg, D.; Rivier, J.; Sawchenko, P.; Vale, W.; Riek, R. Functional amyloids as natural storage of peptide hormones in pituitary secretory granules. *Science* **2009**, *325*, 328-332. DOI: 10.1126/science.1173155.
- 56 Soragni, A.; Yousefi, S.; StoECKle, C.; Soriaga, A. B.; Sawaya, M. R.; Kozłowski, E.; Schmid, I.; Radonjic-Hoesli, S.; Boutet, S.; Williams, G. J.; Messerschmidt, M.; Seibert, M. M.; Cascio, D.; Zatsepin, N. A.; Burghammer, M.; Riek, C.; Colletier, J. P.; Riek, R.; Eisenberg, D. S.; Simon, H. U. Toxicity of eosinophil MBP is repressed by intracellular crystallization and promoted by extracellular aggregation. *Mol. Cell* **2015**, *57*, 1011-1021. DOI: 10.1016/j.molcel.2015.01.026.

- 57 Wang, L.; Maji, S. K.; Sawaya, M. R.; Eisenberg, D.; Riek, R. Bacterial inclusion bodies contain amyloid-like structure. *PLoS Biol.* **2008**, *6*, e195. DOI: 10.1371/journal.pbio.0060195.
- 58 Fowler, D. M.; Koulou, A. V.; Alory-Jost, C.; Marks, M. S.; Balch, W. E.; Kelly, J. W. Functional amyloid formation within mammalian tissue. *PLoS Biol.* **2006**, *4*, e6. DOI: 10.1371/journal.pbio.0040006.
- 59 Chapman, M. R.; Robinson, L. S.; Pinkner, J. S.; Roth, R.; Heuser, J.; Hammar, M.; Normark, S.; Hultgren, S. J. Role of Escherichia coli curli operons in directing amyloid fiber formation. *Science* **2002**, *295*, 851-855. DOI: 10.1126/science.1067484.
- 60 Dueholm, M. S.; Petersen, S. V.; S nderk er, M.; Larsen, P.; Christiansen, G.; Hein, K. L.; Enghild, J. J.; Nielsen, J. L.; Nielsen, K. L.; Nielsen, P. H.; Otzen, D. E. Functional amyloid in Pseudomonas. *Mol. Microbiol.* **2010**, *77*, 1009-1020. DOI: 10.1111/j.1365-2958.2010.07269.x.
- 61 Zeng, G.; Vad, B. S.; Dueholm, M. S.; Christiansen, G.; Nilsson, M.; Tolker-Nielsen, T.; Nielsen, P. H.; Meyer, R. L.; Otzen, D. E. Functional bacterial amyloid increases Pseudomonas biofilm hydrophobicity and stiffness. *Front. Microbiol.* **2015**, *6*, 1099. DOI: 10.3389/fmicb.2015.01099.
- 62 Macindoe, I.; Kwan, A. H.; Ren, Q.; Morris, V. K.; Yang, W.; Mackay, J. P.; Sunde, M. Self-assembly of functional, amphipathic amyloid monolayers by the fungal hydrophobin EAS. *Proc. Natl. Acad. Sci. U.S.A.* **2012**, *109*, E804-811. DOI: 10.1073/pnas.1114052109.
- 63 Morris, V. K.; Kwan, A. H.; Sunde, M. Analysis of the structure and conformational states of DewA gives insight into the assembly of the fungal hydrophobins. *J. Mol. Biol.* **2013**, *425*, 244-256. DOI: 10.1016/j.jmb.2012.10.021.
- 64 W sten, H. A.; de Vocht, M. L. Hydrophobins, the fungal coat unravelled. *Biochim. Biophys. Acta Biomembr.* **2000**, *1469*, 79-86. DOI: 10.1016/S0304-4157(00)00002-2.
- 65 Guyonnet, B.; Egge, N.; Cornwall, G. A. Functional amyloids in the mouse sperm acrosome. *Mol. Cell. Biol.* **2014**, *34*, 2624-2634. DOI: 10.1128/mcb.00073-14.
- 66 Iconomidou, V. A.; Vriend, G.; Hamodrakas, S. J. Amyloids protect the silkworm oocyte and embryo. *FEBS Lett.* **2000**, *479*, 141-145. DOI: 10.1016/S0014-5793(00)01888-3.
- 67 Podrabsky, J. E.; Carpenter, J. F.; Hand, S. C. Survival of water stress in annual fish embryos: dehydration avoidance and egg envelope amyloid fibers. *Am. J. Physiol. Regul. Integr. Comp. Physiol.* **2001**, *280*, R123-131. DOI: 10.1152/ajpregu.2001.280.1.R123.
- 68 True, H. L.; Lindquist, S. L. A yeast prion provides a mechanism for genetic variation and phenotypic diversity. *Nature* **2000**, *407*, 477-483. DOI: 10.1038/35035005.
- 69 Du, Z.; Park, K. W.; Yu, H.; Fan, Q.; Li, L. Newly identified prion linked to the chromatin-remodeling factor Swi1 in Saccharomyces cerevisiae. *Nat. Genet.* **2008**, *40*, 460-465. DOI: 10.1038/ng.112.
- 70 Alberti, S.; Halfmann, R.; King, O.; Kapila, A.; Lindquist, S. A systematic survey identifies prions and illuminates sequence features of prionogenic proteins. *Cell* **2009**, *137*, 146-158. DOI: 10.1016/j.cell.2009.02.044.
- 71 Baxa, U.; Cheng, N.; Winkler, D. C.; Chiu, T. K.; Davies, D. R.; Sharma, D.; Inouye, H.; Kirschner, D. A.; Wickner, R. B.; Steven, A. C. Filaments of the Ure2p prion protein have a cross-beta core structure. *J. Struct. Biol.* **2005**, *150*, 170-179. DOI: 10.1016/j.jsb.2005.02.007.
- 72 Caudron, F.; Barral, Y. A super-assembly of Whi3 encodes memory of deceptive encounters by single cells during yeast courtship. *Cell* **2013**, *155*, 1244-1257. DOI: 10.1016/j.cell.2013.10.046.
- 73 Herv s, R.; Rau, M. J.; Park, Y.; Zhang, W.; Murzin, A. G.; Fitzpatrick, J. A. J.; Scheres, S. H. W.; Si, K. Cryo-EM structure of a neuronal functional amyloid implicated in memory persistence in Drosophila. *Science* **2020**, *367*, 1230-1234. DOI: 10.1126/science.aba3526.
- 74 Majumdar, A.; Cesario, W. C.; White-Grindley, E.; Jiang, H.; Ren, F.; Khan, M. R.; Li, L.; Choi, E. M.; Kannan, K.; Guo, F.; Unruh, J.; Slaughter, B.; Si, K. Critical role of amyloid-like oligomers of Drosophila Orb2 in the persistence of memory. *Cell* **2012**, *148*, 515-529. DOI: 10.1016/j.cell.2012.01.004.
- 75 Saad, S.; Cereghetti, G.; Feng, Y.; Picotti, P.; Peter, M.; Dechant, R. Reversible protein aggregation is a protective mechanism to ensure cell cycle restart after stress. *Nat. Cell. Biol.* **2017**, *19*, 1202-1213. DOI: 10.1038/ncb3600.

- 76 Coustou, V.; Deleu, C.; Saupe, S.; Begueret, J. The protein product of the het-s heterokaryon incompatibility gene of the fungus *Podospira anserina* behaves as a prion analog. *Proc. Natl. Acad. Sci. U.S.A.* **1997**, *94*, 9773-9778. DOI: 10.1073/pnas.94.18.9773.
- 77 Maddelein, M. L.; Dos Reis, S.; Duvezin-Caubet, S.; Couлары-Salin, B.; Saupe, S. J. Amyloid aggregates of the HET-s prion protein are infectious. *Proc. Natl. Acad. Sci. U.S.A.* **2002**, *99*, 7402-7407. DOI: 10.1073/pnas.072199199.
- 78 Daskalov, A.; Paoletti, M.; Ness, F.; Saupe, S. J. Genomic clustering and homology between HET-S and the NWD2 STAND protein in various fungal genomes. *PLoS One* **2012**, *7*, e34854. DOI: 10.1371/journal.pone.0034854.
- 79 Kelly, R. B. Pathways of protein secretion in eukaryotes. *Science* **1985**, *230*, 25-32. DOI: 10.1126/science.2994224.
- 80 Dannies, P. S. Concentrating hormones into secretory granules: layers of control. *Mol. Cell. Endocrinol.* **2001**, *177*, 87-93. DOI: 10.1016/s0303-7207(01)00437-3.
- 81 Nelson, R.; Sawaya, M. R.; Balbirnie, M.; Madsen, A. Ø.; Riek, C.; Grothe, R.; Eisenberg, D. Structure of the cross-beta spine of amyloid-like fibrils. *Nature* **2005**, *435*, 773-778. DOI: 10.1038/nature03680.
- 82 Paroutis, P.; Touret, N.; Grinstein, S. The pH of the secretory pathway: measurement, determinants, and regulation. *Physiology (Bethesda)* **2004**, *19*, 207-215. DOI: 10.1152/physiol.00005.2004.
- 83 Cohlberg, J. A.; Li, J.; Uversky, V. N.; Fink, A. L. Heparin and other glycosaminoglycans stimulate the formation of amyloid fibrils from alpha-synuclein in vitro. *Biochemistry* **2002**, *41*, 1502-1511. DOI: 10.1021/bi011711s.
- 84 Kolset, S. O.; Prydz, K.; Pejler, G. Intracellular proteoglycans. *Biochem. J.* **2004**, *379*, 217-227. DOI: 10.1042/bj20031230.
- 85 Reggio, H. A.; Palade, G. E. Sulfated compounds in the zymogen granules of the guinea pig pancreas. *J. Cell. Biol.* **1978**, *77*, 288-314. DOI: 10.1083/jcb.77.2.288.
- 86 Snow, A. D.; Mar, H.; Nochlin, D.; Kimata, K.; Kato, M.; Suzuki, S.; Hassell, J.; Wight, T. N. The presence of heparan sulfate proteoglycans in the neuritic plaques and congophilic angiopathy in Alzheimer's disease. *Am. J. Pathol.* **1988**, *133*, 456-463.
- 87 Abdul Latif, A. R.; Kono, R.; Tachibana, H.; Akasaka, K. Kinetic analysis of amyloid protofibril dissociation and volumetric properties of the transition state. *Biophys. J.* **2007**, *92*, 323-329. DOI: 10.1529/biophysj.106.088120.
- 88 Nespovitaya, N.; Gath, J.; Barylyuk, K.; Seuring, C.; Meier, B. H.; Riek, R. Dynamic Assembly and Disassembly of Functional β -Endorphin Amyloid Fibrils. *J. Am. Chem. Soc.* **2016**, *138*, 846-856. DOI: 10.1021/jacs.5b08694.
- 89 Wentink, A.; Nussbaum-Krammer, C.; Bukau, B. Modulation of Amyloid States by Molecular Chaperones. *Cold Spring Harb. Perspect. Biol.* **2019**, *11*. DOI: 10.1101/cshperspect.a033969.
- 90 Geraghty, N. J.; Satapathy, S.; Kelly, M.; Cheng, F.; Lee, A.; Wilson, M. R. Expanding the family of extracellular chaperones: Identification of human plasma proteins with chaperone activity. *Protein Sci.* **2021**, *30*, 2272-2286. DOI: 10.1002/pro.4189.
- 91 Jacob, R. S.; Anoop, A.; Maji, S. K. Protein Nanofibrils as Storage Forms of Peptide Drugs and Hormones. In *Biological and Bio-inspired Nanomaterials: Properties and Assembly Mechanisms*, Perrett, S., Buell, A. K., Knowles, T. P. J. Eds.; Springer Singapore, 2019; pp 265-290.
- 92 Badtke, M. P.; Hammer, N. D.; Chapman, M. R. Functional Amyloids Signal Their Arrival. *Sci. Signaling* **2009**, *2*, pe43-pe43. DOI: 10.1126/scisignal.280pe43.
- 93 Beuret, N.; Hasler, F.; Prescianotto-Baschong, C.; Birk, J.; Rutishauser, J.; Spiess, M. Amyloid-like aggregation of provasopressin in diabetes insipidus and secretory granule sorting. *BMC Biol.* **2017**, *15*, 5. DOI: 10.1186/s12915-017-0347-9.
- 94 Berson, J. F.; Theos, A. C.; Harper, D. C.; Tenza, D.; Raposo, G.; Marks, M. S. Proprotein convertase cleavage liberates a fibrillogenic fragment of a resident glycoprotein to initiate melanosome biogenesis. *J. Cell. Biol.* **2003**, *161*, 521-533. DOI: 10.1083/jcb.200302072.

- 95 Wang, X.; Zhou, Y.; Ren, J. J.; Hammer, N. D.; Chapman, M. R. Gatekeeper residues in the major curlin subunit modulate bacterial amyloid fiber biogenesis. *Proc. Natl. Acad. Sci. U.S.A.* **2010**, *107*, 163-168. DOI: 10.1073/pnas.0908714107.
- 96 Jackson, M. P.; Hewitt, E. W. Why are Functional Amyloids Non-Toxic in Humans? *Biomolecules* **2017**, *7*, 71. DOI: 10.3390/biom7040071.
- 97 Hervás, R.; Li, L.; Majumdar, A.; Fernández-Ramírez Mdel, C.; Unruh, J. R.; Slaughter, B. D.; Galera-Prat, A.; Santana, E.; Suzuki, M.; Nagai, Y.; Bruix, M.; Casas-Tintó, S.; Menéndez, M.; Laurents, D. V.; Si, K.; Carrión-Vázquez, M. Molecular Basis of Orb2 Amyloidogenesis and Blockade of Memory Consolidation. *PLoS Biol.* **2016**, *14*, e1002361. DOI: 10.1371/journal.pbio.1002361.
- 98 Andreasen, M.; Meisl, G.; Taylor, J. D.; Michaels, T. C. T.; Levin, A.; Otzen, D. E.; Chapman, M. R.; Dobson, C. M.; Matthews, S. J.; Knowles, T. P. J. Physical Determinants of Amyloid Assembly in Biofilm Formation. *mBio* **2019**, *10*. DOI: 10.1128/mBio.02279-18.
- 99 Ragonis-Bachar, P.; Landau, M. Functional and pathological amyloid structures in the eyes of 2020 cryo-EM. *Curr. Opin. Struct. Biol.* **2021**, *68*, 184-193. DOI: 10.1016/j.sbi.2021.01.006.
- 100 Wolynes, P. G. Evolution, energy landscapes and the paradoxes of protein folding. *Biochimie* **2015**, *119*, 218-230. DOI: 10.1016/j.biochi.2014.12.007.
- 101 Tayeb-Fligelman, E.; Tabachnikov, O.; Moshe, A.; Goldshmidt-Tran, O.; Sawaya, M. R.; Coquelle, N.; Colletier, J.-P.; Landau, M. The cytotoxic Staphylococcus aureus PSM α 3 reveals a cross- α amyloid-like fibril. *Science* **2017**, *355*, 831-833. DOI: 10.1126/science.aaf4901.
- 102 Lu, J. X.; Qiang, W.; Yau, W. M.; Schwieters, C. D.; Meredith, S. C.; Tycko, R. Molecular structure of β -amyloid fibrils in Alzheimer's disease brain tissue. *Cell* **2013**, *154*, 1257-1268. DOI: 10.1016/j.cell.2013.08.035.
- 103 Paravastu, A. K.; Leapman, R. D.; Yau, W. M.; Tycko, R. Molecular structural basis for polymorphism in Alzheimer's beta-amyloid fibrils. *Proc. Natl. Acad. Sci. U.S.A.* **2008**, *105*, 18349-18354. DOI: 10.1073/pnas.0806270105.
- 104 Ghosh, U.; Thurber, K. R.; Yau, W. M.; Tycko, R. Molecular structure of a prevalent amyloid- β fibril polymorph from Alzheimer's disease brain tissue. *Proc. Natl. Acad. Sci. U.S.A.* **2021**, *118*. DOI: 10.1073/pnas.2023089118.
- 105 Kollmer, M.; Close, W.; Funk, L.; Rasmussen, J.; Bsoul, A.; Schierhorn, A.; Schmidt, M.; Sigurdson, C. J.; Jucker, M.; Fändrich, M. Cryo-EM structure and polymorphism of A β amyloid fibrils purified from Alzheimer's brain tissue. *Nat. Commun.* **2019**, *10*, 4760. DOI: 10.1038/s41467-019-12683-8.
- 106 Salinas, N.; Tayeb-Fligelman, E.; Sammito, M. D.; Bloch, D.; Jelinek, R.; Noy, D.; Usón, I.; Landau, M. The amphibian antimicrobial peptide uperin 3.5 is a cross- α /cross- β chameleon functional amyloid. *Proc. Natl. Acad. Sci. U.S.A.* **2021**, *118*. DOI: 10.1073/pnas.2014442118.
- 107 Kreplak, L.; Aebi, U. From the Polymorphism of Amyloid Fibrils to their Assembly Mechanism and Cytotoxicity. *Adv. Protein Chem.* **2006**, *73*, 217-233. DOI: 10.1016/S0065-3233(06)73007-8.
- 108 Röder, C.; Kupreichyk, T.; Gremer, L.; Schäfer, L. U.; Pothula, K. R.; Ravelli, R. B. G.; Willbold, D.; Hoyer, W.; Schröder, G. F. Cryo-EM structure of islet amyloid polypeptide fibrils reveals similarities with amyloid- β fibrils. *Nat. Struct. Mol. Biol.* **2020**, *27*, 660-667. DOI: 10.1038/s41594-020-0442-4.
- 109 Fändrich, M.; Nyström, S.; Nilsson, K. P. R.; Böckmann, A.; LeVine III, H.; Hammarström, P. Amyloid fibril polymorphism: a challenge for molecular imaging and therapy. *J. Intern. Med.* **2018**, *283*, 218-237. DOI: 10.1111/joim.12732.
- 110 Dueholm, M. S.; Nielsen, S. B.; Hein, K. L.; Nissen, P.; Chapman, M.; Christiansen, G.; Nielsen, P. H.; Otzen, D. E. Fibrillation of the major curli subunit CsgA under a wide range of conditions implies a robust design of aggregation. *Biochemistry* **2011**, *50*, 8281-8290. DOI: 10.1021/bi200967c.
- 111 Ulamec, S. M.; Radford, S. E. Spot the Difference: Function versus Toxicity in Amyloid Fibrils. *Trends Biochem. Sci.* **2020**, *45*, 635-636. DOI: 10.1016/j.tibs.2020.04.007.

- 112 Oosawa, F.; Asakura, S. *Thermodynamics of the polymerization of protein*; Academic Press, 1975.
- 113 Nielsen, L.; Khurana, R.; Coats, A.; Frokjaer, S.; Brange, J.; Vyas, S.; Uversky, V. N.; Fink, A. L. Effect of environmental factors on the kinetics of insulin fibril formation: elucidation of the molecular mechanism. *Biochemistry* **2001**, *40*, 6036-6046. DOI: 10.1021/bi002555c.
- 114 LeVine III, H. Thioflavine T interaction with synthetic Alzheimer's disease beta-amyloid peptides: detection of amyloid aggregation in solution. *Protein Sci.* **1993**, *2*, 404-410. DOI: 10.1002/pro.5560020312.
- 115 Arosio, P.; Knowles, T. P. J.; Linse, S. On the lag phase in amyloid fibril formation. *Phys. Chem. Chem. Phys.* **2015**, *17*, 7606-7618. DOI: 10.1039/c4cp05563b.
- 116 Meisl, G.; Rajah, L.; Cohen, S. A. I.; Pfammatter, M.; Šarić, A.; Hellstrand, E.; Buell, A. K.; Aguzzi, A.; Linse, S.; Vendruscolo, M.; Dobson, C. M.; Knowles, T. P. J. Scaling behaviour and rate-determining steps in filamentous self-assembly. *Chem. Sci.* **2017**, *8*, 7087-7097. DOI: 10.1039/c7sc01965c.
- 117 Lomakin, A.; Teplow, D. B.; Kirschner, D. A.; Benedek, G. B. Kinetic theory of fibrillogenesis of amyloid beta-protein. *Proc. Natl. Acad. Sci. U.S.A.* **1997**, *94*, 7942-7947. DOI: 10.1073/pnas.94.15.7942.
- 118 Cohen, S. I.; Vendruscolo, M.; Welland, M. E.; Dobson, C. M.; Terentjev, E. M.; Knowles, T. P. J. Nucleated polymerization with secondary pathways. I. Time evolution of the principal moments. *J. Chem. Phys.* **2011**, *135*, 065105. DOI: 10.1063/1.3608916.
- 119 Knowles, T. P. J.; Waudby, C. A.; Devlin, G. L.; Cohen, S. I.; Aguzzi, A.; Vendruscolo, M.; Terentjev, E. M.; Welland, M. E.; Dobson, C. M. An analytical solution to the kinetics of breakable filament assembly. *Science* **2009**, *326*, 1533-1537. DOI: 10.1126/science.1178250.
- 120 Michaels, T. C. T.; Šarić, A.; Habchi, J.; Chia, S.; Meisl, G.; Vendruscolo, M.; Dobson, C. M.; Knowles, T. P. J. Chemical Kinetics for Bridging Molecular Mechanisms and Macroscopic Measurements of Amyloid Fibril Formation. *Annu. Rev. Phys. Chem.* **2018**, *69*, 273-298. DOI: 10.1146/annurev-physchem-050317-021322.
- 121 Cohen, S. I. A.; Linse, S.; Luheshi, L. M.; Hellstrand, E.; White, D. A.; Rajah, L.; Otzen, D. E.; Vendruscolo, M.; Dobson, C. M.; Knowles, T. P. J. Proliferation of amyloid- β 42 aggregates occurs through a secondary nucleation mechanism. *Proc. Natl. Acad. Sci. U.S.A.* **2013**, *110*, 9758-9763. DOI: 10.1073/pnas.1218402110.
- 122 Lorenzen, N.; Cohen, S. I.; Nielsen, S. B.; Herling, T. W.; Christiansen, G.; Dobson, C. M.; Knowles, T. P. J.; Otzen, D. Role of elongation and secondary pathways in S6 amyloid fibril growth. *Biophys. J.* **2012**, *102*, 2167-2175. DOI: 10.1016/j.bpj.2012.03.047.
- 123 Meisl, G.; Yang, X.; Dobson, C. M.; Linse, S.; Knowles, T. P. J. Modulation of electrostatic interactions to reveal a reaction network unifying the aggregation behaviour of the A β 42 peptide and its variants. *Chem. Sci.* **2017**, *8*, 4352-4362, 10.1039/C7SC00215G. DOI: 10.1039/C7SC00215G.
- 124 Eden, K.; Morris, R.; Gillam, J.; MacPhee, C. E.; Allen, R. J. Competition between primary nucleation and autocatalysis in amyloid fibril self-assembly. *Biophys. J.* **2015**, *108*, 632-643. DOI: 10.1016/j.bpj.2014.11.3465.
- 125 Šarić, A.; Buell, A. K.; Meisl, G.; Michaels, T. C. T.; Dobson, C. M.; Linse, S.; Knowles, T. P. J.; Frenkel, D. Physical determinants of the self-replication of protein fibrils. *Nat. Phys.* **2016**, *12*, 874-880. DOI: 10.1038/nphys3828.
- 126 Šarić, A.; Michaels, T. C. T.; Zaccone, A.; Knowles, T. P. J.; Frenkel, D. Kinetics of spontaneous filament nucleation via oligomers: Insights from theory and simulation. *J. Chem. Phys.* **2016**, *145*. DOI: 10.1063/1.4965040.
- 127 Ziaunys, M.; Sneideris, T.; Smirnovas, V. Self-inhibition of insulin amyloid-like aggregation. *Phys. Chem. Chem. Phys.* **2018**, *20*, 27638-27645. DOI: 10.1039/c8cp04838j.
- 128 Elenbaas, B. O. W.; Khemtournian, L.; Killian, J. A.; Sinnige, T. Membrane-Catalyzed Aggregation of Islet Amyloid Polypeptide Is Dominated by Secondary Nucleation. *Biochemistry* **2022**, *61*, 1465-1472. DOI: 10.1021/acs.biochem.2c00184.

- 129 Brender, J. R.; Krishnamoorthy, J.; Sciacca, M. F. M.; Vivekanandan, S.; D'Urso, L.; Chen, J.; La Rosa, C.; Ramamoorthy, A. Probing the Sources of the Apparent Irreproducibility of Amyloid Formation: Drastic Changes in Kinetics and a Switch in Mechanism Due to Micellelike Oligomer Formation at Critical Concentrations of IAPP. *J. Phys. Chem. B* **2015**, *119*, 2886-2896. DOI: 10.1021/jp511758w.
- 130 Jarrett, J. T.; Lansbury, P. T. J. Seeding "one-dimensional crystallization" of amyloid: a pathogenic mechanism in Alzheimer's disease and scrapie? *Cell* **1993**, *73*, 1055-1058. DOI: 10.1016/0092-8674(93)90635-4.
- 131 Waxman, E. A.; Giasson, B. I. Induction of intracellular tau aggregation is promoted by α -synuclein seeds and provides novel insights into the hyperphosphorylation of tau. *J. Neurosci.* **2011**, *31*, 7604-7618. DOI: 10.1523/jneurosci.0297-11.2011.
- 132 Törner, R.; Kupreichyk, T.; Gremer, L.; Debled, E. C.; Fenel, D.; Schemmert, S.; Gans, P.; Willbold, D.; Schoehn, G.; Hoyer, W.; Boisbouvier, J. Structural basis for the inhibition of IAPP fibril formation by the co-chaperonin prefoldin. *Nat. Commun.* **2022**, *13*, 2363. DOI: 10.1038/s41467-022-30042-y.
- 133 Cohen, S. I.; Vendruscolo, M.; Dobson, C. M.; Knowles, T. P. J. Nucleated polymerisation in the presence of pre-formed seed filaments. *Int. J. Mol. Sci.* **2011**, *12*, 5844-5852. DOI: 10.3390/ijms12095844.
- 134 Chatani, E.; Lee, Y.-H.; Yagi, H.; Yoshimura, Y.; Naiki, H.; Goto, Y. Ultrasonication-dependent production and breakdown lead to minimum-sized amyloid fibrils. *Proc. Natl. Acad. Sci. U.S.A.* **2009**, *106*, 11119-11124. DOI: 10.1073/pnas.0901422106.
- 135 Arosio, P.; Cukalevski, R.; Frohm, B.; Knowles, T. P. J.; Linse, S. Quantification of the concentration of A β 42 propagons during the lag phase by an amyloid chain reaction assay. *J. Am. Chem. Soc.* **2014**, *136*, 219-225. DOI: 10.1021/ja408765u.
- 136 Rodriguez Camargo, D. C.; Sileikis, E.; Chia, S.; Axell, E.; Bernfur, K.; Cataldi, R. L.; Cohen, S. I. A.; Meisl, G.; Habchi, J.; Knowles, T. P. J.; Vendruscolo, M.; Linse, S. Proliferation of Tau 304-380 Fragment Aggregates through Autocatalytic Secondary Nucleation. *ACS Chem. Neurosci.* **2021**, *12*, 4406-4415. DOI: 10.1021/acscchemneuro.1c00454.
- 137 Buell, A. K. The growth of amyloid fibrils: rates and mechanisms. *Biochem. J.* **2019**, *476*, 2677-2703. DOI: 10.1042/bcj20160868.
- 138 Karamanos, T. K.; Jackson, M. P.; Calabrese, A. N.; Goodchild, S. C.; Cawood, E. E.; Thompson, G. S.; Kalverda, A. P.; Hewitt, E. W.; Radford, S. E. Structural mapping of oligomeric intermediates in an amyloid assembly pathway. *Elife* **2019**, *8*. DOI: 10.7554/eLife.46574.
- 139 Meisl, G.; Yang, X.; Hellstrand, E.; Frohm, B.; Kirkegaard, J. B.; Cohen, S. I.; Dobson, C. M.; Linse, S.; Knowles, T. P. J. Differences in nucleation behavior underlie the contrasting aggregation kinetics of the A β 40 and A β 42 peptides. *Proc. Natl. Acad. Sci. U.S.A.* **2014**, *111*, 9384-9389. DOI: 10.1073/pnas.1401564111.
- 140 Cohen, S. I.; Vendruscolo, M.; Dobson, C. M.; Knowles, T. P. J. From macroscopic measurements to microscopic mechanisms of protein aggregation. *J. Mol. Biol.* **2012**, *421*, 160-171. DOI: 10.1016/j.jmb.2012.02.031.
- 141 Peng, Z.; Parker, A. S.; Peralta, M. D. R.; Ravikumar, K. M.; Cox, D. L.; Toney, M. D. High Tensile Strength of Engineered β -Solenoid Fibrils via Sonication and Pulling. *Biophys. J.* **2017**, *113*, 1945-1955. DOI: 10.1016/j.bpj.2017.09.003.
- 142 Meisl, G.; Kirkegaard, J. B.; Arosio, P.; Michaels, T. C. T.; Vendruscolo, M.; Dobson, C. M.; Linse, S.; Knowles, T. P. J. Molecular mechanisms of protein aggregation from global fitting of kinetic models. *Nat. Protoc.* **2016**, *11*, 252-272. DOI: 10.1038/nprot.2016.010.
- 143 Dear, A. J.; Meisl, G.; Šarić, A.; Michaels, T. C. T.; Kjaergaard, M.; Linse, S.; Knowles, T. P. J. Identification of on- and off-pathway oligomers in amyloid fibril formation. *Chem. Sci.* **2020**, *11*, 6236-6247. DOI: 10.1039/c9sc06501f.
- 144 Muschol, M.; Hoyer, W. Amyloid oligomers as on-pathway precursors or off-pathway competitors of fibrils. *Front. Mol. Biosci.* **2023**, *10*, 1120416. DOI: 10.3389/fmolb.2023.1120416.

- 145 Michaels, T. C. T.; Šarić, A.; Curk, S.; Bernfur, K.; Arosio, P.; Meisl, G.; Dear, A. J.; Cohen, S. I. A.; Dobson, C. M.; Vendruscolo, M.; Linse, S.; Knowles, T. P. J. Dynamics of oligomer populations formed during the aggregation of Alzheimer's A β 42 peptide. *Nat. Chem.* **2020**, *12*, 445-451. DOI: 10.1038/s41557-020-0452-1.
- 146 Iljina, M.; Garcia, G. A.; Horrocks, M. H.; Tosatto, L.; Choi, M. L.; Ganzinger, K. A.; Abramov, A. Y.; Gandhi, S.; Wood, N. W.; Cremades, N.; Dobson, C. M.; Knowles, T. P. J.; Klenerman, D. Kinetic model of the aggregation of alpha-synuclein provides insights into prion-like spreading. *Proc. Natl. Acad. Sci. U.S.A.* **2016**, *113*, E1206-1215. DOI: 10.1073/pnas.1524128113.
- 147 Kjaergaard, M.; Dear, A. J.; Kundel, F.; Qamar, S.; Meisl, G.; Knowles, T. P. J.; Klenerman, D. Oligomer Diversity during the Aggregation of the Repeat Region of Tau. *ACS Chem. Neurosci.* **2018**, *9*, 3060-3071. DOI: 10.1021/acscchemneuro.8b00250.
- 148 Powers, E. T.; Powers, D. L. Mechanisms of protein fibril formation: nucleated polymerization with competing off-pathway aggregation. *Biophys. J.* **2008**, *94*, 379-391. DOI: 10.1529/biophysj.107.117168.
- 149 Perez, C.; Miti, T.; Hasecke, F.; Meisl, G.; Hoyer, W.; Muschol, M.; Ullah, G. Mechanism of Fibril and Soluble Oligomer Formation in Amyloid Beta and Hen Egg White Lysozyme Proteins. *J. Phys. Chem. B* **2019**, *123*, 5678-5689. DOI: 10.1021/acs.jpcc.9b02338.
- 150 Buell, A. K.; Dhulesia, A.; White, D. A.; Knowles, T. P. J.; Dobson, C. M.; Welland, M. E. Detailed analysis of the energy barriers for amyloid fibril growth. *Angew. Chem. Int. Ed.* **2012**, *51*, 5247-5251. DOI: 10.1002/anie.201108040.
- 151 Buell, A. K.; Dobson, C. M.; Knowles, T. P. J. The physical chemistry of the amyloid phenomenon: thermodynamics and kinetics of filamentous protein aggregation. *Essays Biochem.* **2014**, *56*, 11-39. DOI: 10.1042/bse0560011.
- 152 Sear, R. P. Nucleation: theory and applications to protein solutions and colloidal suspensions. *J. Phys. Condens. Matter* **2007**, *19*, 033101. DOI: 10.1088/0953-8984/19/3/033101.
- 153 Lee, J.; Culyba, E. K.; Powers, E. T.; Kelly, J. W. Amyloid- β forms fibrils by nucleated conformational conversion of oligomers. *Nat. Chem. Biol.* **2011**, *7*, 602-609. DOI: 10.1038/nchembio.624.
- 154 Serio, T. R.; Cashikar, A. G.; Kowal, A. S.; Sawicki, G. J.; Moslehi, J. J.; Serpell, L.; Arnsdorf, M. F.; Lindquist, S. L. Nucleated conformational conversion and the replication of conformational information by a prion determinant. *Science* **2000**, *289*, 1317-1321. DOI: 10.1126/science.289.5483.1317.
- 155 Hall, Z.; Schmidt, C.; Politis, A. Uncovering the Early Assembly Mechanism for Amyloidogenic β 2-Microglobulin Using Cross-linking and Native Mass Spectrometry. *J. Biol. Chem.* **2016**, *291*, 4626-4637. DOI: 10.1074/jbc.M115.691063.
- 156 Ceccon, A.; Tugarinov, V.; Clore, G. M. Kinetics of Fast Tetramerization of the Huntingtin Exon 1 Protein Probed by Concentration-Dependent On-Resonance R(1 ρ) Measurements. *J. Phys. Chem. Lett.* **2020**, *11*, 5643-5648. DOI: 10.1021/acs.jpcclett.0c01636.
- 157 Ceccon, A.; Tugarinov, V.; Ghirlando, R.; Clore, G. M. Abrogation of prenucleation, transient oligomerization of the Huntingtin exon 1 protein by human profilin I. *Proc. Natl. Acad. Sci. U.S.A.* **2020**, *117*, 5844-5852. DOI: 10.1073/pnas.1922264117.
- 158 Ceccon, A.; Tugarinov, V.; Torricella, F.; Clore, G. M. Quantitative NMR analysis of the kinetics of prenucleation oligomerization and aggregation of pathogenic huntingtin exon-1 protein. *Proc. Natl. Acad. Sci. U.S.A.* **2022**, *119*, e2207690119. DOI: 10.1073/pnas.2207690119.
- 159 Kotler, S. A.; Tugarinov, V.; Schmidt, T.; Ceccon, A.; Libich, D. S.; Ghirlando, R.; Schwieters, C. D.; Clore, G. M. Probing initial transient oligomerization events facilitating Huntingtin fibril nucleation at atomic resolution by relaxation-based NMR. *Proc. Natl. Acad. Sci. U.S.A.* **2019**, *116*, 3562-3571. DOI: 10.1073/pnas.1821216116.
- 160 Cline, E. N.; Bicca, M. A.; Viola, K. L.; Klein, W. L. The Amyloid- β Oligomer Hypothesis: Beginning of the Third Decade. *J. Alzheimer's Dis.* **2018**, *64*, S567-S610. DOI: 10.3233/JAD-179941.
- 161 Michaels, T. C. T.; Knowles, T. P. J. Mean-field master equation formalism for biofilament growth. *Am. J. Phys.* **2014**, *82*, 476-483. DOI: 10.1119/1.4870004.

- 162 Krapivsky, P. L.; Redner, S.; Ben-Naim, E. *A kinetic view of statistical physics*; Cambridge University Press, 2010.
- 163 Cohen, S. I.; Vendruscolo, M.; Dobson, C. M.; Knowles, T. P. J. Nucleated polymerization with secondary pathways. II. Determination of self-consistent solutions to growth processes described by non-linear master equations. *J. Chem. Phys.* **2011**, *135*, 065106. DOI: 10.1063/1.3608917.
- 164 Michaels, T. C. T.; Lazell, H. W.; Arosio, P.; Knowles, T. P. J. Dynamics of protein aggregation and oligomer formation governed by secondary nucleation. *J. Chem. Phys.* **2015**, *143*. DOI: 10.1063/1.4927655.
- 165 Oosawa, F.; Kasai, M. A theory of linear and helical aggregations of macromolecules. *J. Mol. Biol.* **1962**, *4*, 10-21. DOI: 10.1016/s0022-2836(62)80112-0.
- 166 Auer, S.; Dobson, C. M.; Vendruscolo, M. Characterization of the nucleation barriers for protein aggregation and amyloid formation. *HFSP J.* **2007**, *1*, 137-146. DOI: 10.2976/1.2760023.
- 167 Lee, C. T.; Terentjev, E. M. Mechanisms and rates of nucleation of amyloid fibrils. *J. Chem. Phys.* **2017**, *147*, 105103. DOI: 10.1063/1.4995255.
- 168 Šarić, A.; Chebaro, Y. C.; Knowles, T. P. J.; Frenkel, D. Crucial role of nonspecific interactions in amyloid nucleation. *Proc. Natl. Acad. Sci. U.S.A.* **2014**, *111*, 17869-17874. DOI: 10.1073/pnas.1410159111.
- 169 Šarić, A.; Michaels, T. C. T.; Zaccone, A.; Knowles, T. P. J.; Frenkel, D. Kinetics of spontaneous filament nucleation via oligomers: Insights from theory and simulation. *J. Chem. Phys.* **2016**, *145*, 211926. DOI: 10.1063/1.4965040.
- 170 Vekilov, P. G. The two-step mechanism of nucleation of crystals in solution. *Nanoscale* **2010**, *2*, 2346-2357. DOI: 10.1039/c0nr00628a.
- 171 Dear, A. J.; Michaels, T. C. T.; Meisl, G.; Klenerman, D.; Wu, S.; Perrett, S.; Linse, S.; Dobson, C. M.; Knowles, T. P. J. Kinetic diversity of amyloid oligomers. *Proc. Natl. Acad. Sci. U.S.A.* **2020**, *117*, 12087-12094. DOI: 10.1073/pnas.1922267117.
- 172 Harper, J. D.; Lansbury, P. T. J. Models of amyloid seeding in Alzheimer's disease and scrapie: mechanistic truths and physiological consequences of the time-dependent solubility of amyloid proteins. *Annu. Rev. Biochem.* **1997**, *66*, 385-407. DOI: 10.1146/annurev.biochem.66.1.385.
- 173 O'Nuallain, B.; Shivaprasad, S.; Kheterpal, I.; Wetzel, R. Thermodynamics of A β (1-40) Amyloid Fibril Elongation. *Biochemistry* **2005**, *44*, 12709-12718. DOI: 10.1021/bi050927h.
- 174 Wetzel, R. Kinetics and Thermodynamics of Amyloid Fibril Assembly. *Acc. Chem. Res.* **2006**, *39*, 671-679. DOI: 10.1021/ar050069h.
- 175 Baldwin, A. J.; Knowles, T. P. J.; Tartaglia, G. G.; Fitzpatrick, A. W.; Devlin, G. L.; Shamma, S. L.; Waudby, C. A.; Mossuto, M. F.; Meehan, S.; Gras, S. L.; Christodoulou, J.; Anthony-Cahill, S. J.; Barker, P. D.; Vendruscolo, M.; Dobson, C. M. Metastability of Native Proteins and the Phenomenon of Amyloid Formation. *J. Am. Chem. Soc.* **2011**, *133*, 14160-14163. DOI: 10.1021/ja2017703.
- 176 So, M.; Hall, D.; Goto, Y. Revisiting supersaturation as a factor determining amyloid fibrillation. *Curr. Opin. Struct. Biol.* **2016**, *36*, 32-39. DOI: 10.1016/j.sbi.2015.11.009.
- 177 Crespo, R.; Rocha, F. A.; Damas, A. M.; Martins, P. M. A generic crystallization-like model that describes the kinetics of amyloid fibril formation. *J. Biol. Chem.* **2012**, *287*, 30585-30594. DOI: 10.1074/jbc.M112.375345.
- 178 Hasegawa, K.; Ono, K.; Yamada, M.; Naiki, H. Kinetic Modeling and Determination of Reaction Constants of Alzheimer's β -Amyloid Fibril Extension and Dissociation Using Surface Plasmon Resonance. *Biochemistry* **2002**, *41*, 13489-13498. DOI: 10.1021/bi020369w.
- 179 Agus, Z. S.; Gardner, L. B.; Beck, L. H.; Goldberg, M. Effects of parathyroid hormone on renal tubular reabsorption of calcium, sodium, and phosphate. *Am. J. Physiol.* **1973**, *224*, 1143-1148. DOI: 10.1152/ajplegacy.1973.224.5.1143.
- 180 MacGregor, R. R.; Cohn, D. V. The intracellular pathway for parathormone biosynthesis and secretion. *Clin. Orthop. Relat. Res.* **1978**, 244-258.

- 181 Habener, J. F.; Potts, J. T. J. Biosynthesis of parathyroid hormone (first of two parts). *N. Engl. J. Med.* **1978**, *299*, 580-585. DOI: 10.1056/nejm197809142991105.
- 182 Wiren, K. M.; Potts, J. T. J.; Kronenberg, H. M. Importance of the propeptide sequence of human preproparathyroid hormone for signal sequence function. *J. Biol. Chem.* **1988**, *263*, 19771-19777.
- 183 Kritmetapak, K.; Pongchaiyakul, C. Parathyroid Hormone Measurement in Chronic Kidney Disease: From Basics to Clinical Implications. *Int. J. Nephrol.* **2019**, *2019*, 5496710. DOI: 10.1155/2019/5496710.
- 184 Naveh-Many, T.; Silver, J. Regulation of parathyroid hormone gene expression by hypocalcemia, hypercalcemia, and vitamin D in the rat. *J. Clin. Invest.* **1990**, *86*, 1313-1319. DOI: 10.1172/jci114840.
- 185 Kilav, R.; Silver, J.; Naveh-Many, T. A conserved cis-acting element in the parathyroid hormone 3'-untranslated region is sufficient for regulation of RNA stability by calcium and phosphate. *J. Biol. Chem.* **2001**, *276*, 8727-8733. DOI: 10.1074/jbc.M005471200.
- 186 Zhang, C. X.; Weber, B. V.; Thammavong, J.; Grover, T. A.; Wells, D. S. Identification of carboxyl-terminal peptide fragments of parathyroid hormone in human plasma at low-picomolar levels by mass spectrometry. *Anal. Chem.* **2006**, *78*, 1636-1643. DOI: 10.1021/ac051711o.
- 187 Kremer, R.; Bolivar, I.; Goltzman, D.; Hendy, G. N. Influence of Calcium and 1,25-Dihydroxycholecalciferol on Proliferation and Proto-Oncogene Expression in Primary Cultures of Bovine Parathyroid Cells. *Endocrinology* **1989**, *125*, 935-941. DOI: 10.1210/endo-125-2-935.
- 188 Goltzman, D. Physiology of Parathyroid Hormone. *Endocrinol. Metab. Clin. N. Am.* **2018**, *47*, 743-758. DOI: 10.1016/j.ecl.2018.07.003.
- 189 Abou-Samra, A. B.; Jüppner, H.; Force, T.; Freeman, M. W.; Kong, X. F.; Schipani, E.; Urena, P.; Richards, J.; Bonventre, J. V.; Potts, J. T. J.; et al. Expression cloning of a common receptor for parathyroid hormone and parathyroid hormone-related peptide from rat osteoblast-like cells: a single receptor stimulates intracellular accumulation of both cAMP and inositol trisphosphates and increases intracellular free calcium. *Proc. Natl. Acad. Sci. U.S.A.* **1992**, *89*, 2732-2736. DOI: 10.1073/pnas.89.7.2732.
- 190 Jüppner, H.; Abou-Samra, A. B.; Freeman, M.; Kong, X. F.; Schipani, E.; Richards, J.; Kolakowski, L. F. J.; Hock, J.; Potts, J. T. J.; Kronenberg, H. M.; et al. A G protein-linked receptor for parathyroid hormone and parathyroid hormone-related peptide. *Science* **1991**, *254*, 1024-1026. DOI: 10.1126/science.1658941.
- 191 Tregear, G. W.; Van Rietschoten, J.; Greene, E.; Keutmann, H. T.; Niall, H. D.; Reit, B.; Parsons, J. A.; Potts, J. T. J. Bovine parathyroid hormone: minimum chain length of synthetic peptide required for biological activity. *Endocrinology* **1973**, *93*, 1349-1353. DOI: 10.1210/endo-93-6-1349.
- 192 Gardella, T. J.; Wilson, A. K.; Keutmann, H. T.; Oberstein, R.; Potts, J. T. J.; Kronenberg, M.; Nussbaum, S. R. Analysis of parathyroid hormone's principal receptor-binding region by site-directed mutagenesis and analog design. *Endocrinology* **1993**, *132*, 2024-2030. DOI: 10.1210/endo.132.5.8386605.
- 193 Shimizu, M.; Potts, J. T. J.; Gardella, T. J. Minimization of parathyroid hormone. Novel amino-terminal parathyroid hormone fragments with enhanced potency in activating the type-1 parathyroid hormone receptor. *J. Biol. Chem.* **2000**, *275*, 21836-21843. DOI: 10.1074/jbc.M909861199.
- 194 Li, X.; Liu, H.; Qin, L.; Tamasi, J.; Bergenstock, M.; Shapses, S.; Feyen, J. H.; Notterman, D. A.; Partridge, N. C. Determination of dual effects of parathyroid hormone on skeletal gene expression in vivo by microarray and network analysis. *J. Biol. Chem.* **2007**, *282*, 33086-33097. DOI: 10.1074/jbc.M705194200.
- 195 Usdin, T. B. The PTH2 receptor and TIP39: a new peptide-receptor system. *Trends Pharmacol. Sci.* **2000**, *21*, 128-130. DOI: 10.1016/s0165-6147(00)01455-3.
- 196 Ullrich, K. J.; Rumrich, G.; Klöss, S. Active Ca²⁺ reabsorption in the proximal tubule of the rat kidney. Dependence on sodium- and buffer transport. *Pflugers Arch.* **1976**, *364*, 223-228. DOI: 10.1007/bf00581759.

- 197 Brenza, H. L.; Kimmel-Jehan, C.; Jehan, F.; Shinki, T.; Wakino, S.; Anazawa, H.; Suda, T.; DeLuca, H. F. Parathyroid hormone activation of the 25-hydroxyvitamin D3-1 α -hydroxylase gene promoter. *Proc. Natl. Acad. Sci. U.S.A.* **1998**, *95*, 1387-1391. DOI: 10.1073/pnas.95.4.1387.
- 198 Lombardi, G.; Ziemann, E.; Banfi, G.; Corbetta, S. Physical Activity-Dependent Regulation of Parathyroid Hormone and Calcium-Phosphorous Metabolism. *Int. J. Mol. Sci.* **2020**, *21*, 5388. DOI: 10.3390/ijms21155388.
- 199 Bisello, A.; Friedman, P. A. Parathyroid hormone and parathyroid hormone-related protein actions on bone and kidney. In *Principles of Bone Biology (Fourth Edition)*, Bilezikian, J. P., Martin, T. J., Clemens, T. L., Rosen, C. J. Eds.; Academic Press, 2020; pp 645-689.
- 200 Lee, M.; Partridge, N. C. Parathyroid hormone signaling in bone and kidney. *Curr. Opin. Nephrol. Hypertens.* **2009**, *18*, 298-302. DOI: 10.1097/MNH.0b013e32832c2264.
- 201 Simonet, W. S.; Lacey, D. L.; Dunstan, C. R.; Kelley, M.; Chang, M. S.; Lüthy, R.; Nguyen, H. Q.; Wooden, S.; Bennett, L.; Boone, T.; Shimamoto, G.; DeRose, M.; Elliott, R.; Colombero, A.; Tan, H. L.; Trail, G.; Sullivan, J.; Davy, E.; Bucay, N.; Renshaw-Gegg, L.; Hughes, T. M.; Hill, D.; Pattison, W.; Campbell, P.; Sander, S.; Van, G.; Tarpley, J.; Derby, P.; Lee, R.; Boyle, W. J. Osteoprotegerin: a novel secreted protein involved in the regulation of bone density. *Cell* **1997**, *89*, 309-319. DOI: 10.1016/s0092-8674(00)80209-3.
- 202 Burgess, T. L.; Qian, Y.; Kaufman, S.; Ring, B. D.; Van, G.; Capparelli, C.; Kelley, M.; Hsu, H.; Boyle, W. J.; Dunstan, C. R.; Hu, S.; Lacey, D. L. The ligand for osteoprotegerin (OPGL) directly activates mature osteoclasts. *J. Cell Biol.* **1999**, *145*, 527-538. DOI: 10.1083/jcb.145.3.527.
- 203 Huang, J. C.; Sakata, T.; Pflieger, L. L.; Bencsik, M.; Halloran, B. P.; Bikle, D. D.; Nissenson, R. A. PTH Differentially Regulates Expression of RANKL and OPG. *J. Bone Miner. Res.* **2004**, *19*, 235-244. DOI: 10.1359/JBMR.0301226.
- 204 Dobnig, H.; Turner, R. T. The effects of programmed administration of human parathyroid hormone fragment (1-34) on bone histomorphometry and serum chemistry in rats. *Endocrinology* **1997**, *138*, 4607-4612. DOI: 10.1210/endo.138.11.5505.
- 205 Silva, B. C.; Bilezikian, J. P. Parathyroid hormone: anabolic and catabolic actions on the skeleton. *Curr. Opin. Pharmacol.* **2015**, *22*, 41-50. DOI: 10.1016/j.coph.2015.03.005.
- 206 Orwoll, E. S.; Shapiro, J.; Veith, S.; Wang, Y.; Lapidus, J.; Vanek, C.; Reeder, J. L.; Keaveny, T. M.; Lee, D. C.; Mullins, M. A.; Nagamani, S. C.; Lee, B. Evaluation of teriparatide treatment in adults with osteogenesis imperfecta. *J. Clin. Invest.* **2014**, *124*, 491-498. DOI: 10.1172/jci71101.
- 207 Blick, S. K.; Dhillon, S.; Keam, S. J. Teriparatide: a review of its use in osteoporosis. *Drugs* **2008**, *68*, 2709-2737. DOI: 10.2165/0003495-200868180-00012.
- 208 Kim, E. S.; Keating, G. M. Recombinant Human Parathyroid Hormone (1-84): A Review in Hypoparathyroidism. *Drugs* **2015**, *75*, 1293-1303. DOI: 10.1007/s40265-015-0438-2.
- 209 Anderson, T. J.; Ewen, S. W. Amyloid in normal and pathological parathyroid glands. *J. Clin. Pathol.* **1974**, *27*, 656-663. DOI: 10.1136/jcp.27.8.656.
- 210 Kedar, I.; Ravid, M.; Sohar, E. In vitro synthesis of "amyloid" fibrils from insulin, calcitonin and parathormone. *Isr. J. Med. Sci.* **1976**, *12*, 1137-1140.
- 211 Gopalswamy, M.; Kumar, A.; Adler, J.; Baumann, M.; Henze, M.; Kumar, S. T.; Fändrich, M.; Scheidt, H. A.; Huster, D.; Balbach, J. Structural characterization of amyloid fibrils from the human parathyroid hormone. *Biochim. Biophys. Acta Proteins Proteom* **2015**, *1854*, 249-257. DOI: 10.1016/j.bbapap.2014.12.020.
- 212 Marx, U. C.; Adermann, K.; Bayer, P.; Forssmann, W. G.; Rösch, P. Solution structures of human parathyroid hormone fragments hPTH(1-34) and hPTH(1-39) and bovine parathyroid hormone fragment bPTH(1-37). *Biochem. Biophys. Res. Commun.* **2000**, *267*, 213-220. DOI: 10.1006/bbrc.1999.1958.
- 213 Gast, K.; Zirwer, D.; Müller-Frohne, M.; Damaschun, G. Trifluoroethanol-induced conformational transitions of proteins: insights gained from the differences between alpha-lactalbumin and ribonuclease A. *Protein Sci.* **1999**, *8*, 625-634. DOI: 10.1110/ps.8.3.625.

- 214 Goldschmidt, L.; Teng, P. K.; Riek, R.; Eisenberg, D. Identifying the amyloids, proteins capable of forming amyloid-like fibrils. *Proc. Natl. Acad. Sci. U.S.A.* **2010**, *107*, 3487-3492. DOI: 10.1073/pnas.0915166107.
- 215 Chou, P. Y.; Fasman, G. D. Prediction of the secondary structure of proteins from their amino acid sequence. *Adv. Enzymol. Relat. Areas Mol. Biol.* **1978**, *47*, 45-148. DOI: 10.1002/9780470122921.ch2.
- 216 Gasteiger, E.; Hoogland, C.; Gattiker, A.; Duvaud, S.; Wilkins, M. R.; Appel, R. D.; Bairoch, A. Protein Identification and Analysis Tools on the ExPASy Server. In *The Proteomics Protocols Handbook*, Walker, J. M. Ed.; Humana Press, 2005; pp 571-607.
- 217 Close, W.; Neumann, M.; Schmidt, A.; Hora, M.; Annamalai, K.; Schmidt, M.; Reif, B.; Schmidt, V.; Grigorieff, N.; Fändrich, M. Physical basis of amyloid fibril polymorphism. *Nat. Commun.* **2018**, *9*, 699. DOI: 10.1038/s41467-018-03164-5.
- 218 Skalidis, I.; Kyrilidis, F. L.; Tüting, C.; Hamdi, F.; Träger, T. K.; Belapure, J.; Hause, G.; Fratini, M.; O'Reilly, F. J.; Heilmann, I.; Rappsilber, J.; Kastiris, P. L. Structural analysis of an endogenous 4-megadalton succinyl-CoA-generating metabolon. *Commun. Biol.* **2023**, *6*, 552. DOI: 10.1038/s42003-023-04885-0.
- 219 Micsonai, A.; Wien, F.; Kernya, L.; Lee, Y. H.; Goto, Y.; Réfrégiers, M.; Kardos, J. Accurate secondary structure prediction and fold recognition for circular dichroism spectroscopy. *Proc. Natl. Acad. Sci. U.S.A.* **2015**, *112*, E3095-3103. DOI: 10.1073/pnas.1500851112.
- 220 Hasecke, F.; Niyangoda, C.; Borjas, G.; Pan, J.; Matthews, G.; Muschol, M.; Hoyer, W. Protofibril-Fibril Interactions Inhibit Amyloid Fibril Assembly by Obstructing Secondary Nucleation. *Angew. Chem. Int. Ed.* **2021**, *60*, 3016-3021. DOI: 10.1002/anie.202010098.
- 221 Afitska, K.; Fucikova, A.; Shvadchak, V. V.; Yushchenko, D. A. α -Synuclein aggregation at low concentrations. *Biochim. Biophys. Acta Proteins Proteom* **2019**, *1867*, 701-709. DOI: 10.1016/j.bbapap.2019.05.003.
- 222 Young, L. J.; Kaminski Schierle, G. S.; Kaminski, C. F. Imaging A β (1-42) fibril elongation reveals strongly polarised growth and growth incompetent states. *Phys. Chem. Chem. Phys.* **2017**, *19*, 27987-27996, 10.1039/C7CP03412A. DOI: 10.1039/C7CP03412A.
- 223 Sidhu, A.; Vaneyck, J.; Blum, C.; Segers-Nolten, I.; Subramaniam, V. Polymorph-specific distribution of binding sites determines thioflavin-T fluorescence intensity in α -synuclein fibrils. *Amyloid* **2018**, *25*, 189-196. DOI: 10.1080/13506129.2018.1517736.
- 224 Gopalswamy, M. Aggregation and post-translational modification of the parathyroid hormone and its agonistic activity towards the G-protein coupled PTH receptors. *doctoral thesis*, Martin-Luther-Universität Halle-Wittenberg, Halle (Saale), **2017**.
- 225 Baumann, M. Biophysikalische Untersuchungen an Amyloidfibrillen. *doctoral thesis*, Martin-Luther-Universität Halle-Wittenberg, Halle (Saale), **2017**.
- 226 Tian, Y.; Viles, J. H. pH Dependence of Amyloid- β Fibril Assembly Kinetics: Unravelling the Microscopic Molecular Processes. *Angew. Chem. Int. Ed.* **2022**, *61*, e202210675. DOI: 10.1002/anie.202210675.
- 227 Sachan, S.; Gonzalez Moya, C.; Voigt, B.; Köhn, M.; Balbach, J. The pro-sequence of parathyroid hormone prevents premature amyloid fibril formation. *FEBS Lett.* **2023**, *597*, 995-1006. DOI: 10.1002/1873-3468.14587.
- 228 Yang, T.; Li, S.; Xu, H.; Walsh, D. M.; Selkoe, D. J. Large Soluble Oligomers of Amyloid β -Protein from Alzheimer Brain Are Far Less Neuroactive Than the Smaller Oligomers to Which They Dissociate. *J. Neurosci.* **2017**, *37*, 152-163. DOI: 10.1523/jneurosci.1698-16.2016.
- 229 Shankar, G. M.; Welzel, A. T.; McDonald, J. M.; Selkoe, D. J.; Walsh, D. M. Isolation of low-n amyloid β -protein oligomers from cultured cells, CSF, and brain. *Methods Mol. Biol.* **2011**, *670*, 33-44. DOI: 10.1007/978-1-60761-744-0_3.
- 230 Ainavarapu, S. R.; Brujic, J.; Huang, H. H.; Wiita, A. P.; Lu, H.; Li, L.; Walther, K. A.; Carrion-Vazquez, M.; Li, H.; Fernandez, J. M. Contour length and refolding rate of a small protein controlled by engineered disulfide bonds. *Biophys. J.* **2007**, *92*, 225-233. DOI: 10.1529/biophysj.106.091561.

- 231 Housmans, J. A. J.; Houben, B.; Monge-Morera, M.; Asvestas, D.; Nguyen, H. H.; Tsaka, G.; Louros, N.; Carpentier, S.; Delcour, J. A.; Rousseau, F.; Schymkowitz, J. Investigating the Sequence Determinants of the Curling of Amyloid Fibrils Using Ovalbumin as a Case Study. *Biomacromolecules* **2022**, *23*, 3779-3797. DOI: 10.1021/acs.biomac.2c00660.
- 232 Paschold, A.; Voigt, B.; Hause, G.; Kohlmann, T.; Rothemund, S.; Binder, W. H. Modulating the Fibrillization of Parathyroid-Hormone (PTH) Peptides: Azo-Switches as Reversible and Catalytic Entities. *Biomedicines* **2022**, *10*. DOI: 10.3390/biomedicines10071512.
- 233 Voigt, B. Chimaeren zwischen einem thermoresponsiven Polymer und dem Parathormon. *master thesis*, Martin-Luther-Universität Halle-Wittenberg, Halle (Saale), **2017**.
- 234 Nespovitaya, N.; Mahou, P.; Laine, R. F.; Schierle, G. S. K.; Kaminski, C. F. Heparin acts as a structural component of β -endorphin amyloid fibrils rather than a simple aggregation promoter. *Chem. Commun.* **2017**, *53*, 1273-1276. DOI: 10.1039/c6cc09770g.
- 235 Seuring, C.; Verasdonck, J.; Gath, J.; Ghosh, D.; Nespovitaya, N.; Wälti, M. A.; Maji, S. K.; Cadalbert, R.; Güntert, P.; Meier, B. H.; Riek, R. The three-dimensional structure of human β -endorphin amyloid fibrils. *Nat. Struct. Mol. Biol.* **2020**, *27*, 1178-1184. DOI: 10.1038/s41594-020-00515-z.
- 236 Kumar, A.; Baumann, M.; Balbach, J. Small Molecule Inhibited Parathyroid Hormone Mediated cAMP Response by N-Terminal Peptide Binding. *Sci. Rep.* **2016**, *6*, 22533. DOI: 10.1038/srep22533.
- 237 Kumar, A.; Gopalswamy, M.; Wishart, C.; Henze, M.; Eschen-Lippold, L.; Donnelly, D.; Balbach, J. N-terminal phosphorylation of parathyroid hormone (PTH) abolishes its receptor activity. *ACS Chem. Biol.* **2014**, *9*, 2465-2470. DOI: 10.1021/cb5004515.
- 238 Warren, J. R.; Gordon, J. A. On the refractive indices of aqueous solutions of urea. *J. Phys. Chem.* **1966**, *70*, 297-300.
- 239 Groenning, M.; Norrman, M.; Flink, J. M.; van de Weert, M.; Bukrinsky, J. T.; Schluckebier, G.; Frokjaer, S. Binding mode of Thioflavin T in insulin amyloid fibrils. *J. Struct. Biol.* **2007**, *159*, 483-497. DOI: 10.1016/j.jsb.2007.06.004.
- 240 Sulatsky, M. I.; Sulatskaya, A. I.; Povarova, O. I.; Antifeeva, I. A.; Kuznetsova, I. M.; Turoverov, K. K. Effect of the fluorescent probes ThT and ANS on the mature amyloid fibrils. *Prion* **2020**, *14*, 67-75. DOI: 10.1080/19336896.2020.1720487.
- 241 Evgrafova, Z.; Voigt, B.; Baumann, M.; Stephani, M.; Binder, W. H.; Balbach, J. Probing Polymer Chain Conformation and Fibril Formation of Peptide Conjugates. *Chemphyschem* **2019**, *20*, 236-240. DOI: 10.1002/cphc.201800867.
- 242 Lauth, L. M.; Voigt, B.; Bhatia, T.; Machner, L.; Balbach, J.; Ott, M. Heparin promotes rapid fibrillation of the basic parathyroid hormone at physiological pH. *FEBS Lett.* **2022**, *596*, 2928-2939. DOI: 10.1002/1873-3468.14455.
- 243 Voigt, B.; Ott, M.; Balbach, J. A Competition of Secondary and Primary Nucleation Controls Amyloid Fibril Formation of the Parathyroid Hormone. *Macromol. Biosci.* **2023**, *23*, e2200525. DOI: 10.1002/mabi.202200525.
- 244 Voigt, B.; Bhatia, T.; Hesselbarth, J.; Baumann, M.; Schmidt, C.; Ott, M.; Balbach, J. The Prenucleation Equilibrium of the Parathyroid Hormone Determines the Critical Aggregation Concentration and Amyloid Fibril Nucleation. *Chemphyschem.* **2023**, e202300439. DOI: 10.1002/cphc.202300439.
- 245 Wägele, J.; De Sio, S.; Voigt, B.; Balbach, J.; Ott, M. How Fluorescent Tags Modify Oligomer Size Distributions of the Alzheimer Peptide. *Biophys. J.* **2019**, *116*, 227-238. DOI: 10.1016/j.bpj.2018.12.010.
- 246 Evgrafova, Z.; Voigt, B.; Roos, A. H.; Hause, G.; Hinderberger, D.; Balbach, J.; Binder, W. H. Modulation of amyloid β peptide aggregation by hydrophilic polymers. *Phys. Chem. Chem. Phys.* **2019**, *21*, 20999-21006. DOI: 10.1039/c9cp02683e.
- 247 Evgrafova, Z.; Rothemund, S.; Voigt, B.; Hause, G.; Balbach, J.; Binder, W. H. Synthesis and Aggregation of Polymer-Amyloid β Conjugates. *Macromol. Rapid. Commun.* **2020**, *41*, e1900378. DOI: 10.1002/marc.201900378.

- 248 Deike, S.; Rothmund, S.; Voigt, B.; Samantray, S.; Strodel, B.; Binder, W. H. β -Turn mimetic synthetic peptides as amyloid- β aggregation inhibitors. *Bioorg. Chem.* **2020**, *101*, 104012. DOI: 10.1016/j.bioorg.2020.104012.
- 249 Piersimoni, L.; Abd El Malek, M.; Bhatia, T.; Bender, J.; Brankatschk, C.; Calvo Sánchez, J.; Dayhoff, G. W.; Di Ianni, A.; Figueroa Parra, J. O.; Garcia-Martinez, D.; Hesselbarth, J.; Köppen, J.; Lauth, L. M.; Lippik, L.; Machner, L.; Sachan, S.; Schmidt, L.; Selle, R.; Skalidis, I.; Sorokin, O.; Ubbiali, D.; Voigt, B.; Wedler, A.; Wei, A. A. J.; Zorn, P.; Dunker, A. K.; Köhn, M.; Sinz, A.; Uversky, V. N. Lighting up Nobel Prize-winning studies with protein intrinsic disorder. *Cell. Mol. Life Sci.* **2022**, *79*, 449. DOI: 10.1007/s00018-022-04468-y.
- 250 De Sio, S.; Waegele, J.; Bhatia, T.; Voigt, B.; Lilie, H.; Ott, M. Inherent Adaptivity of Alzheimer Peptides to Crowded Environments. *Macromol. Biosci.* **2023**, *23*, e2200527. DOI: 10.1002/mabi.202200527.

Appendix

This section contains the supporting information (SI) files for Papers I-III (A.1-A.3) as well as supporting information for the additional results presented in this thesis (A.4)

A.1 Supporting Information for Paper I

The original Supporting Information for Paper I are included on the following pages (pp. XIV-XVI).

Supporting Information

**A Competition of Secondary and Primary Nucleation Controls Amyloid Fibril
Formation of the Parathyroid Hormone**

*Bruno Voigt, Maria Ott, Jochen Balbach**

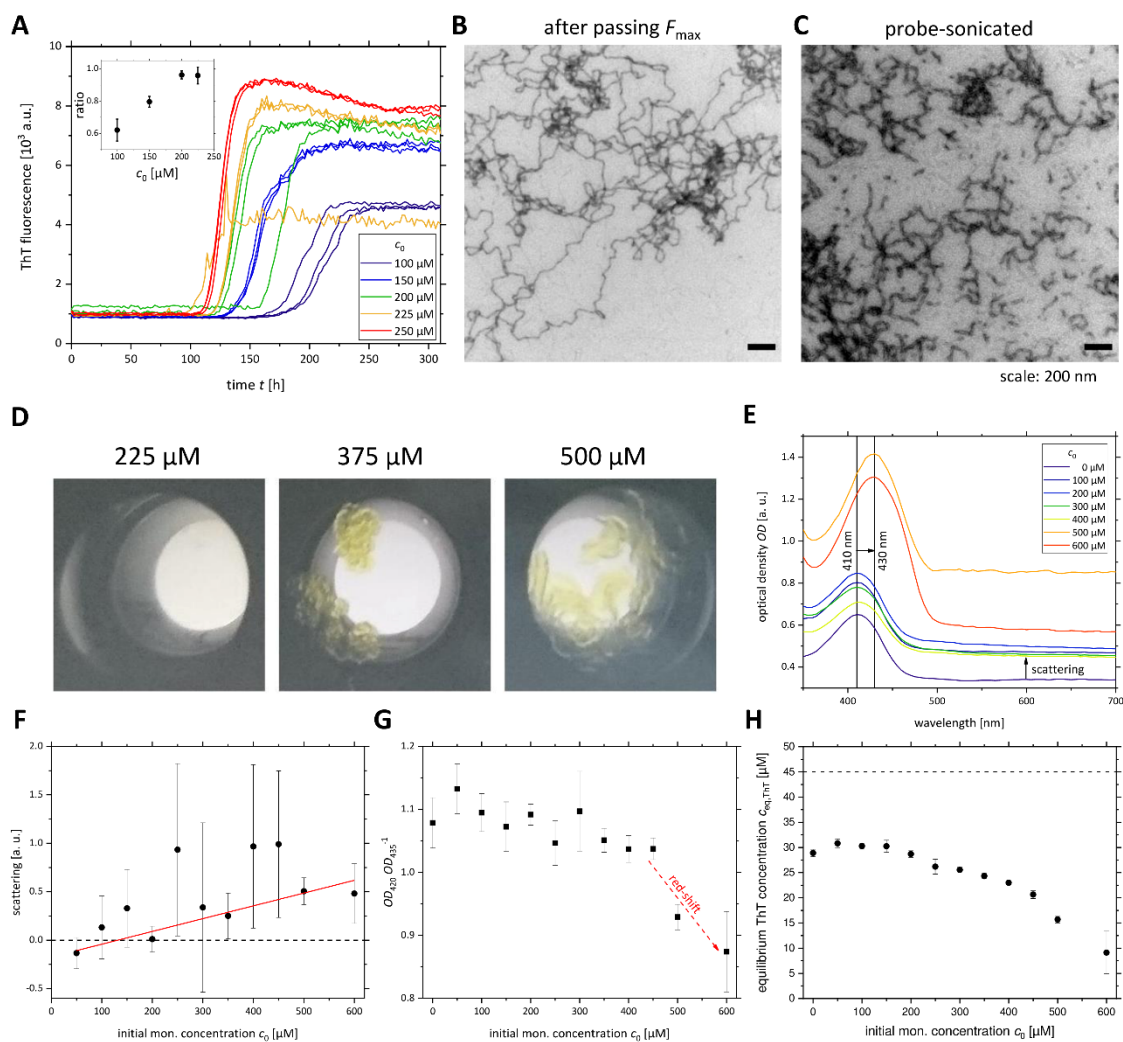


Figure S1. Fibril formation of PTH₈₄. **A** - kinetic traces for low c_0 ($\leq 250 \mu\text{M}$) of PTH₈₄. The experimental data are the same as presented in Figure 2A of the main text and are shown here again for clarity. Inset: ratio of the major kinetic component, as calculated by Equation 17. **B** - negative staining electron micrograph of a PTH₈₄ sample ($c_0 = 500 \mu\text{M}$) taken 20 h after passing the maximum in the kinetic assay. **C** - negative staining electron micrograph of a PTH₈₄ sample ($c_0 = 500 \mu\text{M}$), after 310 h of incubation, which was probe-sonicated. The scale bars in B and C correspond to 200 nm. **D** - Photographs of representative cavities, showing samples with $c_0 = 225 \mu\text{M}$, $375 \mu\text{M}$ and $500 \mu\text{M}$, of the 96-well plate directly after removing from the plate reader. **E** - UV-Vis spectra of the samples in the ThT region (350 - 700 nm) at various c_0 after completion of fibril formation. Representative spectra are shown. Vertical lines indicate the wavelengths of the maximum OD for ThT alone (corresponding to dark blue curve) or in the presence of $600 \mu\text{M}$ PTH₈₄ (corresponding to red curve). **F** - scattering intensity (Equation 5). **G** - Signal ratio of the two wavelengths shown in panel E. **H** - Equilibrium free ThT concentration. Data points in A (inset) and F-H represent the mean of three replicates and one standard deviation.

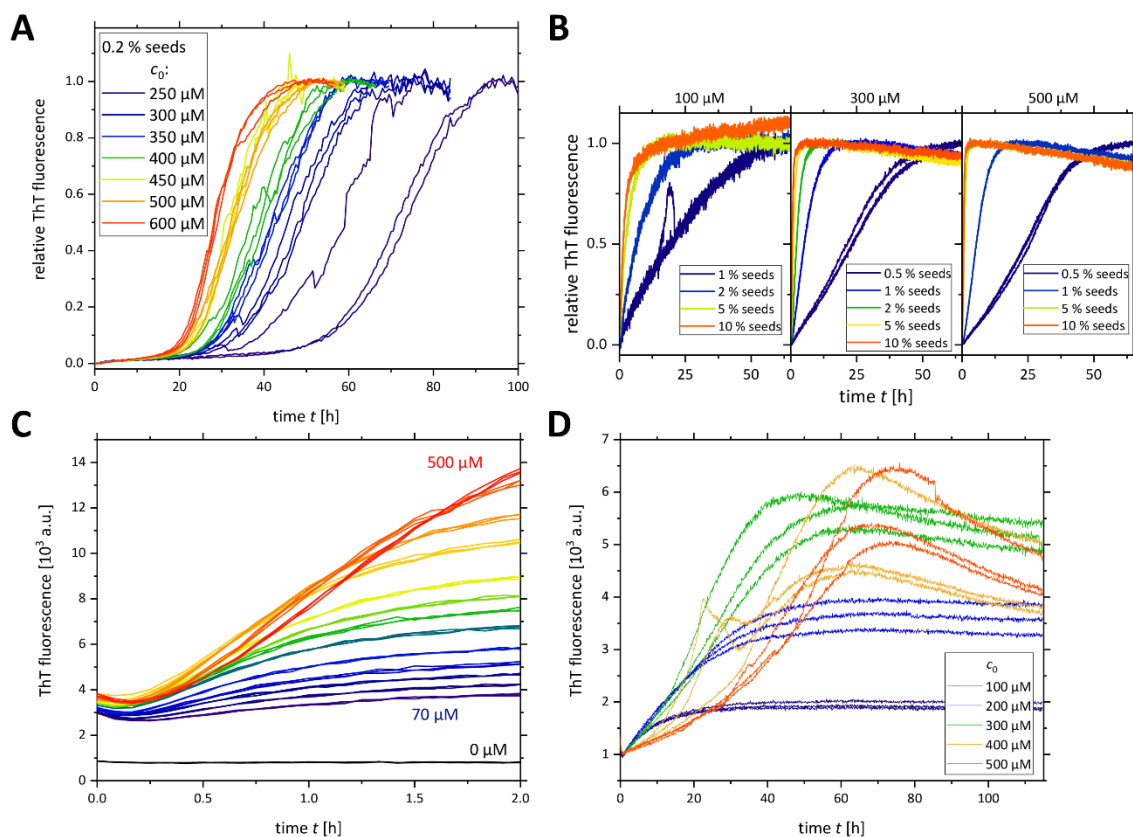


Figure S2. Seeded fibril growth of PTH₈₄. **A** - normalized kinetic data at various c_0 with the addition of 0.2 % pre-formed probe-sonicated seeds (given in monomer equivalents). **B** - normalized kinetic data at three individual c_0 with various amounts of pre-formed sonicated seeds. The half-times were extracted and used for the plot shown in Figure 4C. **C** - initial time traces of PTH₈₄ at various c_0 with the addition of pre-formed sonicated seeds ($c_{\text{seed}} = 25 \mu\text{M}$). The extracted linear initial gradients r_0 are shown in Figure 4D. **D** - time traces of PTH₈₄ at various c_0 with the addition of pre-formed non-sonicated seeds ($c_{\text{seed}} = 25 \mu\text{M}$). The extracted linear initial and maximum gradients r_0 and r_{max} are shown in Figure 4E. For all curves triplicates are shown. The seeds have been added at time zero.

A.2 Supporting Information for Paper II

The original Supporting Information for Paper II are included on the following pages (pp. XX-XXVIII).

ChemPhysChem

Supporting Information

The Prenucleation Equilibrium of the Parathyroid Hormone Determines the Critical Aggregation Concentration and Amyloid Fibril Nucleation

Bruno Voigt, Twinkle Bhatia, Julia Hesselbarth, Monika Baumann, Carla Schmidt, Maria Ott, and Jochen Balbach*

Supplementary Figures S1-S8

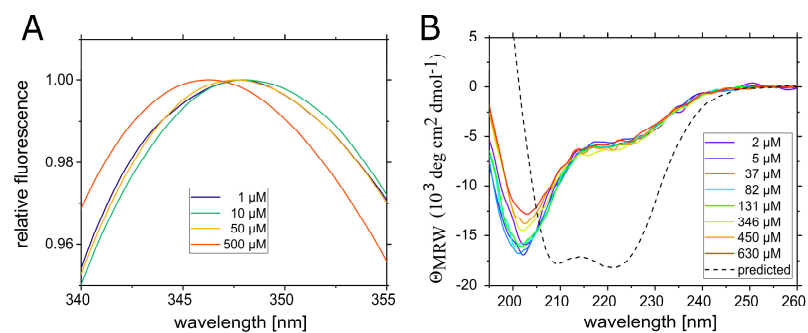


Figure S1: Exemplary (A) intrinsic W23 fluorescence and (B) CD spectra at various c_0 . All spectra have been baseline-corrected. In panel A, the highest value of each spectrum was set to the relative fluorescence value of 1 for direct comparability. In panel B, the c_0 series is indicated by the color scheme, whereas the black dotted line marks the predicted spectrum from the AlphaFold 2.0 structure prediction. All experiments were conducted in buffer containing 50 mM Na_2HPO_4 , 150 mM NaCl, pH 7.4 at 25 °C.

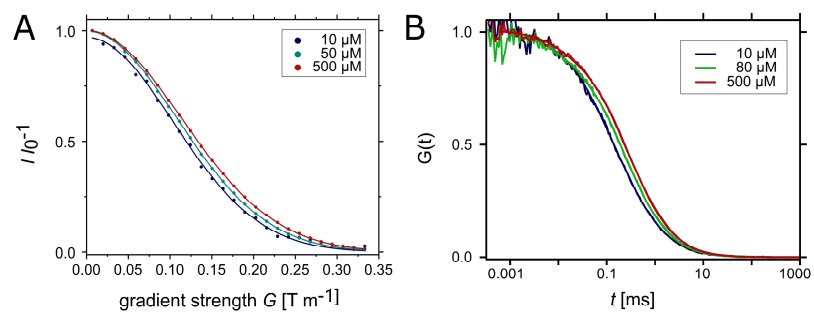


Figure S2: Representative data for (A) the intensity decay obtained by PFG-NMR and (B) for FCCS autocorrelation curves. Shown are the data points as well as the respective fits (Equation 6 and 4 for panels A and B, respectively). All experiments were conducted in buffer containing 50 mM Na₂HPO₄, 150 mM NaCl, pH 7.4 at 25 °C.

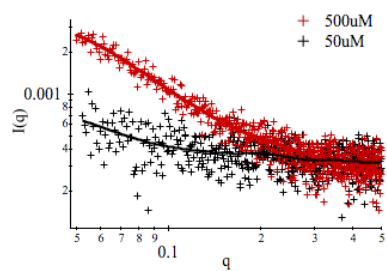


Figure S3: X-ray scattering intensity curves for 50 μM (black crosses) and 500 μM (red crosses). The solid lines indicate the theoretical curves from the r_G distributions calculated by the EOM analysis. All experiments were conducted in buffer containing 50 mM Na_2HPO_4 , 150 mM NaCl , pH 7.4 at 25 $^\circ\text{C}$.

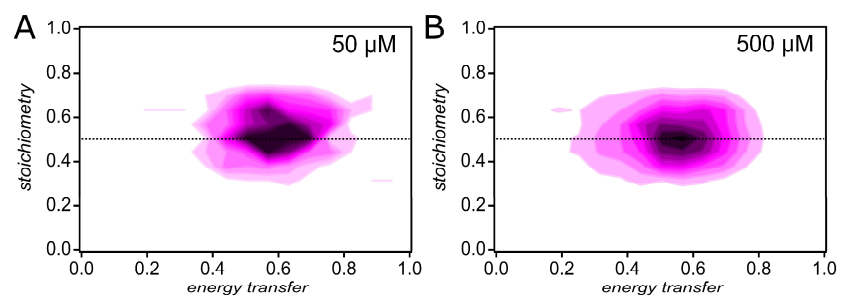


Figure S4: FRET stoichiometry plots for **A** – 50 μM and **B** – 500 μM PTH₈₄. Stoichiometry values of 1.0 or 0.0 reflect donor-only or acceptor-only fluorescence, respectively, whereas 0.5 indicates energy transfer from one donor to one acceptor molecule. All experiments were conducted in buffer containing 50 mM Na₂HPO₄, 150 mM NaCl, pH 7.4 at 25 °C.

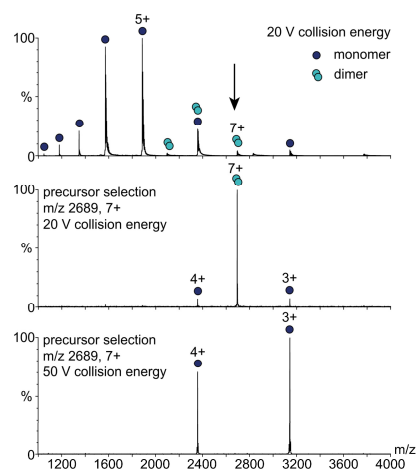


Figure S5: Identification of the PTH₈₄ homo-dimer at $c_0 = 30 \mu\text{M}$ (regime II) by native MS. The native mass spectrum shows charge state distributions corresponding to PTH₈₄ monomers (upper panel, blue circles) and dimers (cyan circles). Precursor selection of the 7+ charge state (m/z 2689) of the dimer at a collisional voltage of 20 V already lead to partial dissociation (middle panel). Applying a collision energy of 50 V to the same precursor (lower panel) the PTH₈₄ dimer completely dissociated. The sample was incubated in buffer containing 50 mM Na₂HPO₄, 150 mM NaCl, pH 7.4 at 25 °C. Directly prior to the measurement, the buffer was exchanged to 200 mM (NH₄)CH₃COO.

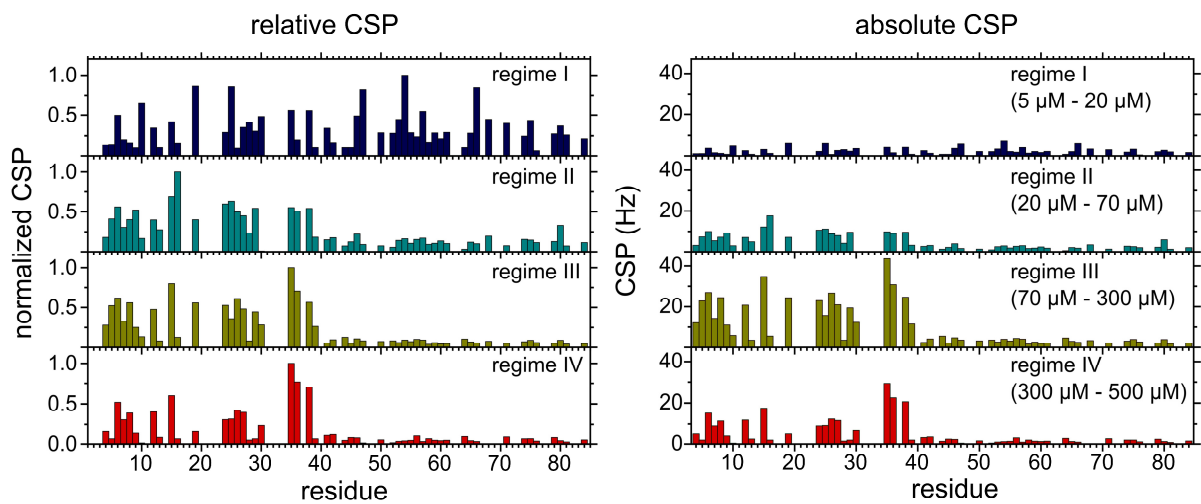


Figure S6: CSP for the four concentration regimes in relative (left panel) and absolute values (right panel), obtained from ^1H - ^{15}N -HSQC chemical shift differences between spectra of 5 μM /20 μM (regime I, blue), 20 μM /70 μM (regime II, blue-green), 70 μM /300 μM (regime III, dark yellow) and 300 μM /500 μM (regime IV, red). In the left panel, CSP values for each regime are divided by the highest respective value for direct comparability of affected segments. All experiments were conducted in buffer containing 50 mM Na_2HPO_4 , 150 mM NaCl, pH 7.4 at 25 $^\circ\text{C}$.

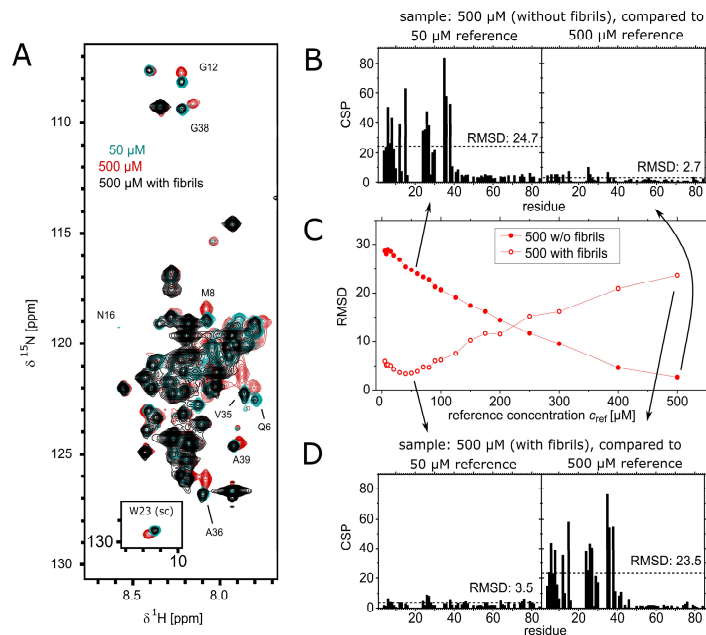


Figure S7: Representative 2D-NMR spectrum of PTH₈₄ in the presence of fibrils. **A** – ^1H - ^{15}N -HSQC spectrum of a sample ($c_0 = 500 \mu\text{M}$) to which 5 % pre-formed seeds have been added (7 days incubation time) (black), compared to reference spectra without fibrils with $c_0 = 50 \mu\text{M}$ (blue-green) and $500 \mu\text{M}$ (red). The reference spectra are the same as shown in Figure 4B. **B** – exemplary CSP patterns of the $500 \mu\text{M}$ sample without fibrils compared to the $50 \mu\text{M}$ (left) and $500 \mu\text{M}$ reference samples (right), corresponding RMSD values are indicated by a dashed line. **C** – RMSD of backbone chemical shifts in ^1H - ^{15}N -fHSQC spectra without (closed circles) and in equilibrium with fibrils (open circles) compared to reference spectra acquired in the absence of fibrils. The plot displays data already shown in Figure 5A in the main manuscript and is included here for clarity. **D** – exemplary CSP patterns of the $500 \mu\text{M}$ sample in equilibrium with fibrils compared to the $50 \mu\text{M}$ (left) and $500 \mu\text{M}$ reference samples (right), corresponding RMSD values are indicated by a dashed line. Arrows connect the CSP patterns from panels B and D with the respective data points in panel C. All experiments were conducted in buffer containing 50 mM Na_2HPO_4 , 150 mM NaCl, pH 7.4 at 25 °C.

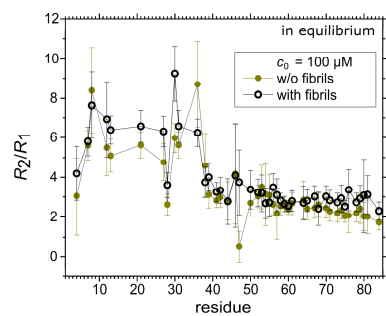


Figure S8: NMR relaxation analysis of the soluble peptide fraction in equilibrium with fibrils. R_2/R_1 ratio for a 100 μM sample before (closed dark yellow circles) and after (open black circles) fibril formation. All experiments were conducted in buffer containing 50 mM Na_2HPO_4 , 150 mM NaCl, pH 7.4 at 25 $^\circ\text{C}$.

A.3 Supporting Information for Paper III

The original Supporting Information for Paper III are included on the following pages (pp. XXXII-XXIV).

Supplemental Information for "Heparin promotes rapid fibrillation of the basic Parathyroid Hormone at physiological pH"

Luca M. Lauth,^{*,†} Bruno Voigt,[‡] Twinkle Bhatia,[†] Lisa Machner,[¶] Jochen Balbach,[‡] and Maria Ott^{*,†}

*†Department of Biochemistry and Biotechnology, Martin-Luther-University
Halle-Wittenberg, Halle, Germany*

‡Department of Biophysics, Martin-Luther-University Halle-Wittenberg, Halle, Germany

*¶Department of Molecular Medicine, Martin-Luther-University Halle-Wittenberg, Halle,
Germany*

E-mail: luca.lauth@bct.uni-halle.de; maria.ott@bct.uni-halle.de

Phone: +49 (0)345 55 24946

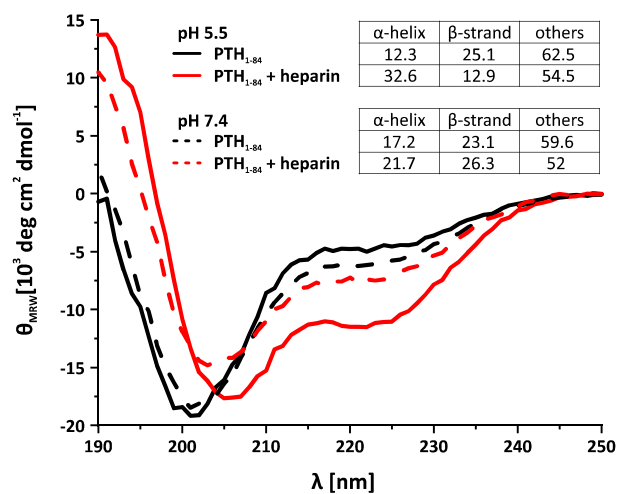


Figure S1: Buffer effect on circular dichroism spectra of PTH₁₋₈₄ in absence and presence of heparin (1:10 molar ratio heparin:PTH₁₋₈₄). Secondary structure calculation was performed using the BeStSel online tool [38].

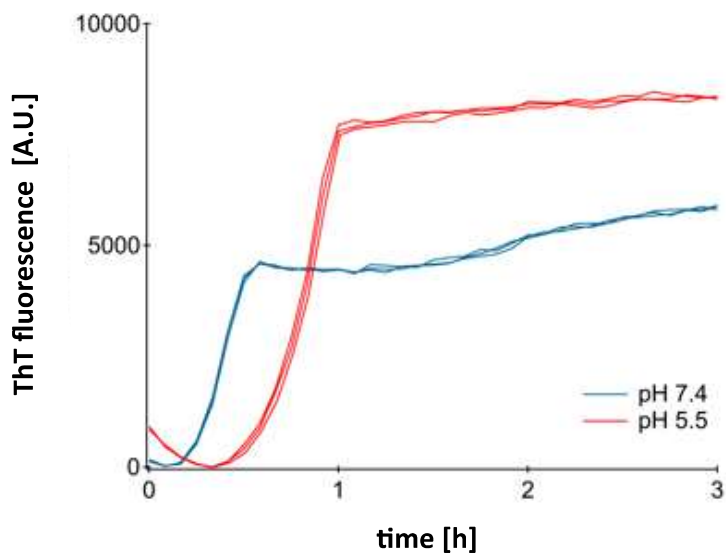


Figure S2: Buffer effect on ThT curves of PTH₁₋₈₄ in presence of heparin (1:10 molar ratio heparin:PTH₁₋₈₄).

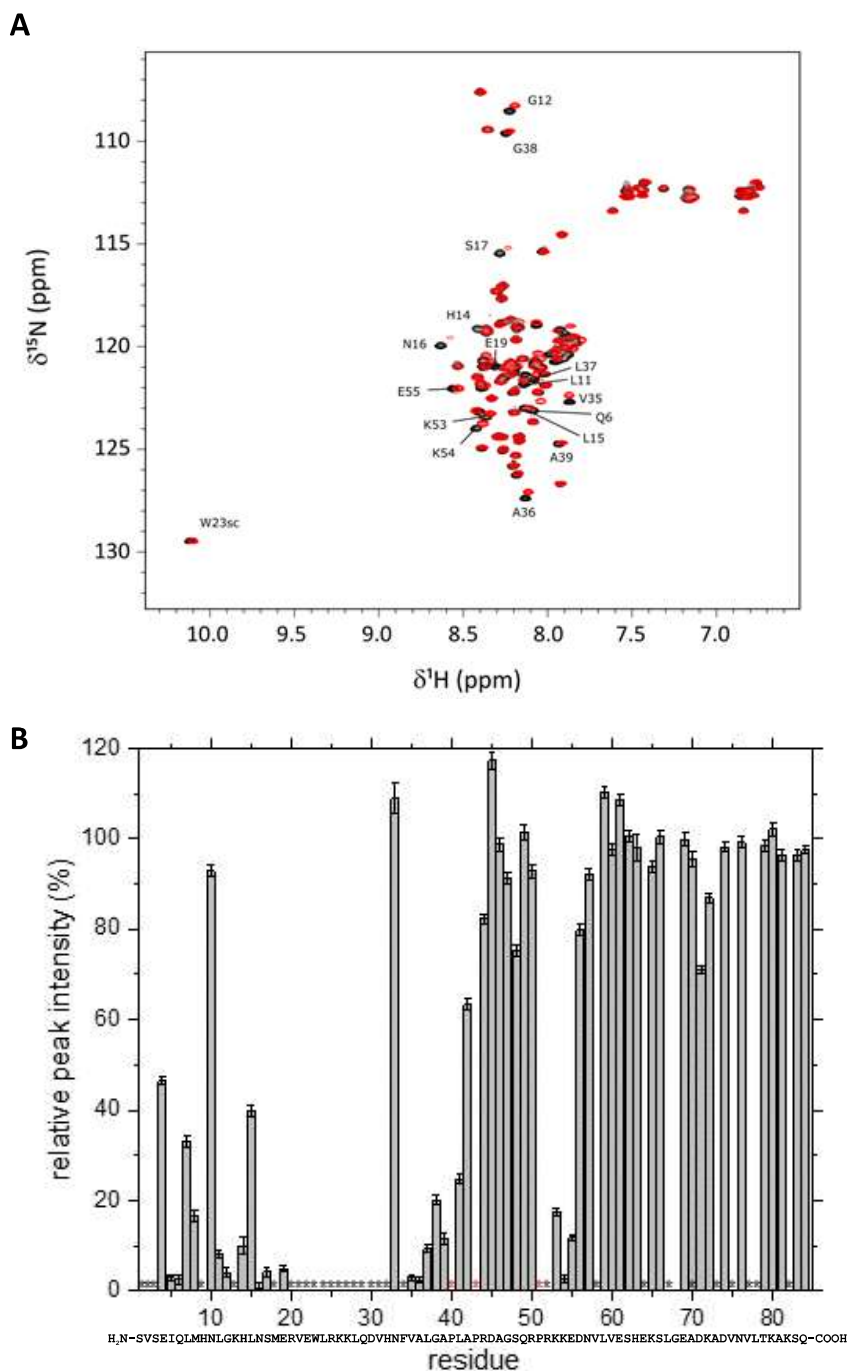


Figure S3: NMR detected interaction of PTH₁₋₈₄ with fondaparinux. A: 2D ¹H-¹⁵N HSQC spectrum of 100 μ M PTH₁₋₈₄ at pH 5.5 and 25 °C in the absence (black) and presence (red) of fondaparinux at a 1:1 stoichiometry. Residues showing major changes in chemical shifts upon addition of the sugar are labeled. B: Relative NMR intensity of the PTH₁₋₈₄ backbone amides in the presence of fondaparinux. Residues with missing or ambiguous assignments are marked by a black asterisk, prolyl residues with a red asterisk. The PTH₁₋₈₄ primary sequence is shown.

A.4 Supporting Information for Chapter 2.4

SI for “Effects of Denaturing and α -Helix Inducing Agents on the Structure of Free PTH₈₄”

The concentration of urea was adjusted using a stock solution (8 M urea in buffer) and determined for each sample by refractometry using the equation

$$[\textit{urea}] = 117.66 \Delta n + 29.753 \Delta n^2 + 185.56 \Delta n^3 \quad \text{Equation A.1}$$

where Δn is the difference of the refractive indices of a sample and a urea-free reference.²³⁸ Samples were incubated overnight to ensure an equilibrium of the oligomeric states.

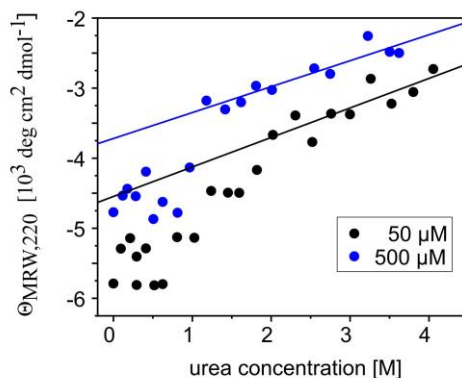


Figure A.1: CD monitored analysis of urea mediated PTH₈₄ unfolding at peptide concentrations of 50 μ M (regime II, black) and 500 μ M (regime IV, blue). Θ_{MRW} at 220 nm is plotted *versus* the urea concentration. The solid lines are linear fits to the data at high urea concentrations representing a baseline. Each data point represents a distinct sample. All experiments were conducted at 25 °C in buffer containing 50 mM Na₂HPO₄, 150 mM NaCl, pH 7.4 with increasing concentrations of urea.

SI for “Effects of Urea on Seeded Fibril Growth and the Critical Concentration”

PTH₈₄ seeded fibril growth was investigated in the presence of various amounts of urea. For all three analyzed initial PTH₈₄ concentrations ($c_0 = 100 \mu\text{M}$, $300 \mu\text{M}$ and $500 \mu\text{M}$), the fluorescence plateau values decreased with increasing urea concentration (Figure A.2A), indicating a decrease of fibrillar mass in the thermodynamic equilibrium. Interestingly, in the normalized curves fibril growth at PTH₈₄ concentrations of $300 \mu\text{M}$ and $500 \mu\text{M}$ appeared to be faster for low urea concentrations compared to the urea-free sample, while no such effect was indicated for $100 \mu\text{M}$ (Figure A.2B). Moreover, $100 \mu\text{M}$ PTH₈₄ displayed a growth behavior independent from the urea concentration.

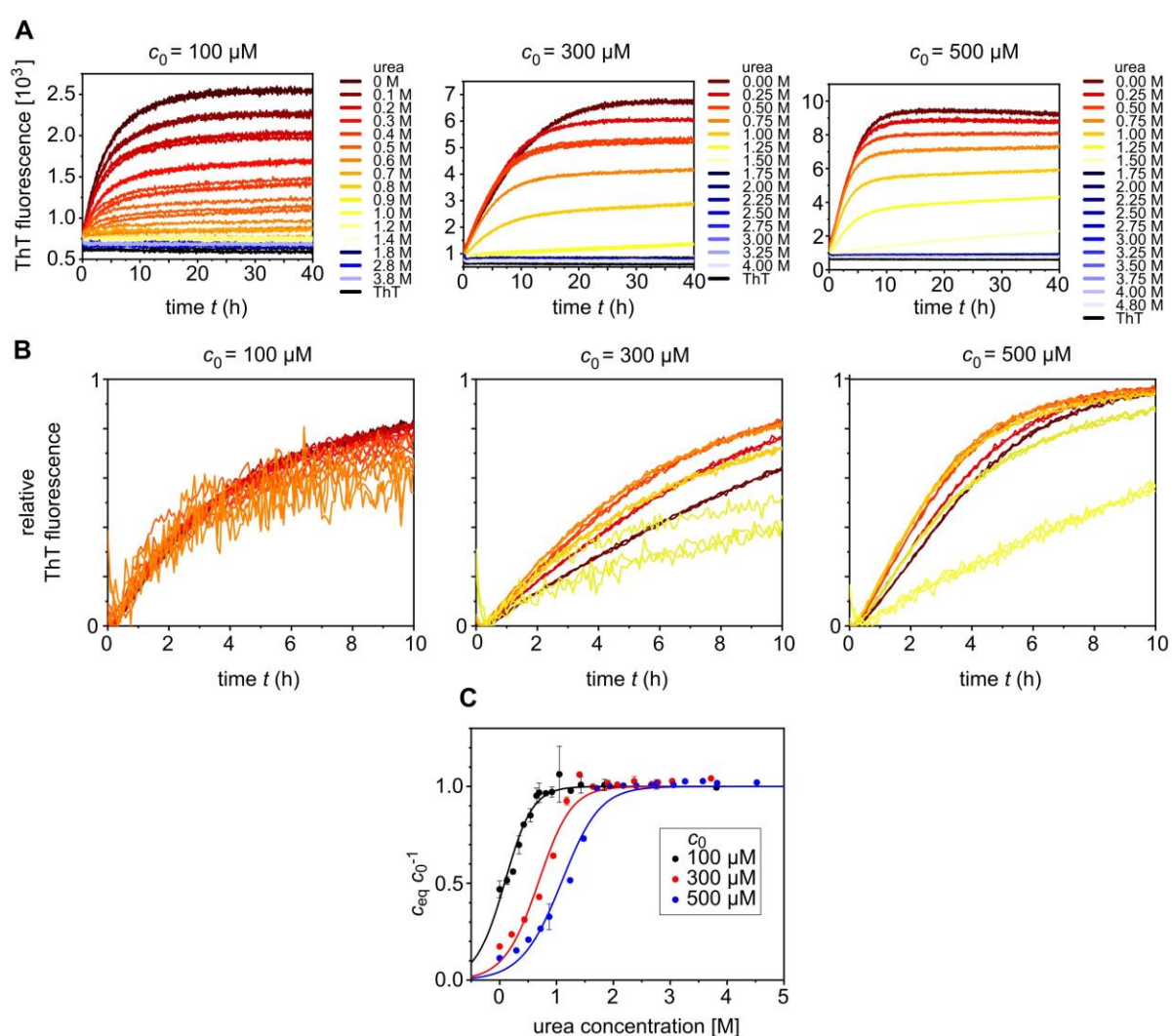


Figure A.2: Effects of urea on seeded fibril growth of PTH₈₄. **A** – Seeded fibril growth by means of ThT fluorescence increase for initial monomer concentrations of $100 \mu\text{M}$ (left), $300 \mu\text{M}$ (middle) and $500 \mu\text{M}$ (right) in the presence of increasing amounts of urea. Urea concentrations are indicated by the respective color codes. **B** – Normalized representation focusing on the initial “burst” at low urea concentrations. **C** – Normalization of the data shown in Figure 2.3B of the main text according to the initial concentration as $c_{eq} c_0^{-1}$. The solid lines represent fits of the data to Equation A.2. All measurements were performed in triplicates. The data points and error bars in C represent the arithmetic means of triplicate measurements with the standard deviations as error bars. All experiments were conducted at $25 \text{ }^\circ\text{C}$ in buffer containing $50 \text{ mM Na}_2\text{HPO}_4$, 150 mM NaCl , $\text{pH } 7.4$.

The soluble fractions at all urea concentrations are shown in Figure 2.3B of the main text. In Figure A.2C, the same data are displayed normalized to the initial concentration c_0 . The dependence of this ratio $c_{eq} c_0^{-1}$ is given by

$$\frac{c_{eq}}{c_0} = \frac{c_0 K (1 M)^{-1} + 0.5 - \sqrt{c_0 K (1 M)^{-1} + 0.25}}{(c_0 K (1 M)^{-1})^2}$$

Equation A.2

with $K = e^{-\left(\frac{\Delta G_{el}^0 + m[urea]}{RT}\right)}$

where K is the equilibrium constant (see also Equation 1.23), ΔG_{el}^0 the Gibbs free energy of elongation in the absence of urea, m a cooperativity factor related to the slope in the transition region, R the gas constant and T the temperature.¹⁷⁵ This formula is used in analogy to approaches from the analysis of protein (un-)folding. Although the fits only poorly agreed with the data, especially in the range of low urea concentrations, the corresponding parameters revealed insights into the thermodynamics and are listed in Table A.1.

Interestingly, ΔG_{el}^0 as well as m displayed small trends towards more negative or decreasing values, respectively, with increasing c_0 . Given the fact that the fits were unable to satisfyingly reproduce the data at low urea concentrations (Figure A2C), this trend should not be overinterpreted. It seemed to be more likely that both ΔG_{el}^0 and m did not significantly change with c_0 . Most importantly, ΔG_{el}^0 agreed well with the more general ΔG^0 according to Equation 1.23 ($\Delta G^0 = -23.8 \text{ kJ mol}^{-1}$, Paper II) analyzed in the absence of urea.

Table A.1: Results of the analysis of the soluble fraction in dependence on the urea concentration. The free energy of the elongation process ΔG_{el}^0 and the cooperativity factor m have been determined by fitting of the data with Equation A.2.

c_0 [μM]	ΔG_{el}^0 [kJ mol^{-1}]	m [$\text{kJ mol}^{-1} \text{M}^{-1}$]
100	-22.6 ± 0.2	11.0 ± 0.1
300	-25.0 ± 0.9	9.2 ± 1.1
500	-26.1 ± 0.8	7.9 ± 0.7

SI for “Evidence of a Second Kinetic Phase in Seeded Fibril Growth at Low Concentrations”

In Figure A.3A, the conversion from arbitrary ThT fluorescence units (primary data, see also Paper I - Figure 4) to fibril mass $M(t)$ for the y-axis is shown considering that the maximum yield of fibrils in equilibrium is given by $M_{max} = c_0 - c_{crit}$. A focus on the initial seeding process within the first 3.5 h is shown in Figure A.3B. This allows a quantification of fibrils as well as of unconsumed monomers.

To analyze the late-stage behavior (increasing or decreasing slope at $t > 10$ h), model-free linear fits were applied for the data from 20 – 50 h. The slopes are shown in Figure A.3C. For $c_0 \leq 180 \mu\text{M}$ a positive slope was found indicating a second phase of fibrillar mass increase in addition to the initial growth. The intersection of the linear fits for the early- (Paper I) and late-stage gradients was used to

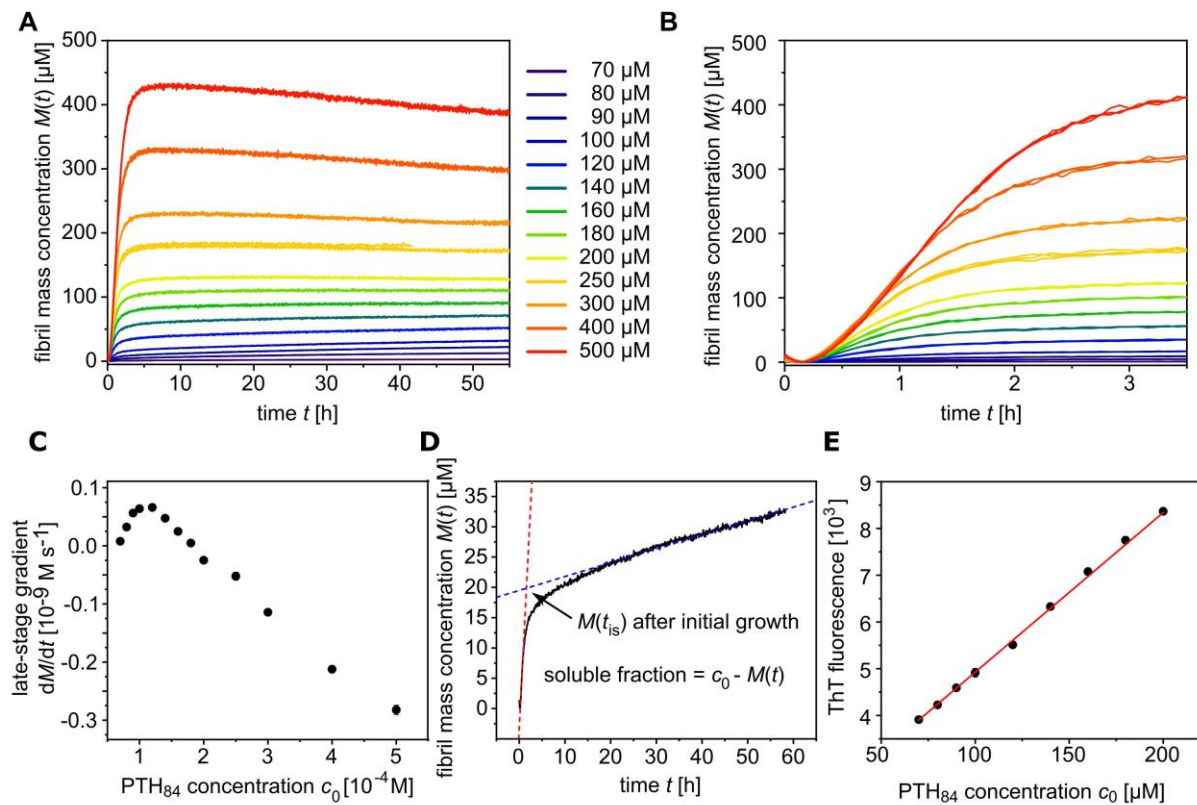


Figure A.3: Increase of fibril mass $M(t)$ during seeded fibril growth and effects of fibril elongation at low concentrations. **A** – Initial concentration dependent seeded fibril growth with a constant seed concentration of $25 \mu\text{M}$, given in monomer equivalents. The primary data set is the same as shown in Paper I - Figure 4. Here, the y-axis is converted from ThT fluorescence to the fibril mass concentration $M(t)$ (considering $M_{max} = c_0 - c_{crit}$; consequently, only curves for $c_0 > c_{crit}$ are shown). The color code is given in the figure legend. **B** – The data from panel A are expanded for the initial phase, $0 < t < 3.5$ h. **C** – Slopes dM/dt of linear fits to the late-stage gradients. For $c_0 \geq 200 \mu\text{M}$, the gradient is negative. **D** – Example for the determination of the fibril mass concentration at the intersection time point $M(t_{is})$ after the initial burst growth. The intersection of the two linear fits $dM/dt|_0$ and $dM/dt|_{t > 15 \text{ h}}$ indicates $M(t_{is})$. The corresponding soluble fraction is given by $c_{sol} = c_0 - M(t_{is})$. **E** – ThT fluorescence at the intersection time-points. All measurements were performed in triplicates. Data points and error bars represent the arithmetic means and the corresponding standard deviation. All experiments were conducted at 25°C in buffer containing $50 \text{ mM Na}_2\text{HPO}_4$, 150 mM NaCl , $\text{pH } 7.4$.

estimate the concentration of free monomers that have not been consumed at the end of the “burst” growth (an example is shown in Figure A.3D). The ThT fluorescence at these intersection points is displayed in Figure A.3E. The soluble monomer is given by $c_0 - M(t_{\text{intersection}})$ and is shown in Figure 2.4B in the main text.

SI for “Approximation of the Elongation Rate Constant”

For an approximation of the elongation rate constant k_+ for PTH₈₄ fibril formation, the method described by Meisl *et al.* (2014) was used and is referred to in the following section.¹³⁹

Since M_0 of the seed fibrils is known, an approximation of the average number of PTH₈₄ monomers per fibril will allow to conclude the number concentration P_0 needed according to Equation 1.1. This was achieved using TEM images of seed fibrils directly after the ultrasonication treatment. The average length of fibrils was determined at two different magnifications (3000 x and 20000 x, Figure A.4A and B, respectively). The former allowed the investigation of longer filaments, while the latter was more suitable for smaller fragments. The plot in Figure A.4C demonstrated that the length distribution is very broad and heterogenous. Additionally, a bias towards smaller values needed to be considered due to the curvilinear appearance of long fibrils forming local clusters, which impeded a length measurement. To account for this bias, the average length was used rather than the center of a

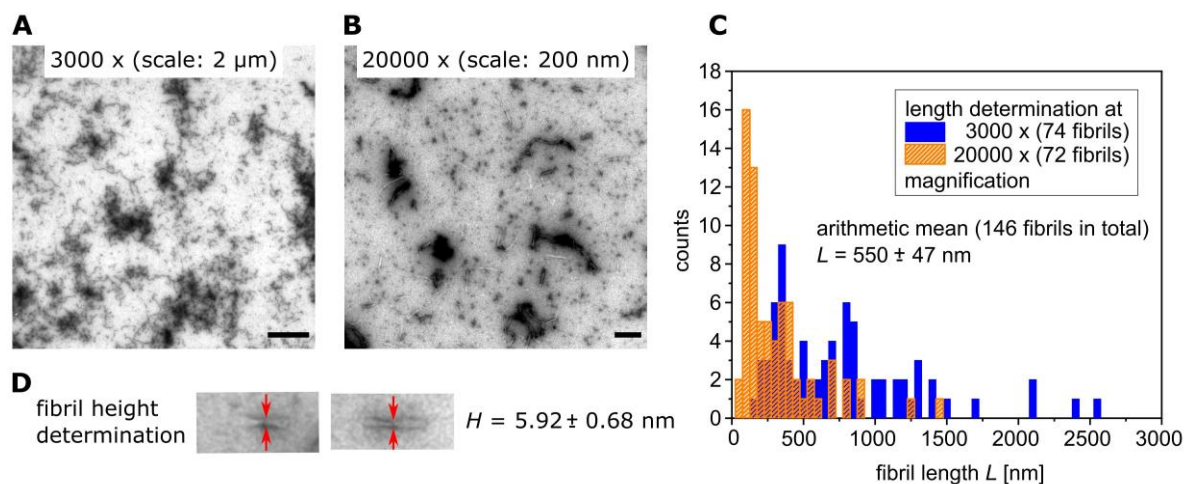


Figure A.4: Estimation of the average length and height of fibril seeds. The length was determined from TEM images acquired at **A** – 3000 x and **B** – 20000 x magnification enabling the measurement of different length scales. **C** – Plot of the determined lengths from panel A (blue) and B (orange). **D** – Height analysis from short twisted fibril seeds. TEM samples were prepared after sonication of the original fibrils inducing a fragmentation into the seeds. All experiments were conducted at 25 °C in buffer containing 50 mM Na₂HPO₄, 150 mM NaCl, pH 7.4.

Gaussian distribution, revealing $L = 545 \pm 474$ nm. The high experimental error reflected the broad length distribution.

The average height was determined from twist regions (examples are shown in Figure A.4D) as $H = 5.92 \pm 0.68$ nm. This value closely corresponded to the diameter of one subfilament (Paper I - Figure 3), suggesting a cylindrical form. The average volume of a fibril (consisting of three subfilaments) is therefore given by

$$\begin{aligned} V &= 3 \pi \left(\frac{H}{2}\right)^2 L = 3 \pi \left(\frac{5.92 \text{ nm}}{2}\right)^2 545 \text{ nm} = 3.96 \cdot 10^4 \text{ nm}^3 \\ &= 3.93 \cdot 10^{-17} \text{ ml} \end{aligned} \quad \text{Equation A.3}$$

The number of monomers per fibril $N_{m/f}$ can be concluded from the definition of the density in classical mechanics ($\rho = m V^{-1}$) and the Avogadro relation ($n = N N_A^{-1} = m M_W^{-1}$), leading to

$$\begin{aligned} N_{m/f} &= \frac{\rho V N_A}{M_W} = \frac{1.3 \text{ g ml}^{-1} * 3.96 \cdot 10^{-17} \text{ ml} * 6.032 \cdot 10^{23} \text{ mol}^{-1}}{9424 \text{ g mol}^{-1}} \\ &= 3265 \text{ monomers per fibril} \end{aligned} \quad \text{Equation A.4}$$

From the ultrasonicated pre-formed seeds (with $c_0 = 500 \mu\text{M}$), $24 \mu\text{l}$ have been added to the new samples. Due to the critical concentration, about $433 \mu\text{M}$ of the peptide is present as fibrils. This gives a total number of PTH₈₄ monomers incorporated in seed fibrils N_{mon} of

$$\begin{aligned} N_{mon} &= M_0 V N_A = 4.33 \cdot 10^{-4} \text{ mol l}^{-1} * 2.4 \cdot 10^{-5} \text{ l} * 6.023 \cdot 10^{23} \text{ mol}^{-1} \\ &= 6.26 \cdot 10^{15} \text{ monomers} \end{aligned} \quad \text{Equation A.5}$$

The absolute number of fibrils N_{fib} is given by the ratio of monomers present as seed fibrils and the average number of monomers per fibril with

$$N_{fib} = \frac{6.26 \cdot 10^{15} \text{ monomers}}{3265 \text{ monomers per fibril}} = 1.92 \cdot 10^{12} \text{ fibrils} \quad \text{Equation A.6}$$

This allows an estimation of the initial number concentration of seeds P_0 in the final sample ($V_{\text{new sample}} = 480 \mu\text{l}$) containing pre-formed seeds and fresh monomers with

$$P_0 = \frac{N_{fib}}{V_{new\ sample} N_A} = \frac{9.59 \cdot 10^{10} \text{ fibrils}}{4.8 \cdot 10^{-4} \text{ l} * 6.023 \cdot 10^{23} \text{ mol}^{-1}} = 6.64 \cdot 10^{-9} \frac{\text{mol}}{\text{l}} \quad \text{Equation A.7}$$

The slope of the initial gradient was found to be $2 k_+ P_0 = 2.17 \times 10^{-4} \text{ s}^{-1}$ (Figure 2.5B), resulting in the approximation of the elongation rate constant k_+ (numerator in Equation 1.1) of

$$k_+ = \frac{\text{slope}}{2 P_0} = \frac{2.17 \cdot 10^{-4} \text{ s}^{-1}}{2 * 6.64 \cdot 10^{-9} \text{ M}} = 1.63 \cdot 10^4 \text{ M}^{-1} \text{ s}^{-1} \approx \underline{10^4 \text{ M}^{-1} \text{ s}^{-1}} \quad \text{Equation A.8}$$

Note that due to the broad length distribution leading to a high uncertainty of P_0 , the estimated rate constant should be considered as a rough approximation.

SI for “Structural Aspects of PTH₈₄ Fibrils”

The molecular structure of PTH₈₄ was planned to be investigated by employing model reconstruction on the basis of cryoEM imaging. This was conducted in close collaboration with the research group of Jun.-Prof. Dr. Panagiotis Kastiris (ZIK HALOmem, Martin Luther University Halle-Wittenberg). This section focuses on issues of the fibril sample preparation for future investigations.

CryoEM of amyloidogenic material requires single fibrils with a regular, repetitive twist. PTH₈₄ fibrils grown *de novo* (I) imply a long time for sample preparation and (II) are heterogenous (Paper I - Figures 2 and 3). The fibrils are flat and irregular regarding the pitch length of the twists. This led to the consideration of controlled, seeded growth with 5 % sonicated seeds from primary (*de novo*) fibrils. The protocols refer to the methodologies described in Paper I. Buffers were always prepared directly prior to the use. For the initial testing, 500 μM and 200 μM PTH₈₄ monomer was used. Since ThT potentially influences the molecular structure,^{239,240} the cryoEM samples were kept ThT free. The dye was only added to reference samples for monitoring fibril growth (Figure A.5A). ThT free samples were incubated simultaneously. At both concentrations, fibrils were formed within hours with time traces comparable to those shown in Paper I - Figure S1. To ensure the integrity of the ThT-free sample,

Table A.2: Determination of the soluble fraction after seeded fibril growth in the presence and absence of ThT.

c_0 [μM]	c_{eq} with ThT	c_{eq} without ThT
200	60.0 μM	85.8 μM
500	68.8 μM	71.6 μM

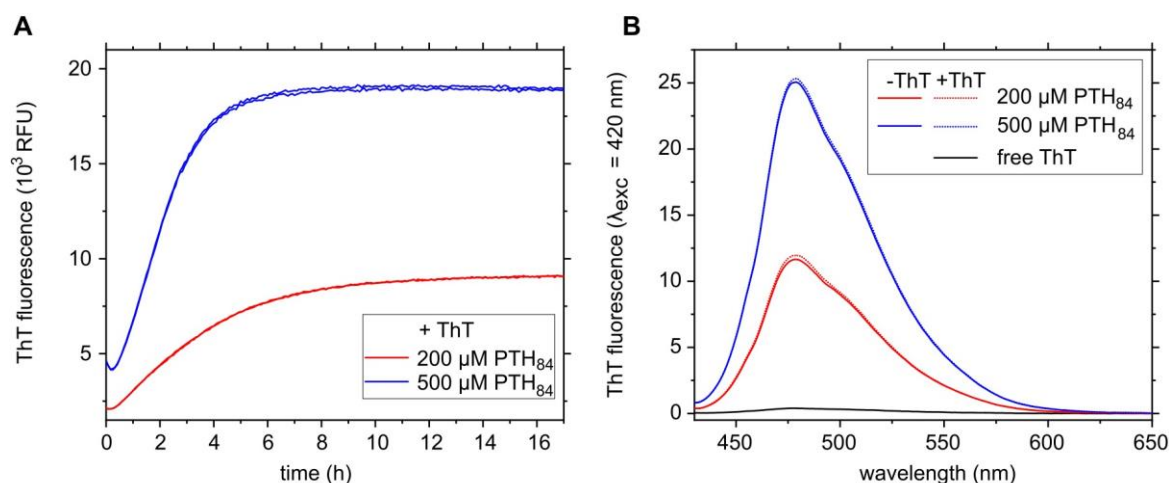


Figure A.5: Monitoring of seeded fibril growth for cryoEM fibril preparation. **A** – ThT detected kinetics of PTH₈₄ fibril formation in the presence of 5 % seeds. **B** – ThT fluorescence emission spectra ($\lambda_{exc} = 412$ nm) after fibril formation. The spectra were acquired on a Jasco F-6500 fluorescence spectrometer. ThT has been added to the samples grown without ThT to a concentration of 50 μ M (dashed line, equal concentration as for the time tracked samples shown in panel A).

the soluble fraction as well as fluorescence spectra of ThT added after fibril growth were analyzed (Figure A.5B). The spectra for the samples grown in the presence and absence of ThT are almost identical. Additionally, the soluble fractions in equilibrium with fibrils were determined and are in the expected range for the critical concentration (Table A.2). This verifies the integrity of the samples grown without ThT concerning possible effects of the dye on growth behavior.

These samples were directly processed and imaged with cryoEM, details are given in Chapter 2.2.4 of the main text. Dilutions of factor 20 and 50 were tested. In analogy to nsTEM (see Paper I - Figure 3), long, curvilinear fibrils forming fibril “communities” were found (Figure A.6A). The background was found noisy which was attributed to residual monomers (due to the high c_{crit}). This effect was more pronounced for the 200 μ M sample due to the higher monomer fraction (not shown). In addition, the fibrils were irregularly covered with dark spots (Figure A.6B). These possibly originate from regions exposed to and denatured at the air-water/ice interface abetted by the length and curliness of the fibrils (Figure A.6C). The dark spots interfere with the particle picking algorithm leading to unreliable 2D classes aligning the spots. Taken together, these factors impede a structural investigation. Consequently, the sample preparation protocol needed to be improved to obtain single fibrils displaying straight segments for the analysis. This probably requires the fragmentation of fibrils (Figure A.6D).

A reduction of the background could in principle be realized by spinning down the fibrils, removing the monomers, with a subsequent resolubilization. Centrifugation in Amicon filters (100 kDa molecular weight cut-off) led to a very heterogenous appearance both of the filtrate and the retentate without

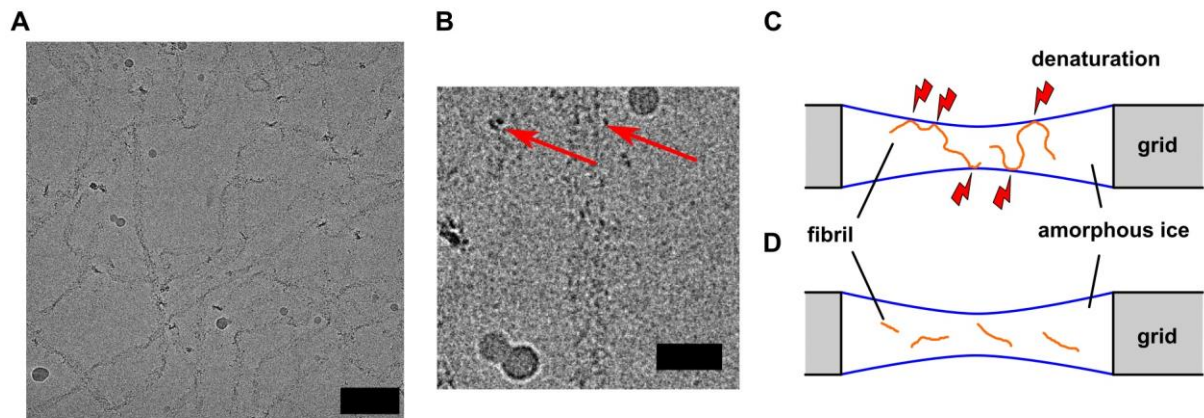


Figure A.6: Examples of cryoEM images from the first PTH₈₄ fibril sample. **A** and **B** show images acquired at 92000 x magnification on a Glacios 200 keV Cryo transmission electron microscope. Fibrils can clearly be recognized and correspond to those observed in negative staining EM imaging (Paper I - Figure 3). The red arrows in **B** indicate regions with a strong degree of denaturation, resulting in black spots. The scale bars in panels **A** and **B** refer to 100 nm and 25 nm, respectively. **C** and **D** schematically represent fibrils (orange) in the amorphous ice (blue). Curvilinear fibrils (**C**) can have several contacts to the ice-air interface during preparation, resulting in denaturation. Short, straight fibrils (**D**) can be completely embedded in the ice without contact to the interface.

the desired separation of monomers from fibrils (Figure A7A). Additionally, centrifugation in general might facilitate clustering, as pointed out above.

To control the length distribution of the fibrils, other strategies were tested. These included (I) adding an incubation step after diluting in ddH₂O or buffer to induce a separation of the fibrils due to a readjustment of the equilibrium, (II) seeded fibril growth interrupted at certain time points ($t = 30$ min, 60 min, 120 min), (III) fibril fragmentation by rigorous vortexing or (IV) ultrasonication and (V) sequential seeding to potentially promote the proliferation of single morphs. The fraction of soluble monomer is defined by c_{crit} . To reduce the monomer contribution to the background, the method screening was only conducted with samples of $c_0 = 500 \mu\text{M}$. The form and morphology of fibrils in nsTEM were chosen as indicators.

Interestingly, the fibrils displayed distinct appearances when diluted in ddH₂O and buffer (Figure A.7B). In ddH₂O, very small fibril fragments were obtained, as well as big clusters which seem morphologically distinct from those grown *de novo* in buffer at neutral pH (compare to Paper I - Figure 3). In contrast, fibrils diluted in buffer showed the expected morphology and even an increased number of individual fibrils in addition to the bigger networks were evident. The considerable difference of fibril morphology upon dilution in ddH₂O might be a consequence of the reduction of pH as well as the ionic strength. This effect should be considered also in other experiments requiring a dilution of PTH₈₄ fibrils.

Stopping seeded fibril growth after 30 min (quiescent incubation at 37 °C) led only to a very small fibril fraction while stopping after 60 or 120 min led in part to single, relatively short, straight fibrils (Figure A.7C). Also, the typical curvilinear fibrils in large clusters were observed, which was more

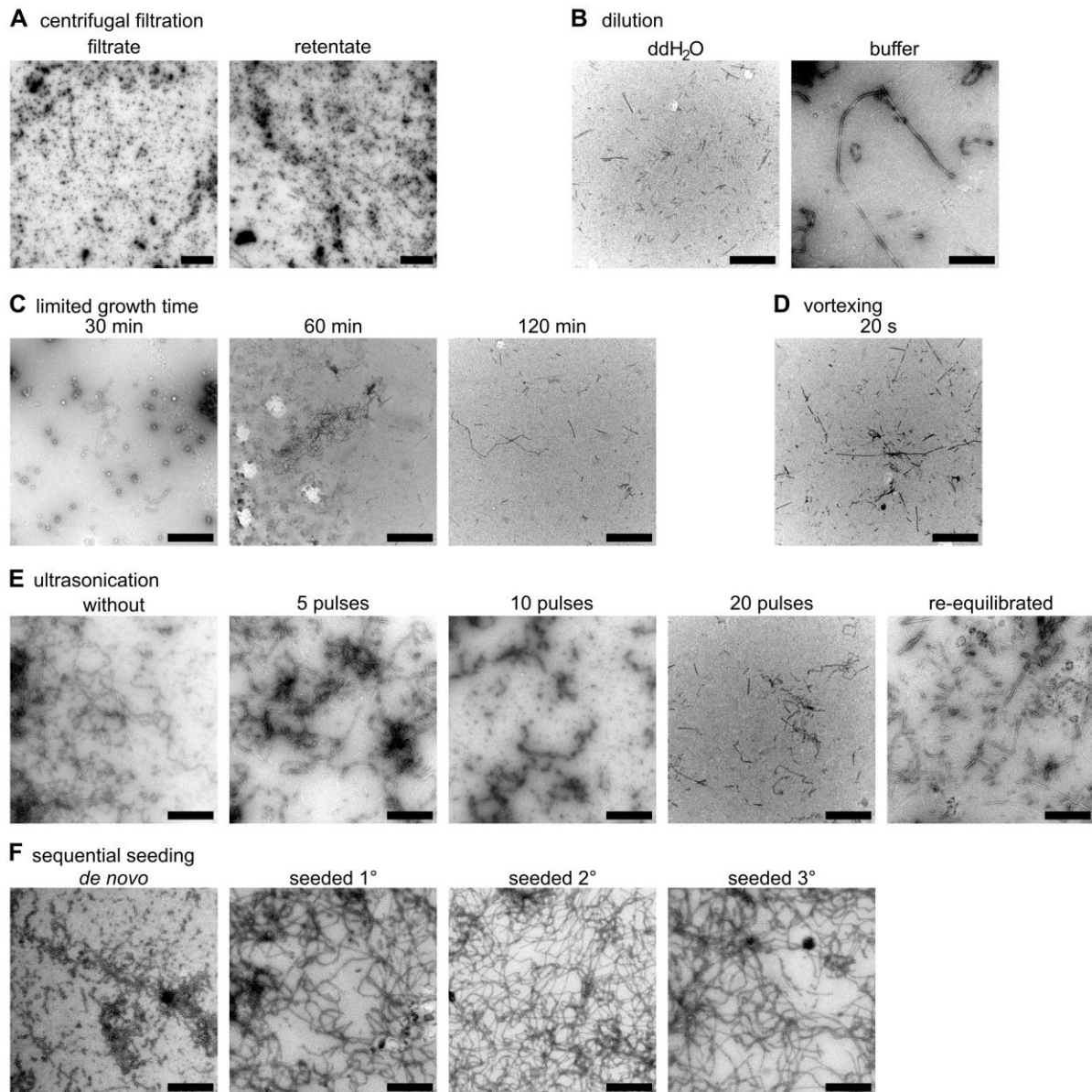


Figure A.7: TEM monitored screening of potential PTH₈₄ fibril preparation protocols for the structural analysis by cryoEM. **A** – Centrifugal filtration. An Amicon 2 ml filter with a cut-off of 100 kDa was used. **B** – Dilution by a factor of 20 in ddH₂O (left panel) or buffer (right panel). **C** – limited growth time with $t = 30$ min, 60 min, 120 min (from left to right). **D** – Vortexing for 20 s. **E** – ultrasonication with zero, five, ten or twenty pulses (from left to right). Ultrasonication with ten pulses followed by an incubation time of one hour (right panel). **F** – Sequential seeding. The images were acquired on a Zeiss EM900 electron microscope with an acceleration voltage of 80 keV. The scale bar in panel A corresponds to 2 μm , in panels B-F to 0.5 μm .

evident with increasing time. This method in principle led to individual fibrils but the samples still contained a substantial fraction of unconsumed monomer negatively affecting the background.

Vortexing the fibrils for 20 s (at full speed) directly after diluting by a factor of 20 surprisingly led to a considerable reduction of the number of fibrils on the grid (Figure A.7D). The visible fibrils were very short and heterogenous in size.

Ultrasonication using a sonication needle (probe) effectively reduced the size and number of fibril clusters and additionally induced fragmentation of fibrils as a function of applied sonication pulses (Figure A.7E). This effect was easily adjustable by the amplitude and the number of pulses (1 s pulse, 1 s pause). Both should be kept as small as possible to reduce potential side effects. The presented samples were sonicated with 10 % amplitude (Sonifier W-250 D, Branson Ultraschall, Dietzenbach, Germany). It is advised to use a sample volume high enough to reduce foam formation (which must be avoided) but low enough to maintain effective fibril fragmentation. Volumes of 50 to 150 μl sample fulfilled these requirements.

Sequential seeding was tested to promote single fibril morphs. Primary (*de novo*) fibrils were grown in 50 mM sodium borate, pH 9.0 at 60 °C over night.²¹¹ Three generations of seeded fibrils were generated (50 mM Na_2HPO_4 , 150 mM NaCl, pH 7.4 (Paper I)) by adding 5 %, referring to monomer equivalents, of generation $n-1$ as seeds to generation n . The seeded samples were quiescently incubated at 37 °C for 24 h. In summary, sequential seeding did not lead to a significant reduction of the sample complexity (Figure A.7F). Only a small increase of straight segments in the second and third generation was observed.

Probe-sonication as well as dilution in buffer led to the desired results of shorter, single fibrils with a good quality. A combination was chosen consisting of probe-sonication with ten pulses (1 s pulse, 1 s pause) at 10 % amplitude followed by dilution in freshly prepared buffer with an incubation time of 1 h prior to vitrification. Importantly, fibril growth needed to be conducted directly before sample preparation. This protocol was used for the sample which was chosen for image acquisition, particle picking and helical reconstruction as discussed in Chapter 2.4.4. An analysis of the β -turn propensity of pentapeptides as part of the theoretical structure considerations is displayed in Figure A.7A. An

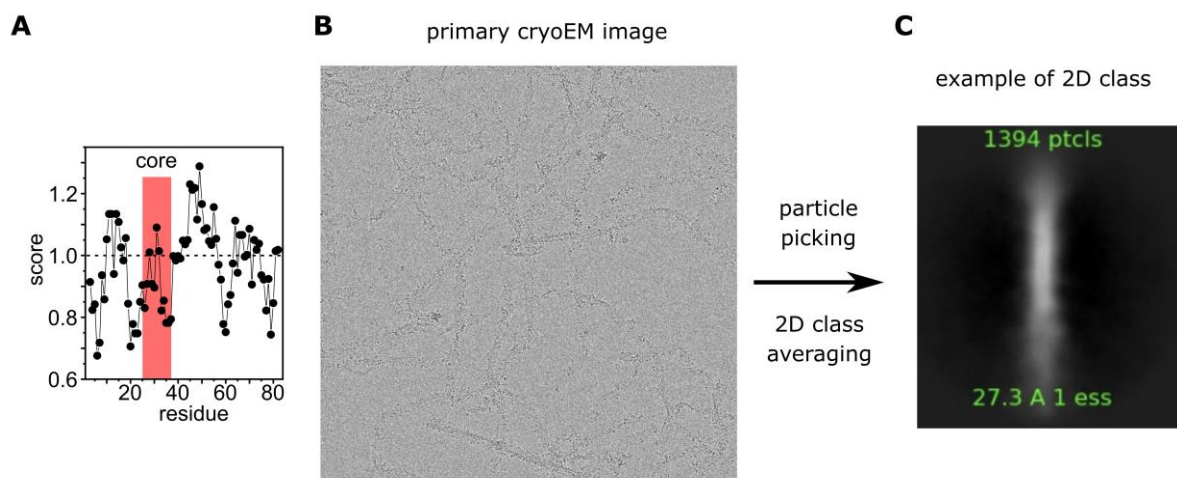


Figure A.8: Structural analysis of PTH_{84} fibrils. **A** – Analysis of the β -turn propensity using a window size of 5 residues.^{215,216} Scores > 1.0 are considered. The fibril core fragment is highlighted in red. **B** – Exemplary cryoEM image acquired at 92000 x magnification. **C** – Exemplary 2D classification from 1394 particles, showing the filamentous structure.

exemplary cryoEM image as well as a representative 2D class used for reconstruction are shown in Figure A.7B and C, respectively. The new sample preparation strategy was able to reduce the number of dark spots. However, fibril networks were still observed rather than individual fibrils.

In order to obtain a reconstructed model with a residue-resolution structure the sample preparation strategy will still need to be improved. It is suggested to vary the number of pulses during probe-sonication as well as the incubation time after dilution, or even interchange the two preparation steps. For the first approach, mesh-hole grids were used. Another suggestion is the usage of grids offering a surface for the fibrils to attach. This might have the advantage of eliminating the 3D orientation within the amorphous ice as a degree of freedom as well as enabling a washing step to remove residual monomers. Similar grids with a formvar/carbon coating were used with good experiences in nsTEM. Since fibrils grown at pH 5.3 in the presence of heparin were considerably more straight and rigid as well as regularly twisted (Figure 2.9 in the main text), this growth protocol might bear a high potential for successful cryoEM sample preparation.

List of Publications

All peer-reviewed publications with contributions from the author of this thesis released during the time of PhD studentship are listed below in the order of the date of publication. Papers associated to the PTH project as well as additional papers are given in their respective chronological order.

Papers Associated to the PTH project

Probing Polymer Chain Conformation and Fibril Formation of Peptide Conjugates (ref.²⁴¹)

Z. Evgrafova*, **B. Voigt***, M. Baumann, M. Stefani, W.H. Binder, J. Balbach

ChemPhysChem 2019, 20, 236-240

DOI: 10.1002/cphc.201800867

(* authors contributed equally)

contribution: recombinant production of label-free and ¹⁵N-labelled PTH₈₄ as well as the point mutation variants V2C and Q84C, conjugation of PTH₈₄ variants with thermoresponsive polymers and purification of the variants, fibril formation kinetics, NMR spectroscopy, electron microscopy (sample preparation and imaging)

Modulating the Fibrillization of Parathyroid-Hormon (PTH) Peptides: Azo-Switches as Reversible and Catalytic Entities (ref.²³²)

A. Paschold, **B. Voigt**, G. Hause, T. Kohlmann, S. Rothemund, W.H. Binder

Biomedicines 2022, 10, 1512

DOI: 10.3390/biomedicines10071512

contribution: assay set-up, supervision and partial interpretation of fibrillation kinetics

Heparin promotes rapid fibrillation of the basic parathyroid hormone at physiological pH (Paper III of this thesis, ref.²⁴²)

L.M. Lauth, **B. Voigt**, T. Bhatia, L. Machner, J. Balbach, M. Ott

FEBS Lett. 2022, 596, 2928-2939

DOI: 10.1002/1873-3468.14455

contribution: see Section 2.3 of this thesis

The Pro-Sequence of Parathyroid Hormone Prevents Premature Amyloid Fibril Formation (ref.²²⁷)

S. Sachan, C. Gonzalez Moya, **B. Voigt**, M. Köhn, J. Balbach

FEBS Lett. 2023, 597, 995-1006

DOI: 10.1002/1873-3468.14587

contribution: supervision of fibrillation kinetics, electron microscopy (imaging)

A Competition of Secondary and Primary Nucleation Controls Amyloid Fibril Formation of the Parathyroid Hormone (Paper I of this thesis, ref.²⁴³)

B. Voigt, M. Ott, J. Balbach

Macromol. Biosci. 2023, e2200525

DOI: 10.1002/mabi.202200525

contribution: see Section 2.1 of this thesis

The Prenucleation Equilibrium of the Parathyroid Hormone Determines the Critical Aggregation Concentration and Amyloid Fibril Nucleation (Paper II of this thesis, ref.²⁴⁴)

B. Voigt, T. Bhatia, J. Hesselbarth, M. Baumann, C. Schmidt, M. Ott, J. Balbach

ChemPhysChem 2023, e202300439

DOI: 10.1002/cphc.202300439

contribution: see Section 2.2 of this thesis

Papers Not Associated to the PTH Project

How Fluorescent Tags Modify Oligomer Size Distributions of the Alzheimer Peptide (ref.²⁴⁵)

J. Wägele, S. De Sio, **B. Voigt**, J. Balbach, M. Ott

Biophys. J. 2019, 116, 227-238

DOI: 10.1016/j.bpj.2018.12.010

contribution: electron microscopy (imaging)

Modulation of Amyloid β Peptide Aggregation by Hydrophilic Polymers (ref.²⁴⁶)

Z. Evgrafova, **B. Voigt**, A.H. Roos, G. Hause, D. Hinderberger, J. Balbach, W.H. Binder

Phys. Chem. Chem. Phys. 2019, 21, 20999-21006

DOI: 10.1039/c9cp02683e

contribution: electron microscopy (sample preparation and imaging)

Synthesis and Aggregation of Polymer-Amyloid β Conjugates (ref.²⁴⁷)

Z. Evgrafova, S. Rothmund, **B. Voigt**, G. Hause, J. Balbach, W.H. Binder

Macromol. Rapid Commun. 2020, 41, e1900378

DOI: 10.1002/marc.201900378

contribution: electron microscopy (sample preparation and imaging)

β -Turn Mimetic Synthetic Peptides as Amyloid- β Aggregation Inhibitors (ref.²⁴⁸)

S. Deike, S. Rothmund, **B. Voigt**, S. Samantray, B. Strodel, W.H. Binder

Bioorg. Chem. 2020, 101, 104012

DOI: 10.1016/j.bioorg.2020.104012

contribution: supervision of fibrillation experiments (including set-up of the assay), electron microscopy (imaging)

Lighting up Nobel Prize-Winning Studies with Protein Intrinsic Disorder (ref.²⁴⁹)

L. Piersimoni, M. Abd El Malek, T. Bhatia, J. Bender, C. Brankatschk, J. Calvo Sánchez, G.W. Dayhoff, A. Di Ani, J.O. Figueroa Parra, D. Garcia-Martinez, J. Hesselbarth, J. Köppen, L.M. Lauth, L. Lippik, L. Machner, S. Sachan, L. Schmidt, R. Selle, I. Skalidis, O. Sorokin, D. Ubbiali, **B. Voigt**, A. Wedler, A.A.J. Wei, P. Zorn, A.K. Dunker, M. Köhn, A. Sinz, V.N. Uversky

Cell Mol. Life Sci. 2022, 79, 449

DOI: 10.1007/s00018-022-04468-y

contribution: literature review and writing on G-protein coupled receptors (GPCR)

Inherent Adaptivity of Alzheimer Peptides to Crowded Environments (ref.²⁵⁰)

S. De Sio, J. Wägele, T. Bhatia, **B. Voigt**, H. Lilie, M. Ott

Macromol. Biosci. 2023, e2200527

DOI: 10.1002/mabi.202200527

contribution: electron microscopy (sample preparation and imaging)

Other Contributions

Scientific Contributions to Conferences (without SFB TRR 102 miniworkshops and retreats)

Chimaeras of a Thermoresponsive Polymer and the Parathyroid Hormone (poster)

International Discussion Meeting on Polymer Crystallization (IDMPC) 2017, 18.-20.09.2017,
Lutherstadt Wittenberg

Chimaeras of a Thermoresponsive Polymer and the Parathyroid Hormone (poster)

28th Conference on Protein Folding (Faltertage), 20.-22.10.2017, Halle (Saale)

Insights into the Amyloid Fibrillation Mechanism of the Parathyroid Hormone (poster)

2nd Meeting on Biophysics of Amyloid Formation, 20.-21.02.2018, Ulm

Probing Polymer Chain Conformation and Fibril Formation of Peptide Conjugates (talk)

5th Minisymposium of the SFB TRR 102, 08.06.2018, Leipzig

Probing Polymer Chain Conformation and Fibril Formation of Peptide Conjugates (poster)

Biennial Meeting of the German Biophysical Society, 16.-19.09.2018, Düsseldorf

Amyloid Fibril Formation of the Parathyroid Hormone and its Hybrids (talk)

29th Conference on Protein Folding (Faltertage), 26.-28.10.2018, Halle (Saale)

Amyloid Assembly of Peptide-Polymer Mixtures and Chimaeras (poster)

3rd Meeting on Biophysics of Amyloid Formation, 19.-21.02.2019, Ulm

Insights into the Monomer-Oligomer Equilibrium of the Parathyroid Hormone (poster)

4th Meeting on Biophysics of Amyloid Formation, 18.-20.02.2020, Ulm

Early Events in Amyloid Formation of the Parathyroid Hormone (poster)

65th Annual Meeting of the Biophysical Society, 22.-26.02.2021, held online

Supervised Graduation Theses

Umlandt, Marvin E.P.: *Thermodynamik und Kinetik der Fibrillierung des Parathormons (English translation: Thermodynamics and Kinetics of Fibril Formation of the Parathyroid Hormone)*, Bachelor thesis, Halle (Saale), 2017

Hennig, Florian: *Untersuchung der Fibrillenbildungskinetik des Parathormons und Seeding-Bedingungen (English translation: Investigation of Fibril Formation Kinetics of the Parathyroid Hormone under Seeding Conditions)*, Master thesis, Halle (Saale), 2018

Michael, Birte: *Kinetische und strukturelle Untersuchungen am Parathormon unter Crowding-Bedingungen (English translation: Kinetic and Structural Investigations of the Parathyroid Hormone under Crowding Conditions)*, Bachelor thesis, Halle (Saale), 2018

Kaffka, Tobias: *Einfluss Kovalent Gebundener Fluorophore auf Aggregation und Fibrillierung des humanen Parathormons (English translation: Influence of covalent Fluorophors on Aggregation and Fibril Formation of Human Parathyroid Hormone)*, Master thesis, Halle (Saale), 2019 (Master student in the lab of Dr. Maria Ott; contribution: supervision of fibrillation experiments, acquisition of TEM images)

Mielke, Frances: *Biophysikalische Untersuchungen von Parathormonfibrillen unter dem Einfluss von Hofmeistersalzen (English translation: Biophysical Investigation of Fibrils of the Parathyroid Hormone under the Influence of Hofmeister Salts)*, Bachelor thesis, Halle (Saale), 2020

Other Student Projects

Steinicke, Lukas: *Untersuchung der Fibrillierung des Parathormons (english: Investigation of the Fibril Formation of the Parathyroid Hormone)*, "Orientierungspraktikum" (2-week internship, medical physics), Halle (Saale), 2018

Schneider, Jakob: *Concentration Dependent Structural and Hydrodynamic Changes of the Parathyroid Hormone*, "Forschungsgruppenpraktikum" (6-week internship, biochemistry), Halle (Saale), 2019

Nosenko, Paul: *Untersuchung zur Konzentrationsabhängigkeit der Struktur und Fibrillenbildung des Parathormonfragments PTH₁₋₃₄ (English translation: Investigation of the Concentration Dependence of the Structure and Fibril Formation of the Parathyroid Hormone Derived Fragment PTH₁₋₃₄)*, "Orientierungspraktikum" (2-week internship, medical physics), Halle (Saale), 2021

Acknowledgments

This thesis would not have been possible without the help, support and contribution of many people. First of all, I would especially like to thank Prof. Dr. Jochen Balbach for letting me autonomously develop the PTH₈₄ project and for his patience which was undoubtedly necessary for this. Thank you for your great supervision, the fruitful discussions as well as the conferences and events we joined together.

I am honestly and very thankful to Prof. Dr. Mike Schutkowski as the first reviewer of my thesis and to Jun.-Prof. Dr. Wolfgang Hoyer that he accepted to be the external reviewer.

This work was financed by and was part of the SFB TRR 102 “polymers under multiple constraints”. I am very grateful to all SFB members, especially to Dr. Ann-Kristin Flieger, Dr. Thomas Michael, Beate Horn and Nicole Haak for the nice atmosphere and for the organization of those many meetings and events. The iRTG provided an environment for me to grow and to learn from other scientists of different fields. As a biochemist working together with (polymer) physicists and chemists, it was an educational, exciting experience to be exposed to the sometimes different terminologies and scientific mindsets (this is based on reciprocity, I assume). In this context, I would like to thank Prof. Dr. Darius Hinderberger who was my mentor in the iRTG. Additionally, I would like to thank the members of RTG 2467 “Intrinsically Disordered Proteins”.

I am grateful to my many collaboration partners at the platereader, electron microscope and beyond: Thank you Dr. Zhanna Evgrafova, Dr. Stefanie Deike, Newton Sen and André Paschold (Binder group), Elana Kysil, as well as Jana Wägele, Dr. Silvia De Sio, Twinkle Bhatia, Luca M. Lauth, Tobias Kaffka and Theresa Simon (Ott group) for the cooperation and the many, many papers we published together!

I would especially like to thank Dr. Gerd Hause and Simone Fraaß for the collaboration and the always warm and friendly atmosphere. Over the years, TEM imaging became one of my favorite techniques. A big thank you also to the cryoEM people Dr. Ioannis Skolidis, Dr. Fotios Kyrillis, Dr. Farzad Hamdi and Jun.-Prof. Dr. Panagiotis Kastiris for the nice and enjoyable collaboration.

I would also like to thank the people who introduced me to new techniques: Thank you Peter Leube (Hinderberger group), Dr. Erik Schreck (Widdra group), Dr. Tobias Thalheim and Martin Frenzel (Cichos group in Leipzig).

A special and big thank you goes to Prof. Dr. Carla Schmidt and Julia Hesselbarth for their important native MS results that really helped to shape the prenucleation project.

A person that was really important for my scientific development, for my understanding of fibril formation and for the fibrillation project in general is Dr. Maria Ott. Thank you so much, also for our joint papers!

This work would not have been possible without all the current and former members of “BHS7”, the biophysics group and the NMR group of Prof. Dr. Kay Saalwächter. Thank you Dr. Andi Klamt, Dr. Anton Mordvinkin, Celia Gonzalez Moya, Constanze Westphal, Prof. Dr. Detlef Reichert, Heike Böcker, Heiner Raum, Manuel Weber, Marco Gumpert (also for the special-ingredient-Met), Dr. Mareen Schäfer, Matthias Altenstein, Dr. Matthias Dreydoppel, Dr. Monika Baumann, Natalie Breitkopf, Dr. Paul Becker, Pierre Seiboth, Rositta Mothes, Dr. Susanne Weininger, Shubhra Sachan, Dr. Tobias Gruber, Dr. Yury Golitsyn (just to name a few) and also to „my students“ Marvin Umlandt, Florian Hennig, Birte Michael, Frances Mielke, Lukas Steinicke, Paul Nosenko and Jacob Schneider for the enjoyable atmosphere and all the social events. I am especially grateful to Dr. Ulli Weininger, Stefan Gröger and Kathrin Waldheim for their educational and extensive scientific, technical and lab support, and to Malte Neudorf for the many unforgettable moments.

I would also like to thank the parathyroid hormone for never failing to surprise me, even when I finally managed to reveal some of its secrets.

Last, but not least, I want to thank my parents, family and friends for their never-ending support. A great and honest thank you goes to my loving wife, who always and in every second supported me, and to my son.

Curriculum Vitae

Name: Bruno Voigt
 Nationality: German
 Date of Birth: 14.08.1991
 Place of Birth: Halle (Saale)

Education

<i>04/2017-present</i>	<p>Doctorate, Martin-Luther-Universität Halle-Wittenberg, Faculty of Natural Sciences II, Institute of Physics, Biophysics Supervisor: Prof. Dr. Jochen Balbach</p> <p><i>including</i></p> <p><i>04/2017-06/2023</i> member of the integrated Research Training School (IRTG) of the SFB/TRR 102 “<i>polymers under multiple constraints</i>”</p> <p><i>06/2022-10/2022</i> parental leave</p> <p><i>10/2019-12/2020</i> associated member of the Research Training School RTG2467 “<i>Intrinsically Disordered Proteins – Molecular Principles, Cellular Functions and Diseases</i>”</p>
<i>10/2014-03/2017</i>	<p>Master studies (Biochemistry), Martin-Luther-Universität Halle-Wittenberg graduation: Master of Science (M. Sc.), grade 1.1</p>
<i>10/2011-10-2014</i>	<p>Bachelor studies (Biochemistry), Martin-Luther-Universität Halle-Wittenberg graduation: Bachelor of Science (B. Sc.), grade 1.9</p>
<i>08/2004-07/2010</i>	<p>High School education, Gymnasium Landsberg graduation: Abitur, grade 1.1</p>



Statutory Declaration (Eidesstattliche Erklärung)

Hiermit erkläre ich an Eides statt, dass ich die vorliegende Arbeit selbstständig und ohne fremde Hilfe angefertigt und keine anderen als die angegebenen Quellen und Hilfsmittel verwendet habe und die den benutzten Werken wörtlich oder inhaltlich entnommenen Stellen als solche kenntlich gemacht habe. Weiterhin versichere ich, dass die vorliegende Arbeit weder in der gegenwärtigen noch in einer anderen Fassung als Dissertation an anderer Stelle eingereicht wurde.

Halle (Saale), den _____

Bruno Voigt